Alma Mater Studiorum – Università di Bologna

DOTTORATO DI RICERCA IN

SCIENZE BIOTECNOLOGICHE, BIOCOMPUTAZIONALI, FARMACEUTICHE E FARMACOLOGICHE

Ciclo XXXV

Settore Concorsuale di afferenza: 03/D1

Settore Scientifico disciplinare: CHIM 08

TITOLO TESI

Strategies to hijack MTs dysfunction in

neurodegenerative tauopathies:

Design and synthesis of novel CNS-disease-modifying tools

Presentata da: Stefania Demuro

Coordinatore Dottorato

Prof. Maria Laura Bolognesi

Relatore

Prof. Andrea Cavalli

Co-relatori

Dott.ssa Rita M.C. Di Martino

Dott. Samuel H. Myers

Esame finale anno 2023

Table of contents

Abstract

Microtubule (MT) assembly and dynamics are essential for the correct maintenance of a proper neuronal functionality. These processes are regulated by several proteins including (MT)-associated protein tau, whose aberrant hyperphosphorylation promotes its dissociation from MTs and its abnormal intraneuronal deposition into neurofibrillary tangles (NFTs), a common neurotoxic hallmarks of neurodegenerative tauopathies. To date, no disease-modifying drugs have been approved by the regulatory bodies to combat central nervous system (CNS) tau-related diseases. The multifactorial etiology of these conditions represents one of the major limits in the discovery of effective therapeutic options. In addition, tau protein functions in the CNS are orchestrated by diverse post-translational modifications (PTMs) among which phosphorylation mediated by protein kinases (PKs) plays a leading role. In this context, conventional single-target therapies are often inadequate in restoring perturbed networks and fraught with adverse side-effects. Therefore, the urgent need to achieve the desired therapeutic effect by simultaneous modulation of key targets and checkpoints, encouraged scientists to apply well-concerned polypharmacology strategies. This thesis reports two distinct approaches to hijack MT defects in neurons. The first is focused on the rational design and synthesis of first-in-class triple inhibitors of GSK-3β, FYN, and DYRK1A, three close-related PKs, which act as master regulators of aberrant tau hyperphosphorylation. Attracted by the potential of multi-target directed ligands (MTDLs), a merged multi-target pharmacophore strategy was applied to simultaneously modulate all three targets and achieve a disease-modifying effect. **ARN25068 (72)**, bearing a thieno[3,2-

d]pyrimidine core, was selected and deeply characterized as a promising starting point endowed with a well-balanced *in vitro* inhibitory potency against GSK-3β and FYN in the low nanomolar range and low micromolar potency against DYRK1A. A computationally and crystallographic driven Structure-Activity Relationship (SAR) exploration around **72** allowed to rationalize the key structural modifications conducive to the improvement of binding affinity towards DYRK1A, while maintaining a balanced potency against all three targets. To achieve this, a new generation of quite well-balanced triple GSK-3β/FYN/DYRK1A analogs exhibiting improved physicochemical properties, a good *in vitro* ADME profile, and promising cell-based anti-tau phosphorylation activity have been developed.

In Part II, MT-stabilizing compounds featuring the 1,2,4-triazolo[1,5-*a*]pyrimidine (TPD) scaffold have been developed, within Prof. Carlo Ballatore's Lab at the University of California San Diego (UCSD), to compensate MT defects in tau-related pathologies. Intensive chemical effort has been devoted to scale up **BL-0884** (**184**), identified as a promising MT-normalizing TPD, which exhibited favorable ADME-PK, including brain penetration and oral bioavailability, as well as brain pharmacodynamic activity. A suitable functionalization of the exposed hydroxyl moiety of **BL-0884** (**184**) with properly selected amino acids was carried out to generate corresponding esters and amides possessing a wide range of applications as prodrugs and active targeting for cancer chemotherapy.

Contribution statement

Fruitful and inspiring collaborations with scientists of different backgrounds led to the achievement of important goals and very promising results in both the medicinal chemistry projects illustrated in this thesis. The drug discovery campaign described in chapter 2, aimed at the development of the first-in-class triple GSK-3β/FYN/DYRK1A inhibitors for the treatment of tauopathies, has been conducted at the Italian Institute of Technology (IIT) in collaboration with Prof. Ruben Abagyan's laboratory (Dr. Conall Savey, C.S.) who provided a computational support of pivotal importance. Enzymatic assays were performed by Dr. Debora Russo (D.R.) and Dr. Ilaria Penna (I.P.) as part of the D3 PharmaChemistry research line under the guidance of Dr. Tiziano Bandiera at the IIT. Dr. Shailesh Tripathi (S.T.) from Prof. Cavalli's group carried out X-ray crystallographic studies corroborating molecular modeling results. *In vitro* metabolic stability analyses were conducted by Dr. Giuliana Ottonello (G.O.) from the Analytical Chemical facility in IIT. Additional biological studies illustrated in this thesis were outsourced (please see the experimental section and appendix for further information).

The second project, illustrated in chapter 3, focused on the development of MT-stabilizing TPDs, was conducted in collaboration with Prof. Kurt R. Brunden at the Center for Neurodegenerative Disease Research-University of Pennsylvania (UPenn), whose group designed and performed both *in vitro* and *in vivo* studies on the synthesized TPDs. Furthermore, Dr. Karol Francisco (K.F.), a former student of Prof. Carlo Ballatore, carried out a cytotoxicity evaluation on the synthesized compounds to assess their potential for cancer therapy.

As a Medicinal Chemistry Ph.D. student, I will empathize my medicinal chemistry effort with a focus on the synthesis and optimization of chemical entities possessing drug-like properties. I will therefore illustrate both project's development and their progress, during which mentors and contributors shaped and broadened my knowledge as a scientist.

Abbreviations

6-BIO	6-bromoindirubin-3′-oxime
6-OHDA	6-hydroxydopamine
A/T/N	Aβ biomarkers/tau biomarkers/neurodegeneration
AChEIs	Acetylcolinesterase inhibitors
ACN	Acetonitrile
AcOH	Acetic Acid
AcTub	Acetylated α-tubulin
AD	Alzheimer's disease
AGD	Argyrophilic grain disease
APP	Amyloid precursor protein
ASF	Alternative splicing factor
ATP	Adenosine triphosphate
Aβ	Amyloid beta
B/P	Brain-to-plasma
BBB	Blood–brain barrier
bvFTD	Behavioral FTD
CADD	Computer-assisted drug design
CBD	Corticobasal degeneration
CDCl$_3$	Deuterated chloroform
CDCl$_3$	Deuterated chloroform

CDK	Cyclin-dependent kinase
CDK1	Cyclin-dependent kinase 1
CH$_2$Cl$_2$	Dichloromethane
CHCl$_3$	Chloroform
CLKs	CDC2-like kinases
ClogD	Calculated distribution coefficient
ClogP	Calculated partition coefficient
CNS	Central nervous system
cryo-EM	Cryo-electron microscopy
CSF	Cerebrospinal fluid
C-spine	Catalytic spine
CTD	*C*-terminal domain
CTE	Chronic traumatic encephalopathy
DCC	*N,N′*-Dicyclohexylcarbodiimide
DFG	Asp-Phe-Gly
DH	DYRK homology
DIPEA	*N,N*-Diisopropylethylamine
DMAP	4-Dimethylaminopyridine
DMSO-*d6*	Deuterated dimethyl sulfoxide
DS	Down syndrome
DSCR	Down syndrome critical region
DYRK1A	Dual specificity tyrosine-phosphorylation regulated kinase 1A
E10	Exon 10
EOAD	Early onset AD

EtOAc	Ethyl acetate
EtOH	Ethanol
fAD	Familial AD
FDA	Food and Drug Administration
FTD	Frontotemporal dementia
FTLD	Frontotemporal lobar degeneration
GDP	Guanosine-5'-diphosphate
GGT	Globular glial tauopathy
GluTub	De-tyrosinated α-tubulin
G-rich	Glycine-rich
GSK-3	Glycogen synthase kinase 3
GTP	Guanosine-5'-triphosphate
HATU	Hexafluorophosphate Azabenzotriazole Tetramethyl Uronium
HB	H-bond
HLM	Human liver microsomes
LBs	Lewy's bodies
LOAD	Late onset AD
LSP	Local spatial pattern
MAO-A	Monoamine oxidase
MAP	MT-associated protein
MAPK	Mitogen-activated protein kinase
MAPT	MT-associated protein tau
MeOH	Methanol
MLM	Mouse liver microsomal

mnb	Minibrain
MPTP	4-phenyl-1-methyl-1,2,3,6-tetrahydropyridine
MRI	Magnetic resonance imaging
MT	Microtubule
MTAs	MT-Targeting Agents
MTBPs	MT-binding proteins
MTBR	MT binding region
MTDLs	Multi-target directed ligands
MTDs	MT-destabilizers
MTOCs	MT-organizing centers
MTSs	MT-stabilizers
MW	molecular weight
MW	Microwave
Na_2SO_4	Sodium sulfate
$NaNO_2$	Sodium nitrite
***n*-BuOH**	*N*-butanol
NDDs	Neurodegenerative disorders
NFTs	Neurofibrillary tangles
NH_4OAc	Ammonium acetate
NMDA	*N*-methyl-*D*-aspartate
NTPD	*N*-terminal projection domain
NTs	Neuropil threads
OA	Okadaic Acid
PD	Parkinson's diseases

PET	Positron emission tomography
PFs	Protofilaments
P-gp	P-glycoprotein
Ph1	Phase I
Ph2	Phase II
PHF	Paired helical filaments
PiD	Pick's disease
PK	Protein kinase
PK	Pharmacokinetic
pK$_a$	Acid dissociation constant
PKA	Protein kinase A
PNFA	Progressive non-fluent aphasia
POCl$_3$	Phosphoryl chloride
PP	Protein phosphatase
PPA	Polyphosphoric acid
PROTAC	Proteolysis targeting chimera
PRR	Proline-rich region
PSEN	Presenilin
PSP	Progressive supranuclear palsy
P-tau	Phosphorylated tau
PTMs	Post-translational modifications
QC	Quality control
QP	QikProp
R	Repeat

R-spine	Regulatory spine
SAR	Structure-Activity Relationship
SCID	Severe combined immune deficiency
SD	Semantic dementia
SFK	Src family kinase
S_k	Kinetic solubility
SN2	Nucleophilic substitution
SN_{Ar}	Nucleophilic aromatic substitution
SP	Senile plaques
SQD	Single Quadropole Detector
TEMPO	2,2,6,6-Tetramethylpiperidine 1-oxyl
THF	Tetrahydrofuran
TK	Tyr kinase
TLC	Thin-layer chromatography
TPDs	Triazolopyrimidines
TR-FRET	Time-resolved fluorescence energy transfer
T-tau	Total tau
TTM	Tumor-targeting module
WHO	World Health Organization
α-Tub	α-Tubulin

Chapter 1

1. Introduction

1.1 Microtubules (MTs) structure and functionality

MTs represent one of the major cytoskeletal components of most eukaryotic cells, including neurons. They serve as "railways" for intracellular transport, interact with accessory proteins to assemble into larger structures, which give rise to an organizational framework essential for orchestrating several intra and extra-cellular developmental processes such as proliferation, migration, and differentiation of neurons[1], vesicles transport within the cell unit, mitotic spindle formation during mitosis[2], maintenance of cell morphology and cell motility.[3,4] These multitasking protein polymers possess a highly complex structure, which vary widely among different cell types, and undergo diverse evolutionarily conserved post-translational modifications (PTMs). Methods such as X-ray crystallography and cryo-electron microscopy (cryo-EM) have enabled a reconstruction of the 3D structure of MTs gaining insights into their dynamic mechanisms and interactions with binding partners.[5-7] MTs structure generally comprises of 13 chains of head to tail arrangement of α–β heterodimers subunits mainly known as tubulin, stacked together in

protofilaments (PFs), which assemble forming hollow tubules of ~25 nM (Figure 1.1). The resulting highly dynamic polarized structure is characterized by a fast growing plus end with exposed β-tubulin, and a slow growing minus end with exposed α-tubulin. Although both α- and β-tubulin bind to one molecule of GTP (guanosine-5'-triphosphate) at the *N*-site and *E*-site, respectively, only the nucleotide on β-tubulin is hydrolyzed and exchangeable.
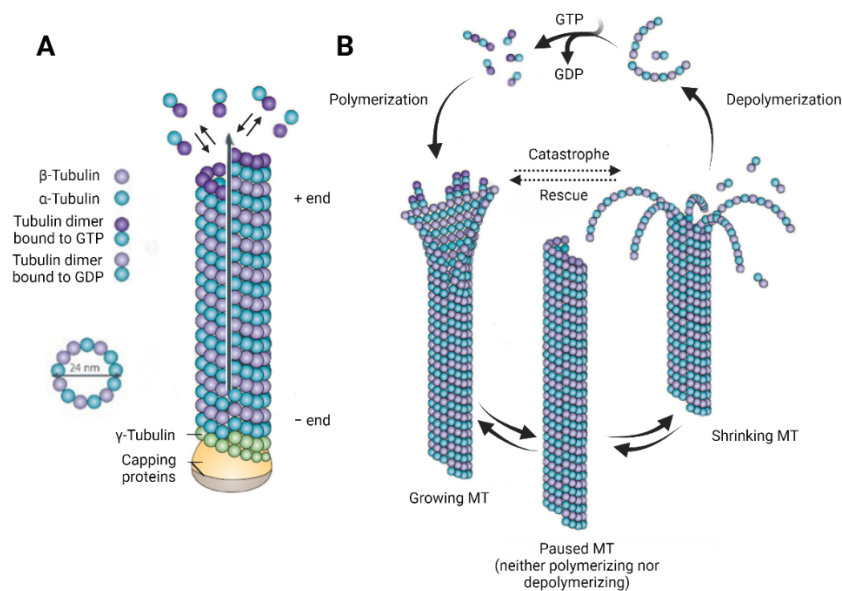
Figure 1.1 (A) Schematic representation of MTs structure; (B) growing and shrinking phases.[8]

GTP phosphorylation and hydrolysis drive the so-called dynamic instability of MTs, described as the alternation of "rescue" and "catastrophes" phases. This behavior is well explained by the GTP-cap model developed by Mitchison and Kirschner.[9] During their studies, the existence of MTs in two distinct phases of elongation and shortening, which do not interconvert frequently, was distinguished by the presence or absence of a GTP-liganded cap. The ends without the cap were observed to be unstable

going through a rapid depolymerization, while the GTP-capped lattice showed stability as a result of a slightly delayed GTP hydrolysis in respect to GTP-cap formation. Therefore, upon stochastic loss of the GTP-cap, MT ends undergo a rapid depolymerization, and collapse into tubulin– guanosine-5'-diphosphate (GDP) dimers (catastrophe). On the other hand, the GTP-capped β-tubulin interacts with α-tubulin subunits to allow the reverse process of polymerization (rescue).

The mechanisms at the base of the transitions between growth and shrinkage are poorly understood and have not yet been elucidated. Different *in vitro* investigations have suggested an "ageing" behavior as catastrophe-promoting event likely involving the accumulation of MT-lattice defects in old MTs.[10] MT rescues are understood even less than catastrophes. Structurally this happens because only dimers with GTP in their *E*-site can polymerize, but, after polymerization, the nucleotide is hydrolyzed and becomes nonexchangeable.[11]

Each α and β tubulin protomer is made up a compact folded "body" that participates in MT interactions (α and β tubulin intra and interdimer) and two C-terminal tails (two per dimer), which represent an essential part of the binding sites of cargo molecules and MT associated proteins (MAPs). To expand further, the *N*-terminal nucleotide-binding domain (residues 1–206) is formed by the alternation of parallel β-strands (S1–S6) and helices (H1–H6). The nucleotide-binding pocket is formed by each of the loops which connects each strand and helix (loops T1–T6) to the *N*-terminal end of the core helix (H7). After the core helix there is a smaller, second domain formed by three helices (H8–H10) and a mixed β-sheet (S7–S10). The intrinsically disordered, negatively charged C-terminal region is formed by two antiparallel helices (H11 and H12) that cross over the previous two domains.[11, 12]

Multicellular organisms contain multiple tubulin genes which express cell-type specific tubulin isoforms.[13] Among these, γ-tubulin is of note as the driving force for the so-called nucleation process. This protein possess high homology to α and β-

tubulins and localizes at the MT-organizing centers (MTOCs).[14] γ-tubulin interacts with the minus ends of MTs forming ring structures that serve as templates for MT growth through interaction with α-tubulin subunits. The other isotypes mainly differ in the terminal highly acidic 15 residues in the *C*-terminal region exposed on the outside surface of the MT. This latter surface not only interacts with motor and MT stabilizing proteins, but it is also prone to several PTMs such as glutamylation, glycylation, tyrosination, detyrosination and removal of glutamate residues.

1.1.1 PTMs upregulate MT activity

Acetylation and phosphorylation are frequent and highly conserved PTMs in living cells and contribute to generate on–off signals switches by adding or removing acetyl and phosphate groups on specific MT sites; others PTMs, namely polyamination, polyglutamylation and polyglycylation, gradually modulates MTs activity by adding different units of residues (Figure 1.2).[15, 16]
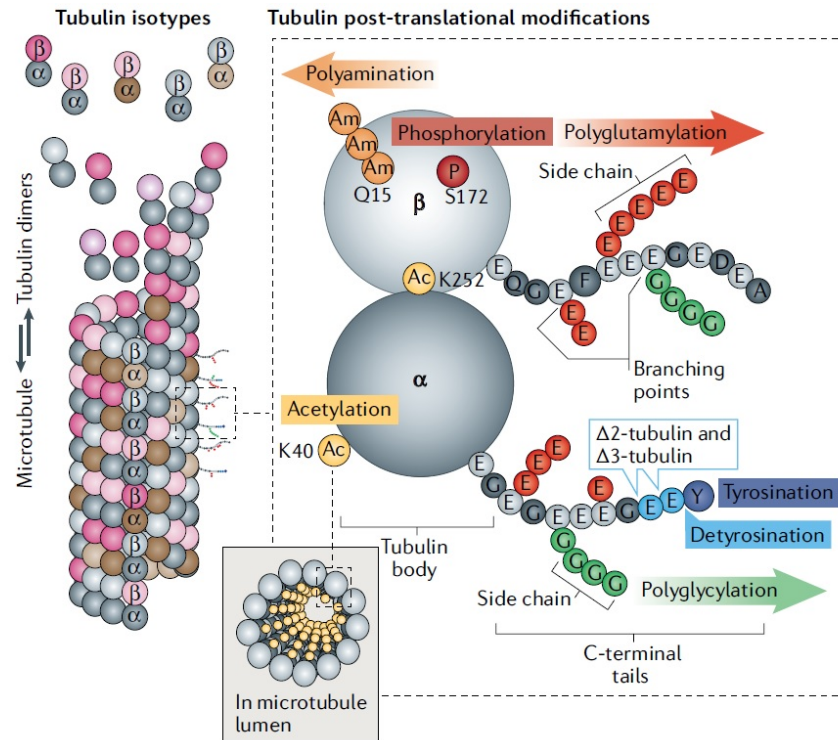
Figure 1.2 From Janke, C. *et al.*[15] Schematic representation of tubulin PTMs. Tubulin (light grey and pink) PTMs are catalyzed by a range of enzymes located either at the globular, highly structured tubulin bodies (acetylation (Ac), phosphorylation (P) and polyamination (Am)), or at the unstructured C- terminal tails of tubulin (glutamylation, glycylation, tyrosination, detyrosination and removal of glutamate residues to produce Δ2- tubulin and Δ3-tubulin).

Some of these biochemical transformations assist in the regulation of the mechanical properties of MTs by promoting their growth or shrinkage. For example, tubulin polyamination causes MTs to become resistant to depolymerization by adding positive charges.[17] Acetylation of α-tubulin at Lys 40 is also a marker of stable MTs and provokes a conformational change in their structure, which results in loss of interaction between Lys 60 and His 283 from α-tubulin molecules of the adjacent PFs. This lattice rearrangement reduces the flexural rigidity of MTs making them more resistant to mechanical breakage and disassembly.[18] Conversely, Lys 252 acetylation

or phosphorylation at Ser 172 of β-tubulin subunits by either cyclin-dependent kinase 1 (CDK1)[19] and dual specificity tyrosine-phosphorylation regulated kinase 1A (DYRK1A)[20], induces an opposite effect by hampering the incorporation of tubulin dimers into MTs.

1.1.2 MT-binding proteins (MTBPs)

Despite the intense contribution of different enzymes involved in stabilizing PTMs, naked MTs are unstable structures at the edge of catastrophe. To maintain the correct MT structure dynamic, it is therefore crucial the activity of a large group of MTBPs properly categorized by Goodson and Jonasson according to their function, activity and localization within the MTs environment.[4] MT-stabilizers (MTSs) and destabilizers (MTDs) together with capping proteins and bundlers/cross-linkers denote those proteins involved in MT-assembly, while MT-motors such as kinesin and dynein[21, 22] and motors modulators allow cargo processes onto the MT railways. Cytoskeletal integrators instead, coordinate interactions between MTs and at least one cytoskeletal entity.[23]

1.1.3 MT-associated proteins (MAPs)

While the acronym MTBPs broadly describes any protein that experimentally binds MTs, the term MAPs, is often used to describe a subfamily of MTBPs that contribute to maintain MTs function.

MAPs represent a variety of structural proteins that modulate the dynamic turnover of MTs across the binding to the MT-lattice through phosphorylation and dephosphorylation processes. Generally, they are filamentous and flexible positively charged proteins with a disordered tertiary structure. It has been proposed that they aid tubulin subunits to come together in the polymer by shielding the negatively charged *C*-terminal end of the α- β-subunits.[11]

This subgroup includes MAP4 (expressed in most tissues) and axonal and dendritic proteins as MAP2 and tau.[8] Tau, MAP2, and MAP4 share a conserved *C*-terminal containing the MT-binding domain, and contribute to MT stability as well as MT dynamics downregulation. For instance, MAP2 and tau compete with kinesin and dynein for binding to MTs, blocking these motor proteins to transport vesicle or organelle cargos.[24]

1.2 Protein tau as a master regulator in MT-stabilization

Tau was first discovered by Weingarten *et al.*[25] in 1785. They isolated a novel, heat stable protein in association with tubulin purified from porcine brain, which was essential for MT assembly.

Since then, extensive investigations have been performed to define tau structure and the related mechanisms underlining its activity and regulation. This protein is located in neuronal cells where it contributes, together with MAP2, to regulate the dynamic assembly and spatial organization of the neuronal cytoskeleton by supporting neurite differentiation and growth, as well as transporting motor proteins along the axons, which use MTs as support tracks.[26]

Tau function is mainly up and down regulated by phosphorylation from a wide range of proteins (primarily kinases, PKs, and phosphatases, PPs), which dysregulation is often linked to tau pathological behavior in several multifactorial neurodegenerative disorders (NDDs).[27] Thus, it represents one of the most studied MAPs due to its implication in tauopathies such as Alzheimer's disease (AD) and frontotemporal dementia (FTD), diseases that to date, have no cure and are in dire need of new treatment options.

1.2.1 Expression, structure and phosphorylation sites of tau

Tau is an intrinsically disordered protein encoded by the MT-associated protein tau (MAPT) gene, which comprises of 16 exons on chromosome 17q21 (Figure 1.3). Exon 1 (E1), E4, E5, E7, E9, E11, E12 and E13 are constitutive, while the others (E2, E3 and E10) undergo alternative splicing, which generates six different tau isoforms.[28] The alternative splicing of E10 has a lot of influence on the pathophysiology of different tauopathies since it may contribute to the differential vulnerability of brain regions to tau-associated disorders.
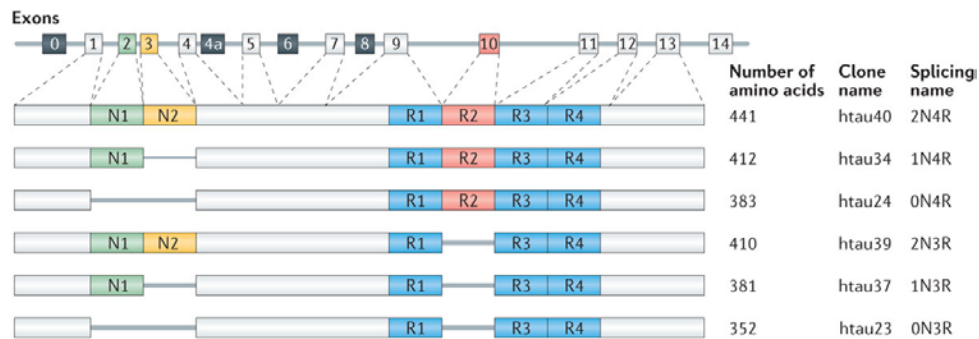
Figure 1.3 Schematic representation of the human MAPT gene and the splice isoforms of tau in the human brain.[29]

Tau structure is divided into four major functional domains: a *N*-terminal projection domain (NTPD), which modulates MT bundles formation by influencing specific processes such as MT nucleation,[30, 31] a proline-rich region (PRR), which aids MT binding; a MT binding region (MTBR) with 3 or 4 repeat sequences (R1-R4) essential for MT binding and assembly; a *C*-terminal domain (CTD) as MT-binding enhancer together with the abovementioned PRR.[32, 33]

Isoforms differ by the presence or lack of one or two inserts in the NTPD (N1 and/or N2), encoded by E2 and E3, and by three repeat sequences at the MTBR (R2 presence or not), encoded by E10.[29] A further classification distinguishes forms

containing 0, 1 or 2 inserts at the NTPD (0N, 1N and 2N, respectively) from others containing 3 or 4 repeat (R) sequences known as 3R or 4R.[34] The subcellular distribution of tau seems to be isoform-specific. Fetal human brain expresses only 3R tau, while adult brain expresses approximately equal amounts of both R-tau isoforms.[31, 35]

The highly disordered character of tau protein impedes the accurate determination of its interaction with MTs. However, thanks to several structural studies conducted by X-ray cristallography, cryo-EM and docking simulations, significant progress has been made over the course of the years.[36, 37]

Globally, tau is randomly distributed on the MTs outer surface (both MT tips and lattice[38]) and forms a "fuzzy coat"[39] with tubulin adopting a hairpin conformation through interaction with R2 and R3 repeats.[40, 41]

The correct functionality, folding and interaction of tau protein with MTs are complex physiological processes ensured by PTMs[27] where phosphorylation (Figure 1.4) represents one of the earliest and most prevalent modifications associated to the formation of pathological inclusions and aggregates in NDDs.

A total of 85 putative Ser, Thr and Tyr phosphorylation sites are exposed to the insertion or the removal of negatively charged phosphate groups by an extensive variety of PKs and PPs, respectively. Nowadays, more than 40 phosphorylation sites have been identified (a summarizing table can be found at "https://www.kcl.ac.uk/people/diane-hanger", accessed on January 30th, 2023), with the highest concentration of modifications in the MT interaction aiding regions such as the PRR and *C*-terminal tail adjacent the MTBR.[42]
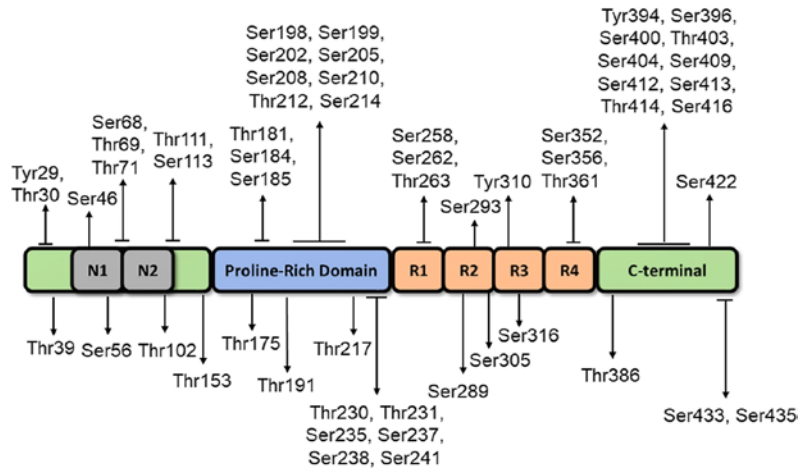
Figure 1.4 Schematic representation of the longest isoform of tau protein expressed in human brain (2N4R tau, 441 amino acids) containing some of the position of identified phosphorylation sites found in AD brains.[43]

Although phosphorylation of tau protein by tau-associated PKs will be better discussed in the following sections, it is relevant to briefly mention the biologically equivalent dephosphorylation processes performed by PPs.

PPs carry out the removal of phosphate groups balancing the activity of PKs. Protein phosphatase 2A (PP2A) is recognized as the major enzyme in the brain, which accounts for ~ 71% of tau phosphatase activity; the remaining 29% activity is carried out by PP1, PP5, and PP2B.[44, 45]

1.3 MT dysfunction in complex disorders

Neurons are particularly vulnerable to MTs cytoskeleton defects. Catastrophic depolymerization of MTs is associated to the development of neurotoxic events, which lead to synaptic loss and consequent neuronal death. One of the major causes of this phenomenon is the aberrant hyperphosphorylation of tau protein, which promotes its dissociation from MTs, formation of its insoluble aggregates (paired helical filaments or PHF-tau) and consequent intracellular accumulation into neurofibrillary tangles

26

(NFTs), which constitutes one of the recurrent neuropathological hallmarks of disorders related to tau protein known as tauopathies.[46-48]

1.3.1 Tauopathies

Tauopathy is an umbrella term used to describe a group of adult-onset dementias, in turn, characterized by a phenotypic loss of memory. According to the World Health Organization (WHO), every three seconds someone in the world is diagnosed with dementia.[49]

The WHO Global status report of 2021 stated that 55 million people were affected by dementia in 2019 and the alarming estimates of 78 million of people living with these diseases in 2030, increasing to 139 million in 2050, with projections for increases in global costs of the disorder up to 2.8 trillion US dollars by 2030.

Along with the aforementioned aberrant tau hyperphosphorylation, different modifications provoke tau dissociation from MTs including altered regulatory mutations, which cause an unbalancing in tau isoform expression profile associated to different clinical features.[31, 50, 51] On the basis of the isoforms that constitute NFTs, tauopathies can be divided into three groups. Aggregates featuring a high amount of 3R tau are defined as 3R tauopathies, 4R tau isoforms as 4R tauopathies and 3R/4R tauopathies show approximately an equal ratio of both isoforms. The same diseases have also been more recently described based on their fold similarity, broadening the knowledge in the field.[52]

Although tauopathies share the same common disease-relevant process, another medically significant classification distinguishes between primary and secondary disorders.

Primary tauopathies are characterized by having tau as a predominant component of the pathology (such as frontotemporal lobar degeneration (FTLD)-tau

subtype), while tau aggregation in secondary ones is a response to other pathological proteins or events (such as amyloid beta (Aβ) in AD).

An overview of tauopathies with their schematic description (classification, hallmarks symtoms and current treatments) is reported in Table 1. In the following sections one example of 3R and 4R tauopathies (Pick's disease (PiD) and progressive supranuclear palsy (PSP), respectively) will be briefly discussed, together with two major representatives of 3R/4R tauopathies (AD and FTLD-tau); a more detailed description is reviewed by Zhang *et al*.[53]

Table 1.1 Overview of different types of tauopathies according to their tau isoform classification

Tauopathy	tau isoform	Hallmarks	Symptoms	Current treatments	Ref.
Primary tauopathies					
PiD	3R	Pick bodies inclusions, ballooned neurons	Behavior change, social disinhibition, parkinsonism	No FDA approved disease-modifing drugs. AChE inhibitors and other symptom-reducing agents	54, 55
PSP	4R	Pretangles, globose NFTs	Vertical supranuclear gaze, palsy, postural instability with falls	No FDA approved disease-modifing drugs. AChE inhibitors and other symptom-reducing agents Non-pharmacological management	56, 57
CBD	4R	Pretangles, ballooned neurons, coiled bodies	Asymmetric limb apraxia and rigidity, executive dysfunction	No FDA approved disease-modifing drugs. Symptom-reducing agents (including botulinum toxin injections)	58

AGD	4R	Grains, ballooned neurons and coiled bodies	Personality change, emotional dysregulation, memory impairment	No FDA approved disease-modifing drugs. Symptom-reducing agents	[59]
GGT	4R	Pretangles, globular glial inclusions	Highly variable: may include behavior change, parkinsonism, cognitive impairment	No FDA approved disease-modifing drugs. Symptom-reducing agents	[60]
FTDL-tau	3R + 4R	NFTs	Personality change, cognitive impairment	No FDA approved drugs. Symptom- reducing agents (AChE inhibitors)	[61-64]
Secondary tauopathies					
AD	3R + 4R	Aβ plaques, NFTs	Memory loss, other cognitive dysfunction	AChE inhibitors, Aβ monoclonal antibodies	[65, 66]
CTE	3R + 4R	NFTs	Memory loss, personality change, motor decline	No available treatments	[67, 68]
Anti-IgLON5-related tauopathy	3R + 4R	NFTs	Sleep apnea, non-REM, sleep parasomnias, bulbar dysfunction	No available treatments	[69, 70]

1.3.1.1 PiD

PiD is a rare NND, which was described by Arnold Pick as a focal degeneration syndrome phenotypically associated with frontal and temporal lobes.[71] First linked to AD and other types of dementia, it was then defined as FTD to include other manifestations, which did not exhibit Pick-type histological changes.[72, 73]

Nowadays, PiD is defined as an unique primary tauopathy characterized by "Pick bodies", which are round shaped accumulated filaments possessing mainly 3R tau isoforms.[53, 74] It belongs to the 3R subgroup of tauopathies and has been reported to account for between 0.4 to 2.0% of all the dementia types, 3 up to 5 times less common than AD.[55] It is phenotypically characterized by circumscribed frontotemporal atrophy, which primary involves the left hemisphere rather than the right in 60% of cases.

The onset is generally between those aged of 35 to 75 years and is equally distributed between both male and females with appearance of an early change in social and personal behavior often associated with a lack of inhibition and a progressive change in language function.[75]

1.3.1.2 PSP

In 1964, Steele J.C. and collaborators analyzed nine cases of males affected by a progressive brain disorder, which they named PSP.[76]

For the majority of those cases the symptoms onset in the sixth decade with a steady progression, a mean survival rate of 5-7 years, and evidence of NFTs upon postmortem evaluation were seen.

PSP shows the common clinical features of dementia, summarized as (1) forgetfulness, (2) slowing of thought processes, (3) emotional or personality changes (apathy or depression with occasional outbursts of irritability), and (4) impaired ability to manipulate acquired knowledge.[77]

Peculiar histopathological hallmarks of this primary tauopathy is represented by star-shaped astrocytic clumps and NFTs with accumulation of a high percentage of 4R tau isoforms in the pallidum, subthalamic nucleus, red nucleus, substantia nigra, pontine tegmentum, striatum, oculomotor nucleus, medulla, and dentate nucleus.[56]

1.3.1.3 AD

Described for the first time in 1907 by Alois Alzheimer [78], who reported the case of a 51-year-old woman possessing a seriously impaired memory, with a post-mortem atrophic brain without macroscopic focal degeneration[79], AD represents a public health priority worldwide and it has been recognized as the most costly, deadly, and burdening disease of this century.[80]

This complex neurologic disorder is the most common cause of dementia[49] and thus subject to intense investigations. It has been defined as a secondary tauopathy histopathologically characterized by two main hallmark lesions: senile plaques (SP), made of Aβ and NFTs including both 3R and 4R tau isoforms.[81, 82]

Familial inheritance is associated with rare forms of AD, namely early onset AD (EOAD) and familial AD (fAD) characterized by symptoms that appear between 30-50 years of age. The primary factors of these sporadic forms of the disorder are mutations in three genes which encode: the amyloid precursor protein (APP), presenilin 1 (PSEN1), and presenilin 2 (PSEN2). On the other hand, aging and environment, along with a growing number of genetic factors have been reported as the major risk factors associated with the late onset AD (LOAD)[83] which clinical manifestations are observed after the age 65.[84, 85] Mixed pathologies often occur specifically in older individuals where along with SP and NFTs appear aggregates of α-sinuclein, known as Lewy's bodies (LBs), typical lesions of Parkinson's diseases (PD), suggesting common molecular pathogenic mechanisms between these NDDs.[86]

Affirmation of the amyloid hypothesis has placed the Aβ cascade at the center of AD pathophysiology[87, 88], despite it poorly explaining the sporadic AD forms.[89]

According with this theory, flaws in the production, accumulation or disposal of Aβ are the primary cause of the disease. The cleavage of the APP protein by β and γ-secretase enzymes in the brain produces two primary forms consisting of 40 or 42 amino acids of Aβ (Aβ40 and Aβ42). Failure in the clearance mechanisms of those two APP-cleaved forms and their consequent misfolding contribute to the formation of Aβ oligomers with a prevalence of Aβ42, these are less soluble and more prone to aggregation in comparison to Aβ40.

AD is a multifactorial disorder, which pathogenesis is better explained by the idea that a complex network of events, namely neuroinflammation, oxidative stress, and mitochondrial disfunctions, interact in a feed-forward loop. In further detail, a complex cross-talk of different pathogenic events lead to SP formations, which drive the formation of NFTs through a cascade mechanism. This sequence of complex events can cause neuronal loss of function and progressive cognitive impairment, affecting activities of daily living.[82, 85]

1.3.1.4 FTLD-tau

FTD is the third most prevalent form of mental deterioration after AD and Lewis body dementia and the second before the age of 65.[82, 90]

Generally, FTD denotes a cluster of syndromes (often including some abovementioned primary tauopathies such as PiD and PSP)[91] characterized by circumscribed degeneration of the prefrontal and anterior temporal lobes, which is better represented by FTLD pathology.[74, 92] It clinically presents three subtypes: behavioral FTD (bvFTD), semantic dementia (SD), and progressive non-fluent aphasia (PNFA), each bearing different phenotypes such as gradually arising executive, behavioral, or language dysfunction.[61]

The heterogeneity of this disorder is underlined by numerous sub classifications such as the nature of lesions causing neuronal defects. Thus, a neuropathological characterization divides FTLD into three molecular subgroups: FTLD-tau presenting a mutation in the MAPT gene, FTLD-TDP which attributes its name to alteration of the TPD-43 protein and FTLD-FET possessing aberrant inclusions of FUS and its phylogenetically associated proteins (EWS and TAF15).[93]

The first two are the most recurrent variants of FTLD accounting for ~ 40% (tau subtype) and 50% (TPD-43), while the latter is less frequent with ~ 5–10% of FTLD cases.

In this thesis, particular attention will be devoted to the possible therapeutic targeting of FTLD-tau subtype which etiology is largely suspected to be associated with MAPT mutations and the related alternative splicing surrounding E10.[94]

1.3.2 Early diagnosis of tauopathies

The multifactorial nature of AD and related tauopathies have hindered the discovery of effective interventions and diagnostic tools that could prevent or delay the onset of symptoms and support their early detection, respectively. The main issue is strictly related to the lack of a common biologically-based definition of these diseases.

Recently, AD in living people has been characterized based on the developmental biomarkers (imaging and biofluids), which are divided into three main categories (A/T/N) of neuropathologic change. In this A/T/N system "A" refers to the value of Aβ biomarkers, "T" the value of tau biomarkers and "N" to biomarkers of neurodegeneration.[95, 96] On the contrary, there are no clinically validated fluid biomarkers for FTLD-tau early detection or prediction of underlying pathologic change.[97] Structural and functional neuroimaging (Magnetic Resonance Imaging, MRI and positron emission tomography, PET) might help identify brain atrophy only

partially supporting the diagnosis of FTLD especially in the early course of the illness.[98]

The core AD cerebrospinal fluid (CSF) biomarkers Aβ42, total tau (T-tau), and phosphorylated tau (P-tau) reflect key elements of AD pathophysiology. For instance , increased levels of T-tau and P-tau together with decreased Aβ42 extent, stand for the typical AD biomarker pattern often called the 'Alzheimer's CSF profile'.[99] Furthermore, some tau phosphorylation state changes such as an increase in pThr 217 and pThr181 levels occur simultaneously to Aβ aggregation about 20 years before the onset of AD.[100]

Despite both CSF and PET scan are essential procedures to detect the main pathological biomarkers of AD, they represent costly and risky procedures possessing limited availability. For these reasons novel approaches in retinal imaging as an easy method to study NDDs[101], together with the evaluation of inflammation-related molecules[102], have been recently investigated. This is because, compared with CSF biomarkers and PET imaging scans, blood-based biomarkers are attractive as affordable alternatives for the diagnosis of AD.[103] The blood levels of Aβ peptides, tau protein and enzymes related to its phosphorylation including glycogen synthase kinase 3β (GSK-3β), DYRK1A are strictly related to both early onset and development of tauopathies and therefore represent potential biomarkers in dementia assessment.[103]

1.3.3 Current treatments for AD and related neurodegenerative tauopathies

To date, only six drugs (Figure 1.5) are available in the market for the treatment of AD[65], while no current U.S. Food and Drug Administration (FDA)-approved disease-modifying agents are available in the clinic for FTD.[98]
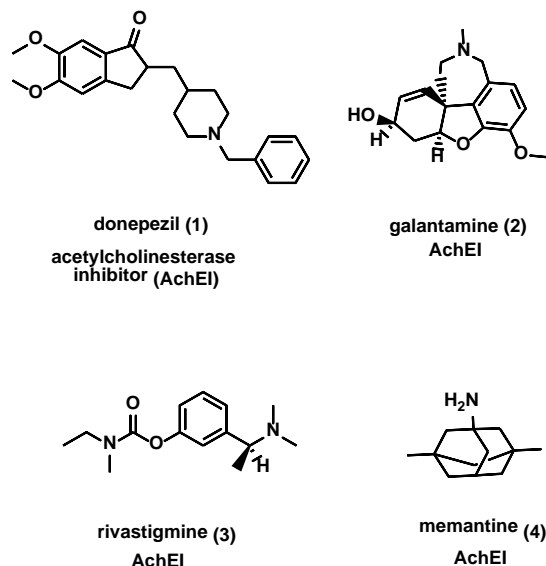
Figure 1.5 FDA approved drugs for the treatment of AD.

Despite advancements in the understanding of FTLD pathophysiology, genetics, neuropathology, and recent breakthroughs in neurodegenerative biomarkers, available treatments are directed into the modulation of behavioral, cognitive and motor symptoms management, providing a limited benefit.[104]

The outlook for AD therapy seems to be recently slightly improved, with the FDA approval of the monoclonal Aβ aggregates antibody Aducanumab (**5**) (Aduhelm™, Biogen, Figure 1.6).[105] Although still an object of debate, this drug demonstrated efficacy in the clearance of brain Aβ plaques, becoming the first disease-modifying therapy approved, 18 years since the last drug approved in 2021 (memantine, **4**, Figure 1.5). Notably, molecular dynamic simulations have been carried out to better understand **5** interactions with aggregated Aβ-forms compared to Aβ monomers (Figure 1.6). On January 6th,[106] 2023, Lecanemab (lecanemab-irmb; LEQEMBI™, Eisai and BioArctic), a more selective[66] humanized immunoglobulin gamma 1 (IgG1) anti-Aβ protofibril monoclonal antibody, was approved in in the USA via an Accelerated Approval Pathway. This immunotherapy agent demostrated

promising benefits in significantly decreasing loss of cognition versus the placebo in adults aged 50–90 years with early AD in a randomized, double-blind, phase III study [Clarity AD (NCT03887455)]. To full evaluate safety and efficacy of Lecanemab in AD, further trials are required.[107]
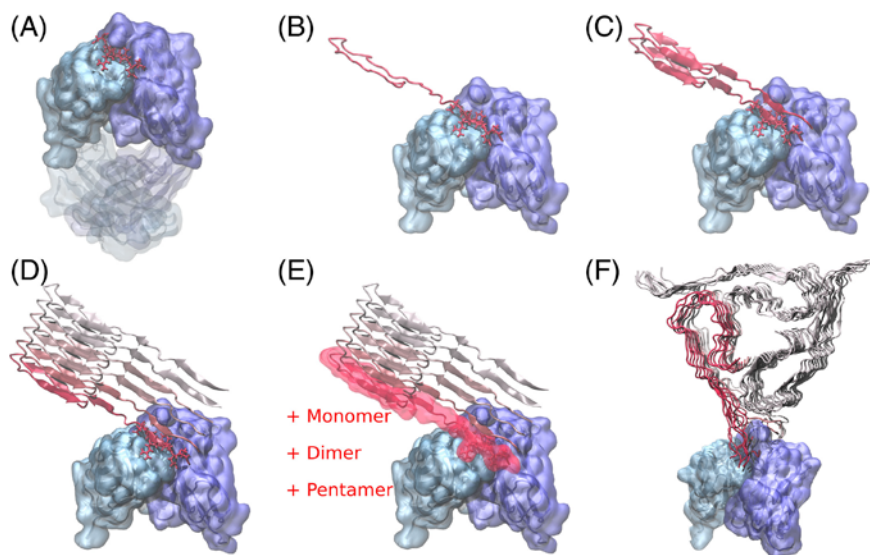

Figure 1.6 Modeling the interaction between AduFab (**5**) and Aβ1 − 40 amyloid from Frost *et al* [108]A) Crystal structure of Aβ peptide fragment (red) bound to AduFab (light and dark blue)(PDB ID. 6CO3).B-D) The bound Aβ fragment is completed to a full-length Aβ1 − 40 monomer, dimer and hexamer based on the disease-relevant Aβ fibril structure PDB 2M4J. The Aβ peptides are shown in cartoon representation colored in gray and red, with red corresponding to monomers closer to the AduFab crystal-binding site. E) The bound Aβ hexamer is elongated by an additional monomer (hexamer + 1), dimer (hexamer + 2), and pentamer (hexamer + 5), respectively, in order to study growth of an already bound Aβ protofilament. F) The Aβ undecameric protofilament (hexamer + 5 model) is extended to an entire fibril bound to AduFab, consisting of three parallel, undecameric PFs.

126 agents are currently in clinical trials for AD with the 82.5% mainly devoted to address the underlying biology of this complex multifactorial disorder (Figure 1.7)[109], showing the intense effort of both academia and industry to treat this unmet need. Moreover, the approval of novel disease-modifying agents for both AD and

related tauopathies represents a first step towards the advent of novel generation therapeutics.
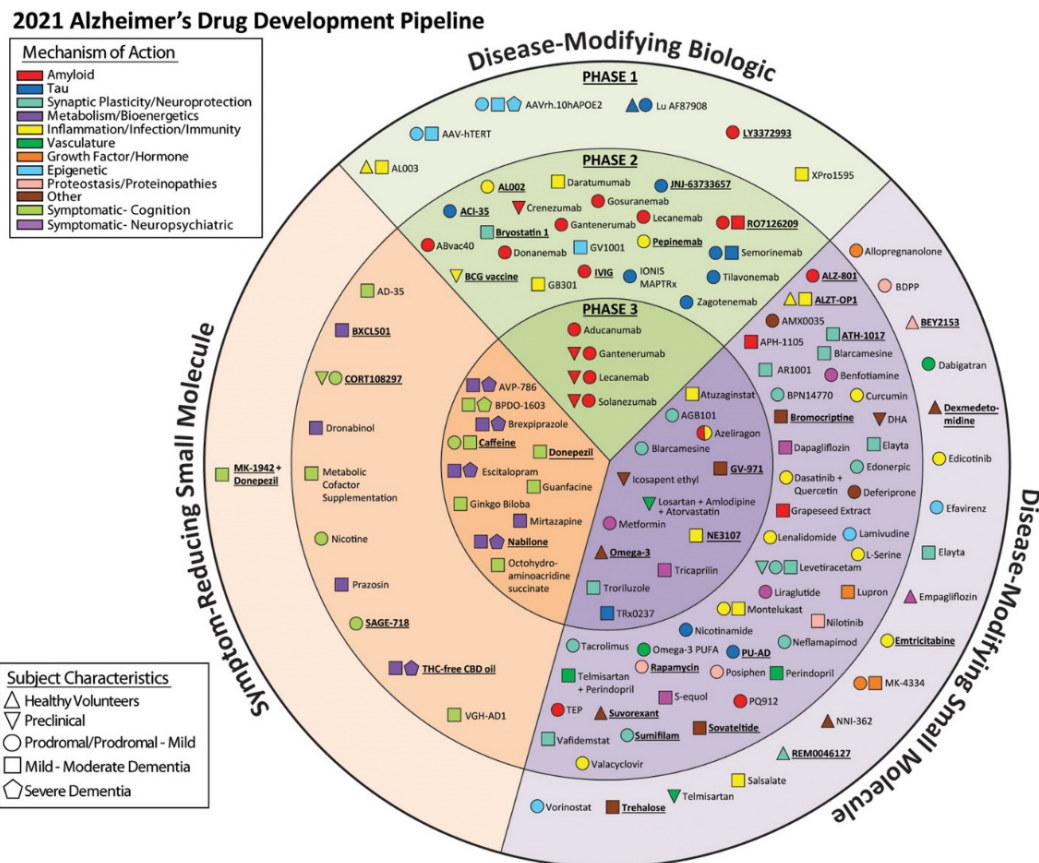
Figure 1.7 Graph showing agents in clinical trials for treatment of AD in 2021 (from Cumming *et al*).[109] The inner ring shows Phase 3 agents; themiddle ring comprises Phase 2 agents; the outer ring presents Phase 1 therapies; agents in green areas are biologics; agents in purple are disease-modifying small molecules; agents in orange are symptomatic agents addressing cognitive enhancement or behavioral and neuropsychiatric symptoms; the shape of the icon shows the population of the trial; the icon color shows the common AD ResearchOntology (CADRO)-based class of the agent. Agents underlined are new to the pipeline since 2020.

1.4 Challenges in central nervous system (CNS) drug discovery

CNS drug discovery presents unique challenges when compared with other research areas. The limited knowledge of the processes underlying diseases combined with the complexity of blood–brain barrier (BBB) and the lack of translational animal models to test new drug candidates (Figure 1.8) represent the bottleneck for the approval of novel therapeutics.[110, 111]

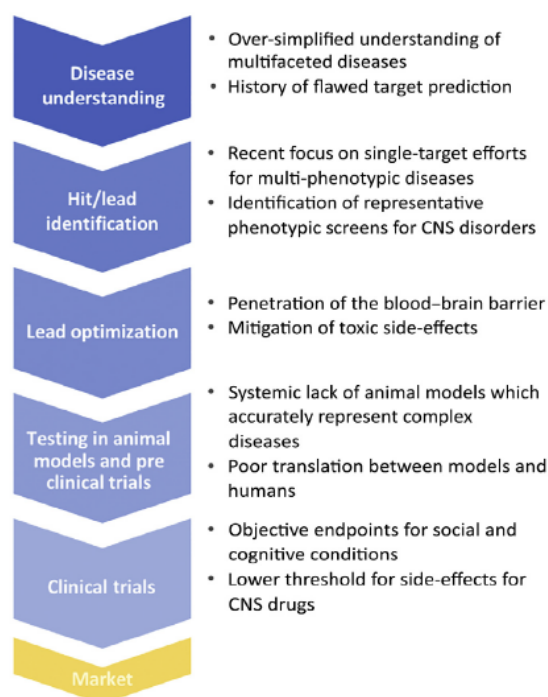**Figure 1.8** Examples of challenges in the drug development process for CNS agents, from Danon *et al*.[111]

1.4.1 BBB as dynamic and selective gatekeeper of the CNS

The BBB has been extensively investigated as a dynamic and selectively protective membrane responding to changes in its environment and as part of a more complex neurovascular unit in which endothelial cells, astrocytes, pericytes, and

neurons interact to restrict the flow of internal and external agents between the blood and the CNS. Furthermore, the BBB acts as a structural/physical barrier composed of endothelial cells and tight intercellular junctions that regulate diffusion of solutes between blood and brain (Figure 1.9). It also acts as biochemical selective barrier due to the presence of specific CNS-gatekeeper transport proteins expressed on the luminal (blood-facing) and abluminal (brain-facing) plasma membranes of the endothelial cells, which selectively increase brain permeability to essential nutrients or effectively prevent permeation of foreign compounds.[110] Moreover, a key element of this barrier is P-glycoprotein (P-gp), which is an ATP-driven efflux pump localized to the luminal plasma membrane, which handles a vast variety of substrates endowed with molecular weight (MW) ranging between 300 and 4000 Da. It limits penetration of drugs into the brain, greatly influencing CNS pharmacotherapy, contributing to cross-resistance to commonly prescribed drugs, including multiple classes of chemotherapeutics.[112, 113]
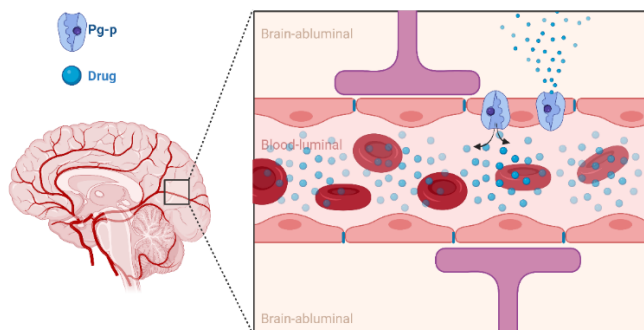
Figure 1.9 Schematic representation of the BBB and its dynamic selectivity. BBB is composed of endothelial cells and tight intercellular junctions that regulate diffusion of solutes between blood and brain. P-gp is expressed on the blood-luminal and brain-abluminal plasma membranes of the endothelial cells, contributing to selectively increase brain permeability to essential nutrients or effectively prevent permeation of foreign compounds (blue circles).

Particular attention in the CNS drug discovery is thus devoted to the design of ligands featuring chemical properties, which possibly allow passive BBB penetration,

including large size, high polar surface area and hydrogen-bonding ability. Size and lipophilicity are two crucial properties influencing the brain exposure and efficacy of a CNS drug candidate. Often, a balance must be found between decreasing size and increasing lipophilicity to make a drug more brain-penetrable, while simultaneously avoiding both efflux mechanisms (e.g., P-gp-mediated efflux) and drug sequestration elsewhere in the body (*e.g.*, plasma proteins, fatty tissue).[111]

As a rule of thumb, BBB crossing molecules possess: a polar surface area between 25–60 $Å^2$, at least one nitrogen, fewer than seven linear chains outside of rings, zero or one polar hydrogen atoms, the volume of 740–970 $Å^3$, the solvent accessible surface area of 460–580 $Å^2$, and a positive QikProp (QP) CNS parameter (https://www.schrodinger.com/products/qikprop, accessed on 13 January 2023). [114] Another useful tool to prioritize CNS lead candidates consists in the Pfizer's CNS multiparameter optimization,[115] which takes into account calculated partition coefficient (ClogP), calculated distribution coefficient at pH 7.4 (ClogD), MW, acid dissociation constant (pK_a) of ionizable groups, together with total polar surface area and the number of hydrogen bond (HB) donors.

1.5 Drug discovery strategies to combat neurodegenerative tauopathies

Tauopathies are NDDs characterized by neuronal tau inclusions, which contribute to the alteration of the cytoskeletal structure and function, a mechanism that offers a broad range of targets for disease-modifying therapeutics. Rösler *et al.* divided therapeutic agents into four main classes according to their targets: PTMs and aggregation of tau, proteostasis, disease propagation, and tau genetics (Figure 1.10).[116]

In this section, I will describe agents able to modulate PTMs and aggregation of tau protein focusing on MT-stabilizing agents and protein kinase inhibitors.
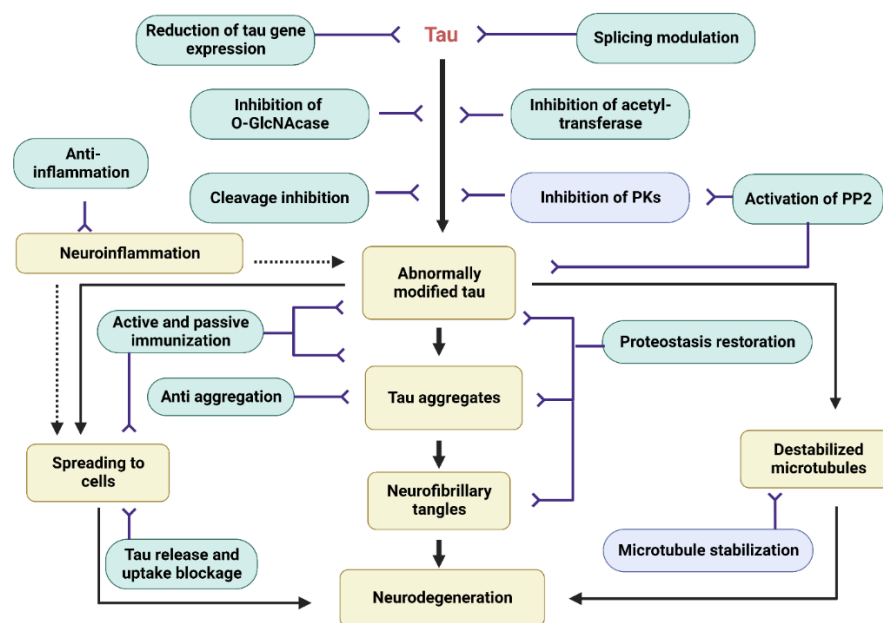
Figure 1.10 Circuit of disease-modifying therapeutics for primary tau-related pathologies from Rösler *et al.*[116] During the disease process, tau is abnormally modified and forms aggregates that trigger neurodegeneration. This process is accompanied by other events, such as neuroinflammation, spreading to other cells and a destabilization of microtubules. The yellow boxes represent key events in the disease process, whereas the round-shaped teal boxes show possible disease-modifying interventions; blue boxes represent the two chemical approaches described in this thesis.

1.5.1 MT-Targeting Agents (MTAs) in tauopathies

MTAs are a group of chemically diverse molecules able to interact with α and β-tubulin dimers via a stabilizing or a destabilizing activity. They have been widely employed in cancer therapy for their MT destabilizing properties and are now arising particular interest in NDDs thanks to the tau loss-of-function hypothesis, which attributes MT destabilization as consequence of tau loss of function. [117]

Tubulin binders possess wide chemical scaffolds mainly originating from plants, marine sponges, bacteria, and their synthetic derivatives.[118] Structural analysis of their interactions with MTs have enabled their extensive characterization and

allowed a classification based on their specific binding domain within tubulin, the building block of MTs.[119]

Six distinct MTA-binding sites on tubulin, referred to as the taxane site, the colchicine site, the vinca site, the maytansine site, the laulimalide/peloruside site, and the pironetin site have been structurally characterized in high resolution (Figure 1.11 A). Two of these are associated with MT stabilization (taxane and laulimalide/peloruside), while the other four binding sites causes MT destabilization (vinca, maytansine, colchicine, and pironetin sites). More recently, researchers from the University of Florida, identified a novel chemical cyclodepsipeptide entity isolated from marine cyanobacteria blooms, named gatorbulin-1 (**6**)[120] (Figure 1.11 B), able to interact with a seventh site of tubulin and possessing anticancer activity.

A critical challenge encountered by these natural products such as the taxanes paclitaxel (**7**) and docetaxel (**8**) (Figure 1.11 A) is to cross the BBB at nontoxic doses, crucial prerequisite that a CNS directed therapies need to address.[121]

Despite a tau transgenic mouse model treated with paclitaxel showing increased spinal nerve MT density and improved motor function, **7** was revealed to be a P-gp substrate in addition to its poor BBB permeability, making it unsuitable for the treatment of human tauopathies.[122]

Epothilone D (**9**) (Figure 1.11 B) instead, share the same binding site on β-tubulin of paclitaxel, but possesses favorable properties and brain penetration compared to its competing binders.

A

Lumen view Wall view

Maytansine/Tip

Taxane

Pelo/Lau

Colchicine

Gatorbulin

Pironetin

Vinca

α–tub (grey)

β-tub (white)

B

gatorbulin-1 (6)

R_1 = Ac, R_2 = Ph paclitaxel (7)
R_1 = H, R_2 = tBuO docetaxel (8)

ephothilone D (9)

R = CHO vincristine (10)
R = CH₃ vinblastine (11)

peloruside (12)

maytansine (13)

laulimalide (14)

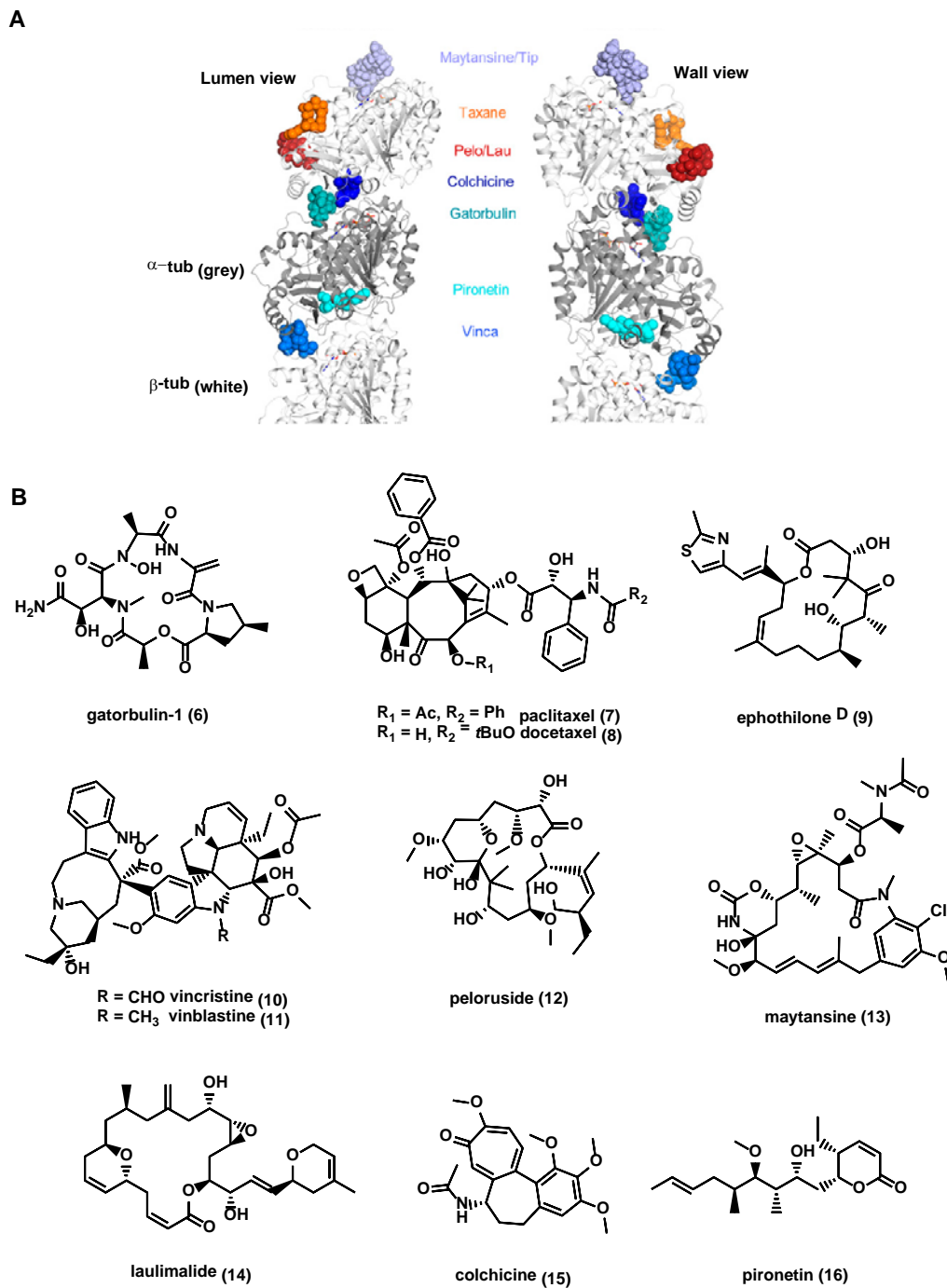colchicine (15)

pironetin (16)

Figure 1.11 Binding sites and structures of MTAs. (A) Tubulin heterodimer (α-tubulin in gray and β-tubulin in white) in ribbon representation, where six known binding sites have

43

been highlighted showing representative ligands in sphere representation: Gatorbulin (**6**) (PDB ID 7ALR, teal), epothilone (**9**) (PDB ID 4O4I, orange), vinblastine (**11**) (PDB ID 4EB6, light blue), peloruside (**12**) (PBD ID 4O4J, red), maytansine (**13**) (PDB ID 4TV8, violet), colchicine (**15**) (PDB ID 4O2B, dark blue); pironetin (**16**) (PDB ID 5FNV, cyan); B) Representative compounds targeting tubulin binding sites.[120]

Recently, the anti-cancer class of MT-active triazolopyrimidines (TPDs), phenylpyrimidines and related structures (**17**-**23**, Figure 1.12), have shown high potential for the development of novel CNS MT-stabilizing tools generally showing more favorable drug-like absorption than natural products.
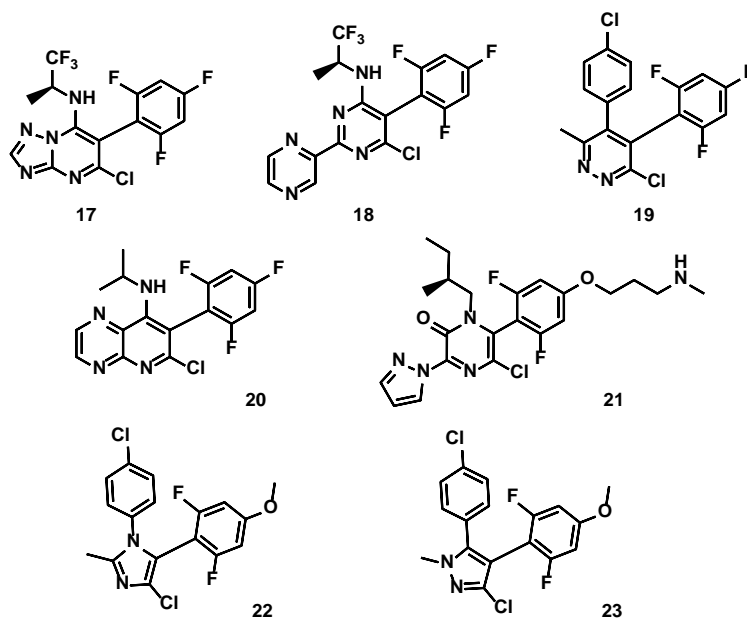

Figure 1.12 Chemical representation of small molecules characterized by MT-stabilizing and destabilizing activity

A better discussion on TPDs will be presented in the chapter 3 of this thesis where I will focus my attention on the development of brain-penetrant TPDs as disease-modifying therapies for AD and related disorders.

1.5.2 The Neurokinome in drug discovery

The human kinome, composed of 538 different PKs,[123] offers a wide range of new CNS-disease-relevant targets thanks to the master regulatory role of these enzymes in a myriad of signal transduction cascades.[124,125]

PKs dysregulation has been associated with a large portion of multifactorial disorders, including cancer and neurodegeneration, with a dramatic impact on the aging population. For this reason, PKs constitute very attractive and challenging targets for both industry and academia to tackle complex unmet medical needs.[126, 127] There are several small molecule kinase inhibitors in clinical trials for neurodegenerative indications.[109] However, the development of PK-targeted therapies in neuroscience has not been yet investigated heavily due to the several issues met within the CNS-related disorders research and development. These include the multifactorial nature of CNS diseases, the failure of many advanced CNS clinical trials, and the lengthy approval process of a novel CNS drug by the regulatory bodies.[128, 129]

1.6 PKs structure and functionality

PKs are dynamically and highly regulated signaling switches with the main function of carrying out phosphorylation of specific target proteins in cells, primarily on Ser, Thr, and Tyr residues.

PKs catalyze the following reaction:

$$MgATP^{1-} + protein\text{-}O:H \rightarrow protein\ O:PO_3^{2-} + MgADP + H^+$$

They are able to perform over a myriad of different substrates possessing a wide versatility in terms of regulation and function maintaining high degree of structural and sequence similarity among the family members.[130]

The conserved PK core includes a small *N*-lobe and a larger *C*-lobe (Figure 1.13 A and B). The first consists of five-stranded antiparallel β-sheet (β1–β5) and an αC-helix and encompasses a conserved glycine-rich (G-rich) binding loop essential to maintain active conformation and to consent the catalytic function of the enzyme. The *C*-lobe consists of α-helices with six conserved segments (αD - αI) and contains the catalytic loop K/E/D/D (Lys, Glu, Asp, Asp). The first aspartate (D, Asp) serves as a base that removes a proton from the OH function of the protein substrate facilitating the nucleophilic attack onto the γ-phosphorous atom of ATP. The second D instead, is a component of the well-known so-called activation segment, which for the majority of PKs begins with DFG (Asp-Phe-Gly), a key sequence to define active and inactive state of the enzyme.[131] The *N*- and *C*-lobes are connected by an ordered short linker sequence, called the hinge region, that recognizes the adenine base of an ATP molecule through two HBs (Figure 1.13 B). Furthermore, local spatial pattern (LSP) alignment of PK structures led to the discovery of two hydrophobic "spines", namely regulatory (R) and catalytic (C), which act as a bridge between the two N-lobe and C-lobe (Figure 1.13 C). The R-spine represents a hallmark of signature of an active PK and contain the regulatory residue to access to the back cleft mainly known as gatekeeper, while the C-spine binds the adenine ring of ATP and enables catalysis.[132, 133] The ATP-binding site is, therefore, located between the two catalytic domain lobes forming a deep binding cavity, which is rigid and highly conserved in its active state.[134]
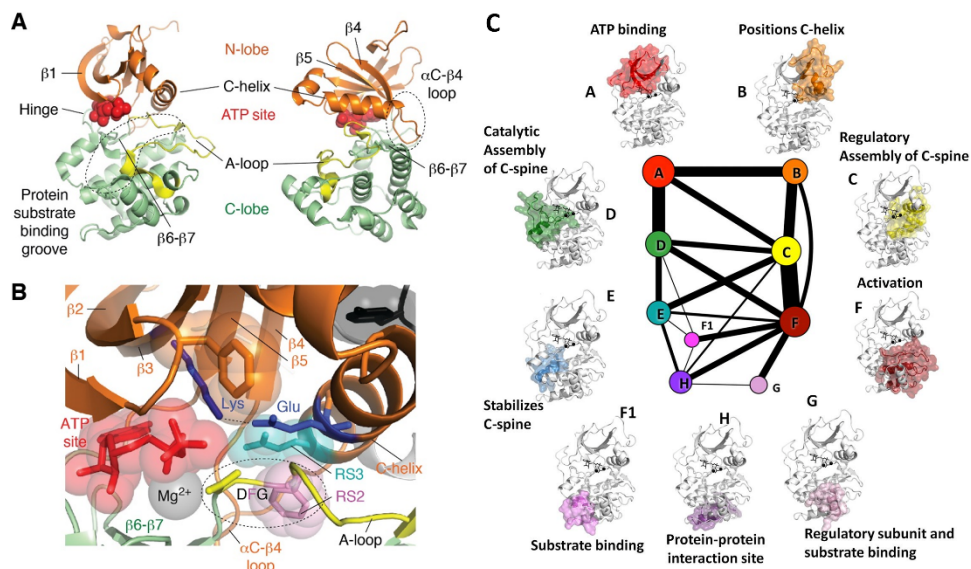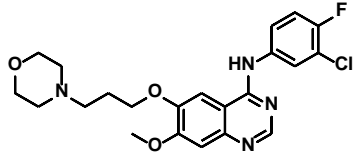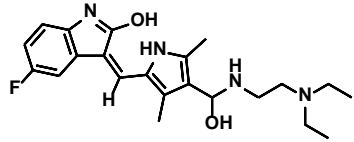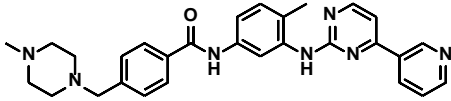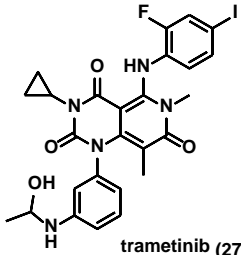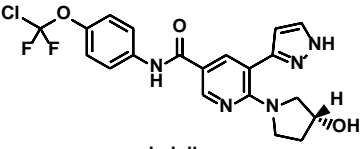
Figure 1.13 A) Key structural features of a kinase domain; B) magnified view of the interface between the lobes, showing the critical interactions[135]; C) Community map of Protein kinase A (PKA), for the closed conformation with ATP and two Mg bound. The size of each node represents the number of members (residue backbones and side-chains) of each community, and the edge weights are proportional to the thickness of the lines. The full kinase is shown in white, the communities are highlighted in red, and ligands are shown in black. The legend annotates each community by its function. [133]

To date, there are more than 90 clinically approved therapeutic agents that inhibit about two dozen different PKs (https://www.ppu.mrc.ac.uk/list-clinically-approved-kinase-inhibitors, accessed on January 30th, 2023).[135, 136]

Inhibition of PKs activity occurs through three different mechanisms of action: ATP-competitive, non-ATP competitive, and allosteric modulation. Furthermore, PK inhibitors have been categorized on the base of their binding mode.[134] For instance, Arter C. *et al.* classified PKs inhibitors as several different types, including type I, $I_{1/2}$ and II primarily interacting with the ATP pocket; III, IV as allosteric modulators adjacent or distant to the ATP binding regions and VI type mainly known as covalent inhibitors, which establish covalent interaction with specific Cys and/or Lys residues in the ATP binding pocket (Table 1.2).[135, 137]

Table 1.2 Examples of FDA approved PKs inhibitors (**24**-**28**) according to their interaction with the enzymes

Inhibitor type	Examples	PKs binding site
ATP competitive I	gefitinib (24)	active conformation (DFG-in and C-in)
ATP competitive I$_{1/2}$	sunitinib (25)	inactive conformation (DFG-in, C-out)
ATP competitive II	imatinib (26)	inactive DFG-out (C-in or C-out)
Allosteric III	trametinib (27)	adjacent to the ATP site
Allosteric IV	asciminib (28)	distant sites of the ATP site
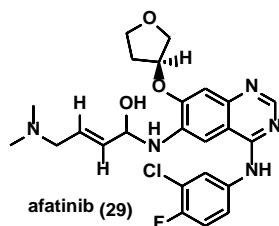
Covalent VI	 **afatinib (29)**	Irreversible interaction with the ATP site

In recent years, the proteolysis targeting chimeras (PROTACs) technology is receiving a great degree of attention from both academia and industry, emerging as a promising ubiquitination based protein-degradation strategy to achieve a disease-modifying effect. Widely directed to cancer therapy, PROTACs are starting to arise interest in the neuroscience field.[138]

One great example is the design and synthesis of PROTAC degraders of GSK-3β from Jiang X. and collaborators, which are the first reported protein degraders against a crucial PK in NDDs pathophysiology. Notably, they described PROTAC PG21 (**30**) (Figure 1.14), which showed GSK-3β degradation activity with 65.8% reduction in GSK-3β levels at 10 μM and neuroprotective effects in BV2 and HT-22 cells and paved the way towards rationalization of GSK-3β role in various disease states.[139]
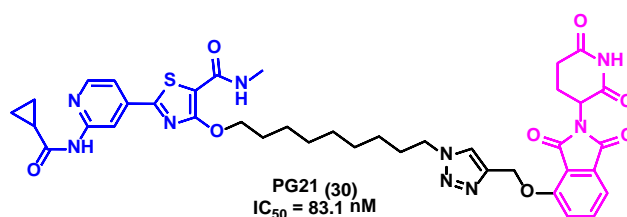

PG21 (30)
IC$_{50}$ = 83.1 nM

Figure 1.14 Chemical structure of GSK-3β degrader PROTAC PG21: the warhead (GSK-3β binder) is reported in blue, thalidomide (the anchor which recuits cereblon, CRBN) is depicted in in pink and the linker bearing a triazole moiety is depicted in black.

49

1.7 GSK-3β, FYN, and DYRK1A, emerging targets in the neurokinome

GSK-3β, FYN, and DYRK1A represent three closely related PKs broadly investigated in the neurokinome context due to their pivotal role in both the onset and development of neurodegenerative tauopathies such as AD, PiD, and FTLD.[140] Although characterized by different clinal manifestations, the discovery of common pathogenic mechanisms, including oxidative stress, abnormal protein deposition, mitochondrial deficit, glutamate excitotoxicity, and neuroinflammation, pointed to converging pathways in neurodegeneration.[141, 142] In this multifaceted pathological context, dysregulation of GSK-3β, FYN, and DYRK1A has been associated to *in vivo* tau-hyperphosphorylation[47] suggesting the great potential of the inhibition of these PKs to reverse aberrant tau phosphorylation.

1.7.1 GSK-3β

GSK-3 (Figure 1.15) is a multitasking Ser/Thr kinase primarily expressed in CNS and involved in regulating several cellular processes, including cellular division, proliferation, differentiation, and adhesion. Moreover, it is heavily implicated in the control of apoptosis, synaptic plasticity, axon formation, and neurogenesis. GSK-3 phosphorylates over a hundred different substrates, with several homologs having been identified in different organisms such as fungi, microorganisms, etc.[143, 144]

GSK-3 was isolated for the first time in 1980, from rabbit skeletal muscle and recognized as one of the five enzymes involved in glycogen synthase phosphorylation. Two different isoforms of this PK exist in mammalian cells, GSK-3α (51 kDa) and GSK-3β (47 kDa), both of which are widely expressed in the brain. High levels of expression of both proteins are seen in the hippocampus, cerebral cortex, and the Purkinje cells of the cerebellum, with high expression ratio towards GSK-3β isoform. The first crystal structures of GSK-3β showed the typical two-domain kinase fold

pattern composed of a β-strand domain (residues 25–138) and a α-helical domain (residues 139–343) at the *N*- and *C*-terminal ends. The ATP-binding site is located between the α-helical and β-strand domains and is surrounded by the glycine-rich loop and the hinge region. The activation loop (residues 200–226) progresses to the surface of the substrate binding groove, and the β-strand domain contains a highly conserved short helix (residue 96–102), containing two residues, Arg 96 and Glu 97, which are mainly involved in the catalytic activity of the protein. Moreover, Cys199 located at the entrance of the GSK-3β ATP binding site, has been recognized to play a key role in the irreversible or pseudo-irreversible inactivation of the enzyme by covalent interaction. [145]
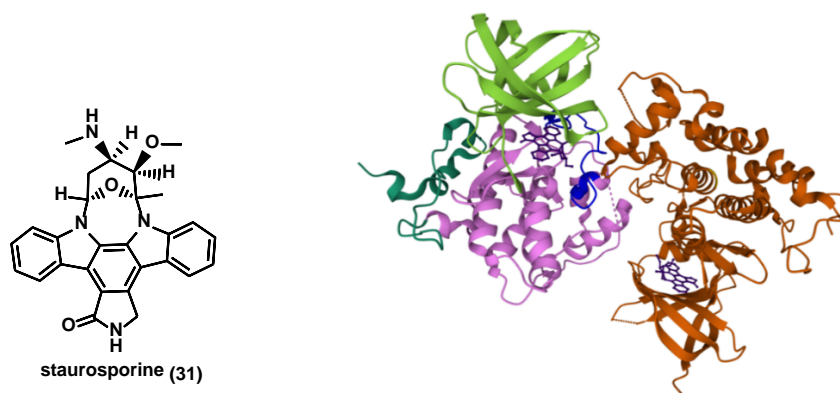
staurosporine (31)

Figure 1.15 Chemical structure of staurosporine (**31**) and stereo pair secondary structure cartoon of human GSK-3β in complex with **31** (purple) PDB ID: 1Q3D.[146] The β-strand domain at the *N*-terminal end is depicted in light green, the α-helical domain at the *C*-terminal end is depicted in pink, and the activation loop is depicted in blue.

1.7.1.1 GSK-3β ATP-competitive modulation for NDDs

The increasing interest in the modulation of GSK-3β led to the discovery of many novel inhibitors of chemically diverse molecular scaffolds.[147] Most reported inhibitors are ATP competitive agents of both synthetic and natural origin (*e.g.*, paullones, maleimides, indirubins, arylindolemaleimides, thiazoles). As GSK-3β

inhibitory activity was widely investigated in the last decade, several of these GSK-inhibitors have been evaluated in preclinical studies (*e.g.*, 6-bromoindirubin-3′-oxime (6-BIO, **32**)[148], hymenialdisine (**33**)[149], kenpaullone (**34**), alsterpaullone (**35**), cazpaullone (**36**)[150], and arylindolemaleimide (**37**)[151], Figure 1.16), with some of them reporting promising CNS-related preclinical data. Among them, the highly selective nanomolar GSK-3 inhibitor developed by GlaxoSmithKline, arylindolemaleimide **37**, showed neuroprotective effects against a variety of pro-apoptotic conditions with reduction of Aβ neurotoxic effects and tau phosphorylation in an AD model of mice injected with Aβ peptide. However, the same inhibitor produced neurodegenerative-like effects and behavior deficits in healthy mice, suggesting that a mild inhibition of GSK-3β able to restore the homeostasis on the enzyme activity would be sufficient to produce a therapeutic effect.[143, 152]
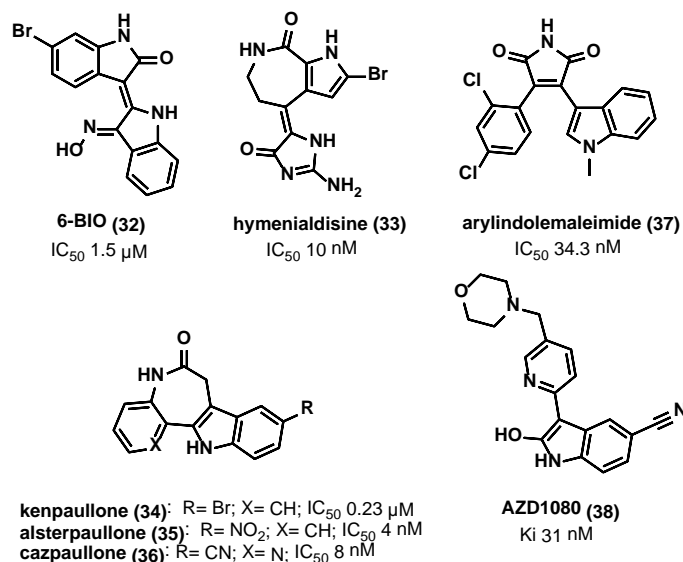

Figure 1.16 GSK-3β ATP-competitive inhibitors characterized by CNS activity.

AZD1080 (**38**, Figure 1.16) has been also reported by AstraZeneca as a potent, orally active and brain permeable GSK-3 inhibitor, with proven *in vitro* inhibition of

both recombinant human GSK-3α and GSK-3β in the nanomolar range (K_i = 6.9 nM and 31 nM, respectively). **38** possesses also high selectivity toward CDK2 (K_i = 1150 nM; 37-fold), CDK5 (K_i = 429 nM; 14-fold), CDK1 (K_i = 1980 nM; 64-fold), and Erk2 (K_i > 10 μM; >323-fold), as well as 23 different kinases and 65 diverse receptors, enzymes, and ion channels. Notably, **38** was able to reduce tau phosphorylation at Ser 396 in 3T3 fibroblasts engineered to stably express 4-repeat human tau protein (IC_{50} = 324 nM).[153] Moreover, the high permeability (8×10^{-3} cm min^{-1}) of **38** predicted using an *in vitro* bovine endothelial cell assay suggested significant *in vivo* brain exposure. The same inhibitor was advanced in phase I clinical trials for the treatment of AD; however, further development was halted due to the observed nephrotoxicity.[154]

1.7.2 FYN

The 59 kDa non-receptor Tyr kinase (TK) FYN, was first identified and characterized by Kypta R. M. and collaborators in 1988.[155] It belongs to the Src family kinases (SFKs) as part of the subfamily SrcA, together with Yes and Src enzymes. It is encoded by a gene located on chromosome 6q21 and consists of 537 amino acids.as part of the subfamily SrcA, together with Yes and Src enzymes and consists of 537 amino acids, with it being encoded by a gene located on chromosome 6q21. FYN mediates various cellular processes, including the T-cell receptor signaling pathway, regulation of brain function, adhesion-mediated signaling, and cell survival.[156] It prevails in many regions of the brain and is involved in both development and adult brain physiology. Moreover, FYN plays a unique role in CNS myelination by coupling with cell surface proteins, including myelin-associated glycoprotein. In agreement with these functions, it has been found that FYN-knockout mice show significantly reduced brain myelination, disrupting hippocampal architecture and impaired spatial learning.[157]

Three different FYN isoforms have been identified: FYN-B is mainly expressed in the CNS, FYN-T in hematopoietic cells (T-cells), and FYN-Delta7 in peripheral blood mononuclear cells. [158] As for all the SFK members, the FYN structure consist of six different domains: the Src homology (SH) domains SH1 (catalytic domain), SH2, SH3, SH4, the so-called unique domain, and a *C*-terminal regulatory region (Figure 1.17).[159-161] All FYN isoforms share the catalytic domain SH1; however, FYN-B and FYN-T differ in the linker sequence between SH1 and SH2, while FYN-Delta7 presents a deletion of residues 233-287 when compared to FYN-B. [158, 162] SH3 interacts with proline-rich sequences on target substrates and is involved in the autoinhibition regulatory mechanism. At the same time, the unique domain is specific for each SFK member and is responsible for specific proteins interactions.
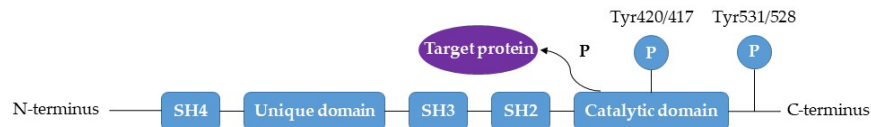
Figure 1.17 Schematic representation of FYN isoforms FYN-B and FYN-T.

FYN activity is regulated through Tyr residues phosphorylation and dephosphorylation processes. The phosphorylation of a specific CTD Tyr residue (Tyr 531 for FYN-B and Tyr 528 for FYN-T) induces a global close protein conformation due to the SH2 domain engagement, leading to the non-accessibility of the catalytic domain. Conversely, the phosphorylation of a distinct Tyr residue in the catalytic domain (Tyr 420 for FYN-B and Tyr 417 for FYN-T) improves the enzyme activity (Figure 1.17).

FYN overexpression has been widely correlated with cancer onset due to the enzyme pivotal role in the morphogenetic transformation and cell growth; nevertheless, recent studies and preclinical evidence have reported the same PK involvement in different NDDs, including AD and PD. [159, 163]

1.7.2.1 FYN ATP-competitive inhibitors and their application in NDDs

As for GSK-3β enzyme, the majority of FYN inhibitors are ATP-competitive agents able to interact with crucial residues of the enzyme catalytic site.[159] Unfortunately, due to the close similarity of most SFKs in their catalytic domains, to date, no selective inhibitors have been reported in literature. Although several FYN inhibitors are primarily intended for cancer therapy, the crucial role of this protein in the CNS has directed the development of FYN-targeted agents to achieve a therapeutic effect in NDDs. For this reason and due to the high degree of similarity of the FYN-B and FYN-T isoforms' catalytic domain,[164] some FYN inhibitors initially developed as non-CNS agents, such as AZD0530 (commonly known as saracatinib, **39**) and masitinib **40** (Figure 1.18), have been repurposed for CNS-related disorders.

39 is a SFK inhibitor based on a quinazoline heterocycle and able to inhibit Src, FYN, Yes, and Lyn with *in vitro* IC_{50} values ranging from 2 to 10 nM.[165] Although possessing limited clinical benefit as an anti-cancer agent, the excellent oral bioavailability (> 90%) and half-life of approximately 40 h,[166] combined with good BBB permeability, and its ability to reduce tau hyperphosphorylation encouraged its repurposing.[47] Tang S. J. *et al.* studied the compound efficacy in PS19 transgenic mice and traumatic tauopathy models underlying its ability to cross the BBB, inhibit FYN and reduce tau phosphorylation without altering both proteins expression.[167]

Despite **39** proved to be generally safe and well-tolerated in a phase Ib (NCT01864655), no beneficial effect was observed on measures of cognitive and neuropsychiatric function,[168] as also confirmed in a further phase IIa study conducted in 2018. [169]

The phenylaminothiazole derivative **40** (Figure 1.18) was first developed as a selective C-Kit receptor inhibitor, and is currently under evaluation to treat several human malignancies (gastro-intestinal stromal tumors, acute myeloid leukemia, systemic mastocytosis, pancreatic cancer, multiple myeloma, non-small cell lung

cancer, melanoma, ovarian and prostate cancer).[170] Furthermore, it has also been repurposed as a promising anti-AD agent able to reduce tau hyperphosphorylation and prevent NFTs formation, due to its nanomolar inhibitory potency against FYN (IC_{50} = 240 nM).[171] This compound caused a reduction in the cognitive decline in patients compared with the placebo group providing evidence for its great potential as an AD-modifying agent (NCT00976118).[172]

Furthermore, pyrazolo[3,4-*d*]pyrimidine core containing ATP-competitive FYN inhibitors with possible application for both tauopathies and cancer treatment are a great example of the current stage of FYN inhibitors development. The hit-to-lead optimization campaign conducted by Tintori C. and collaborators, culminated with the identification of the racemic analogs **41** and **42** (Figure 1.18) as potent FYN inhibitors with the ability to reduce tau phosphorylation on Tyr 18 mediated by FYN in an AD model cell line.[173]
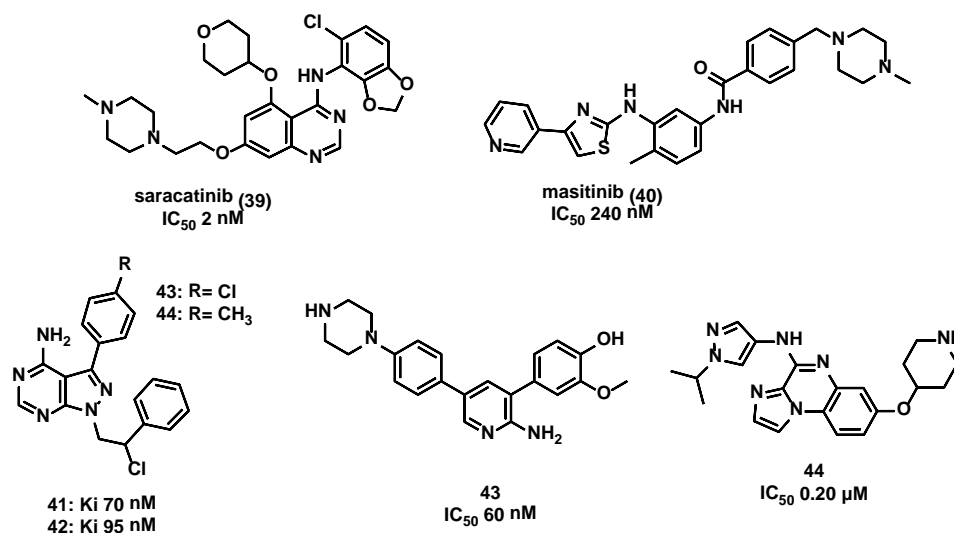

Figure 1.18 Chemical representation of FYN kinase inhibitors at various development stages

Compound **43** (Figure 1.18) is one of the diverse potent inhibitors of FYN reported by Lau W. C. *et al.* endowed with potential therapeutic application within the CNS space, including AD. [174] Likewise, Paraselli B. R. *et al.* presented new small molecules based on a 4-amine-imidazo[1,2-*a*]quinoxalin scaffold and bearing different substituents as FYN inhibitors for PD treatment. Among all the derivatives described, **44** (Figure 1.18) has been selected as the most promising hit, compound showing high nanomolar activity against FYN kinase (IC$_{50}$ = 0.20 μM). [175]

1.7.3 DYRK1A

DYRK1A (Figure 1.19) belongs to a family of dual-specificity protein kinases (DYRK kinases) that possess Ser and Thr phosphorylation activity, as well as autophosphorylation activity on Tyr residues.[176, 177] DYRK family is part of the CMGC group of Ser/Thr kinases, which also includes cyclin-dependent kinases (CDKs), mitogen-activated protein kinases (MAPKs), glycogen synthase kinases (GSKs), and CDC2-like kinases (CLKs). DYRK members participate in critical signaling pathways that control postembryonic neurogenesis, developmental processes, cell survival, differentiation, and death.[178]

DYRK1A plays a key role in the neural proliferation and neurogenesis of the developing brain, and its gene is located on chromosome 21 (21q22.2), which is a region known as the Down syndrome critical region (DSCR). Due to its location, triplication of the DYRK1A locus in Down syndrome (DS) results in a 1.5-fold increase of DYRK1A mRNA and protein levels in the fetal and adult brain. Under-/over-expression in mammals of DYRK1A gene or mutations in the orthologous gene minibrain (mnb) of *Drosophila* have been associated with severe retardation of CNS development and maturation.[178, 179] Moreover, the upregulation of DYRK1A has been reported to contribute to altered neuronal proliferation in DS through the specific phosphorylation of p53 at Ser15.[180]
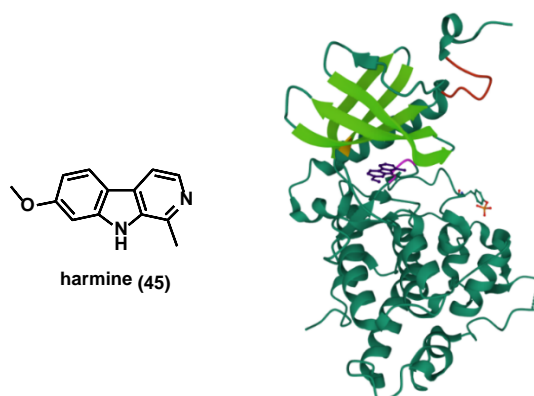
Figure 1.19 Chemical structure of harmine (**45**) and stereo pair secondary structure cartoon of human DYRK1A in complex with **45** (purple) PDB ID: 3ANR [181]. Five antiparallel β-strands at the *N*-terminal lobe are depicted in light green; the DH box is depicted in red; Phe 238 is depicted in orange; the DFG pocket is depicted in magenta.

As all DYRKs, the DYRK1A isoenzyme contains a conserved catalytic kinase domain, which is centrally located in its primary structure, preceded by the *N*-terminal motif DYRK-characteristic known as DYRK homology (DH) box. It rapidly autoactivates during folding by phosphorylation on Tyr 321, the second Tyr residue of the conserved activation loop YxY motif [178]. The kinase domain comprises a *N*-lobe with five antiparallel β-strands and a conserved regulatory α C-helix and a larger *C*-lobe consisting of α-helices.[177] Interestingly, DYRK1A possesses Phe 238 as a gatekeeper residue at the narrow channel, bridging the ATP binding pocket and the DFG-pocket[182] significant for its allosteric modulation. [183]

DYRK1A has attracted interest in cancer therapy given its crucial role in several pathways, including cell proliferation, apoptosis, malignant cells survival[184], and the regulation of cell cycling and differentiation.[185] Since the late nineties[186], its dysregulation has gained ever-increasing attention in a wide range of different human NDDs and impaired neurogenesis, making it an attractive target for further investigation.[187, 188]

1.7.3.1 DYRK1A Inhibitors

Natural products such as harmine (**45**)[189], meridianins[190] and synthetic derivatives like leucettine L41 (**46**)[191] and INDY (**47**)[181] have been widely explored within the DYRK1A inhibition field (Figure 1.20).[177, 192]
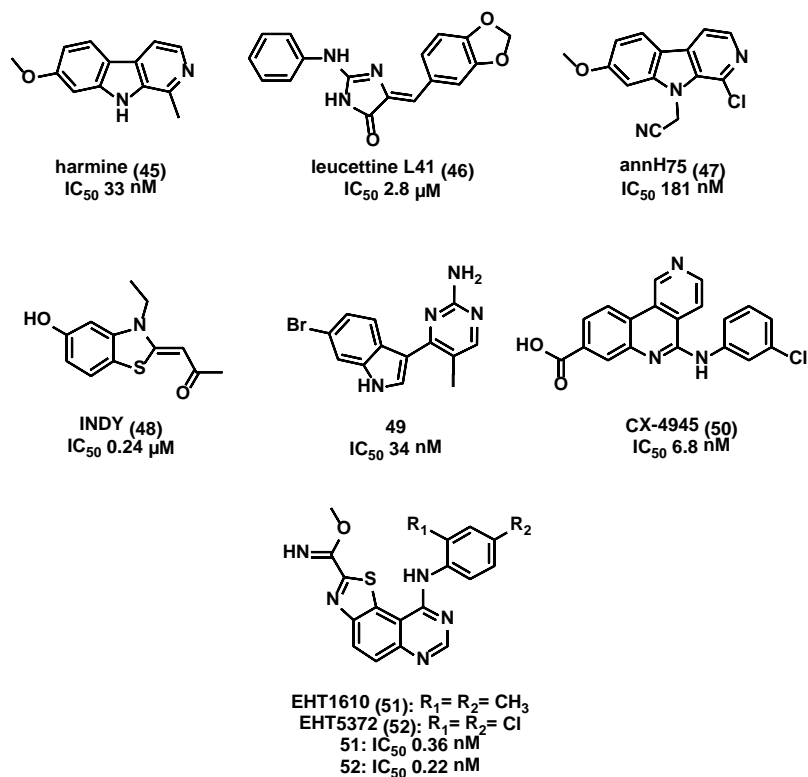
Figure 1.20 Chemical structures of ATP-competitive DYRK1A inhibitors.

Several optimization campaigns have been carried out starting from these representative inhibitors aiming at developing novel agents possessing improved inhibitory potency and selectivity for DYRK1A.[193]

The β-carboline alkaloid **45** (Figure 1.20, IC_{50} = 33 nM), represents one of the most potent and selective ATP-competitive DYRK1A inhibitors currently available,

[194-196] able to significantly interfere with tau phosphorylation by interacting with DYRK1A on Ser 396.[189]

Despite the compelling evidence of **45** and some derivative efficacy as anti-tau hyperphosphorylation agents, their employment as CNS tools has been hampered by promiscuity associated to their high affinity for 5-hydroxytryptamine receptor subtypes 5-HT2 and 5-HT1A, the *N*-methyl-*D*-aspartate (NMDA) receptor, monoamine oxidase (MAO-A) [189, 197], and dopamine receptors. Therefore, different analogs of **45** have been developed to improve the selectivity over off-targets. Among them, AnnH75 (**47**, Figure 1.20), maintaining an *in vitro* nanomolar potency against DYRK1A ($IC_{50} = 181$ nM), displayed a low affinity for MAO-A ($IC_{50} > 10,000$ nM). Moreover, the same derivative inhibited Tyr autophosphorylation of DYRK1A during translation at >1 μM and inhibited DYRK1A activity with an IC_{50} of 1 μM in cellular assays.[198]

The benzothiazole containing **48** (Figure 1.20) was discovered as a novel ATP-competitive inhibitor of DYRK1A able to effectively reverse the aberrant tau phosphorylation at Thr 212 in COS7 cells, suggesting it could be of use in investigating DYRK1A implication in tau aggregates formation.[181]

The marine alkaloid derivative **49** (Figure 1.20) was identified a potent dual-inhibitor of DYRK1A and CDC Like Kinase 1 (CLK1) ($IC_{50} = 0.034$ μM and 0.032 μM, respectively).[199-201]

CX-4945 (**50**, Figure 1.20) is an ATP-competitive DYRK1A inhibitor ($IC_{50} = 6.8$ nM) with an *in vitro* potency about 20-fold higher than that of **45** and **48**. Remarkably, **50** effectively reversed the aberrant phosphorylation of tau at Thr 212 in DYRK1A-overexpressing mice and inhibited DYRK1A-mediated APP and PS1 phosphorylation in 293T cells with estimated IC_{50} values of ≈80 and 100 nM for APP and PS1, respectively. This compound was also able to significantly restore the neurological and phenotypic defects in an AD-like *Drosophila* model, demonstrating the great potential of this inhibitor as a disease-modifying agent for AD.[202]

EHT1610 and EHT5372 (**51** and **52**, respectively, Figure 1.20), two methyl 9-anilinothiazolo[5,4-*f*]quinazoline-2-carbimidates derivatives identified by Chaikuad A. *et al.*, showed subnanomolar and selective DYRK1A/B inhibitory activity with a noncanonical binding mode at the ATP pocket of both enzymes.[203] Among them, derivative **52** with an IC_{50} value of 0.22 nM was able to inhibit DYRK1A-induced tau phosphorylation at multiple AD-relevant sites, including Ser 396, Thr 212, and Thr 231 in biochemical assays, cell lines (*e.g.*, HEK293 cells), and primary cortical neurons without affecting cell viability. Furthermore, it normalized Aβ-induced tau phosphorylation in neuronal cells at 5 and 10 µM and DYRK1A-induced Aβ production in APP over-expressing cells (IC_{50} = 1.06 µM), emerging as a promising tau and amyloid-directed agent to alter the onset or progression of AD and other tauopathies.[204]

1.8 Involvement of GSK-3β, FYN, and DYRK1A in aberrant tau phosphorylation

As previously mentioned, abnormal phosphorylation of MAPT at different sites, including Ser/Thr residues in Ser/Thr-Pro sequences, is one of the main pathological events in AD and other related tauopathies.[205, 206]

In vitro studies have suggested that phosphorylation of tau at Ser 202/396 and Thr 205 represents a critical event and one of the leading causes of the sequestration of hyperphosphorylated tau from MTs and its self-aggregation into NFTs.[207]

While GSK-3β induces human tau phosphorylation mainly at Ser 199, Ser 396, and Ser 413 [208], DYRK1A phosphorylates 11 different Ser/Thr sites of this protein, including Thr 212 as the predominant one.[209] Protein FYN instead, is physically linked to the amino-terminal projection domain of tau and it is responsible for its phosphorylation at Tyr 18 (Figure 1.21).[210]

In vitro studies focused on the evaluation of the general role of DYRK1A as a priming kinase, highlighted that phosphorylation at Thr 212 by DYRK1A primes tau for phosphorylation by GSK at Ser 208, suggesting DYRK1A pivotal role in both physiological and aberrant tau processes.[211] Additionally, DYRK1A, by phosphorylation of the alternative splicing factor (ASF) at Ser 227, Ser 234, and Ser 238, causes dysregulation of alternative splicing of tau, leading to NFTs formation.[212] In contrast, tau overexpression has been reported to promote GSK-3β activation and mediate GSK-3β toxicity, whereas absence of tau in the neurodegenerative and cognitive phenotype observed in GSK-3β overexpressing mice resulted in an improvement. [213]

Recent advances in the elucidation of regulatory crosstalks by these three PKs on different pathological signaling pathways conducive to tau hyperphosphorylation, have suggested the great potential of multi-target strategies to modulate different nodes of the neurodegeneration network and achieve a disease-modifying effect.[205]
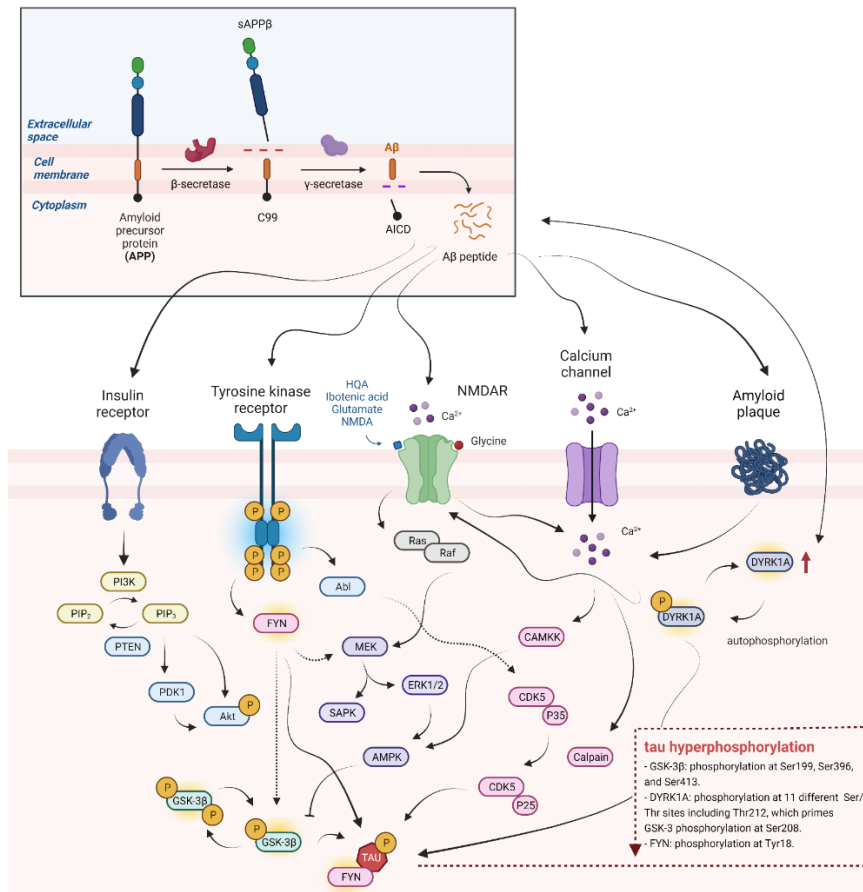
Figure 1.21 Simplified graphic representation of GSK-3β, FYN, and DYRK1A interconnected pathways linked to tau phosphorylation.

1.9 Multi-target directed ligands (MTDLs) approach, a superior polypharmacological approach to tackle NDDs

The multifactorial nature of AD and related tauopathies requires innovative strategies to overcome some limits of single-target drugs, nowadays proposed as inadequate tools to achieve a therapeutic effect.[214, 215] In this context, polypharmacology-based strategies, mainly the MTDLs approach, have become increasingly feasible and attractive options.[216-218]

It is widely accepted that drug combinations are often the only therapeutic options for these intricate pathologies; however, the outcome of these regimes is often limited by drug-drug interactions as well as patients' compliance. To overcome these limitations, new single chemical entities with multi-target properties and a safer profile compared to single-target ones have been sought.[219, 220]

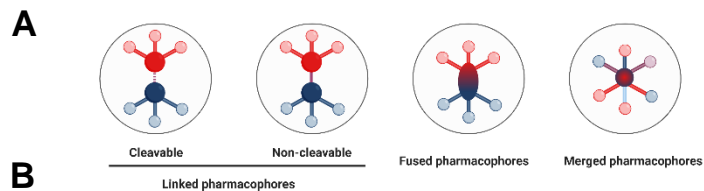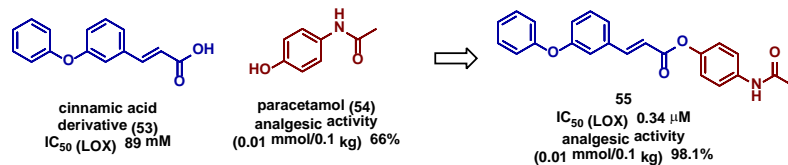Rationally designing multi-target agents requires particular attention to balance the activity of each target of interest while simultaneously achieving a wider selectivity and a suitable pharmacokinetic (PK) profile together with adequate targets engagement.[221]

Multi-target ligands are classified based on the pharmacophore distribution within the molecular framework (Figure 1.22).[222, 223]

Multi-target agents containing the pharmacophore elements for each target connected by a distinct linker that is not found in either of the one-target ligands are defined as conjugates and are characterized by high MWs. The majority of these agents contain a metabolically stable linker and are, therefore, called non-cleavable conjugates.[217] Conversely, cleavable conjugates represent multi-target molecules, which possess a rationally designed linker that, once in the body, is metabolized to release two different drug entities, which interact independently with each target. When different one-target pharmacophores are essentially touching in multi-target compounds, they become fused ligands. In the majority of cases and especially in the field of PKs, the merged frameworks represent a good option to overcome the high MW typical of conjugates while designing multi-target ligands for highly related targets in the same superfamily, giving rise to smaller and simpler molecules.

A

Cleavable | Non-cleavable | Fused pharmacophores | Merged pharmacophores

Linked pharmacophores

B

Cleavable MTDLs

cinnamic acid
derivative (53)
IC$_{50}$ (LOX) 89 mM

paracetamol (54)
analgesic activity
(0.01 mmol/0.1 kg) 66%

55
IC$_{50}$ (LOX) 0.34 μM
analgesic activity
(0.01 mmol/0.1 kg) 98.1%

Non-cleavable MTDLs

56, mepyramine
pK$_B$ (H$_1$R) 9.07

57, roxatidine-type
H$_2$R antagonist
pK$_B$ (H$_2$R) 6.68

58
pK$_B$ (H$_1$R) = 8.42
pK$_B$ (H$_2$R) 6.43

Fused MTDLs

3
rivastigmine
IC$_{50}$ (AChE) 0.92 μM

59
rasagiline
IC$_{50}$ (MAO-A) 0.41 μM
IC$_{50}$ (MAO-B) 0.0044 μM

60
IC$_{50}$ (AChE) 52.4 μM
IC$_{50}$ (MAO-A) 85 μM
IC$_{50}$ (MAO-B) 120 μM

Merged MTDLs

3
rivastigmine
IC$_{50}$ (AChE) 0.92 μM

61
HLA20

62
IC$_{50}$ (AChE) 0.50 μM
IC$_{50}$ (BuChE) 42.58 μM
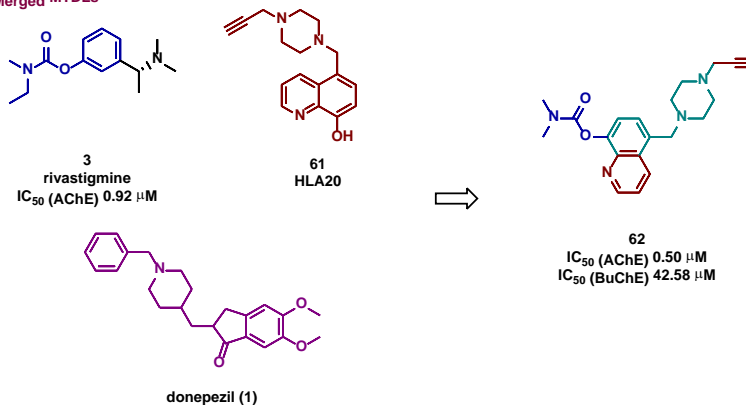
donepezil (1)

Figure 1.22 A) Multitarget drug design strategy based of pharmacophore examples. In the linked MTDLs, the pharmacophores are connected by stable or degradable linkers. In fused MTDLs, the pharmacophores are attached directly. In merged MTDLs, the pharmacophores are merged together; B) Examples (**1,3,61**-**63**) of MTDLs based on their drug design strategies, for further details see [223]

1.9.1 Importance of selectivity in the rational design of PKs MTDLs agents

When designing multi-target compounds, it is of crucial importance acquiring knowledge of how the selected targets interact one another and the various pathways involved. Additionally, analoguos to mono-target agents, the elimination of secondary targets and the obtainment of a 'cleaner' profile is likewise required in the design of multi-target compounds and top priority to advance drugs into the clinic.[224]

More than 500 PKs are encoded by the human genome effecting different roles in their physiological processes. Moreover, the majority of PKs exist within the same superfamily making the development of highly selective inhibitors a major challenge in mono-target kinase drug discovery.

The pursuit of multi-target agents is complicated further where certain pharmacophores are used to exploit structural similarities between the proposed targets, which can induce an inherient degree of promiscuity.[183, 225]

9.1.2 Multi-target inhibitors of GSK-3β and DYRK1A and their potetial CNS application

Although few examples of multi-target FYN kinase inhibitors have been reported in literature so far[226], a discrete number of GSK-3β and DYRK1A-directed MTDLs have been developed as disease-modifying agents to tackle NDDs. Some examples of MTDLs against GSK-3β and DYRK1A are given in this paragraph.

Holzer M. *et al.* report one of the few examples of rationally designed triple PK inhibitors of GSK-3β, CDK1, and CDK5 bearing a benzofuropyridine-based scaffold

to combat AD.[205] Among these PKs, CDK-5 has been found to be abnormally activated in AD. In contrast to the majority of CDKs, which promote cell cycle progression in proliferating cells, CDK5 is activated in post-mitotic neurons via the neuron-specific activator p35 to form the complex CDK5-p35, which plays a critical role in brain development and physiological synaptic activity.

Furthermore, the *N*-terminal truncated form of p35 (p25) generated by cleavage with calpain, is responsible for CDK5 over activation in AD brains, thus contributing to aberrant tau phosphorylation.[206] Also, evidence has demonstrated the crucial role of hyperactivated CDK5 in promoting aberrant CDK1 activation, which in turn induces neuronal death and potentiates the AD pathology. Amongst the triple GSK-3β/CDK1/CDK5 ATP-competitive inhibitors synthesized, the 3-ethoxy derivative **63** displayed submicromolar affinities for CDK1 and CDK5 and nanomolar affinity for GSK-3β (Figure 1.23). The 3-hydroxy analog **64** emerged as the most interesting triple inhibitor, reaching affinities in the nanomolar range for CDK1 and GSK-3β and in the submicromolar range for CDK5. The best nanomolar affinities toward CDK5 and GSK-3β were obtained with compound **65**, which also showed submicromolar affinity for CDK1.
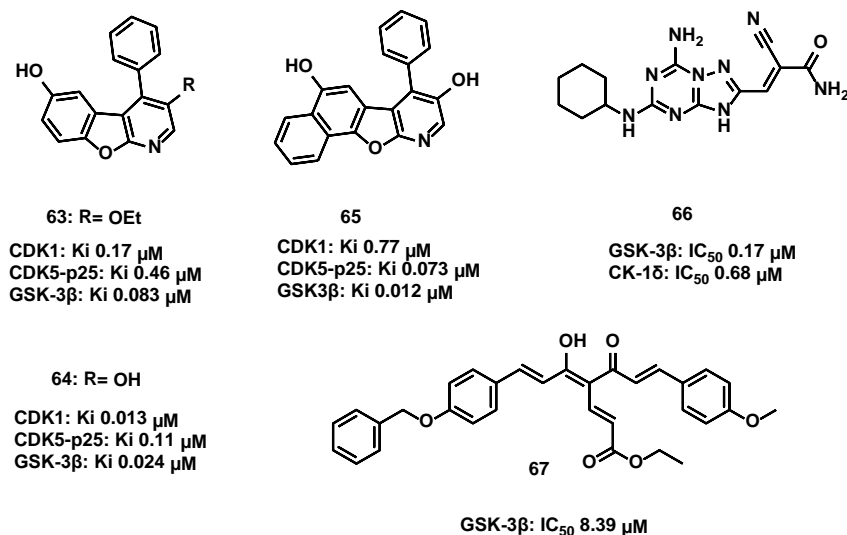
63: R= OEt

CDK1: Ki 0.17 μM
CDK5-p25: Ki 0.46 μM
GSK-3β: Ki 0.083 μM

65

CDK1: Ki 0.77 μM
CDK5-p25: Ki 0.073 μM
GSK3β: Ki 0.012 μM

66

GSK-3β: IC$_{50}$ 0.17 μM
CK-1δ: IC$_{50}$ 0.68 μM

64: R= OH

CDK1: Ki 0.013 μM
CDK5-p25: Ki 0.11 μM
GSK-3β: Ki 0.024 μM

67

GSK-3β: IC$_{50}$ 8.39 μM

Figure 1.23 Chemical structures of some examples of multi-target GSK-3β inhibitors.

Compound **64** showed selectivity versus several PKs, since no activity was observed against members of the PKA family (PKC-α, -γ, -ε, -iota), the receptor TK family (VEGFR2, ErBB2 and TIE2), WEE1, and CK1α. Meanwhile, high micromolar values of activities ranging from 230 to 829 μM were shown against CDK6, EGFR of the receptor TK, and Src of the SRC family. Notably, **63** was shown to reduce tau phosphorylation by 61% at 8 μM concentration in a tau protein phosphorylation assay, in which AT180 monoclonal antibody was used to detect phosphorylated Thr 231 and Ser 235 sites in tau transfected COS-7 cells. In a split-luciferase assay, developed to study the effect of the novel triple inhibitors on the tau self-interaction in a human liver cell line (HuH-**7**), **64** and **65** showed a significant reduction of luminescence and therefore of tau interaction (38% and 29% inhibition at 1 μM, respectively; 71% and 84% inhibition at 10 μM, respectively). **63** caused only a mild inhibition of tau interaction at 1 μM (22%) and a higher inhibition up 65% at 10 μM.[205]

Redenti S. *et al.* developed triazolotriazine-based dual GSK-3β/CK-1δ ligands as potential neuroprotective agents to treat PD, due the involvement of GSK-3β in

microglial-mediated inflammation and of the delta isoform of CK1 family of Ser/Thr kinases (CK-1δ) in the neuroinflammatory process, along with the crucial role of both PKs in the hyperphosphorylation of tau, α-syn, and parkin.

2-Cyanoacrylamide compound **66** (Figure 1.23) showed a submicromolar inhibitory activity against both selected targets (IC$_{50}$ = 0.17 µM for GSK-3β; IC$_{50}$ = 0.68 µM for CK-1δ).

While a classical ATP competition was observed against CK-1δ, a covalent interaction between the cyanoacrylamide warhead of **66** and Cys 199 of GSK-3β was confirmed by X-ray crystallography. In a PAMPA-BBB test, **66**, showed a permeability close to the limit of passively BBB-permeating compounds (P$_e$ = 1.34 × 10^{-6} cm s^{-1}) due to its highly polar moieties. Remarkably, **66** did not display cytotoxicity up to 10 µM and prevented neurotoxin-induced cell death in a concentration-dependent manner using *in vitro* models of PD (rat PC12 pheochromocytoma cells in the presence of neurotoxins 4-phenyl-1-methyl-1,2,3,6-tetrahydropyridine or 6-hydroxydopamine). In additional *in vitro* studies, **66** prevented 6-OHDA-induced cell death by inhibiting GSK-3β, and promoted β-catenin stabilization, thus restoring its neuroprotective potential.[227]

Similarly, to GSK-3β, the multi-target approach has been recently exploited to rationally design and synthetize multifunctional DYRK1A inhibitors.
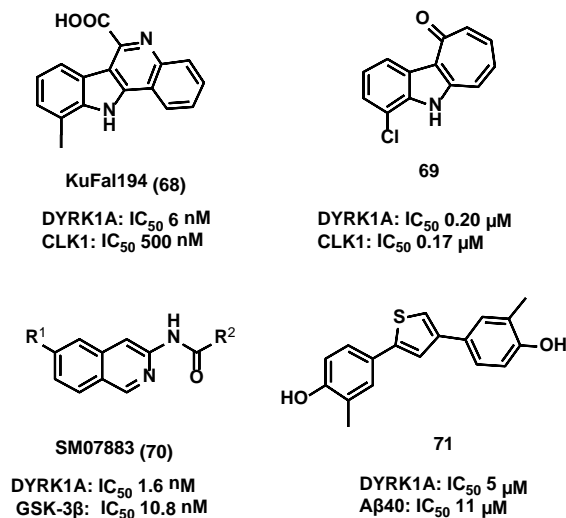
Figure 1.24 Chemical structures of multi-target DYRK1A inhibitors.

Lechner C. *et al.* starting from KuFal194 (**68**, Figure 1.24), a potent DYRK1A inhibitor (IC_{50} = 6 nM) with reasonable selectivity *versus* DYRK1B (IC_{50} = 600 nM) and CLK1 (IC_{50} = 500 nM), carried out an optimization campaign to identify improved DYRKIA inhibitors. The best results were achieved with b-annulated indole **70**, which demonstrated well balanced dual CLK1/DYRK1A submicromolar inhibitor (IC_{50} = 0.17 µM for CLK1; IC_{50} = 0.20 µM for DYRK1A).[228]

Moreover, Melchior B. *et al.* identified SM07883 (**70**, Figure 1.24) as an interesting brain-penetrant dual DYRK1A/GSK-3β inhibitor (IC_{50} = 1.6 nM for DYRK1A and 10.8 nM for GSK-3β) in a kinase panel screen. Notably, this multi-target compound showed a reduction of phosphorylation of multiple tau epitopes, especially the Thr 12 site (EC_{50} = 16 nM) in cell-based assays, and in an anesthesia-induced transient tau hyperphosphorylation mouse hypothermia model, it showed reduced tau phosphorylation by 47% with the lowest dose of 1.25 mg/kg. Moreover, compared to the vehicle, a significant reduction of tau phosphorylation and aggregation was observed with an alternative dose regimen of **70** leading to significantly lower numbers of tau-positive inclusions in brain stem and spinal cord samples.[229] The safety and

70

tolerability of increasing doses of **70** have been also evaluated in a phase I clinical trial (ACTRN12619000327189) in healthy volunteers.[230]

Lastly, Mariano M. *et al.* reported the application of a focused multi-target approach to develop a novel class of selective dual inhibitors of DYRK1A and Aβ aggregation based on the bis(hydroxiphenyl)thiophene scaffold. Compound **71** (Figure 1.24) exhibited the best biological profile with a well-balanced inhibitory potency toward DYRK1A (IC$_{50}$ = 5 µM) and Aβ$_{40}$ inhibition (Aβ$_{40}$ % inhibition at 100 µM = 91%; IC$_{50}$ = 11 µM in a cell-free assay). The same compound was shown to inhibit DYRK1A-catalyzed tau phosphorylation in stably transfected HEK293 cells and thanks to its favorable physicochemical properties deserved attention for further efficacy studies *in vivo* AD models.[231]

Chapter 2

2. Towards triple GSK-3β/FYN/DYRK1A inhibitors to combat neurodegenerative tauopathies

2.1 Rationale

The great potential of MTDLs and, in particular, of multikinase PKs inhibitors to tackle CNS-related disorders inspired us to rationally develop the first-in-class GSK-3β/FYN/DYRK1A inhibitors to reverse the aberrant phosphorylation of tau protein related to tauopathies. In this chapter, I will begin with compound **ARN25068** (**72**), the initial driving force of the project and optimal starting point to design and synthesize improved tools to combat yet unsolved NDDs. This compound was also the subject of a publication in the European Journal of Medicinal Chemistry[232] which I report and readapt. I will then present the extensive medicinal chemistry effort to access novel

derivatives of compound **72** characterized by a potent and well-balanced inhibitory activity towards all of the three targets and good *in vitro* ADME properties.

2.2 ARN25068, a versatile starting point

Considering the crucial role of GSK-3β and FYN in tau phosphorylation, **ARN25068** (**72**, Figure 2.1), featuring a 2,4-di-substituted pyrimidine thiophene core, was discovered as a well-balanced dual GSK-3β/FYN inhibitor among a large set of compounds tested against 172 different PKs,[233] and was selected as a versatile starting point thanks to its chemical feasibility and low promiscuity.[216, 225]

First, docking simulations were performed to predict the bound conformations of **72** at both GSK-3β and FYN ATP binding pockets (Figure 2.1). Flexible receptor models were generated for both proteins, and **72** was docked using the latest version of ICM pro software. Desirable docking scores of -39.3 and -39.5 were observed against GSK-3β and FYN, respectively. The binding poses of **72** in each receptor model resembled those of typical Type I or II inhibitors, with hydrophobic and H-bonding contacts between the compound and key residues in the ATP binding sites of both enzymes (Figure 2.1).[234] When binding to GSK-3β, compound **72** was predicted to form three total HBs between its aminopyrazole moiety and residues Val 135 and Asp 133 at the hinge region (Figure 2.1 A and B). Hydrophobic contacts were also predicted between the pyrimidine group of **72** and residues Ile 62, Thr 138, Arg 141, Glu 137, and Pro 136, between the aminopyrazole of **72** and residues Tyr 134, Leu 188, and Ala 83, between cyclopropyl group of **72** and residues Leu 132 and Cys 199, and between the benzylamine moiety of **72** and residues Val 70, Asp 200, Asn 186, Asn 64, and Gly 63 (Figure 2.1 B). When binding to FYN, compound **72** was predicted to form two total HBs with hinge region residues Met 85 and Glu 83 (Figure 2.1 C and D).

Additionally, several hydrophobic contacts were predicted between aminopyrazole of **72** and Leu 137, between cyclopropyl group of **72** and residues Thr

82, Ala 37, Val 67, and Ala 147, between the benzylamine moiety of **72** and residues Asp 148, Asn 135, Ala 134, Val 25, and Gly 18, and between the pyrimidine moiety of **72** and residues Leu 17, Gly 88, Asn 86, and Tyr 84 (Figure 2.1 D).
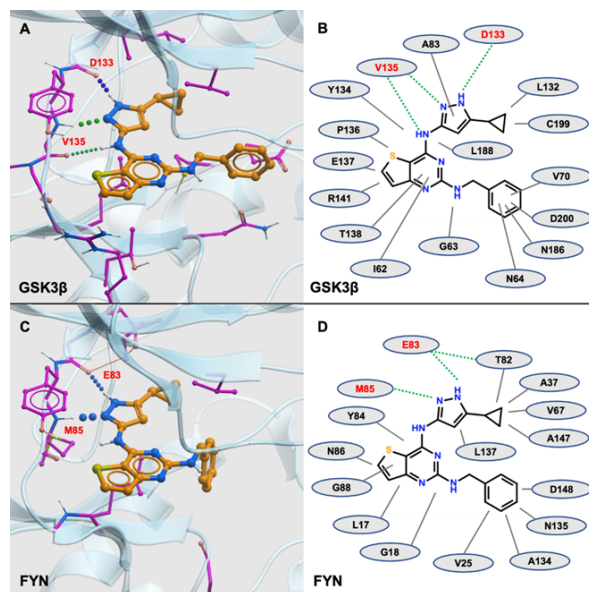

Figure 2.1 Graphical representations of the binding mode of **72** to GSK-3β and FYN. (A, C) Structural models of the binding sites of GSK-3β (A) and FYN (C), respectively, showing the binding poses resulting from *in silico* docking simulations. Flexible receptor model for GSK-3β constructed from the following PDB entries: 4IQ6, 4DIT, 4J1R, 4J71, 2OW3, 3GB2, 4PTC, 3M1S, 4PTE, 4PTG, 3SAY, 3SD0, 3I4B, 1PYX, 3DU8, 1Q3D, 1Q3W, 1Q41, 1Q4L, 1Q5K, 2JLD, 1R0E, 3F7Z, 3F88, 1J1B, 1J1C, 2O5K, 3PUP, 5F94, 5F95, 3Q3B, 4ACH, 4ACG, 4ACD, 4ACC, 3L1S. Receptor model for FYN constructed from PDB entry 2DQ7. (B, D) Schematics showing the binding pocket interactions predicted between **72** and GSK-3β (B) and FYN (D), respectively. Hydrophobic interactions are depicted by dark grey lines, and green dotted lines represent HBs.

Compound **72** was synthesized by applying an easily scalable two-step synthetic procedure (Scheme 2.1) based on two sequential nucleophilic aromatic substitution (SN$_{Ar}$) reactions on 2,4-dichlorothieno[3,2-*d*]pyrimidine (**73**). Taking advantage of the higher reactivity of 4-heterocycle position, a solvent-free substitution of **73** with 3-cyclopropyl-1*H*-pyrazol-5-amine (**74**), in the presence of triethylamine as base, yielded intermediate **75** chemoselectively in very good yields.

Remarkably, **74** was used without performing a preliminary protection of the endocyclic NH of the pyrazole moiety. The regiochemistry of intermediate **75** was corroborated through 1D- and 2D-NMR studies (Figure A4. A5, A6 of Appendix A), confirming the different reactivity of the two chlorine atoms at 2 and 4 positions of **72**. Further SN_{Ar} of intermediate **75** using an excess of benzylamine (**76**) in *n*-butanol at 110 °C afforded the target compound **72**.

Scheme 2.1 Synthesis of compound **72**
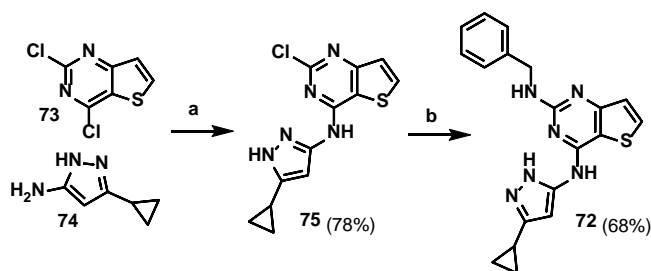
Reagents and conditions: a) Et$_3$N (2.2 equiv.), rt, 16 h; b) benzylamine (**76**) (5 equiv.), *n*-BuOH, 110 °C, 72 h.

The inhibitory potency of compound **72** was first evaluated in a human CMGC Kinase enzymatic radiometric assay and then in HEK293 cells transiently transfected with GSK-3β and FYN NanoLuc fusion vector. In the enzymatic assay, **72** showed single-digit nanomolar inhibition of both GSK-3β and FYN (IC$_{50}$ = 5 and 3 nM, respectively; Table 2.1), in excellent agreement with the data reported in the literature.[233]

The NanoBRET binding assay (Table 2.1) was performed to evaluate the apparent binding affinity and permeability of compound **72** by competitive displacement of a NanoBRET tracer reversibly bound to a NanoLuc fusion protein. In this assay, CHIR-99021 (**77**) and Dasatinib (**78**) were selected as reference compounds for GSK-3β and FYN inhibition respectively. Remarkably, the compound displayed a

kinase-inhibitor-like occupancy in the nanomolar range for both enzymes ($IC_{50} = 9.7$ nM for GSK-3β and 91.1 nM for FYN; Table 2.1). In both cases, primarily against FYN, lower binding affinities were observed in comparison with the inhibition potency observed in the enzymatic assay, suggesting an influence of the cellular environment on the potency profile of **72**.

Table 2.1 GSK-3β and FYN IC_{50} values and binding affinity data of compound **72** in enzymatic radiometric and NanoBRET assays, respectively.

Cmpd ID	Enzymatic Radiometric Assay		NanoBRET Target Engagement Cellular Kinase Assay	
	IC_{50} (nM)		IC_{50} (nM)	
	GSK-3β[a]	FYN[a]	GSK-3β[b]	FYN[c]
72	5	3	9.7	91.1
77			4.8	
78				2.6

IC_{50} values were reported as a mean value of two different determinations; [b]GSK-3β tracer K8 (0.25 µM); [c]Fyn tracer K4 (0.33 µM).

Crystallographic studies were also performed to confirm the computational poses and identify the essential structural features for binding to GSK-3β and FYN. GSK3β-73 crystals were diffracted to a resolution of approximately 2.6 Å (PDB ID: 7OY5, Figure 2.2). Molecular replacement analysis located two protein molecules in the asymmetric unit. Unambiguous positive electron density, corresponding to our compound **72**, was observed in the ATP binding site of GSK-3β (Figure 2.2 A and B). In the refined structure, **72** displays H-bonding interactions with backbone atoms of the hinge region residues of Asp 133 and Val 135 (Figure 2.2 C) in agreement with the initial docking simulations (Figure 2.2 A and B). Moreover, compound **72** occupies the

ATP pocket in "DFG-in" conformation making it consistent with type-I inhibition of the enzyme.
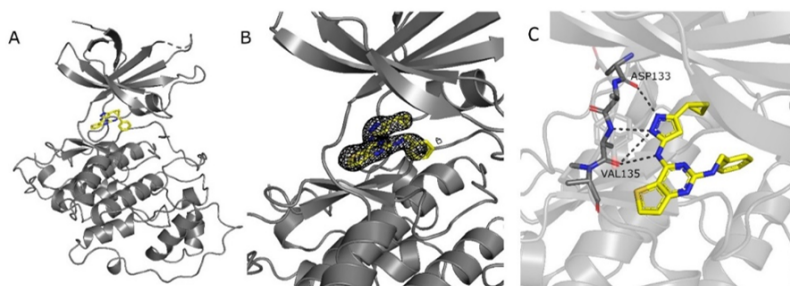

Figure 2.2 Crystal structure of GSK-3β with compound **72**. A. Compound **72** (yellow) in the ATP binding pocket of GSK-3β (grey). B. Electron density map ($2F_O$ - F_C) corresponding to **72** is contoured at 1.2σ level (black mesh). C. Compound **72** (yellow) displays H-bonding interactions (black dashes) with the hinge region backbone atoms of residues Asp 133 and Val 135 of GSK-3β (grey).

Despite several efforts, all attempts to crystallize **72** with human FYN-T protein proved unsuccessful due to poor sample homogeneity. Different patterns of phosphorylation of the protein most likely induced sample heterogeneity, thus preventing the formation of acceptable diffracting crystals.

Therefore, the available X-ray structure of FYN (PDB ID: 2DQ7) was overlapped with the in-house generated GSK3β-**72** crystal structure taking advantage of their high homology (Figure 2.3). According to the overlapped structure, compound **72** may be lodged in the hinge region of FYN adopting a bound conformation very similar to that observed at the GSK-3β ATP binding pocket (Figure 2.3 A) and able to establish H-bonding interactions with Glu 83 and Met 85 backbone residues (Figure 2.3 B). The binding arrangement of **72** inside the FYN ATP binding pocket, deduced from 3D structures superposition, was in agreement with the structural information obtained from the docking model (FYN-**72**). In a similar fashion to GSK3β, compound **72** is likely to adopt type-I inhibition of FYN.
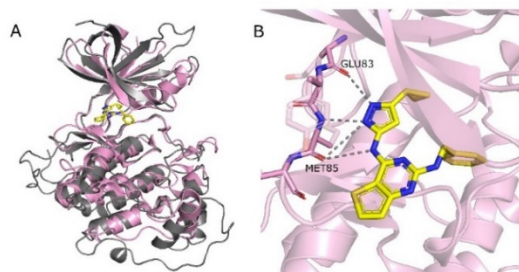
Figure 2.3 Overlapping of GSK3β-**72** complex with FYN structure. A. Overlapping of FYN (pink) structure (PDB ID: 2DQ7) with the structure of GSK-3β (grey) in complex with **72** (RMSD 2.717). Compound **72** at the ATP binding pocket of FYN. B. Potential HB interactions (grey dashes) between **72** and FYN backbone atoms (Glu 83 and Met 85), based on the structures overlapping.

In addition to the well-balanced and potent dual inhibitory activity against both GSK-3β and FYN, compound **72**'s ability to reduce tau hyperphosphorylation was investigated in a fluorescence bundle formation assay in a human recombinant U2OS cell line, which stably expresses triple mutant (TM) tau 0N4R (Tau0N4R-TM-tGFP line).

The binding of tau protein to MTs and consequent bundle-formation are two processes dependent on the phosphorylation of tau protein. High phosphorylation levels lead to tau dissociation from MTs and their aggregation into tangles of PHF. In contrast, tau kinase inhibitors or phosphatase activators promote tau binding to MTs and the formation of MT bundles.

In this cell-based assay Medium (OptiMem) and Vehicle (DMSO) were used as negative controls, and the well-known GSK-3β inhibitor LiCl was employed as a positive control at 30 mM concentration. The bundle increase was monitored and quantified by fluorescence using automated image analysis (Figure 2.4 B).

72 showed a dose-dependent effect in the range of 0.5-10 µM concentrations, and, at 10 µM concentration, an approximetly 10-fold increase in bundle formation was observed (compared to the negative control). Moreover, at 2.5 µM compound **72** proved to be 1.4-fold more active than LiCl in reducing tau phosphorylation. At higher

concentrations (25-100 µM), cytotoxicity effects started to appear, likely because of an excessive reduction of tau phosphorylation, which can lead to cell death for MT destabilization (Figure 2.4 A and B).
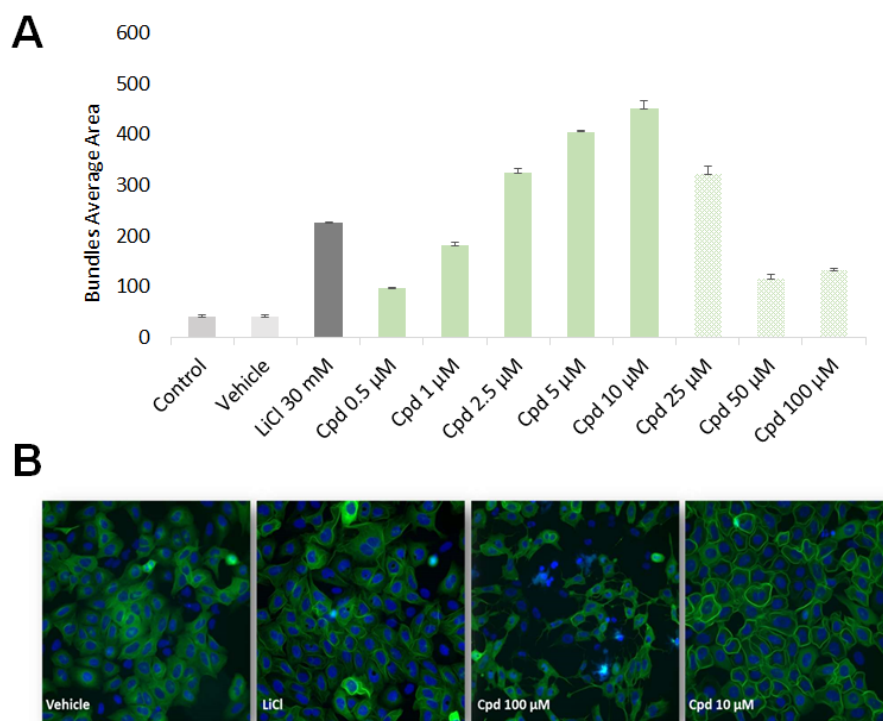

Figure 2.4 A. Dose-response relationship for compound **72** (0.5-100 µM), medium (control), vehicle and LiCl (30 mM). Cells were treated with the indicated concentrations for 6 h. Data points represent the mean ± SD for each condition for a single experiment performed in triplicate. Results are expressed as the total area average of bundles per cell. Images were obtained with an objective of 20X. B. Representative images of the assay. The pictures represent DMSO (vehicle control), LiCl 30 mM (positive control), and test compound at 10 µM and 100 µM.

Given these encouraging results and considering the high degree of homology of PKs catalytic sites, a preliminary assessment of compound **72**'s selectivity at 0.1 and 10 µM concentrations *versus* a small panel of 20 different PKs was performed (reported in the kinome tree, Figure 2.5). These kinases were selected according to their phylogenetic similarity to GSK-3β and FYN, and the involvement in tau

hyperphosphorylation. In the radiometric kinase activity assay, **72** showed a good selectivity at 0.1 µM as it effectively inhibited GSK-3β and FYN by decreasing 94% and 100% kinase activities, respectively (Table 2.2), compared to only marginal or weak inhibition against about half of the kinases in the test panel at the same concentration. However, low selectivity was observed relative to some PKs phylogenetically correlated to GSK-3β and FYN, such as GSK-3α and Yes (Table 2.2).

An unexpected, yet beneficial activity against DYRK1A and CDK5/p25, two additional PKs related to tau hyperphosphorylation, was observed at 10 µM (92% and 97% inhibition, respectively). All PKs from the selectivity panel were also ranked to find the most suitable one to tackle tauopathy-related diseases. Each PK was assigned a score between 0 and 1, representing an informed estimation of the strength of association between each target and the disease. I particularly focused on CNS-related disorders such as NDDs, brain development, and neuromuscular disorders by using the data reported in Open Targets Platform,[235] an open access tool that supports systematic identification and prioritization of potential drug targets.

As depicted in Table 2.2, DYRK1A and CDK5/p25, belonging to the same CMGC group of Ser/Thr kinases (Figure 2.5), were identified along with GSK-3β and FYN as the top four most relevant PKs.[47, 236]
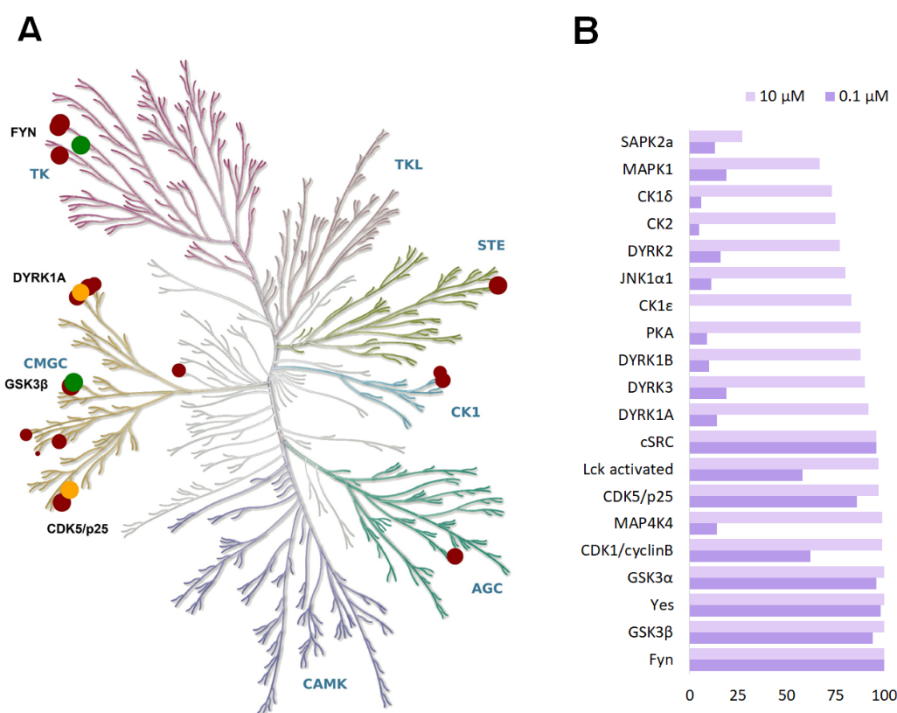
Figure 2.5 A) Kinase tree representation of compound **72** selectivity profile toward 20 different PKs. Protein circles denote % of inhibition at 10 µM (values reported in Table 2.2). GSK-3β and FYN are illustrated as green circles. DYRK1A and CDK5/p25 as orange circles. All the other crossover off-target kinases, including GSK-3α, SAPK2a, MAPK1, MAP4K4, JNK1α1, PKA, cSRC, CDK1/cyclinB, Yes, Lck activated, CK1δ, DYRK1B, CK1ε, CK2, DYRK3, DYRK2 are depicted as red circles. Illustration reproduced courtesy of Cell Signaling Technology, Inc. (www.cellsignal.com)[237] ; B) Bar chart representation of **72** selectivity profile. Percentage of inhibition tested at 10 µM is illustrated in lavender violet and at 0.1 µM in violet.

Table 2.2 Percentage (%) of inhibition of compound **72** at 0.1 and 10 µM against a panel of 20 different PKs and open targets platform-based scores.

Rank	Kinase	Kinase Inhibition %[a]		Overall Nervous System tauopathy like diseases score
		0.1 µM	10 µM	
1	DYRK1A(h)	14	92	0.89
2	CDK5/p25(h)	86	97	0.84

3	FYN(h)	100	100	0.60
4	GSK-3β(h)	94	100	0.59
5	GSK-3α(h)	96	100	0.45
6	SAPK2a(h)	13	27	0.42
7	MAPK1(h)	19	67	0.38
8	MAP4K4(h)	14	99	0.36
9	JNK1α1(h)	11	80	0.32
10	PKA(h)	9	88	0.31
11	cSRC(h)	96	96	0.30
12	CDK1/cyclinB(h)	62	99	0.16
13	Yes(h)	98	100	0.05
14	Lck(h) activated	58	97	0.04
15	CK1δ(h)	6	73	0.03
16	DYRK1B(h)	10	88	0.02
17	CK1ε(h)	0	83	0.02
18	CK2(h)	5	75	0.01
19	DYRK3(h)	19	90	0
20	DYRK2(h)	16	77	0

Kinases are ranked according to the reported overall strength of a given target–disease association from the Open target Platform (https://platform.opentargets.org).[235] Panel of selectivity data are shown according to the following color scale: green color is associated with a high % of inhibition values; orange is associate with a modest % of inhibition; red color corresponds to a low % of inhibition. [a]Data reported as the mean of two independent experiments.

CDK5 is a proline-directed Ser/Thr kinase, which belongs to the CDK family. It is predominantly located in postmitotic neurons, where it plays a vital role in brain development, neuronal survival, synaptic plasticity, MT regulation, and pain signaling. Under neurotoxic conditions, p25, the *N*-terminal truncated isoform of p35, promotes

CDK5 hyperactivation leading to tau hyperphosphorylation and consequent aggregation to form NFTs in AD.[238, 239]

Considering the high values of percentage inhibition at 0.1 µM concentration, first the IC_{50} values of compound **72** were determined for both DYRK1A and CDK5/p25. Then, docking and X-ray studies were performed to identify the structural features of our compound responsible for the reductions in both enzymes' activities. In the enzymatic radiometric assay, compound **72** proved to be a nanomolar inhibitor of both PKs displaying an IC_{50} value of 887 nM on DYRK1A and 40 nM on CDK5/p25 (Table 2.3). Compound **72** was then docked against flexible receptor models of DYRK1A and CDK5 and binding scores of -26.5 and -21.1 were calculated for DRYK1A and CDK5, respectively. Moreover, crucial contacts between **72** and key residues in the ATP-binding sites of both proteins (Figure 2.6) were observed, resembling those typical of type I or II inhibitors.[234] In detail, the aminopyrazole of **72** was predicted to form three HBs with hinge region residues Leu 241 and Glu 239 when binding to DYRK1A (Figure 2.6 A) and three total HBs with hinge region residues Cys 83 and Glu 81 when binding to CDK5 (Figure 2.6 C). When binding to DYRK1A, compound **72** was predicted to form hydrophobic interactions between its pyrimidine moiety and residues Glu 291, Asn 244, Asp 247, Tyr 243, and Ser 242, its aminopyrazole heterocycle and residues Met 240, Phe 239, and Ala 186, its cyclopropyl group and residues Phe 238, Val 222, and Val 173, and between its benzylamine moiety and residues Val 173, Gly 166, Phe 170, and Val 306 (Figure 2.6 B). When binding to CDK5, compound **72** was predicted to form hydrophobic contacts between its pyrimidine moiety and residues Ile 10, Gln 85, Leu 133, and Asp 84, between its aminopyrzole heterocycle and residues Phe 82 and Ala 31, its cyclopropyl group and residues Phe 80, Val 64, and Lys 33, and between its benzylamine moiety and residues Glu 12, Gly 13, Asp 144, Asn 131, Gln 130, and Asp 86 (Figure 2.6 D).
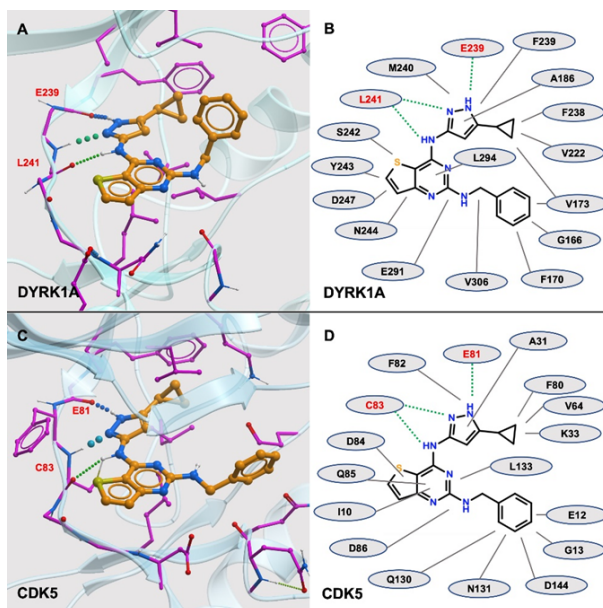
Figure 2.6 Graphical representations of the binding mode of **72** to DYRK1A and CDK5. (A, C) Structural models of DYRK1A (A) and CDK5 (C) from docking simulations. Flexible receptor model for DYRK1A constructed from the following PDB entries: 5AIK, 4YLJ, 4YLK, 4YLL, 4YU2, 4AZE, 3ANQ, 3ANR, 4MQ1, 4MQ2, 4NCT. Flexible receptor model for CDK5 constructed from the following PDB entries: 4AU8, 1H4L, 3O0G, 1UNG, 1UNH, 1UNL. (B, D) Schematics showing the binding pocket interactions predicted between compound **72** and DYRK1A (B) and CDK5 (D), respectively. Dark grey lines indicate hydrophobic interactions; green dotted lines are used for HBs.

To corroborate the docking results, DYRK1A crystals were soaked with **72** (Figure 2.7, PDB ID: 7OY6). The crystals diffracted at 2.4 Å resolution, and, according to molecular replacement analysis, a single protein molecule was found located in the asymmetric unit. A clear electron density corresponding to compound **72** was observed in the ATP binding pocket (Figure 2.7 A and B), as reported above for GSK-3β. Similar to GSK-3β in complex with compound **72**, and in good agreement with docking simulations, **72**-DYRK1A complex displayed H-bonding interactions with backbone atoms of the hinge region residues Glu 239 and Leu 241 (Figure 2.7 C). In a similar fashion to GSK-3β, also compound **72** demonstrates type-I type inhibition in the ATP binding pocket of DYRK1A.
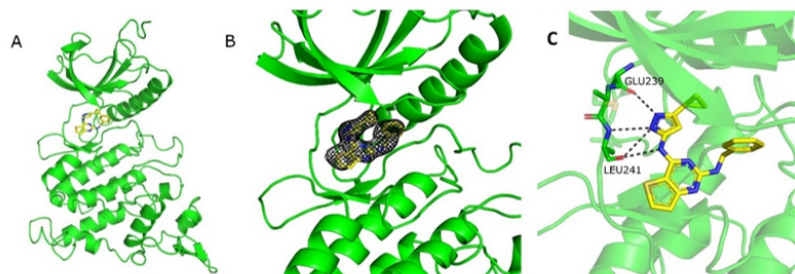
Figure 2.7 Crystal structure of DYRK1A in complex with **72**. A. Compound **72** (yellow) in the ATP binding pocket of DYRK1A (green). B. Electron density map ($2F_O - FC$) corresponding to **72** is contoured at 1.2σ level (black mesh). C. H-bonding interactions (black dashes) of **72** with the backbone atoms of hinge region residues Glu 239 and Leu 241 of DYRK1A (green).

For CDK5/p25, the available X-ray structure of CDK5 (PDB ID: 1UNL) was overlapped with the X-ray structure of GSK-3β in complex with **72** (Figure 2.8). According to the structural overlapping, **72** adopted a binding pose similar to that observed at the ATP GSK-3β binding site (Figure 2.8 A). Compound **72** is likely to form key H-bonding interactions with backbone atoms of CDK5 residues (Glu 81 and Cys 83, Figure 2.8 B) as previously observed for the other kinases (Figures 2.2, 2.3, and 2.7). Here too, the excellent agreement between this structure and that coming from docking simulations testify to the high reliability of the *in silico* studies. Given this, it is highly likely that compound **72** will be a type-I inhibitor also for CDK5/p25 as well.
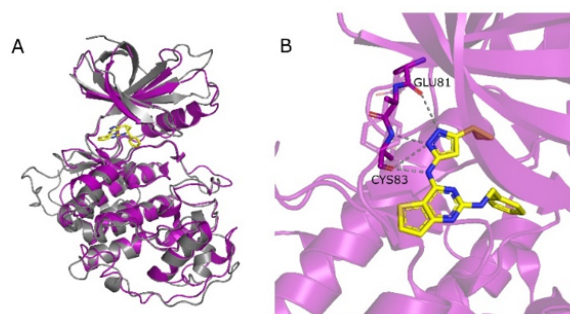

Figure 2.8 Overlapping of GSK3β-**72** complex with CDK5 structure. A. Overlapping of CDK5 (purple) structure (PDB ID: 1UNL) with the structure of GSK-3β (grey) in complex with **72** (RMSD 1.066). Compound **72** at the ATP binding pocket of CDK5. B. Potential HB interactions (grey

dashes) between **72** and CDK-5 backbone atoms (Glu 81 and Cys 83), based on the structures overlapping.

Despite numerous past efforts to find agents able to modulate aberrant CDK5 activity linked to AD and related tauopathies, several CDK5 inhibitors have not shown selectivity relative to other CDKs involved in the cell cycle and mRNA transcription regulation. Additionally, the development of CDK5 inhibitors as promising CNS drug candidates has been hampered by severe off-target adverse effects.[240,239] Conversely, DYRK1A is a relatively recent and promising PK to explore for the treatment of NDDs such as AD (including early-onset AD in DS patients) and PD.[178, 241,242]

Based on these considerations, DYRK1A was selected as the third kinase to be inhibited simultaneously with GSK-3β and FYN to tackle aberrant tau hyperphosphorylation.

To maintain consistency with FYN and GSK-3β, we employed the NanoBRET assay to confirm the capability of compound **72** to bind to DYRK1A in HEK293 cells. As reported in Table 2.3, although with less affinity than observed for FYN and GSK-3β, **72** was able to bind DYRK1A with an IC_{50} value in the low micromolar range. Again, the potency was lower than that observed in the enzymatic biochemical assays, possibly due to an effect of the cellular environment on **72** apparent binding affinity for the enzyme.

Table 2.3 Enzymatic radiometric and NanoBRET assays data of compound **72** on DYRK1A and CDK5.

Cmpd ID	Enzymatic Radiometric Assay		NanoBRET Target Engagement Cellular Kinase Assay
	IC_{50} (nM)		IC_{50} (μM)
	DYRK1A[a]	CDK5[a]	DYRK1A[b]
72	887	40	2.09

CEP701 (79)	0.02

2.3 Design and synthesis of novel triple kinases analogs

Taking into account the versatility of **72** and the information acquired during its proof of concept characterization including both computational and X-ray data together with its promising biological and biophysical results, our group was encouraged to further optimize this chemical entity. A Structure-Activity Relationship (SAR) exploration was thus carried out in order to balance the activity profile against GSK-3β, FYN, and DYRK1A, which is one of the most important prerequisites while designing multi-target agents.

Therefore, the improvement of the inhibitory potency against protein DYRK1A was identified as an initial goal of this project. Computer-assisted drug design (CADD) protocols and synthetic efforts were combined with the aim to better understand the pharmacophoric traits of the molecule towards the three PKs and what type of modifications would have allowed us to gain potency against DYRK1A.

First, some proposed analogs of **72** bearing modifications on the aminopyrazole moiety, crucial structural element for target engagement and activity, were discarded. Among them, three ligands (**80**-**82**, Figure 2.9) were designed and docked to evaluate the possible binding mode in order to underline the importance of this heterocycle for all of the three targets. A decrease in binding affinity was observed for all three PKs as confirmed by the worsening of the docking scores (higher values, Figure 2.9).
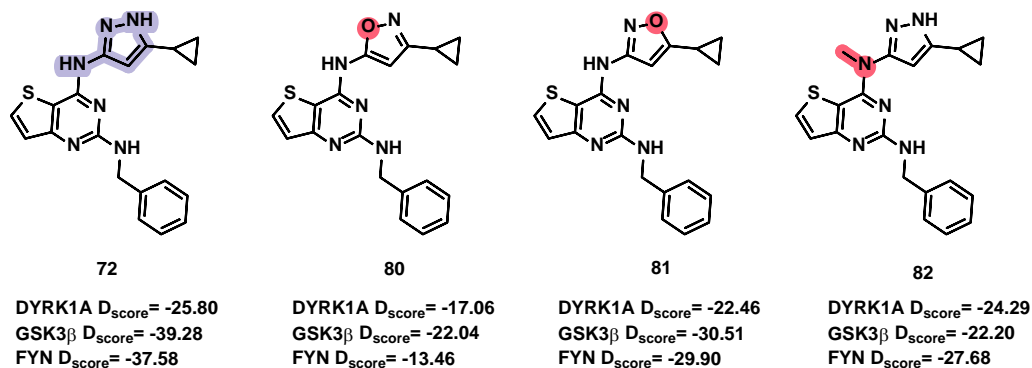
	72	80	81	82
DYRK1A D_{score}	-25.80	-17.06	-22.46	-24.29
GSK3β D_{score}	-39.28	-22.04	-30.51	-22.20
FYN D_{score}	-37.58	-13.46	-29.90	-27.68

Figure 2.9 Structure and calculated docking scores (D_{score}) of the three discarded proposed ligands (**80**-**82**) in comparison with **72**. Aminopyrazole is highlighted in purple, drastic modifications are highlighted in red.

In further detail, while replacing the pyrazole moiety with an isoxazole and its corresponding isomer (**80**, **81**) led to unfavorable values in the docking score for DYRK1A, with methylation of the exocyclic NH group proving to be better tolerated. For all three discarded ligands, the loss of crucial H-bonding interactions as a consequence of the insertion of a HB acceptor in place of an HB donor (Figure 2.10), led to a loss of crucial H-bonding interactions. This may be responsible for the decrease in the affinity of the ligands within the ATP pockets of the three PKs.

80 was the compound possessing the most detrimental modifications for DYRK1A in addition to GSK-3β and FYN, although it retained very similar binding poses to the parent compound **72**.
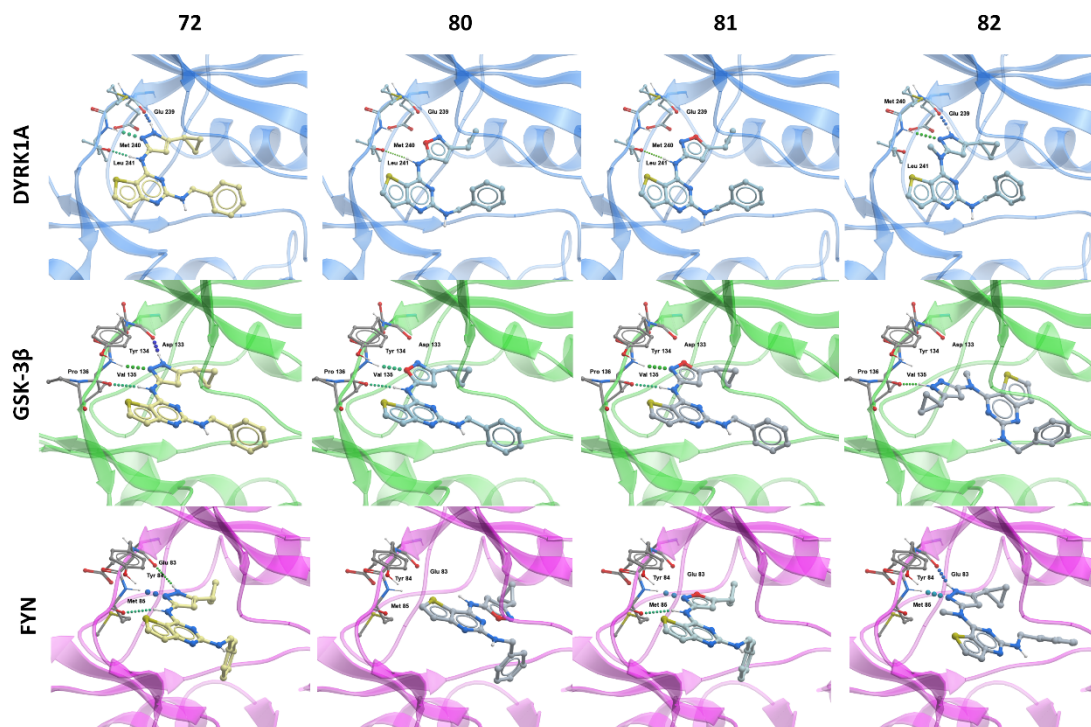
Figure 2.10 Predicted binding poses of **80**-**82** in comparison with **72**; the DYRK1A (blue ribbon), GSK-3β (green ribbon) and FYN (pink ribbon) ATP-binding pockets.

Our SAR investigation was driven by the different size and shape of the ATP-binding cavity of GSK-3β/FYN and DYRK1A though the high homology of all three PKs (Figure 2.11). In detail, the DYRK1A binding site looks to be larger than those of the other two enzymes offering higher possibility in terms of a ligand chemical expansion. Moreover, GSK-3β possesses a slightly more spacious ATP pocket compared to FYN and they both share a thigh niche where the pyrazole moiety of **72** accommodates in. In addition, both GSK-3β and FYN possess a conserved bulky Tyr residue in their ATP pockets (Tyr 134 and Tyr 84, respectively) in the same plane as the aromatic central framework of the starting molecule **72**, likely producing π-π interaction; while a sulfur-containing residue Met 240 is present in DYRK1A.
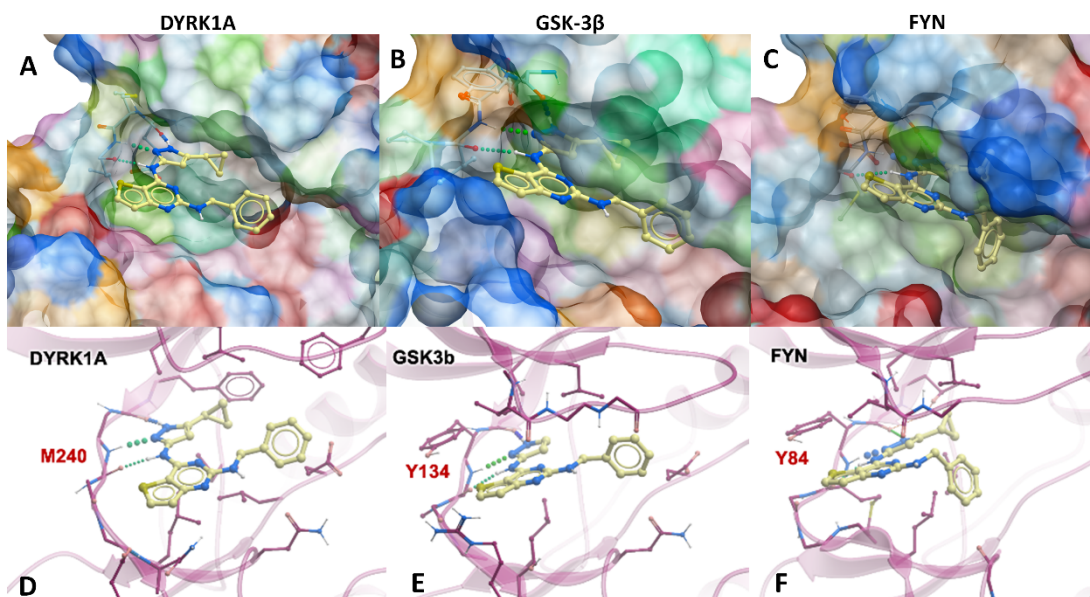
Figure 2.11 Surface representation of DYRK1A (A), GSK-3β (B) and FYN (C) binding pockets, color code associated to amino acid residues. H-bonding interactions of **72** with the three proteins (D, E, F) with the conserved ATP-binding pocket residues labeled in red.

These observations therefore initially suggested investigating the substituents directly attached to the pyrazole and the pyrimidine moiety of **72**. Thus, in order to validate the predictive computational model the chemical space around the 2,4-di-substituted pyrimidine central core was investigated by placing single-properly addressed modifications at three different positions. To do so, we designed and synthetized three different series (I-II-III) of novel derivatives where a modification at a time was introduced (Figure 2.12).
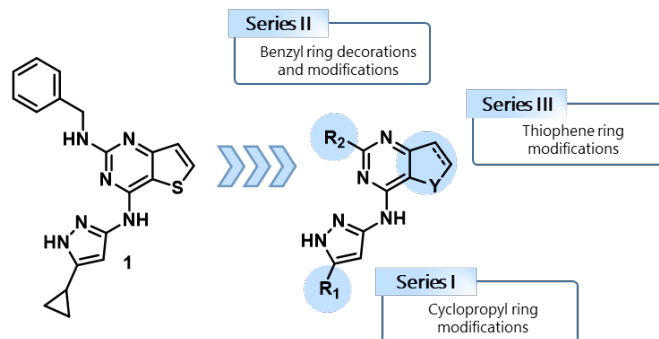
Figure 2.12 Schematic representation of the SAR exploration undertaken starting from compound **72**.

2.3.1 Series I, design synthesis and biological evaluation

To explore the amino pyrazole moiety of **72**, the cyclopropyl ring was exchanged with substituents of different steric hindrance and electronic properties (R_1, Figure 2.13). In detail, the substituent on the pyrazole ring (R_1) was replaced with a hydrogen atom (**83**, Figure 2.13), small lipophilic substituents as the methyl, isopropyl and cyclobutyl groups (**84-86** respectively, Figure 2.13), and aromatic rings as phenyl (**87**, Figure 2.13) and 3-pyridine (**88**, Figure 2.13).
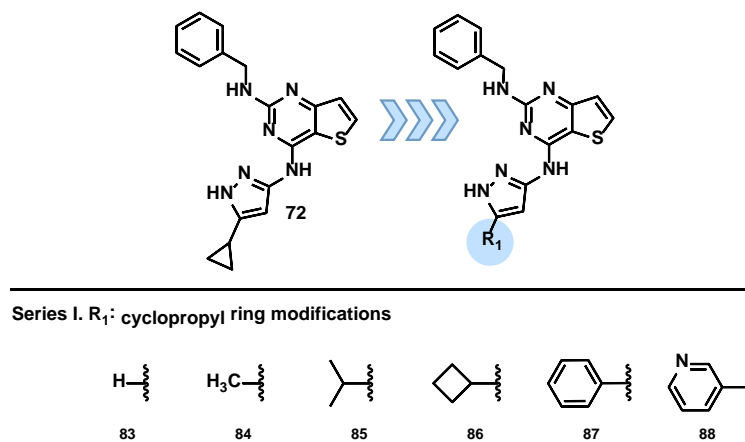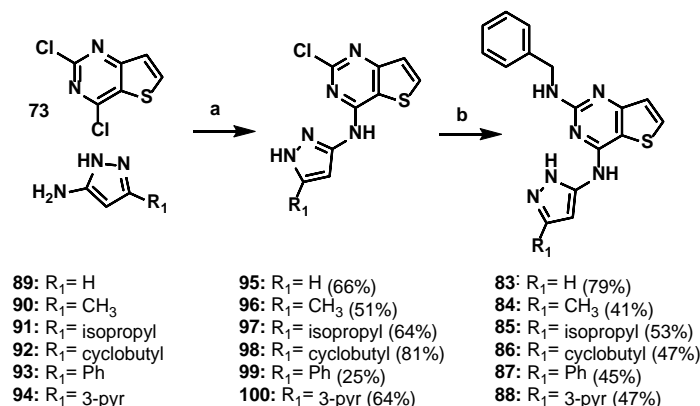

Figure 2.13 Series I modifications (compounds **83-88**).

As the chemical route employed in synthesis of **72** was a mild and simple strategy, the same protocol consisting of two sequential SN$_{Ar}$ reactions on 2,4-dichlorothieno[3,2-*d*]pyrimidine was performed to prepare the first set of analogues in good yields and at a low cost (Scheme 2.2).

All synthetized derivatives were subsequently screened in an in-house LANCE® Ultra time-resolved fluorescence energy transfer (TR-FRET) assay in triplicate against GSK-3β, FYN and DYRK1A (Table 2.4).

Scheme 2.2 Synthesis of compounds **83**-**88**.

89: R$_1$= H
90: R$_1$= CH$_3$
91: R$_1$= isopropyl
92: R$_1$= cyclobutyl
93: R$_1$= Ph
94: R$_1$= 3-pyr

95: R$_1$= H (66%)
96: R$_1$= CH$_3$ (51%)
97: R$_1$= isopropyl (64%)
98: R$_1$= cyclobutyl (81%)
99: R$_1$= Ph (25%)
100: R$_1$= 3-pyr (64%)

83: R$_1$= H (79%)
84: R$_1$= CH$_3$ (41%)
85: R$_1$= isopropyl (53%)
86: R$_1$= cyclobutyl (47%)
87: R$_1$= Ph (45%)
88: R$_1$= 3-pyr (47%)

Reagents and conditions: a) Et$_3$N, rt or 50 °C, 24 h; b) **76**, *n*-BuOH, 110 °C, 72 h.

Table 2.4 GSK-3β, FYN and DYRK1A inhibition data of Series I derivatives.

Cmpd #	GSK-3β IC$_{50}$ (nM)	FYN-A IC$_{50}$ (nM)	DYRK1A	
			nM	% inh[1]
72	4.83 ± 0.30	4.13 ± 0.69	n.d.[2]	53.3 ± 2.6%
83	334.00 ± 9.9	249.00 ± 4.6	n.d.	12.4 ± 0.8%
84	26.9 ± 5.8	13.9 ± 2.9	n.d.	20.1 ± 1.6%
85	26.7 ± 6.4	30.1 ± 2.2	3187.0 ± 248	54.3%
86	10.8 ± 0.31	3.81 ± 0.19	1680.0 ± 132	64.3%

87	54.4 ± 1.14	220.0 ± 67.6	n.d.	9.1 ± 1.4%
88	12.2 ± 1.1	78.1 ± 19.3	n.d.	n.d.

[1]*inhibition at 5 μM data reported due to low solubility of the compounds in the buffer;* [2]*not determined.*

The removal of the cyclopropyl moiety (**83**) proved to be detrimental for the activity against all three PKs particularly towards GSK-3β and DYRK1A according to the predicted decrease in binding affinity for both targets (GSK-3β D_{score}= -36.2; DYRK1A D_{score}= -21.01). This observation confirmed that, despite the differences of this niche between GSK-3β, FYN, and DYRK1A, an appropriate chemical entity attached to the amino pyrazole moiety is required for establishing hydrophobic interactions at the targets ATP-binding sites. The importance of this substituent was confirmed while testing the derivatives featuring alkyl and cycloalkyl groups (**84-86**), which were better tolerated than aryl and heteroaryl groups (**87** and **88**). The detrimental effect of the phenyl ring (**87**) for DYRK1A binding affinity compared to the cyclobutyl (**86**) and cyclopropyl (**73**) moieties was also predicted by docking simulations, which suggested an important role of the substituent steric hindrance in influencing the orientation of the aminopyrazole moiety (Figure 2.14).

The best performing compound of this series possessed the cyclobutyl moiety instead of the cyclopropyl one (**86**).

86 retained a well-balanced low nM activity against GSK-3β and FYN (IC_{50} = 10.8 and 3.81 nM, respectively). Furthermore, it demonstrated a slight improvement in potency against DYRK1A (IC_{50} = 1680 nM; % inh @ 5 μM = 64.3%) in comparison to the parent compound **72** probably due to a wider lipophilic surface of the molecule, which provided a more stable lipophilic interaction with the enzyme gatekeeper Phe 238 (Figure 2.14).
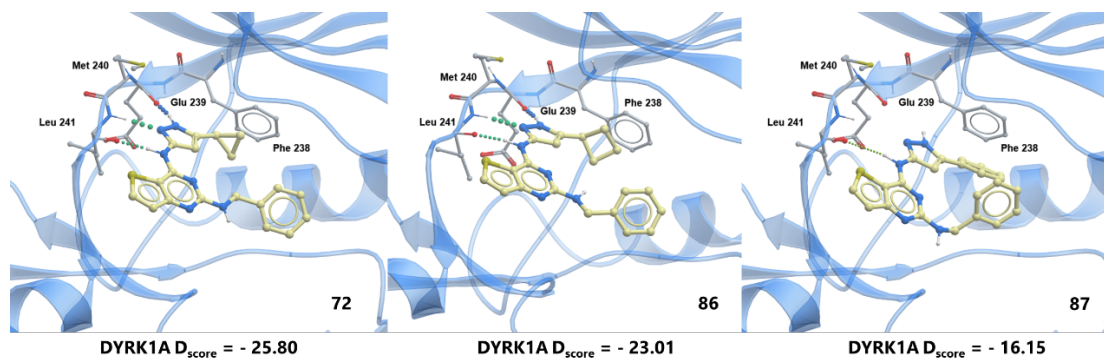
Figure 2.14 Predicted binding mode of **72**, **86** and **87** in the DYRK1A binding pocket and calculated docking scores.

2.3.2 Series II, design synthesis and biological evaluation

In Series II, the benzylic function of **72** was decorated at *para* and *meta* positions, (R_2, Figure 2.15) as the calculated docking scores seemed indicate a consistent improvement in binding affinity compared to the *ortho* substitutions. The aromatic ring was thus enriched with diverse electron withdrawing groups (*e.g.*, -F and -Cl: **101** and **102**; CN: **104**; CONH$_2$: **106** and **109**; and **3**-pyr: **110**) and electron-donating groups of different steric hindrance (OH: **105**, OCH$_3$: **103**, **111,** methandiol: **107** and OBn: **108**). The choice of the nature and position of these substituents was aimed to improve the selectivity and binding affinity of **72** by catching through additional HBs hydrophilic residues present in the big lipophilic niche.
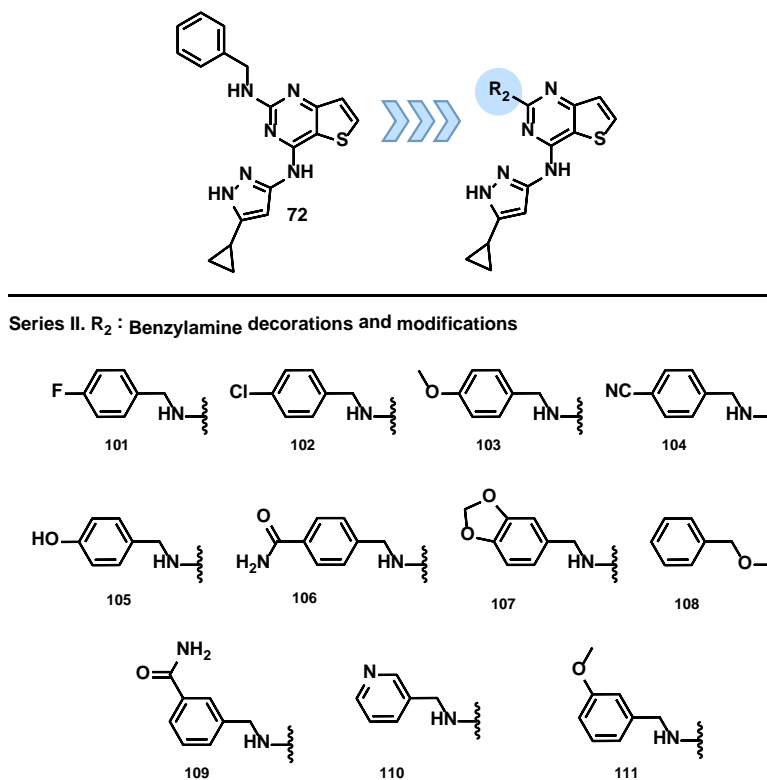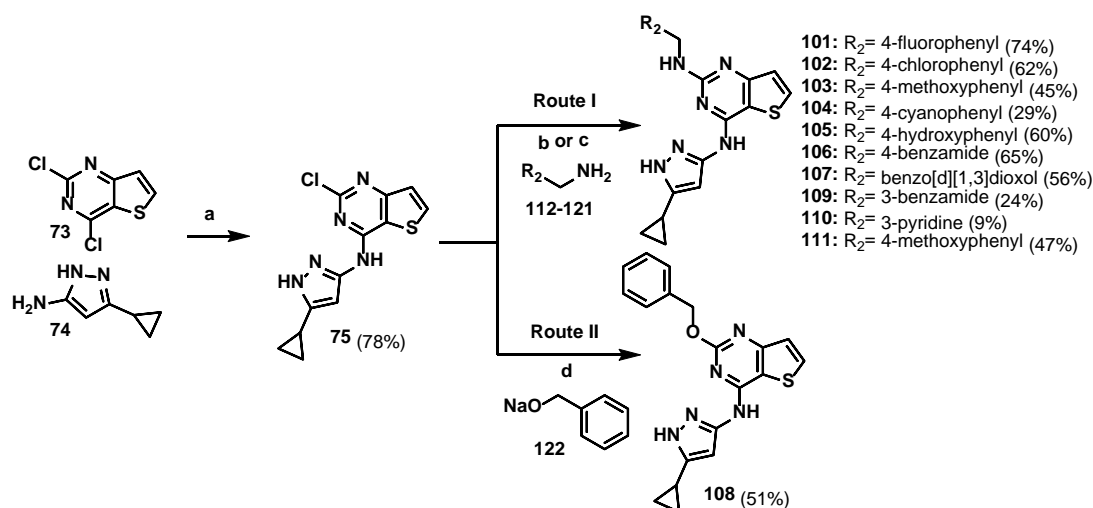
Series II. R$_2$: Benzylamine decorations and modifications

Figure 2.15 Series II modifications (compounds **101**-**111**)

Analogs **101-111** were obtained following the same general procedure employed to access to the starting point **72** and its series I derivatives.

Initially, an SN$_{Ar}$ reaction at room temperature, by employing commercially available aminopyrazole derivatives and triethylamine as base, afforded the corresponding 2-chloro-*N*-(5-alkyl/cycloalkyl/aryl/heteroaryl-1*H*-pyrazol-3-yl)thieno[3,2-*d*]pyrimidin-4-amines (Scheme 2.3). A subsequent SN$_{Ar}$ (Route I) was performed under conventional heating (110 °C) with a large excess of benzylamines (5 equiv.) yielding compounds **101**-**103**. Optimization of the same chemical protocol under MW irradiation allowed to shorten the reaction times from 72 to 6-8 h and reduce the equivalents of the appropriate benzylamines from 5 to 1.5 with a significant facilitation of the purification process (**104-107, 109-111**).

The benzyloxy analog **108** was also accessed via SN_{Ar} in the presence of sodium benzyloxide under MW irradiation (Scheme 2.3, Route II).

Scheme 2.3 Preparation of series II derivatives.

101: R$_2$= 4-fluorophenyl (74%)
102: R$_2$= 4-chlorophenyl (62%)
103: R$_2$= 4-methoxyphenyl (45%)
104: R$_2$= 4-cyanophenyl (29%)
105: R$_2$= 4-hydroxyphenyl (60%)
106: R$_2$= 4-benzamide (65%)
107: R$_2$= benzo[d][1,3]dioxol (56%)
109: R$_2$= 3-benzamide (24%)
110: R$_2$= 3-pyridine (9%)
111: R$_2$= 4-methoxyphenyl (47%)

Reagents and conditions. a) Et$_3$N, rt, 2-5 days; b) *n*-BuOH, DIPEA, 180 °C, 4-6 h, MW, Ar; c) *n*-BuOH, 110 °C, 2 days, Ar; d) THF, 150 °C, 7 h, MW, Ar.

**Scheme 2.4** Synthesis of trifluoracetic acid salt intermediate **123**.
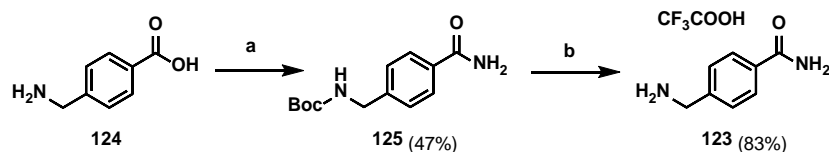
Reagent and conditions. a) (Boc)$_2$O/NH$_4$HCO$_3$, pyridine, 1,4-dioxane dry, 105 °C, 3 h, MW, Ar; b) TFA, CH$_2$Cl$_2$, 0 °C to rt, 1.5 h, Ar.

The 4-(aminomethyl)benzamide **123** to prepare derivative **106** was in turn synthetized by treating the corresponding carboxylic acid **124** with di-*tert*-butyl dicarbonate in the presence of NH$_4$HCO$_3$ followed by cleavage of *N*-Boc protecting group under acid conditions with TFA treatment (Scheme 2.4). An in-dept optimization

of the experimental conditions of the first step reaction improved yield up to 44% (entry 10, Table 2.5).

Table 2.5 Optimization of the experimental conditions for the synthesis of *tert*-butyl *N*-[(4-carbamoylphenyl)methyl]carbamate **125**.
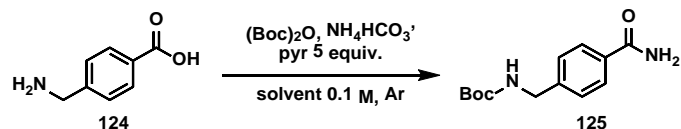
| Entry	NH$_4$HCO$_3$ /(Boc)$_2$O equiv.	Solvent	T (°C)	Time (h)	Yield (%)
1	1.5	1,4-dioxane	25[a]	3	-
2	3	1,4-dioxane	50[a]	12	9
3	1.5	1,4-dioxane	80[a]	20	10[c]
4	1.5	DMF	25[a]	72	4[c]
5	1.5	DMF	120[a]	12	7[c]
6	1.5	1,4-dioxane	105[b]	3	10[c]
7	4.5	1,4-dioxane	105[b]	3	20[c]
8	9.5	1,4-dioxane	105[b]	3	30[c]
9	14.5	1,4-dioxane	105[b]	3	35[c]
10	15	1,4-dioxane	105[b]	3	44

[a] *conventional heating;* [b]*MW;* [c] *estimated yield (%) from UPLC-MS analysis of the reaction crude.*

Since the presence of two nucleophilic functions in the *p*-hydroxy benzylamine scaffold did not allow the chemo-selective synthesis of derivative **105** through the general procedure depicted in Scheme 2.3, a Buchwald cross-coupling reaction was employed (Scheme 2.5, step b). However, despite the conversion of the starting materials into the desired product was observed, the title compound was isolated with a very low yield. Therefore, an alternative strategy was approached starting from the

p-methoxy analog **103** via demethylation reaction by using either BBr$_3$ or BCl$_3$ (Scheme 2.5, steps c and d). Given the formation of side products as no-chromatographically different molecules to **105**, the selective protection of the hydroxyl function of *p*-hydroxy benzylamine (**126**) was carried out starting for the commercially available 4-hydroxybenzonitrile (**128**) (Scheme 2.5, step e). Despite the good feasibility of protection reactions using both TBDMS-Cl and TBDPS-Cl, various conditions of the following nitrile reduction (Scheme 2.5, steps f/g/h) led to simultaneous deprotection of the hydroxyl moiety making the synthetic strategy not suitable for the synthesis of the desired product.

To overcome this issue, the direct chemo-selective silyl protection of **126** by using TBDPS-Cl was attempted. The reaction was conducted either in the polar aprotic solvent THF, where the starting material was not very soluble, and in protic conditions DMF to aid solubility. The use of DMF resulted in a low product formation due to the competition of DMF acting as a Lewis base with the imidazole. The corresponding protected 4-OH-benzylamine (**127**) was finally obtained in moderate yield (58%) and was further employed in the sequential SN$_{Ar}$ with **75**. A final cleavage of the TBDPS group under mild conditions using KHF$_2$ [243] at room temperature yielded the title derivative **105**.

Scheme 2.5 Different synthetic routes to assess derivative **105**.
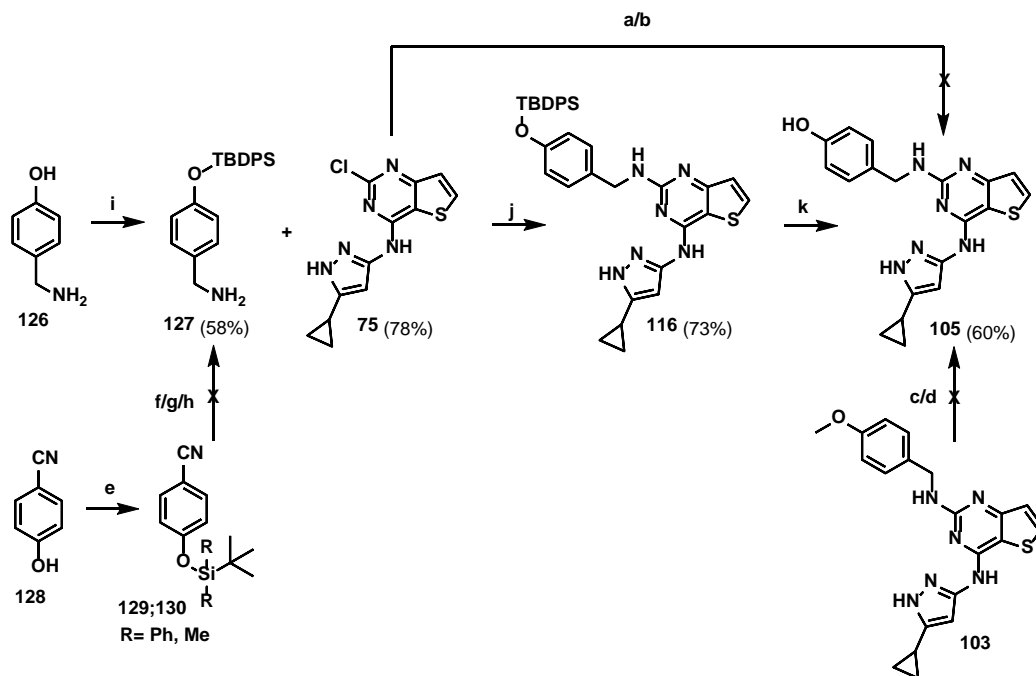
Reagents and conditions. a) *n*-BuOH, DIPEA, 180 °C, 8 h, MW; b) Pd(Ac)$_2$, Xanthphos, Cs$_2$CO$_3$, 1,4-dioxane, 100 °C Ar; c) BBr$_3$, DCM, -78 °C to rt, on; d) BCl$_3$, DCM, -78 °C to rt, on; e) TBDMSCl or TBDPSCl, imidazole, DMF dry, rt, on; f) H$_2$, Pd/C, MeOH, H-cube, 15 bar; g) LiAlH$_4$, THF dry, Ar, reflux, 3 h; h) CuBr$_2$, NaBH$_4$, EtOH, rt, Ar; i) TBDPCl , imidazole, THF rt, on; j) *n*-BuOH, 180 °C, Ar, MW, 6 h; k) KHF$_2$, MeOH, rt, on. No-go crosses indicate the reaction was unsuccessful.

In vitro enzymatic inhibitory activity allowed a comprehensive understanding of the effect of the small modifications upon the benzyl moiety of **72**. All the replacements and decorations proved to be well tolerated against all the three enzymes. In further detail, the introduction of a fluorine atom in the *para* position (**101**, Table 2.6) demonstrated a 11-fold decrease in the potency against GSK-3β compared to **72**, while the insertion of a larger halogen moiety such as the chlorine atom showed a 23-fold decrease in the enzyme inhibition (**102**, Table 2.6). The same modifications were better tolerated by the other two targets, which retained IC$_{50}$ values in the range

between 2-30 nM for FYN and 2-6 μM for DYRK1A. The insertion of the bulky *p*-methoxy moiety (**103**) had a similar outcome to **102** for GSK-3β and DYRK1A and produced a 16-fold decrease in FYN affinity compared to **72**.

Table 2.6 GSK-3β, FYN and DYRK1A inhibition data of Series II derivatives.

Cmpd #	GSK-3β IC$_{50}$ (nM)	FYN-A IC$_{50}$ (nM)	DYRK1A	
			(nM)	% inh[1]
72	4.83 ± 0.30	4.13 ± 0.69	n.d.[2]	$53.3 \pm 2.6\%$
101	53.7 ± 6.82	2.84 ± 0.58	2080 ± 291.2	57.3%
102	109.00 ± 11.1	27.2 ± 6.96	5780 ± 796.8	35.9%
103	101.0 ± 22.1	67.0 ± 18.7	7110 ± 1311	34.5%
104	33.3 ± 10.7	39.8 ± 9.89	3660 ± 496.3	47%
105	3.53 ± 0.42	8.19 ± 2.16	n.d.	$55.3 \pm 4.2\%$
106	16.4 ± 1.61	88.1 ± 2.30	n.d.	$47.5 \pm 1.8\%$
107	57.1 ± 9.65	4.48 ± 0.50	4640 ± 587.0	42.3%
108	7.91 ± 0.275	17.6 ± 4.63	n.d.	$56.0 \pm 1.8\%$
109	1.24 ± 0.24	1.67 ± 0.25	1020 ± 111	64.4%
110	1.11 ± 0.04	5.94 ± 0.73	n.d.	$58.4 \pm 2.2\%$
111	8.85 ± 1.8	9.51 ± 1.68	4910 ± 547.6	35.7%

[1]*inhibition at 5 μM data reported due to low solubility of the compounds in the buffer;* [2]*not determined*

Furthermore, the installation of a carbamoyl function in the same *para* position of the benzylamine group (**106**) slightly reduced the potency against GSK-3β and DYRK1A compared to **72**, while a more marked decrease in FYN inhibition albeit in the two-digit nanomolar range was observed.

Interestingly, while shifting the same substituent in *meta* position (**109**) the activity notably improved in the low nM range against both GSK-3β and FYN and a low µM potency was observed against DYRK1A, suggesting the key role of this modifications for GSK-3β/FYN and DYRK1A inhibition. The successful results obtained with this compound were confirmed by X-ray crystallography, where the engagement of additional H-bonding interactions was seen within the ATP pocket of all three targets (Figure 2.16). The X-ray structure of **109** in complex with GSK-3β shared a similar binding pose with compound **72** characterized by three HBs within the hinge region and a novel interaction between Lys 85 of the enzyme and the *m*-carbamoyl function of the ligand. A similar scenario was observed for DYRK1A, for which Lys 188 was observed to establish contact with the amide moiety of **109**, justifying the higher binding affinity also observed for this target.

Finally, thanks to the high phylogenetic similarity between the ATP binding pocket of the selected PKs, superimposition of FYN in complex with staurosporine (**31**, PDB 2DQ7) with our in-house generated X-ray structure of GSK-3β in complex with **109** was carried out to investigate the structural elements conducive to FYN engagement. Compound **109** retained a similar HB pattern as for GSK-3β and DYRK1A (Figure 2.16 A and B), keeping the hinge region interaction between the aminopyrazole moiety and the backbone atoms of residues Glu 83, Tyr 84, Met 85 and Asn 86 of FYN. The carbamoyl function, instead, engaged the corresponding Lys 39 and Asp 148 (Figure 2.16 C).
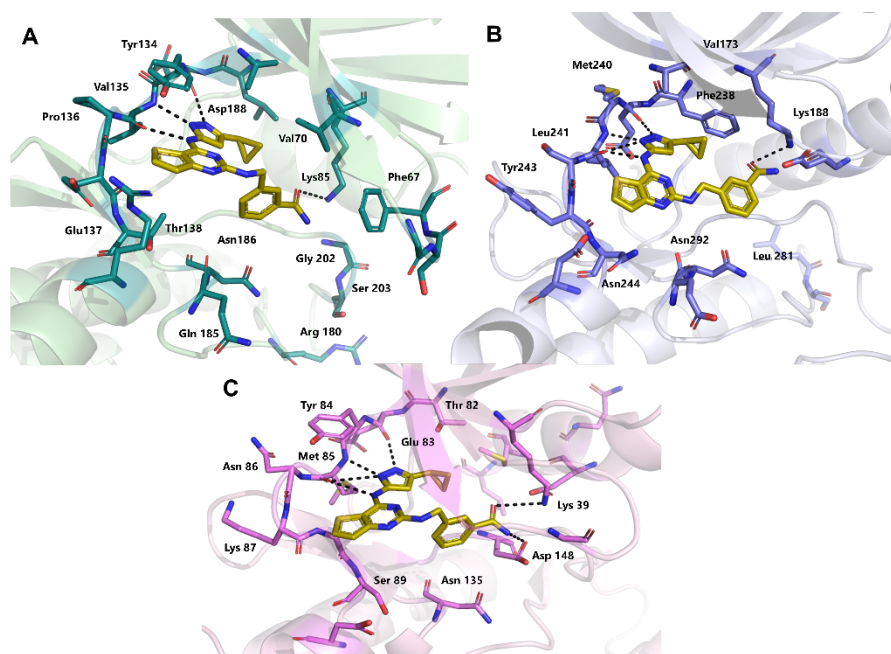
Figure 2.16 A) Compound **109** in complex with GSK-3β (A), DYRK1A (B), and FYN (C)

Similarly to what was observed with compound **109**, the 3-picolylamine derivative (**110**) showed a slight improvement of DYRK1A inhibition up to 58.4% at 5 µM, while retaining the activity against GSK-3β and FYN in the low nanomolar range. Therefore, in good agreement with the predictive computational model, these preliminary results confirmed important differences in the size of the three targets binding pockets involved in the benzyl accommodation, and suggested a higher preference of the DYRK1A pocket for *meta* substitutions rather than for the *para* ones.

2.3.3 Series III, design synthesis and biological evaluation

Considering the high degree of rigidity of the pyrimidine central core and its not direct but essential role in stabilizing the binding conformations of **72** to the three targets ATP pockets, a preliminary exploration (Figure 2.17) around the thiophene ring was performed. In this series, the sulfur atom of the 2,4-substituited-

pyrimidinthiophene central core was first replaced with an HB accepting oxygen atom (**131**) in order to evaluate if additional HB interactions within the DYRK1A binding pocket would have been beneficial for the ligand affinity for the enzyme, while retaining potent and well-balanced nM activity against GSK-3β and FYN. Additionally, the corresponding dihydrothiophene derivative **132** was synthetized to improve the flexibility of the pyrimidin-thiophen ring and assess the importance of the central core aromaticity for all targets inhibition.
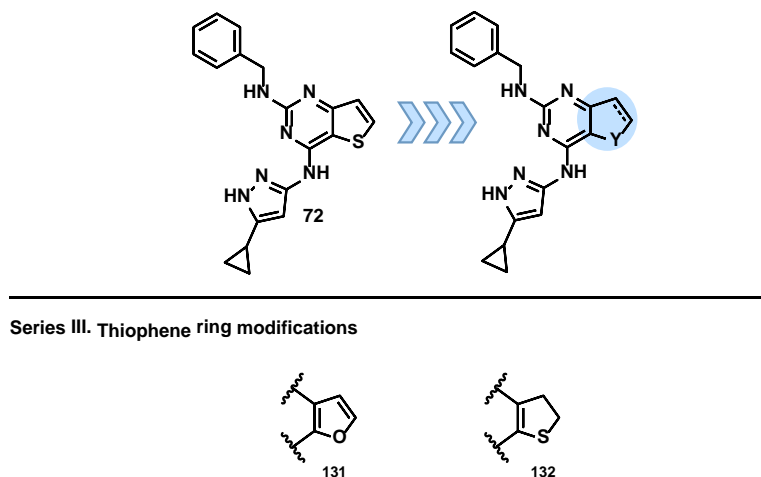
Figure 2.17 Preliminary SAR exploration of the central pyrimidine core.

Table 2.7 GSK-3β, FYN and DYRK1A inhibition data of Series III derivatives.

Cmpd #	GSK-3β IC$_{50}$ (nM)	FYN-A IC$_{50}$ (nM)	DYRK1A % inh[1]
72	4.83 ± 0.30	4.13 ± 0.69	$53.3 \pm 2.6\%$
131	13.72 ± 1.81	15.5 ± 4.04	$60.5 \pm 2.1\%$
132	14.5 ± 0.01	15.7 ± 1.66	47.3 ± 3.1

[1]*inhibition at 5 μM data reported due to low solubility of the compounds in the buffer.*

In this series, the replacement of the thiophene ring of **72** with a furan (**131**) was well tolerated at all three targets with improved binding affinity towards DYRK1A (Table 2.7) probably thanks to the vicinity between the polar furanyl moiety to the backbone nitrogen atom of Leu 241 (Figure 2.18). However, removal of the aromaticity in compound **132** provoked a change in the planarity of the molecule, causing a slight decrease in inhibitory potency (47.3% inhibition at 5 µM) against DYRK1A. The same modification did not notably decrease GSK-3β and FYN inhibition.
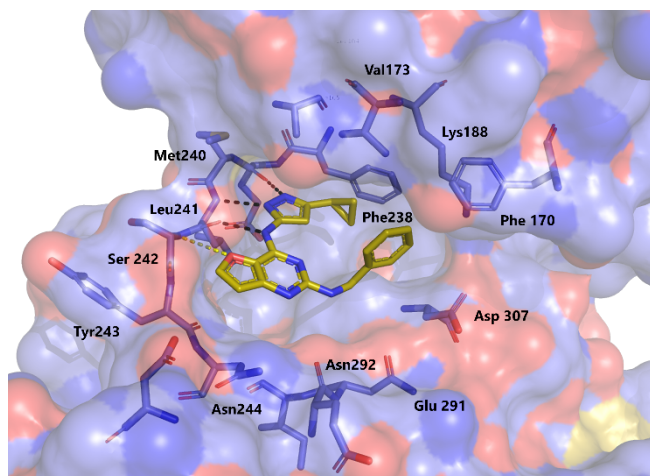
Figure 2.18 X-ray structure of compound **131** in complex with DYRK1A.

These very preliminary results corroborated the docking and X-ray studies suggesting the importance of having a planar molecular frame bridging the two extremities of the molecule and therefore the suitability of an aromatic central core to confer a rigid conformation for optimal targets interaction.

2.3.3.1 Attempt to expand Series III through simplification of the pyrimidinthiophene central core

In line with the just outlined results and to open novel chemical space possibilities, considerable chemical effort was devoted to prepare derivative **133**

(Scheme 2.6), featuring a benzothiophene central core instead of the usual pyrimidinthiophene one, which according to the predicted docking poses did not seem to affect the binding affinity for all the three targets (Figure 2.19). The main reason for pursuing this compound synthesis was not only to investigate the effect of the two nitrogen atoms removal from the molecular framework of **72** in all three targets engagement but also to aid chemical tractability and improve the drug-like properties of **72**.
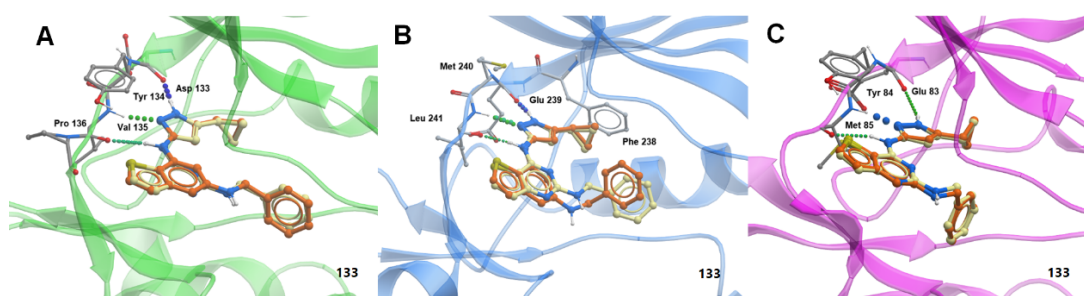

Figure 2.19 Predicted binding pose of **133** (orange) overlapped with **72** (yellow) in the three PKs binding pockets. A) GSK-3β (green); B) DYRK1A C) FYN (pink).

The employed strategy was focused on the construction of the central core starting from the commercially available 2-bromo-4-chloro-aniline (**134**), which reacted in a Sandmeyer reaction with $NaNO_2$ and potassium ethyl xanthate as a sulfur source to give **135**. A further nucleophilic substitution (SN_2) reaction of bromine **136** with 2,4-halogenated phenyl thiol **135** afforded **137**, which, after the screening of different experimental conditions, was successful cyclized in the presence of PPA at 140 °C under an Ar atmosphere to give the di-substituted benzothiophene ring **138** in a good yield.

Scheme 2.6 Multi-step chemical procedure for the synthesis of compound **133**; no-go crosses indicate no chemical reaction success, dotted arrow indicates that the reaction was not performed.
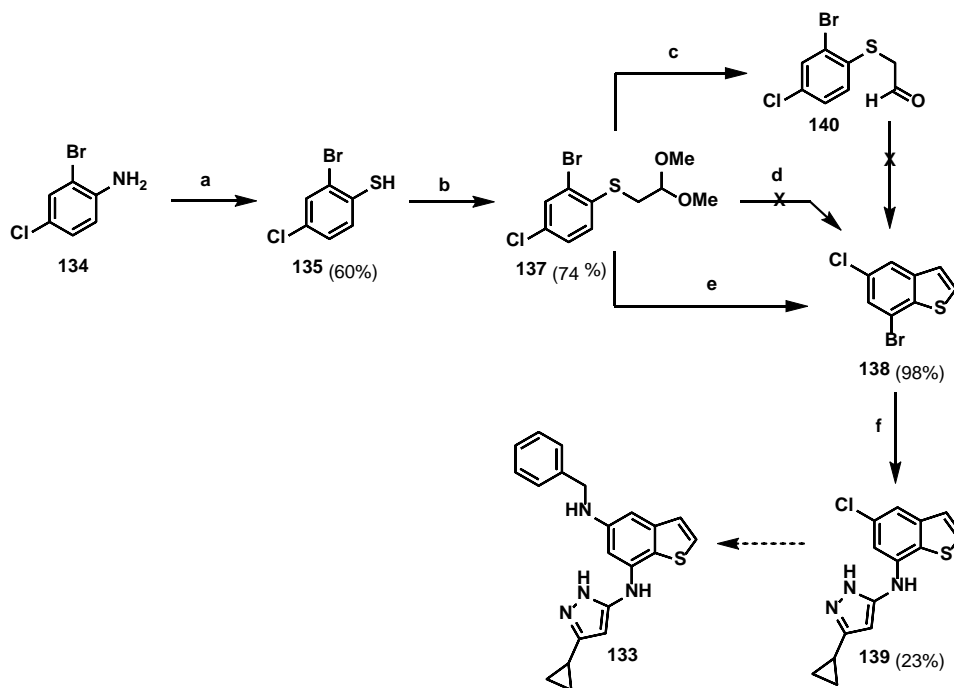
Reagents and conditions. a) NaNO$_2$, HCl conc, -10 °C, potassium ethyl xanthate, 70 °C, 21 h; b) 2-bromo-1,1-dimethoxyethane **136**, K$_2$CO3, DMF dry, 70 °C, 3 h; c) H$_3$PO$_4$ (4.8 equiv.), chlorobenzene, reflux, on d) PPA (1.8 equiv.), chlorobenzene, reflux, on e) PPA (10 equiv., 140 °C, Ar, 21 h); f) **75** BINAP, Pd$_2$(dba)$_3$, Cs$_2$CO$_3$,toluene dry, 150 °C Ar, MW, 10 h.

A Buchwald cross-coupling reaction, conducted at 150 °C in toluene under Ar atmosphere and MW irradiation, allowed the substitution of the more reactive bromine atom of **138** with the 3-amino-5-cyclopropyl-1*H*-pyrazole (**74**) to give **139**. Despite the chemical route allowed the isolation of the bromo-substituted intermediate (**139**), the desired product **133** was not accessible due to the low reactivity of the chlorine atom of **138** in both SN$_{Ar}$ and Buchwald cross-coupling reactions.

2.3.4 Hybrid derivatives of Series IV, design synthesis and characterization

Prior chemical modifications of Series I-II-III allowed us to gain insights into the best substitution patterns, which drove the rational design of a novel set of improved hybrids molecules possessing merged pharmacophoric traits. In detail, six interesting derivatives (**85,86,108-110, 131** Figure 2.20) of the first generation series were selected as a starting platform for a merging strategy to rationally design new hybrid inhibitors (**141-148**) by combining two and three modifications at once on **72** framework (Figure 2.20).
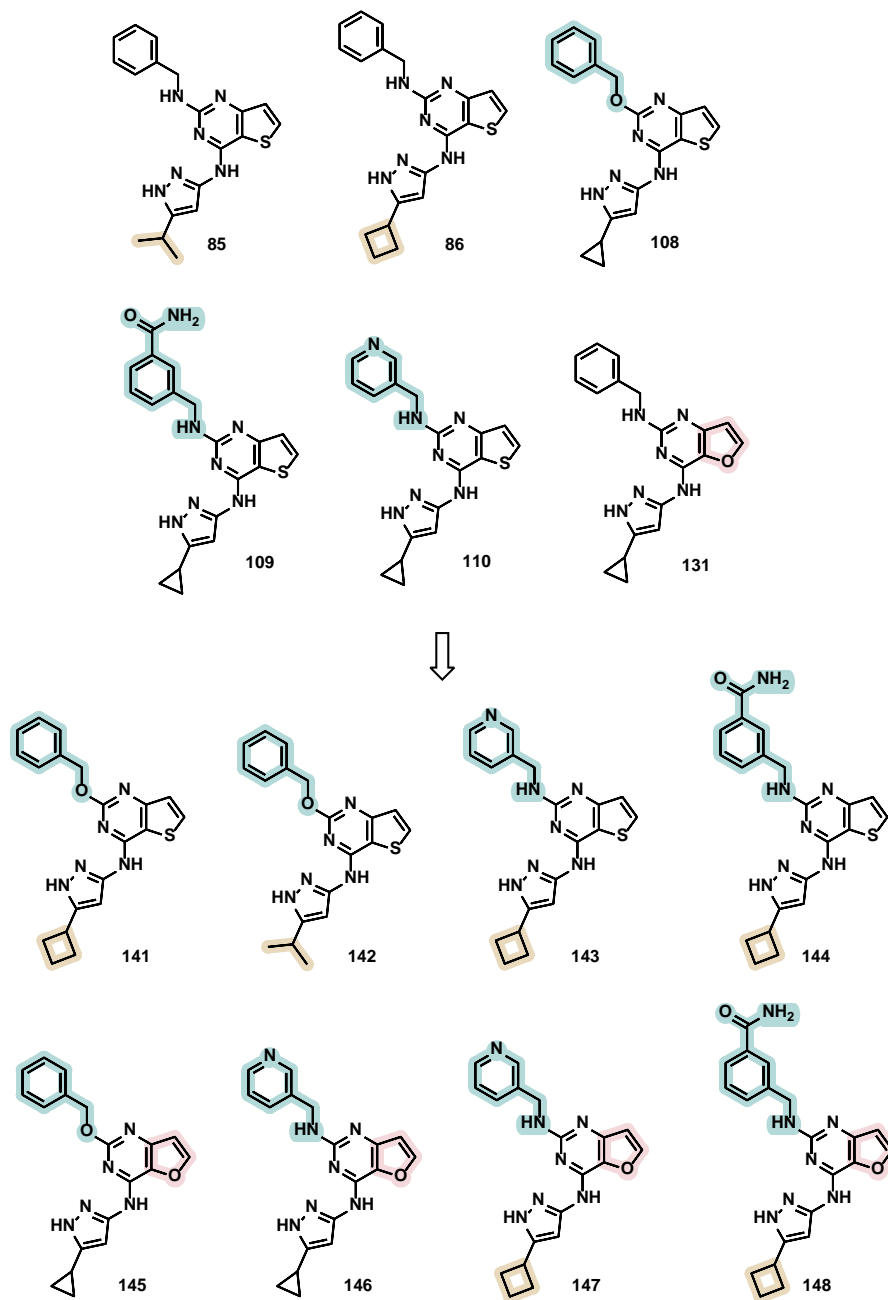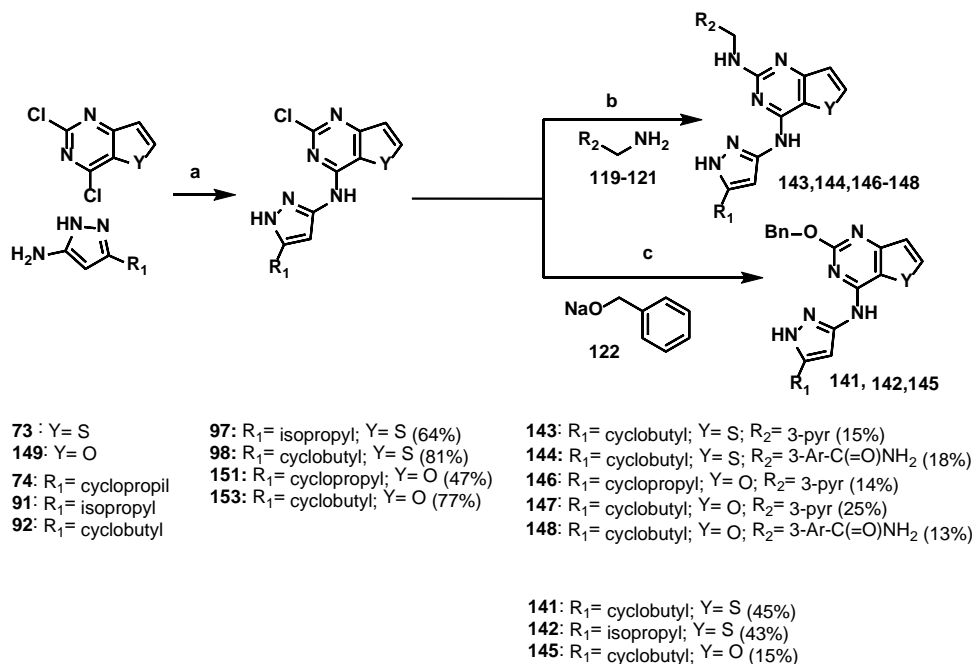
Figure 2.20 Chemical structures of hybrid derivatives and their forerunner compounds. Benzyl ring decorations are highlighted in teal, cyclopropyl ring replacements in beige and central core modifications in pink.

Compound synthesis was performed following the same general procedure employed for the first generation analogues, with overall good yields and at a low cost of the process (Scheme 2.7).

Scheme 2.7 Synthesis of hybrids (Series IV) derivatives **141**-**148**.

73 : Y= S	**97**: R$_1$= isopropyl; Y= S (64%)	**143**: R$_1$= cyclobutyl; Y= S; R$_2$= 3-pyr (15%)
149: Y= O	**98**: R$_1$= cyclobutyl; Y= S (81%)	**144**: R$_1$= cyclobutyl; Y= S; R$_2$= 3-Ar-C(=O)NH$_2$ (18%)
74: R$_1$= cyclopropil	**151**: R$_1$= cyclopropyl; Y= O (47%)	**146**: R$_1$= cyclopropyl; Y= O; R$_2$= 3-pyr (14%)
91: R$_1$= isopropyl	**153**: R$_1$= cyclobutyl; Y= O (77%)	**147**: R$_1$= cyclobutyl; Y= O; R$_2$= 3-pyr (25%)
92: R$_1$= cyclobutyl		**148**: R$_1$= cyclobutyl; Y= O; R$_2$= 3-Ar-C(=O)NH$_2$ (13%)

141: R$_1$= cyclobutyl; Y= S (45%)
142: R$_1$= isopropyl; Y= S (43%)
145: R$_1$= cyclobutyl; Y= O (15%)

Reagents and conditions. a) Et$_3$N, rt, 2-5 days; b) *n*-BuOH, DIPEA, 180 °C, 4-6 h, MW, Ar; c) THF, 150 °C, 7 h, MW, Ar

Similarly to the other compounds, the first chemo-selective amination of the 4-position of the 2,4-dichloropyrimidine ring led to the synthesis of the appropriate 4-substituted intermediates (**97**, **98**, **151**, **153**). A sequential SN$_{Ar}$ allowed installation of different benzylamines (**143, 144, 146-148**) or a benzyloxy group (**141, 142, 145**) at the less reactive 2-position of the 2,4-dichloropyrimidine core. This was achieved through harsher experimental conditions, with the use of DIPEA as a non-nucleophilic base and under MW irradiation, leading to the synthesis of the pyrimidine-fused heterocycle derivatives.

Despite solubility issues in the assay buffer did not allow to determinate the IC$_{50}$ values for DYRK1A of some derivatives for which the percentage of inhibition at 5 µM was reported *in vitro* biological evaluation through the LANCE® Ultra TR-FRET assay (Table 2.8) showed very good results. With the only exception for benzyloxy derivatives **142** and **145** for which a decrease of DYRK1A inhibition was observed (44.5% and 45.1%, respectively) in comparison to **72**, combination of two modifications at a time provoked a significant improvement in DYRK1A affinity up to high nM range (particularly with **143** and **144**), while keeping in the low nM range the activity against the other two targets.

Compounds featuring three merged substitutions (**147** and **148**) showed great improvements, maintaining a well-balanced and low nM inhibitory activity against GSK-3β and FYN and notably increase of potency toward DYRK1A (IC$_{50}$ = 461 nM and 242 nM, respectively). Among them, entry **148** (**ARN25699**), featuring the *meta*-carbamoyl benzylamine moiety and the cyclobutyl group on the aminopyrazole as key replacements, was selected for further investigations due to its nearly 3-fold increase in potency against DYRK1A over compound **72**.

Table 2.8 Inhibition data of hybrid derivatives against GSK-3β, FYN-A and DYRK1A.

Cmpd #	GSK-3β IC$_{50}$ (nM)	FYN-A IC$_{50}$ (nM)	DYRK1A IC$_{50}$ (nM) [1]	% inh
72	4.83 ± 0.30	4.13 ± 0.69	n.d.[2]	53.3 ± 2.6%
141	23.0 ± 4.7	19.4 ± 3.6	n.d.	65.5 ± 0.8%
142	25.5 ± 3.3	69.9 ± 8.2	n.d.	44.5 ± 1.1%
143	1.27 ± 0.3	3.64 ± 0.8	666.0 ± 121	75.2%
144	1.0 ± 0.1	0.9 ± 0.08	399.1 ± 71.5	78.8%
145	31.2 ± 1.0	57.8 ± 6.2	706.0 ± 87.3	45.1%

|				
146	5.33 ± 0.6	31.5 ± 4.5	n.d.	60.3 ± 0.3%
147	9.51 ± 1.9	10.4 ± 3.2	461.0 ± 62.0	77.1%
148	5.51 ± 1.6	2.16 ± 0.4	242.0 ± 50.2	82.7%

[1]*inhibition at 5 μM data reported due to low solubility of the compounds in the buffer;* [2]*not determined*

2.4 Benzyloxy moiety as privileged modification to obtain balanced inhibitors

Driven by the successful results obtained with the first set of analogues, a deeper analysis of the radical modifications installed onto the pyrimidin-fused heterocycle of compound **72** yielded the observation that hybrids molecules featuring the benzyloxy moiety in place of the benzylamine (**141**, **142**, **145**, Figure 2.20) showed a non-dramatic but significant decrease (from one-digit to two-digit nM) of the affinity for GSK-3β and FYN, keeping in the sub-micromolar range the activity against DYRK1A (**141** and **142**). Furthemore, combining benzyloxy moiety insertion with the replacement of the thiophene[3,2-*d*]pyrimidine core with the furano[3,2-*d*]pyrimidine one (**145**) provoked a slightly increase of DYRK1A affinity compared to **72**.

These encouraging results together with the fact that benzyloxy derivatives possess a better chemical tractability (*i.e.* easier purification and solvent removal, improved NMR resolution and overall yields of chemical reactions) guided the design of novel *meta*-substituted benzyloxy hybrids featuring a cyclobutyl group linked to the aminopyrazole ring and a furano[3,2-*d*]pyrimidine (*e.g.*, **154**, **155**, Scheme 2.8).

Scheme 2.8 A) Design of novel *meta*-substituted benzyloxy hybrids (**154**,**155**); B) chemical attempts to access these derivatives; no-go crosses indicate no chemical reaction success
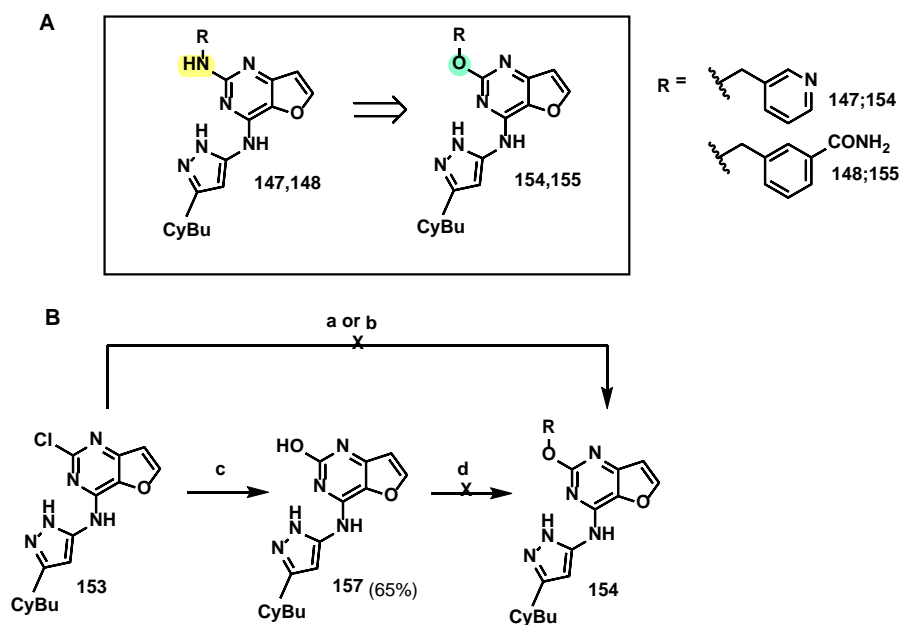
Reagents and conditions. a) 3-(Hydroxymethyl)pyridine (**156**), NaH, DMF rt on; b) **156** NaH, DMF 8 h,160 °C MW; c) Acetic acid, 118 °C on; d) 3-(bromomethyl)pyridine HBr (**158**), K$_2$CO$_3$, DMF, rt, on.

The synthetic strategy to access to **154** and **155** required small changes from the general chemical protocol depicted in Scheme 2.1. Initial attempt of SN$_{Ar}$ between intermediate **153** and the appropriate *meta*-substituted benzyl alcohol (**156**) in the presence of NaH as a base and the polar aprotic solvent DMF was not successful at neither room temperature nor heating up to 160 °C under MW irradiation (Scheme 2.8, a). Thus, an alternative two-step chemical strategy was applied to insert the selected *meta*-substituted benzyloxy groups at the less reactive C2 of the pyrimidine. Insertion of the hydroxy group at the C2 position through an acetic acid catalyzed reaction of **153** yielded **157** (Scheme 2.7, b), which after treatment with 3-(bromomethyl)pyridine (**158**) in the presence of K$_2$CO$_3$ and DMF at room temperature gave an undesired

product of pyrazole substitution. Despite the synthesis of derivatives **154** and **155** not being achieved over the course of my doctoral studies, additional efforts will be devoted in the near future to increase the versatility of the synthetic protocol in assessing the effects of more radical structural variations on the original scaffold towards new triple GSK-3β/FYN/DYRK1A inhibitors.

2.5 ARN25699 (148) X-ray crystal structure, anti-tau phosphorylation activity and selectivity profile, a comparison with ARN25068 (72).

X-ray crystallography studies highlighted the important role of the carbamoyl function of hybrid compound **148** for establishing an additional H-bonding interaction with Lys 188, a key residue at the ATP binding pocket of DYRK1A, in line with the boosting of DYRK1A inhibition (Figure 2.21). Similarly to **72**, this compound showed a good selectivity over half of the PKs selected when tested at 0.1 μM, and it produced an increase in tau and MT bundle formation at 10 uM in a tau phosphorylation assay using the Tau0N4R-TM-tGFP U2OS stable cell line (Figure 2.21).
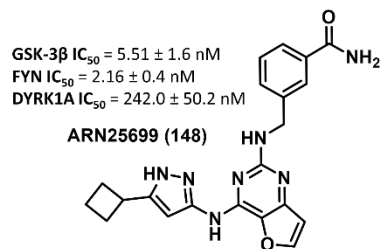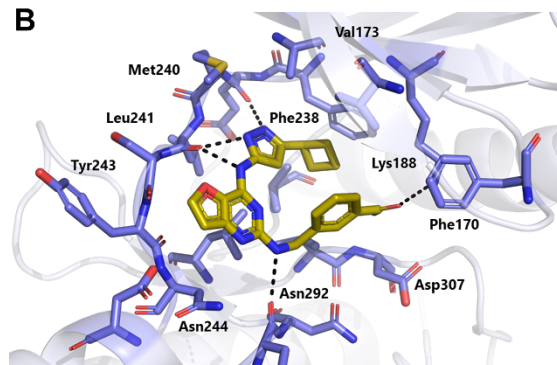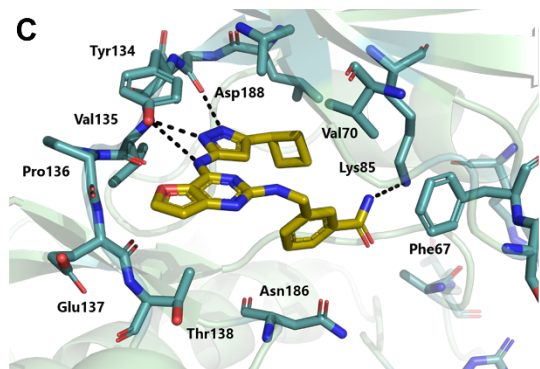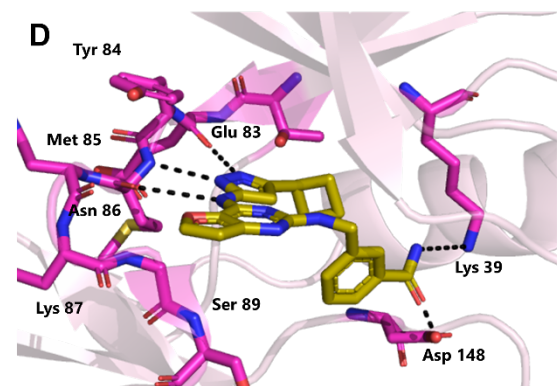
A

GSK-3β IC$_{50}$ = 5.51 ± 1.6 nM
FYN IC$_{50}$ = 2.16 ± 0.4 nM
DYRK1A IC$_{50}$ = 242.0 ± 50.2 nM

ARN25699 (148)

B

Val173
Met240
Leu241
Phe238
Lys188
Tyr243
Phe170
Asn292
Asp307
Asn244

C

Tyr134
Asp188
Val135
Val70
Lys85
Pro136
Phe67
Glu137
Asn186
Thr138

D

Tyr 84
Glu 83
Met 85
Asn 86
Lys 39
Lys 87
Ser 89
Asp 148

E

SAPK2a
MAPK1
CK1δ
CK2
DYRK2
JNK1α1
CK1ε
PKA
DYRK1B
DYRK3
DYRK1A
cSRC
Lck activated
CDK5/p25
MAP4K4
CDK1/cyclinB
GSK3α
Yes
GSK3β
Fyn

■ 0.1 µM
□ 10 µM

0   25   50   75   100

F

Bundles Average Area

600
500
400
300
200
100
0

Control
Vehicle
LiCl 30 mM
Control
Cpd 1 µM
Cpd 2.5 µM
Cpd 5 µM
Cpd 10 µM
Cpd 25 µM
Cpd 50 µM
Cpd 100 µM

G

Vehicle
LiCl (30 mM)
Cpd (10 µM)

Figure 2.21 Structural and biological insights of compound **ARN25699** (**148**). A) 2D chemical representation of compound **148** and its *in vitro* calculated IC$_{50}$ values (nM) against GSK-3β/FYN and DYRK1A (TR-FRET assay); B) X-ray crystal structure representation of **144** in complex with DYRK1A protein, black dotted lines indicate HB interactions; C) Graphical representation of the percentage of inhibition of **148** over a panel of 20 selected protein kinases (radiometric assay); D) Dose-response relationship for compound **148** (0.5-100 μM) in a tau phosphorylation assay on Tau0N4R-TM-tGFP U2OS cell line. Cells were treated with the indicated concentrations for 6 h. Data points represent the mean ± SD for each condition for a single experiment performed in triplicate. Results are expressed as the total area average of bundles per cell after treatment of cells with the triple inhibitor **148**; E) Representative images with the assays obtained with an objective of 20X. Pictures represent DMSO (vehicle control), LiCl 30 mM (positive control), and the test compound at 10 μM.

In vitro ADME and BBB penetration studies are still in progress with the ultimate goal of advancing compound **148** towards pharmacokinetics and brain permeability studies in mice.

2.6 Rational design and *in vitro* characterization of the balanced triple inhibitor ARN26646 (159)

Computational efforts of our collaborators at the Skaggs school of pharmacy in San Diego, together with an intense literature research to find an ideal prototype possessing a well-balanced activity against all the three targets, led to the discovery of **ARN26646** (**159**, Figure 2.22).
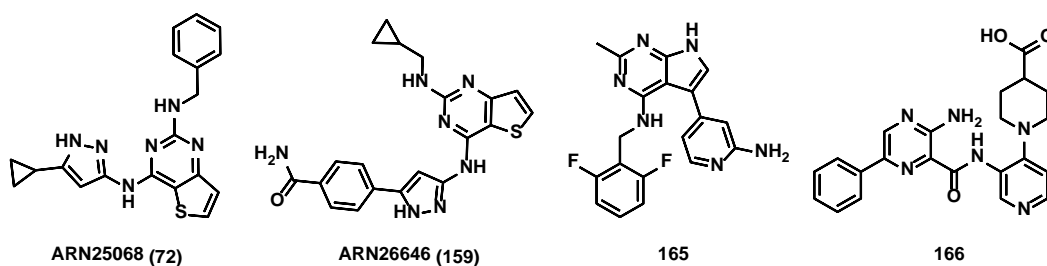

Figure 2.22 Chemical structures of compounds **72**, **159**, **165** and **166**.

As with the majority of the approaches pursued throughout this project, the research of ligands with improved affinity over DYRK1A was the initial driving force. To achieve this goal by assessing the effects of more radical structural variations on the original scaffold of compound **72**, five ligands illustrated in Figure 2.23 were manually built and docked into the enzyme binding pocket.

In all designed derivatives, different *para*-hydroxyphenyl substituents were installed on the pyrazole moiety with linkers of different length and chemical nature to mainly promote additional H-bonding interaction with crucial ATP pocket residues of DYRK1A. Despite the high potential of the computational modelling suggestions, the five proposed molecules were not chemically accessible according to the previously experienced limited reactivity of the pyrazole ring, and the intense chemical effort needed to adapt the general synthetic strategies illustrated in Scheme 2.1.
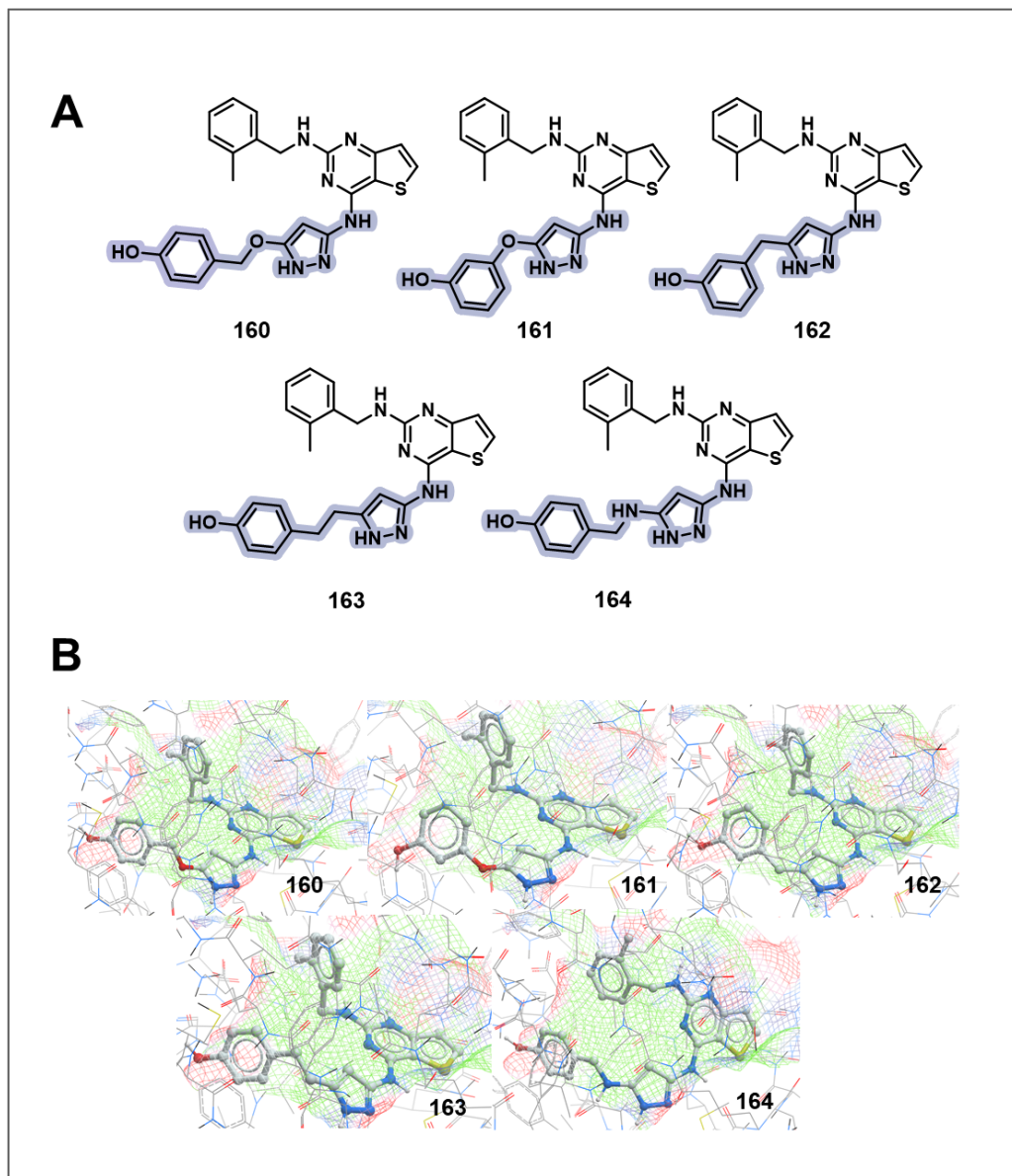
Figure 2.23 A) Chemical structures of designed ligands (**160-164**) to improve affinity against protein DYRK1A and their associated modelling representation within the ATP-binding pocket of the enzyme. Systematic replacement of position 4 of the pyrimidine core is highlighted in purple. B) Predicted binding poses of the designed ligands in the DYRK1A binding pocket.

For these reasons, the synthesis of the proposed ligands was not pursued and attention was shifted towards compound **159**. This compound, which is an analog of previously synthetized compounds characterized by an inversion of the chemical substitution patterns on the pyrazole and at C2 position of the 2,4-dichloropyrimidine core, emerged from a thorough analysis of previously docked molecules.

The selective inhibitor of DYRK1A **165** (IC_{50} = 4 nM)[244], and the dual GSK-3β/DYRK1A inhibitor **166** (GSK-3β IC_{50} = 40 nM; DYRK1A IC_{50} = 100 nM)[245], an antidiabetic drug candidate with 83% reported inhibitory activity at 10 μM against FYN (Figure 2.22), were selected as interesting mono- and dual-target DYRK1A inhibitors to computationally study and compare with our initial hit **72**, and **159**. Thus, compounds **72**, **159**, **165** and **166** were docked in the DYRK1A binding pocket and overlapped (Figure 2.24) as ultimate goal to learn how to more drastically modify **72** and identify common pharmacophoric features.

Notably, the Lys 188 interaction within the binding pocket of the enzyme was confirmed not only for **165** and **166** as reported in literature, but also for **159**. This was in line with what observed from both docking and X-ray crystallographic analysis of **148** aside from that the amide moiety of **159** involved in the HB interaction with Lys 188 residue is directly linked to the phenyl group attached to the position 5 of the pyrazole ring.
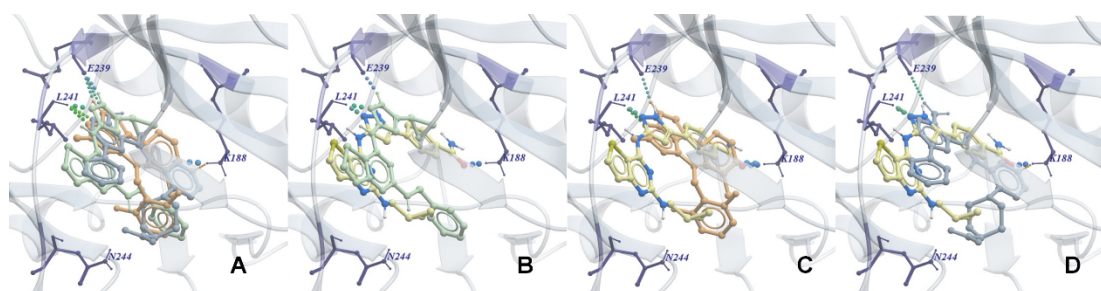

Figure 2.24 Computational modelling of compounds emerged from literature research and their overlap with **ARN25068** (**72**) and **ARN26646** (**159**) within the DYRK1A binding pocket. A) Superimposition of **72** (pale green) with **165** (orange) and **166** (purple); B)

superimposition of **159** (yellow) and **72** (pale green); C) superimposition between **159** (yellow) and **165** (orange), D) superimposition of **159** (yellow) and **166** (purple).

The synthetic strategy first attempted to afford derivative **159** following the general procedure described in Scheme 2.1 was unsuccessful due to the low reactivity of the in-house synthetized 5-substituted pyrazole, side products formation in all the steps of the process, and several purification issues of the final product. Therefore, novel strategies reported in Scheme 2.8 have been explored to overcome this lack of accessibility.

The direct amination of the C4 by substitution of the chlorine atom in presence of NH_4CO_3 was first tried in neat conditions and afterwards in presence of isopropanol to aid solubility. This reaction did not yield the desired product **167** either at room temperature or with gentle heating at 50 °C (Scheme 2.8, route a). In contrast, despite obtaining the corresponding isopropyl substituted derivative **170** in a 1:1 ratio with the desired product **169**, the introduction of the 5-bromo aminopyrazole moiety (**168**) was in part successful by using isopropanol as solvent and heating at 50 °C (Scheme 2.9, route b). While trying to optimize this reaction by switching solvent from isopropanol to DMF, the formation of an undesired pyrazole dimer (**171**) was observed by UPLC-MS analysis and therefore this strategy was abandoned.

Scheme 2.9 Different synthetic strategies for chemo-selective amination of the C4 of 2,4-dichlorothieno[3,2-d]pyrimidine.
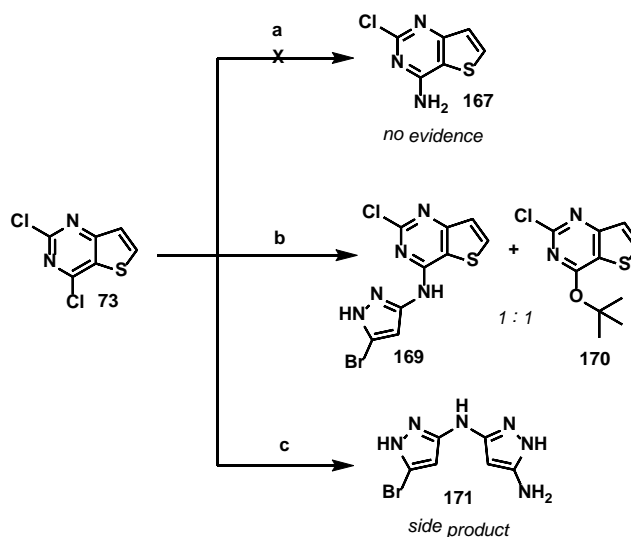
Reagents and conditions. a) NH_4CO_3 (5 equiv.), isopropanol, TEA (5 equiv.), 50 °C, on; b) 5-bromo-1*H*-pyrazol-3-amine (**168**, 2.5 equiv.), isopropanol, TEA, 50 °C, on; c) **168** (2.5 equiv.), DMF, TEA, 50 °C, on. No-go crosses indicate the reaction was unsuccessful.

Extensive optimization of the synthetic protocol allowed the successful synthesis of **159** via a four-step synthetic procedure reported in Scheme 2.10. The gram scale introduction of the hydroxyl moiety to the more reactive C4 of the pyrimidine core proceeded in a quantitative yield and opened the possibility to direct the first SN_{Ar} towards the less reactive C2. The commercially available cyclopropanemethylamine **173** was then reacted with **172** under MW irradiation at 160 °C, in a large milligram scale, affording **174**, which underwent a chlorination reaction in presence of phosphorus oxychloride. A final SN_{Ar} of **175** with the polar 5-substituted pyrazole **177**, in turn prepared via Suzuki cross-coupling reaction, between the bromo containing **168** and the boronic acid **176**, afforded the desired product as the formic acid salt (**178**) after HPLC purification. A final purification of the same compound via exchange cationic chromatography (SCX) separation gave **159** as the free base.

Scheme 2.10 Multi-step procedure employed for the synthesis of compound **159**.
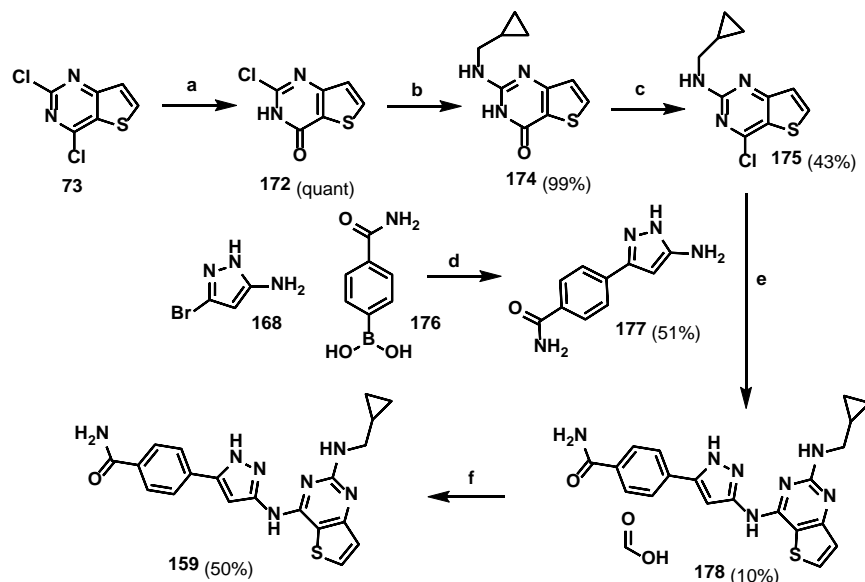
Reagents and conditions. a) i) NaOH, THF/water, 60 °C on ii) Acetic acid, 35 °C, 2 h; b) cyclopropylmethanamine (**173**), DIPEA, *n*-BuOH, Ar, 6 h, 160 °C, MW; c) POCl₃, DMSO (cat.), 105 °C, Ar, 3 h; d) Pd(PPh₃)₄, 1,4-dioxane, K₂CO₃ aq (2M), MW, 130 °C, Ar, 2 h; e) *n*-BuOH, DIPEA, 180 °C, Ar, 8 h; f) SCX separation

Notably, compound **159** showed a quite well-balanced nanomolar activity against all the three targets (GSK-3β IC_{50} = 126 nM; FYN IC_{50} = 83 nM; DYRK1A IC_{50} = 199 nM) when tested in the in-house enzymatic assay, making this compound one of the greatest achievements over the course of this project (summary of SAR exploration reported in Figure 2.25).
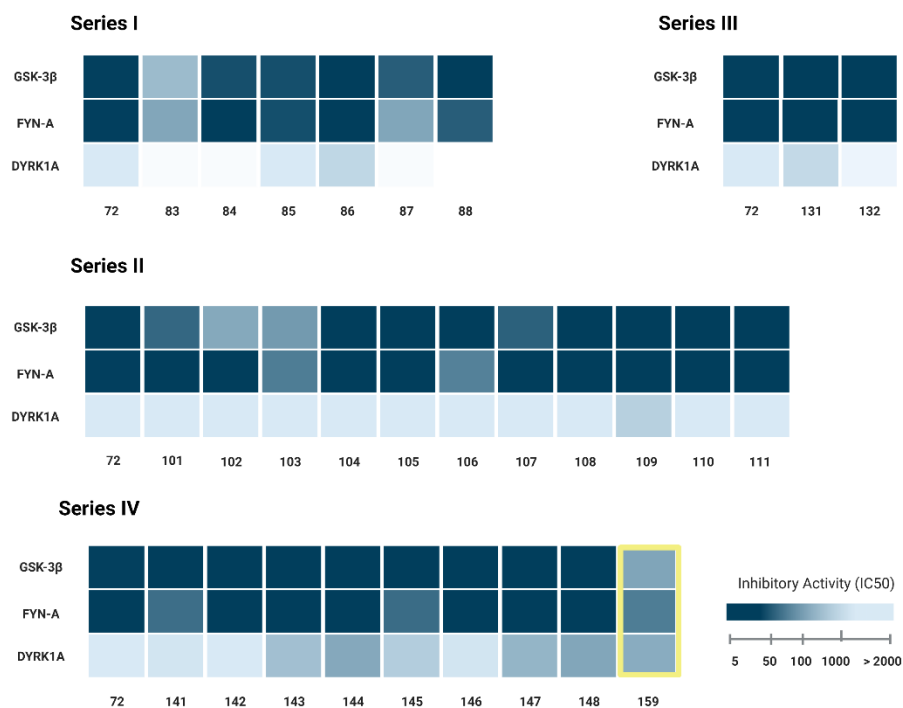
Figure 2.25 Heat map representation of compounds inhibitory activity versus GSK-3β/FYN and DYRK1A

2.7 *In vitro* DMPK screening of ARN25068 and selected derivatives

Preliminary *in vitro* ADME characterization of hit compound **72** and some selected analogs was carried out to select the best candidates for further *in vitro* BBB penetration studies and *in vivo* pharmacokinetic properties evaluation. In detail, as shown in Table 2.9, the compounds stability towards metabolic biotransformation of phase I (Ph1) in mouse liver microsomes (MLM) was investigated to understand the effect of properly addressed modifications in analogues' metabolism. Notably,

compound **72** was confirmed to be an optimal starting point characterized by a half-life of more than 60 min in the presence of MLM (Ph1).

Compound **83**, **84**, **85** and **86** of series I together with **103**, **107**, **110** of series II showed a decrease in metabolic stability compared to **72** as confirmed by half-life values slightly more than 10 min. Hybrids derivatives **145**, **147** and **148** were instead characterized by a better stability compared to the first generation compounds (20 min $\leq t_{1/2} \geq 30$ min) with exception of compounds **143** and **144**, which showed a half-life less than 13 min. Remarkably, derivative **106** of series II, featuring the *p*-carbamoyl moiety, and hybrid **159** displayed a comparable stability in MLM (Ph1) with hit compound **72** greater than 60 min for **106** and of 54 min for **159**.

Table 2.9 Stability in MLM (Ph1 and Ph2) and M-plasma of hit compound **72** and some selected analogs.

Cmpd #	Phase I		Phase II		M-plasma	
	$t_{1/2}$ (min)[1]	Replicates	$t_{1/2}$ (min)[1]	Replicates	$t_{1/2}$ (min)[2]	Replicates
72	> 60	n = 3	>60	n = 2	>120	n = 3
83	13	n = 2	n.d	n.d	n.d	n.d
84	>60	n = 2	n.d	n.d	n.d	n.d
85	12	n = 1	n.d	n.d	n.d	n.d
86	11 ± 0	n = 2	>60	n = 2	>120	n = 3
101	24	n = 1	n.d	n.d	n.d	n.d
103	12	n = 1	n.d	n.d	n.d	n.d
106	>60	n = 2	n.d	n.d	n.d	n.d
107	10	n =2	n.d	n.d	n.d	n.d
108	49	n =1	>60	n =1	n.d	n.d
109	18 ± 1	n = 2	>60	n = 2	>120	n = 3
110	11 ± 3	n = 2	>60	n = 2	>120	n = 3

	Phase I		Phase II		H-plasma	
	$t_{1/2}$ (min)[1]	Replicates	$t_{1/2}$ (min)[1]	Replicates	$t_{1/2}$ (min)[2]	Replicates
131	>30	n = 2	>60	n = 1	111 ± 11	n = 3
143	13 ± 1	n = 2	>60	n = 2	>120	n = 3
144	13 ± 1	n = 3	n.d	n.d	>120	n = 3
145	41 ± 2	n = 3	n.d	n.d	>120	n = 3
147	20 ± 1	n =3	n.d	n.d	>120	n = 3
148	22 ± 1	n =3	n.d	n.d	>120	n = 3
159	54 ± 3	n =3	n.d	n.d	>120	n = 3

[1]Final cpd conc.: 4.6µM in Microsomes + 0.1% DMSO; [2]Final cpd conc.: 2µM in Plasma + 5% DMSO

Regarding metabolic biotransformations of phase II (Ph2) in MLM and stability in mouse plasma (M-plasma), overall, preliminary results of both first and second generation analogs showed very good stability as confirmed by half-life values above 60 and 120 min, respectively (Table 2.9).

Moreover, good stability data ($t_{1/2}$ >60 min) in the presence of human liver microsomes (HLM, both Ph1 and Ph2, Table 2.10) were observed for all derivates with the exception of **86**, **110** and **143**. The stability in human-plasma (H-plasma) was ≥120 min for the majority of the tested compounds suggesting their potential application into preclinical development.

Table 2.10 Stability in HLM (Ph1 and Ph2) and H-plasma of hit compound **72** and some selected analogs.

	Phase I		Phase II		H-plasma	
Cmpd #	$t_{1/2}$ (min)[1]	Replicates	$t_{1/2}$ (min)[1]	Replicates	$t_{1/2}$ (min)[2]	Replicates
72	> 60	n = 2	>60	n = 2	>60	n = 2
86	39 ± 1	n = 2	40 ± 4	n = 2	>60	n = 3
108	> 60	n = 1	50	n =1	n.d	n.d
109	>60	n = 2	>60	n = 2	>120	n = 3

110	35 ± 3	n = 2	36 ± 1	n = 2	>60	n = 3
131	59	n = 1	>60	n = 1	111 ± 12	n = 3
143	27 ± 1	n = 3	55 ± 0	n = 2	>120	n = 3
144	>60	n = 3	n.d	n.d	>120	n = 3
145	>60	n = 3	n.d	n.d	>120	n = 3
147	46 ± 4	n =3	n.d	n.d	>120	n = 3
148	>60	n = 3	n.d	n.d	>120	n = 3
159	45 ± 7	n =3	n.d	n.d	>120	n = 3

[1]*Final cpd conc.: 4.6µM in Microsomes + 0.1% DMSO;* [2]*Final cpd conc.: 2µM in Plasma + 5% DMSO*

Conversely, kinetic solubility (S_k) emerged as one of the major weaknesses of these classes compounds with the majority of them reporting values below 1 µM as previously observed with **72** (Table 2.11). While compounds **84, 85**, and **144**, featuring the methyl and isopropyl group in place of the cyclopropil moiety, and a combination of the cyclobutyl and the *m*-carbamoylbenzyl function, respectively, reported low solubility values ranging between 4 and 16 µM, a great improvement in solubility was achieved with derivatives **109** and **148** (S_k = 121 ± 13 µM and 185 ± 3 µM, respectively).

Table 2.11 S_k of hit compound **72** and some selected analogs.

Cmpd #	$S_{kinetic}$ µM	Replicates
72	<1	n = 3
84	6	n = 1
85	4	n = 1
86	<1	n = 3
101	1	n = 1

103	<1	n = 1
108	<1	n = 3
109	121	n = 1
110	<1	n = 3
131	0	n = 3
143	<1	n = 1
144	16	n = 1
145	<1	n = 1
147	1	n = 1
148	185	n = 1
159	<1	n = 1

2.8 Conclusions and future perspectives

Taking into account all the previously described data, compound **ARN25699** (**148**) and **ARN26646** (**159**) were identified as promising lead compounds to further investigate, paving the way towards the potent and well-balanced simultaneous modulation of GSK-3β, FYN and DYRK1A to combat tau-related disorders.

A summary of the *in vitro* solubility, activity and ADME properties of **148** and **159** in comparison with **72** is reported in Table 2.12.

Table 2.12 *In vitro* activity, solubility, and ADME properties of **72** in comparison with **148** and **159**.

	ARN25068 (72)	ARN25699 (148)	ARN26646 (159)
GSK-3β IC$_{50}$ [nM]	4.83 ± 0.30	5.51 ± 2	126.0 ± 5
FYN IC$_{50}$ [nM]	4.13 ± 0.69	2.16 ± 0.4	83.0 ± 12

	>1000	242.0 ± 50	199.0 ± 11
DYRK1A IC$_{50}$ [nM]			
S$_{K}$ [μM]	< 1	185 ± 3	< 1
MLM (Ph1) [min]	$t_{1/2}$ > 60	$t_{1/2}$ = 20 ± 1	$t_{1/2}$ = 54 ± 3
HLM (Ph1) [min]	$t_{1/2}$ > 60	$t_{1/2}$ > 60	$t_{1/2}$ = 45 ± 7
M-plasma [min]	$t_{1/2}$ > 120	$t_{1/2}$ > 120	$t_{1/2}$ > 120
H-plasma [min]	$t_{1/2}$ >120	$t_{1/2}$ >120	$t_{1/2}$ > 120

IC$_{50}$ evaluated in (LANCE® ultra TR-FRET assay)

Additional pharmacokinetic and brain permeability studies in mouse will be performed to select the best candidates to advance into lead optimization campaigns. Furthermore, extensive SAR studies will be devoted to expand the chemical space around the best compounds, by combining computational and X-ray crystallographic approaches, with the ultimate goal to discover novel potent and well-balanced GSK-3β/FYN/DYRK1A inhibitors possessing drug-like favorable properties to combat neurodegenerative tauopathies.

Chapter 3

3. Design, synthesis and evaluation of novel MT-stabilizing TPDs for NDDs and other indications

3.1 Introduction

As discussed in the introductory chapter of this thesis, major abnormalities of AD are exemplified by the deposition of Aβ plaques in the extracellular space, and accumulation of PHFs in intraneuronal NFTs and neuropil threads (NTs). Lee V. M. and collaborators discovered the role of the incorporation of abnormally phosphorylated protein tau into pathogenic PHFs as triggering factor in disrupting the MTs network, and compromising the function and viability of neurons. Due to MTs association with tau and their importance in neurons, MTs can be considered supplementary therapeutic targets for the treatment of AD.[246, 247]

Several subsequent studies reported compelling evidence of efficacy of different brain penetrant MT-stabilizing compounds, including natural products like

128

epothilone D and dictyostatin, as well as synthetic small molecules belonging to the TPD class, in animal models of tauopathies, strengthened the idea that MTs stabilizing drugs can be use as novel therapeutic agents for AD.[246, 248-252]

As discussed previously, BBB penetration is a critical prerequisite while targeting CNS directed therapies and natural products have known issues in this regard.[121, 122] In contrast, MT-stabilizing TPDs and related structures have shown a generally favorable combination of brain permeability and MTs-stabilizing activity and, therefore, high potential for the development of novel CNS MT-stabilizing tools[253] for NDDs. This chapter focus on the research activity conducted during the third year of my Ph.D. course for 6 months at the Skaggs school of pharmacy and pharmaceutical sciences (UCSD, San Diego, California) within Prof. Carlo Ballatore's Lab working on the rational design and synthesis of MT-stabilizing TDP candidates for future clinical development.

3.1 TDPs, MTAs with binding affinity for the Vinca site of tubulin

MTAs are some of the clinically most successful anti-cancer drugs. Among them, TPDs (Figure 3.1) represent a class of cytotoxic compounds possessing both stabilizing and destabilizing properties, and able to inexplicably bind to the vinblastine binding site on tubulin which is mainly targeted by MDAs.[254]

Compound **179** was part of a group of five selected TPDs exensively characterized by Sáez-Calvo G. *et al* whit the aim of better elucidate the molecular mechanism of action of MTAs on tubulin and MTs.

Crystal structure of **179** in complex with αβ tubulin dimers at 2.4 Å, allowed a deeply characterization of its binding mode providing the basis to rationalize the cellular activity of TPDs congeners and to perform further SAR explorations.[254]
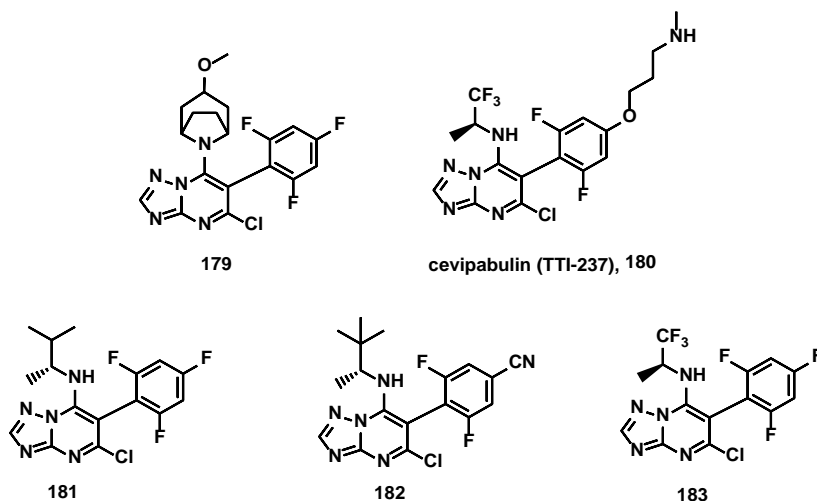
Figure 3.1 Chemical representatives of TPDs with both MT-stabilizing and destabilizing activity.

Similarly to other TPDs, **179** binds between β1 and α2 tubulin dimers and in proximity of the bound GDP nucleotide of the β1-tubulin subunit in the vinblastine site (Figure 3.2). The central pyrimidine core is involved in a π-π stacking interaction with Tyr 224 of β1 subunit (βTyr224) and the guanine nucleobase of the GDP nucleotide. The nitrogen atom of the azabicyclo moiety interacts through HBs with both βTyr 224 and GDP, while the chlorine atom of the pyrimidine group interacts with βThr223 and Thr 357 of α2-tubulin subunit (αThr357). Finally, as for the azabicyclo group, the trifluorophenyl moiety is involved in H-bonding interactions with αAsp 329, βAsp 206 and βGlu 207.
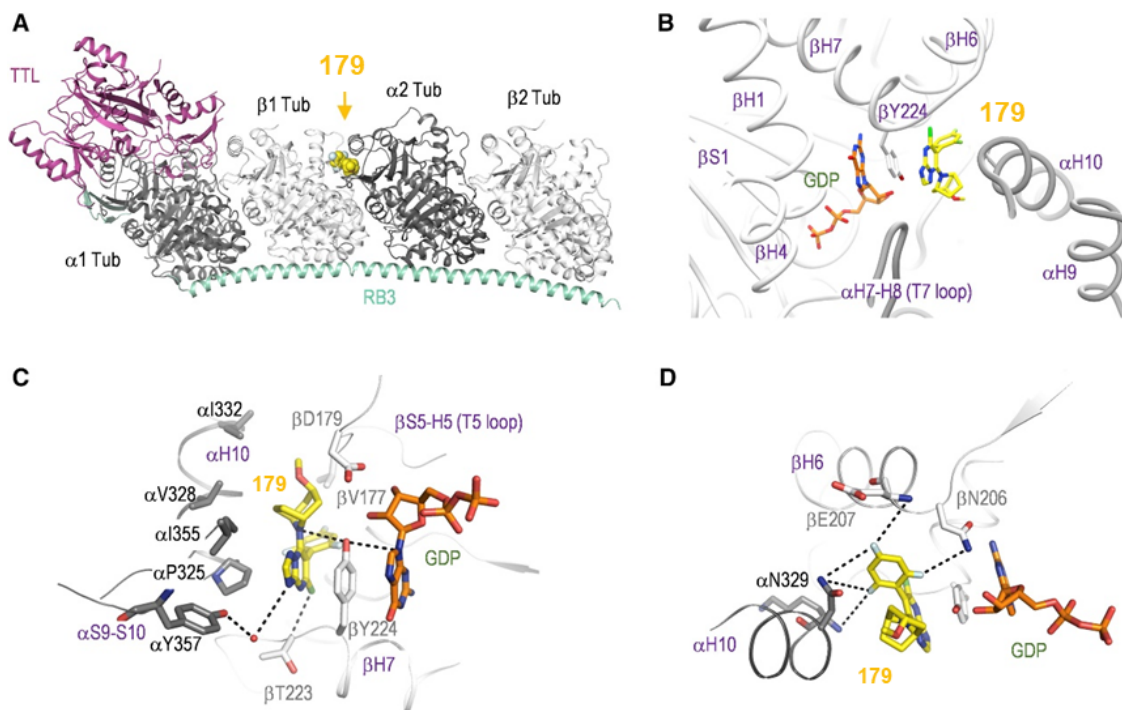
Figure 3.2 Crystal structure of **179** in complex with αβ tubulin dimers[255]: (A) Overall view of the complex structure: α-Tubulin, gray cartoon; β-tubulin, white cartoon; tubulin tyrosine ligase (TTL), purple cartoon; the stathmin-like protein RB3, green cartoon; **179**, yellow spheres. (B) Close-up view of the binding site of **179**. GDP, orange sticks; **179**, yellow sticks. (C and D) Close-up view of **179** complex structure showing interactions of the (C) azobicyclo and pyrimidine groups and (D) trifluorophenyl group of **179** with tubulin. Tubulin secondary structural elements are labeled in purple.

3.2 Matched Molecular Pair Analyses, Computational Studies and SAR evaluation of TPDs

Evaluation of various TPDs in cell (QBI293)-based assays of MT stabilization showed diverse cellular phenotypic responses after short-term (4 h) incubation as the chemical nature of the substituents around the TPD core vary.[46] Moreover, matched molecular pair analyses and computational studies allowed to correlate the markedly different phenotypic responses of TPDs to their interaction with either one or two

spatially distinct binding sites within tubulin heterodimers.[253] In further detail, compounds typified by **181**, **182** and **183**, which produced a dose-dependent increase in markers of stable MTs - such as acetylated α-tubulin (AcTub) and de-tyrosinated α-tubulin (GluTub) - with no decrease of tubulin and interacted exclusively within the vinca binding site on β-tubulin (Figure 3.3), were defined as Class I compounds. While TPDs as **179** and cevipabulin (**180**), which caused a bell-shaped-dose-response in AcTub and GluTub levels with associated proteasome-dependent degradation of α tubulin, and characterized by similar binding affinity to both the vinca site as well as the seventh site, were classified as compounds of Class II (Figure 3.3).

A systematic exploration of the SAR of TPDs also revealed that fragments linked at C6 and C7 of the TPD core play an important role in determining both the phenotypic responses and the ADME-pharmacokinetic properties of TPDs.[249, 256] In detail, analogues featuring electron donating groups at the *para* position of the phenyl moiety linked to the TPD core, are generally associated to a significant loss of α-Tub levels. Chloro substituents, producing opposite mesomeric (+M) and inductive (−I) effects, cause a comparatively more moderate but still significant loss of α-Tub at 10 μM. However, the presence of fluoro-substituents at the *ortho* positions of the phenyl ring at C6, together with an electron-withdrawing group at the *para* position and a relatively lipophilic aliphatic amine at C7 are generally required for Class I activity.[46]

Although SAR and structural biology data allowed to gain insights into the mechanism(s) underlying the different cellular phenotypic responses elicited by TPD congeners, a new class of analogs characterized by an unprecedented cellular activity between that of Class I and II compounds and therefore classified as hybrid compounds was developed (Figure 3.3).[253] These TPDs proved to bind to both the vinca site as well as the seventh site, showing a non-linear dose response with respect to MT AcTub, without evidence of a significant decrease in total tubulin levels.
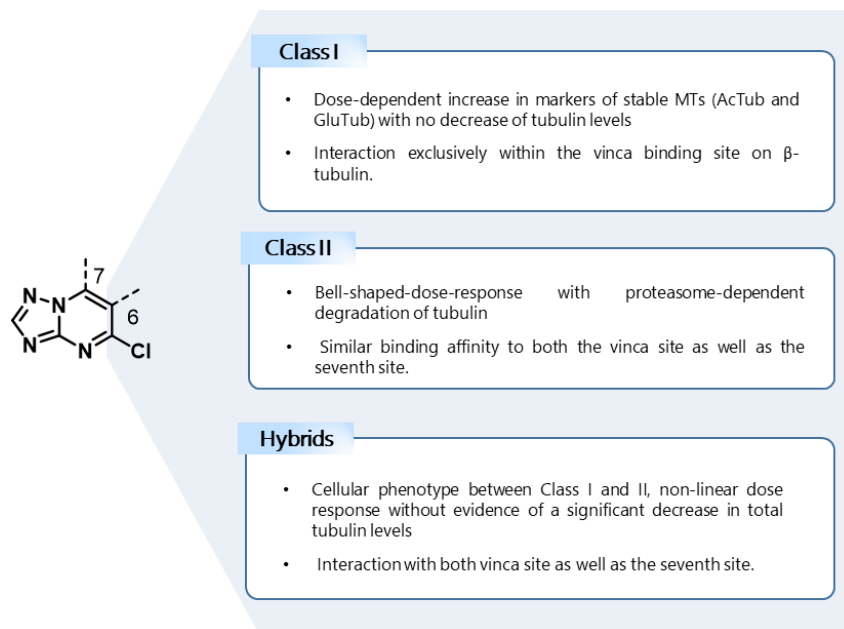
Figure 3.3 Schematic representation of the three different classes of TPDs based on their cellular activity in QBI293 cells and their interaction with α and β tubulin.

3.3 Discovery of BL-0884: a potent MT-stabilizer TPDs

Relatively low doses of brain-penetrant MT-stabilizing compounds have been shown to provide therapeutic benefits in mouse models of tauopathy by normalizing axonal MTs and, consequently, by restoring axonal transport.[249-252, 257] Notably, co-treatment of rodent neurons with Class I or hybrid analogs TPDs, such as derivatives **181** and **182**, along with the phosphatase inhibitor Okadaic Acid (OA, 15 nM) prevents MT collapse with a resulting normalization of MT structure and neuronal processes (Figure 3.4).
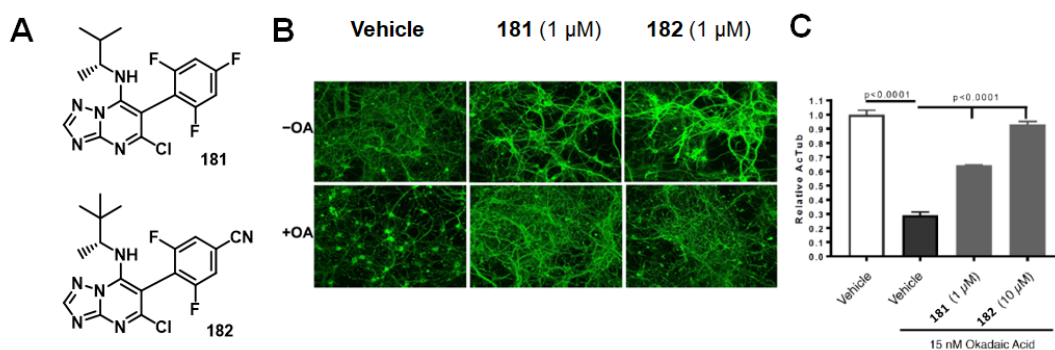
Figure 3.4 A) TPD derivative **181** and nitrile-containing **182** ability to stabilize neuronal MTs under conditions of tau loss-of-function, in rat neuronal cultures with OA (15 nM). (B) Primary rat cortical neurons treatment with compound **181** or **182** (1 µM) in the absence of OA (−OA) showed increased axonal AcTub staining relative to those receiving vehicle only. Upon treatment with OA (+OA) in the absence of the test compound (vehicle), a dramatic reduction in axonal AcTub staining with fragmentation of MTs and neuronal processes was observed. Co-treatment with **181** or **182** (1 µM) along with OA resulted in normalization of AcTub staining and axonal processes. (C) ELISA determination of AcTub levels in homogenates from primary mouse cortical neurons treated with 1 and 10 µM of **182**, or vehicle, in the presence of OA. Compound **182** at 10 µM increased AcTub levels in similar fashion to those in neurons without OA treatment.

In light of these encouraging results, a follow-up SAR exploration[46] driven by a deeper elucidation of the role played by the fragments at C6 and C7 was carried out leading to the discovery of novel derivatives characterized by the presence of an alkyne linkage at the side-chain in the *para* position of the fluorinated ring at the C6 position of the TPD core.

With this in mind, chemical effort was employed to rationally synthesize **BL-0884** (**184**, Figure 3.5 A) featuring the bulkier and lipophilic (*R*)-3,3-dimethylbutan-2-amine at C7 of the pyrimidine core. This analog was found to produce a reduction in total tubulin levels at only higher concentrations (10 µM) contrary to the corresponding alkoxy derivatives such as cevipabulin (**180**) which were characterized by a more marked reduction in tubulin levels at the same concentration.

Additionally, **184** was found to be a potent MT-stabilizer in QBI293 cells and proved to prevent the OA-induced MT-collapse in cortical neurons[46] emerging as a promising lead compound, which deserved further attention and investigation.
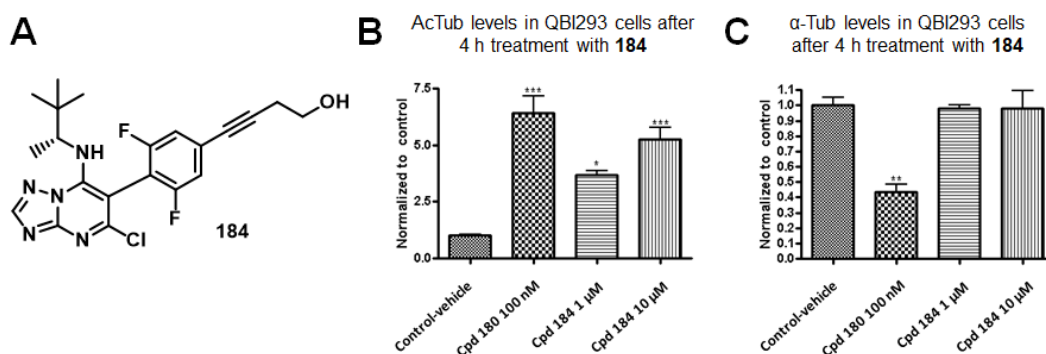

Figure 3.5 A) Chemical structure of **184**; B) ELISA measuring acetylated AcTub levels and C) total α-Tub levels in response to 4-h treatment with TPD **180** (100 nM, used as positive control) or **184** at different concentrations.

3.3.1 Multi-gram scale synthesis of BL-0884 (184)

To advance **184** into pharmacokinetic investigations and further preclinical studies in mice, the seven-step chemical procedure employed to access the rigid alkyne-containing side-chain TPD **184** was performed in a multi-gram scale as depicted in Scheme 3.1.

First, the SN_{Ar} reaction between 1,2,3-trifluoro-5-nitrobenzene (**185**) and diethylmalonate was scaled up from 2.050 g (7.14 mmol) of the limiting reagent **185** to 5 g (28.24 mmol) obtaining a good tolerance in terms of reactivity. The subsequent palladium catalyzed reaction used to reduce the nitro group into the corresponding aniline of **187** was conducted with various amounts of **186** (2.85 g (8.98 mmol), 5.0 g (20 mmol) and 8.9 g (28 mmol)), showing different yields and reaction times based on the amount of starting material used. The best results were observed when starting with 5 g scale (40% yield, after two steps, 2 h, rt), while in a smaller scale from 3 up to 6 h

were needed to obtain complete conversions of the starting material with a similar yield (37%). Despite the bigger scale (8.9 g) showing reasonable reaction times to complete conversion, the yield decreased drastically to 12% due to side product formation.

In contrast, when attempting the following Sandmeyer reaction to convert **187** into the corresponding aryl iodide **188** by starting from 1 g (3.36 mmol, 42%), 1.98 g (6.9 mmol, 45%) and 2.6 g (9.1 mmol, 67%) of **187**, higher yields were seen at a greater scale.

Scheme 3.1 Multi-step procedure to access the MT-stabilizing compound **184**. Optimal reaction scale is reported below the corresponding starting material in italic.
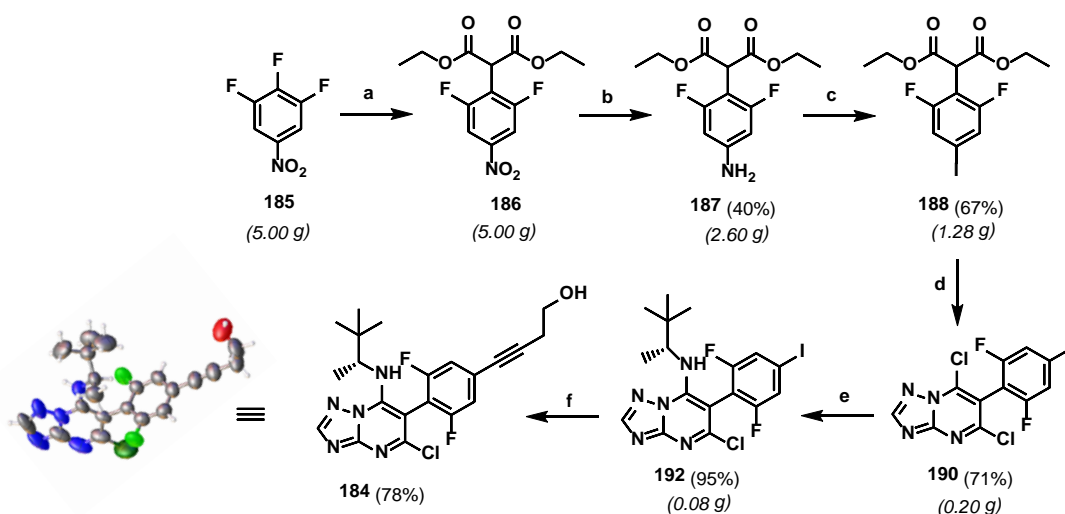
Reaction and conditions. a) Diethylmalonate, NaH, THF, 0 °C to rt, 4 h; b) H₂, Pd/C, MeOH, 2 h, rt; c) i. HCl aq (6 N), NaNO₂, ii. KI, water, 3 h, 0 °C to rt ; d) i. 3-Amino-1*H*-1,2,4-triazole (**189**), TBA, 170 °C, 3 h, ii. Toluene, NaOH 50%, 110 °C to 50 °C, iii. POCl₃, reflux 6 h ; e) (R)-3,3-dimethylbutan-2-amine hydrochloride (**191**), DMF, TEA, 1 h, rt ; f) but-3-yn-1-ol (**193**), CuI, TEA, Pd(PPh₃)₄, DMF, 8 h, rt.

Condensation of **188** with the 3-Amino-1H-1,2,4-triazole (**189**), followed by treatment with neat POCl₃, gave the expected TPD dichloride **190** in good yields: 54% at 0.56 g; 71% at 1.28 g (3.2 mmol); 64% at 2.4 g.

The more reactive chlorine atom of the TPD dichloride **190** was then chemoselectively substituted with the (*R*)-3,3-dimethylbutan-2-amine hydrochloride (**191**) to afford **192** in a scale ranging between 0.2 g (0.6 mmol) and 1.64 g (3.84 mmol) with very good yields between 95.4% and 86%.

Finally, a Sonogashira coupling reaction between but-3-yn-1-ol (**193**) and **192** showed a dramatic decrease in yield when scaling up to 0.36 g (726 mmol) of the monochloro substituted TPD **192** (33% yield). Several synthetic attempts led to identify 80-100 mg as a reasonable starting material loading with a good scale/yield ratio, which led to obtain the desired product **184** with a 78% yield (80 mg, 0.16 mmol). This final reaction was repeated several times *in situ* using a carousel reaction station to obtain more than 500 mg of final compound, whose structure was also confirmed by X-ray crystallography (UC San Diego, Crystallography facility).

3.4 Synthesis and MT-stabilizing activity of possible *in vivo* metabolites of BL-0884 (184).

Identification of metabolic biotransformations represents a crucial phase in the drug discovery process. In detail, the recognition of the site of metabolism in a lead compound could be a significant advance in designing new compounds with a better pharmacokinetic profile and can assist chemists to decide whether a potential candidate should be eliminated from the pipeline or modified to improve chemical stability or safety.[258]With this information in our hand and aware of the crucial role of *N*-dealkylation and oxidation reaction in Phase I metabolism, [259, 260] we designed and synthetized derivatives **194** and **195** (Figure 3.6), as two possible *in vivo* metabolites of **184** to further investigate.
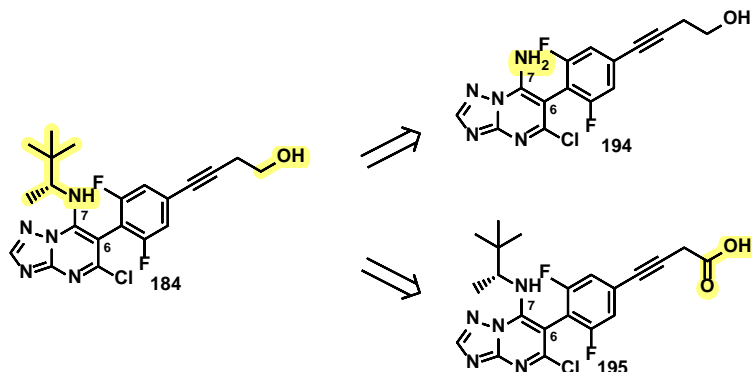
Figure 3.6 A) Design of the *N*-dealkylated derivative **194** and oxidized carboxylic acid **195**, possible *in vivo* metabolites of **184**

Synthesis of **194**, featuring an aliphatic amine substituent at C**7**, was carried out via amination of intermediate **190** in the presence of methanolic ammonia and was successfully followed by a Sonogashira cross-coupling in relatively good yields compared to the corresponding analogue **184** (Scheme 3.2).

Scheme 3.2 Synthetic procedure for **194**, a possible *in vivo* metabolite of **184**.
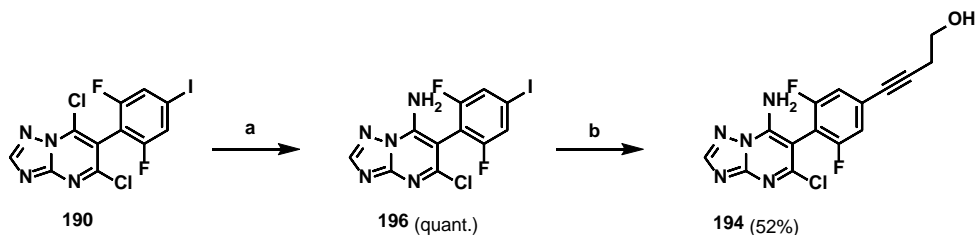
Reagents and conditions. a) NH_3/ MeOH 7 N, 0 °C to rt, 20 min, quant. ; b) **193**, CuI, TEA, $Pd(PPh_3)_4$, DMF, 8 h, rt.

Conversely, the synthetic protocol followed for **195** gave a different outcome. The first attempt of direct oxidation of the exposed alkyl hydroxy group was not successful neither by employing TEMPO nor the Jones reagent as an oxidizing agent (Scheme 3.3).

Scheme 3.3 Unsuccesful direct oxidation of the TPD moiety of **184** to prepare derivative **195**.
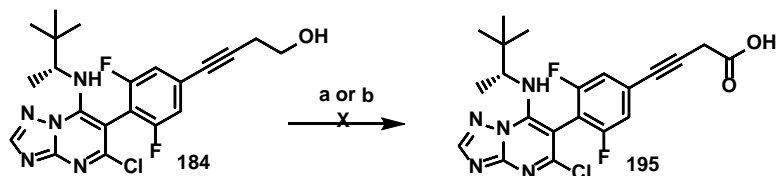
Reagents and conditions. a) TEMPO, BIAB, CH_2Cl_2/H_2O 3:2, 2 h rt, b) $Na_2Cr_2O_7$, $NaIO_4$, HNO_3 water/acetone 1:1, 0 °C, 18 h. No-go crosses indicate the reaction was unsuccessful.

Furthermore, alternative routes such as the direct oxidation of **193** (Scheme 3.4) and the subsequent cross coupling between iodine derivative **190** and but-3-ynoic acid (**193**) did not allow the obtainement of the desired product **195**, probably due to the free carboxylic acid function of the terminal alkyne **197**. For this reason, several efforts were then directed to the preparation of different ester derivatives of the latter by employing several alcohols and experimental conditions.
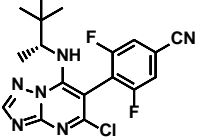
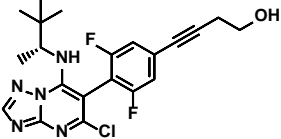**Scheme 3.4** Different synthetic routes to assess **195.**
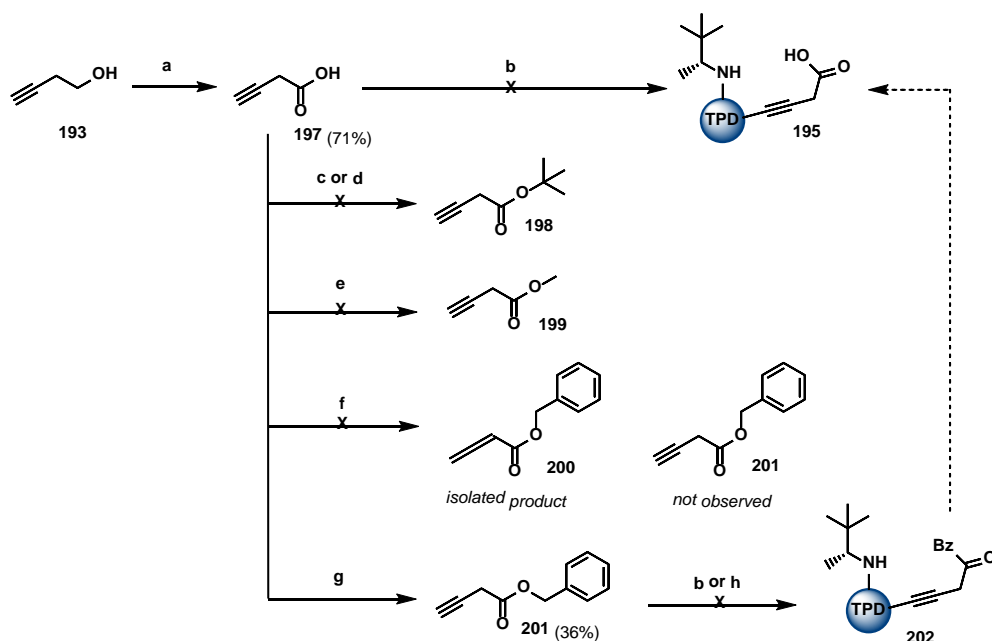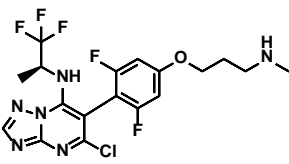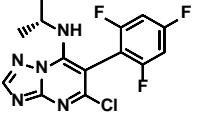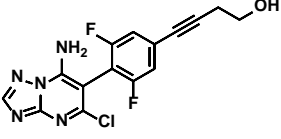
Reagents and conditions. a) $Na_2Cr_2O_7$, $NaIO_4$, HNO_3, water, 0 °C to rt, on, quant.; b) **192**, TEA, CuI, $Pd(PPh_3)_4$, DMF, rt, on; c) i) t-BuOH, DMAP, DCC, rt, on; d) ii) $MgCl_2$ 10 mol%, Boc_2O (1.3 equiv.)/ t-BuOH (2 equiv.); e) TMSCl, MeOH rt, on; f) phenylmethanol, DCC, DMAP, DCM 0 °C to rt, 1 h; g) phenylmethanol, HCl 36%, rt, on h) **192**, K_2CO_3, $Pd(PPh_3)_2Cl_2$,CuI, DME, 70 °C, on. No-go crosses indicate the reaction was unsuccessful; dotted arrows indicate that the reaction was not performed.

The difficulty of working with small volatile molecules lacking UV activity as **198** and **199** was observed with no evidence of the desired products after work-up and purification. Moreover, the formation of unexpected side by-products when a heaver UV visible alcohol such as the benzylic one was employed in amide-coupling conditions did not allow isolating the desired ester **201**. For example, although esterification of carboxylic acid **197** with the benzylic alcohol by using DCC as coupling agent and DMAP as base gave complete consumption of the limiting reagent after three hours (TLC check: 100% EtOAc), ^{1}H NMR in $CDCl_3$ of the obtained product suggested the unexpected isolation of benzyl buta-2,3-dienoate (**200**, Scheme 3.4, f) as a by-product. The finding of a paper focused on the development of catalytic enantioselective [2 + 2] cycloadditions[261] between appropriate alkenes and readily available allenoates, in turn, prepared via coupling reactions of the corresponding terminal alkynes corroborated our hypothesis.

Finally, a Fischer esterification in the presence of HCl as an acid catalyst afforded the desired benzylic ester **201**, which unfortunately did not give the title compound **195** under different conditions of Sonogashira cross-coupling.

Remarkable, **194** showed a beneficial effect in MT-stabilization (Class I) even if it showed low activity in QBI293 cells in accordance to what acquired in previous SAR explorations. Moreover, it showed a good safe profile (CC_{50} Ave >4000 nM) when assessed for cytotoxicity in HEK cells (Table 3.1).

Table 3.1 MT-stabilizing activity of **194** in comparison with representative derivatives **184**, cevipabulin **180**, and **182**. Fold-changes in AcTub and total α-Tub levels in QBI293 cells after 4 h of incubation with test compounds at either 1 or 10 μM concentration are reported.

Structure	#	AcTub		α-Tub		Class	HEK CC$_{50}$ Ave (nM)
		1 μM	**10 μM**	**1 μM**	**10 μM**		
	180	6.98** ± 0.91 (0.92)	1.06 ± 0.38 (0.14)	0.49** ± 0.05	0.27** ± 0.01	II	38.7 ± 8.5
	181	2.14 ± 0.15* (0.59)	2.57 ± 0.15* (0.71)	1.10 ± 0.17	0.90 ± 0.16	I	84.0 ± 0.141
	182	2.83 ± 0.33** (0.68)	4.60 ± 0.35** (1.10)	0.98 ± 0.03	1.03 ± 0.03	I	29.10 ± 1.45
	184	3.67** ±0.34 (0.57)	5.25** ±0.89 (0.81)	0.98±0.04	0.98±0.21	I	40.3 ± 10.3
	194	0.85 ± 0.27 (0.11)	1.12 ± 0.02 (0.14)	0.96 ±0.23	1.06 ±0.01	I	>4000

Reported values for AcTub and α-Tub represent the fold-change over control (DMSO)-treated cells (*$p < 0.05$ and **$p < 0.01$ by one-way ANOVA); numbers in parentheses represent the fold-change of AcTub over positive control-treated cells. Class I compounds are those producing a concentration-dependent increase in AcTub levels and that do not cause >15% reduction in α-tubulin at either concentration; Class II compounds are those that cause >15% decrease in α-tubulin at either 1 or 10 μM compound concentration.

3.5 *In vivo* characterization of BL-0884 (184)

The chemical effort directed towards scaling up the Class I TPD **184** has thus far allowed its assessment in a preliminary pharmacokinetics evaluation in CD-1 male mice as a potential candidate for tauopathy treatment.

In detail, determination of its brain-to-plasma (B/P) ratios at 1 h post administration (i.p. injections of 5 mg/kg) confirmed this TPD as a brain penetrant compound with a B/P ratio of ~0.5 (data not shown) (Figure 3.7 A).

Moreover, in a further pharmacodynamic investigation to determine compound-dependent elevations in the stable MT markers (GluTub) in brain homogenates from compound-treated WT mice, **184** caused significant elevations in GluTub, when administered at 1 mg/kg (i.p.) once daily for two consecutive days, showing comparable pharmacodynamics effects to the two analogs **204** and the previously identified Class I TPD **182** (Figure 3.7 B).
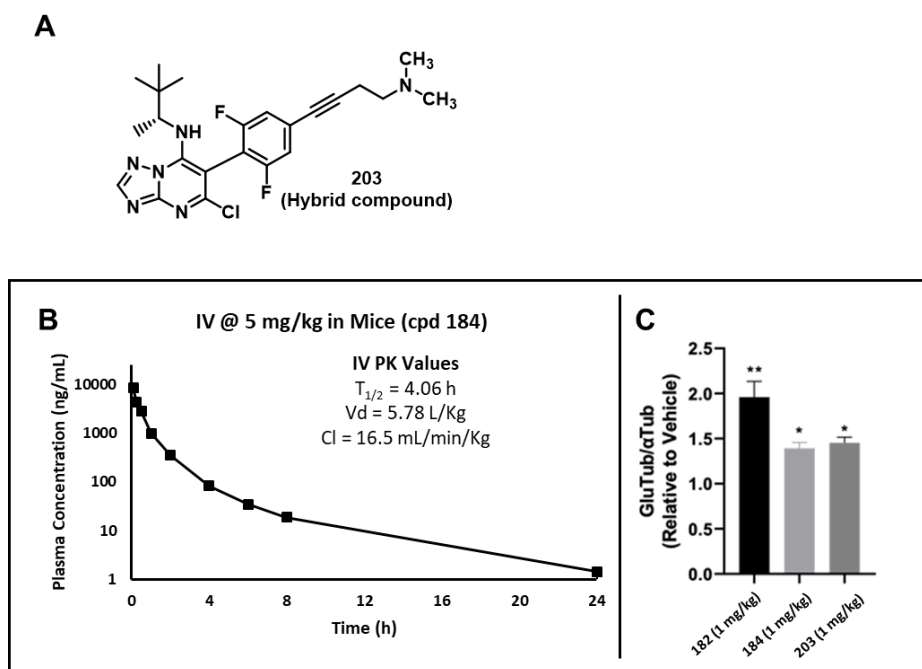

Figure 3.7 A) Chemical structure of the hybrid compound **203**; B) Plasma concentration of 180 after oral administration (5 mg/kg) and pharmacokinetic data after i.v.

injection (1 mg/kg). Error bars represent SD; C) Increases in the GluTub-to-total α-Tub ratio in the brains of WT mice after i.p. dosing of **182**, **184** and **203** at 1 mg/kg once daily for two consecutive days, relative to vehicle-treated mice. The data represent a summary of independent experiments with each compound in which n=4 CD-1 mice received a test compound or vehicle. Error bars represent SEM, with *, $p<0.05$ and **, $p<0.01$ as determined by a two-tailed t-test.

3.6 BL-0884 analogues, optimal starting point for pro-drugs synthesis and active targeting

The incorporation of an acetylene linkage in the aliphatic side-chain at the *para* position of the fluorinated ring at C6 can provide potent MT-stabilizing derivatives that do not cause loss of total tubulin and that exhibit excellent pharmacokinetic/pharmacodynamic profiles, offering several opportunities for CNS-directed MT-stabilizing therapies and as a potential cancer therapy.[262]

The previously discussed class II compound **180** represents a successful example of TPDs, which have reached phase I (NCT00195325 and NCT00195247) for use as anticancer agent thanks to its tubulin polymerization properties and therefore its ability to halt metaphase-anaphase transition.[263]

180, a small molecule rather than the natural product taxanes, demonstrated more favorable parmacokinetic properties and was not susceptible to common tumor drug resistance mechanisms. Despite this, the compound did not progress through clinical trials due to drug-related toxicity. It was therefore concluded that this compound would not offer an improved safety profile compared to the taxes currently available on the market.

In this respect, the toxicity of **180** could be related to the proteasome dependent α-tubulin degradation associated with the interaction between the fluorinated amine moiety at C7 with the deoxyribose of the nonexchangeable GTP[264], which characterize Class II compounds, suggesting that the MT-stabilizing TPDs belonging to Class I and hybrids could be promising substitutes for a safer chemotherapy.

This inspired us to select **184**, characterized by a privileged scaffold possessing a hydroxyl moiety suitable for late -stage functionalization, to develop a library of amino acid esters prodrugs with improved solubility, formulation and oral delivery or active-targeting agents for a safer and directed-cancer therapy.

3.6.1 Pro-drugs definition and uses in medicinal chemistry

The design and development of active compounds able to successfully interact with a target and produce a pharmacological effect with limited side effects is a prerequisite for novel compounds to reach the clinic. However, a wide range of obstacles including low water solubility,[265] poor absorption, distribution, metabolism, and excretion (known as ADME profile) or the already mentioned reduced BBB penetration[266] obstruct a molecule's journey into the marketplace.

Many examples of drugs currently available have required extensive chemical efforts in the lead optimization process to address these issues and favor *in vivo* target engagement.[265]

In this context, pro-drug strategy, consisting in the rational design and synthesis of precursors of biologically active molecules, which are recovered in the human body upon bioconversion, is one of the most appealing approaches.

Prodrug bioconversion processes can be grouped into two categories: 1) prodrug degradation/drug recovery and 2) prodrug activation (Figure 3.8). Within the first class, bioconversion reactions involve removal of a masking group from a conjugate of the parent drug; while, the second class encompasses prodrugs, which undergo a point chemical modification or a conjugation reaction.[267, 268]
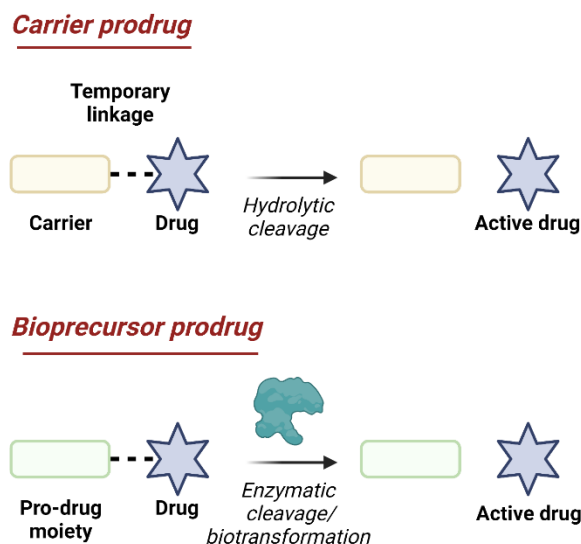
Figure 3.8. Schematic representation of carrier and bioprecursor prodrug mechanism.

Common chemical transformations of bioprecursor prodrugs consist in hydrolytic cleavage of an ester function by esterases – one of the most important enzymes exploited by the prodrug approach in contemporanery drug design and development[269] – or the removal of a phosphate ester by phosphoesterases. Prodrug synthesis has been widely applied to taxanes to improve brain penetration and water solubility and reduce the significant toxicity associated to the high doses required.[270]

In this pursuit, Prof. C. Ballatore and collaborators elegantly demonstrated the C-10 functionalization of the anticancer agent paclitaxel possessing MT-stabilizing activity (**204**, Figure 3.9) to construct bifunctional moieties with hydrolytically stable carbamate linkages.[271]

The versatility of the paclitaxel scaffold was also investigated by Ayalew L. *et al.* through esterification of the C2′-OH position with a succinate linker, and further coupling with an helical peptide obtaining a 400-fold increase in water solubility (**205**, Figure 3.9) in comparison with the parent active compound.[272]
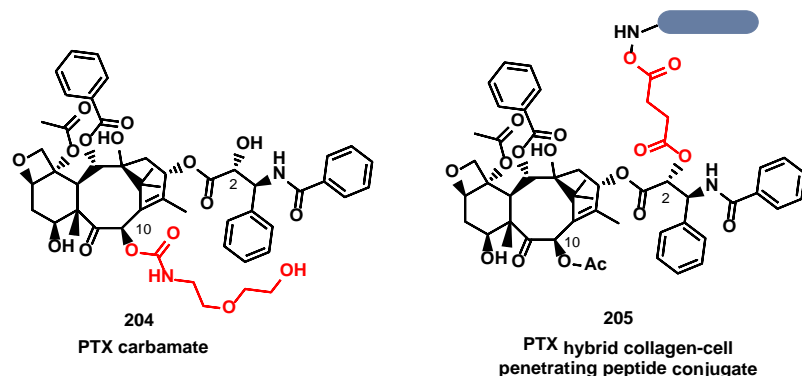
204
PTX carbamate

205
**PTX hybrid collagen-cell
penetrating peptide conjugate**

Figure 3.9 Structure of PTX carbamate (**204**) designed by Prof. Ballatore *et al.* and PTX hybrid collagen-cell penetrating peptide conjugate (**205**).

3.6.2 Active targeting for cancer application

Similarly to the above mentioned prodrugs, also molecules intended for active targeting as tumor-targeting drug conjugates are composed by two distinct chemical components consisting in a tumor-targeting module (TTM) connected to an active cytotoxic chemical warhead directly or through a suitable linker (Figure 3.10).[255]
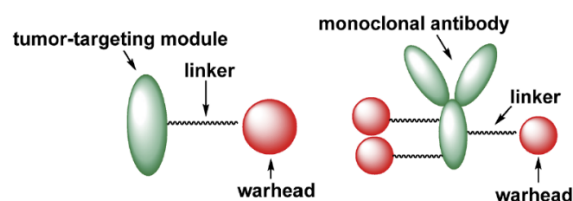

Figure 3.10 Schematic representation of the general structure of tumor-targeting drug conjugates.

This medicinal chemistry tool attempts to overcome the toxicity and narrow selectivity showed by the majority of cancer drugs currently applied in the clinic, including the previously mentioned **180**. The intended mechanism consists in minimizing the systemic toxicity through effective internalization of the cytotoxic

146

moiety inside the target tumor cells where the conjugate should efficiently release. Monoclonal antibody conjugates represent one of the several possibilities to achieve this goal due to cancer cells overexpressing certain antigen in their surface indicating that tumor-specific antigens can be used as biomarkers to differentiate tumor tissues from normal tissues.[255] A great example of targeted prodrugs is KS61-SB-T-12136 (**206**), an highly cytotoxic C-10 methyldisulfanylpropanoyl taxoid conjugated to different immunoglobin G class mAbs through a disulfide-containing linker (Figure 3.11), developed by Ojiwa I. *et al.* Notably, **206** exhibited remarkable antitumor activity against human tumor xenografts in severe combined immune deficiency (SCID) mice.[273]
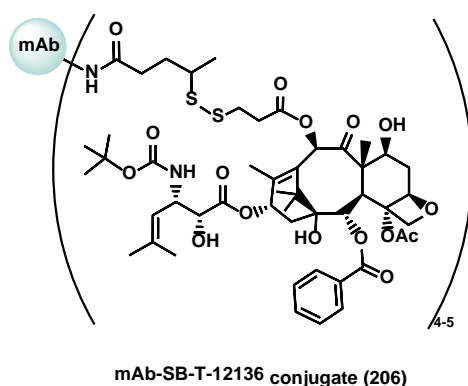

mAb-SB-T-12136 conjugate (206)

Figure 3.11 Chemical structure of mAb–taxoid conjugate **206**, readapted from Ojiwa I. *et al.* [273]

The two previous sections give a brief description of both pro drugs and bifunctional molecule for directed cancer therapy as it pertains to this project. A broad overview of an expansive medicinal chemistry field has been discussed however an in depth discussion was beyond the scope of this thesis. Thus for a more extensive survey please see references [265, 267, 268] for prodrugs and [255, 274] for active targeting.

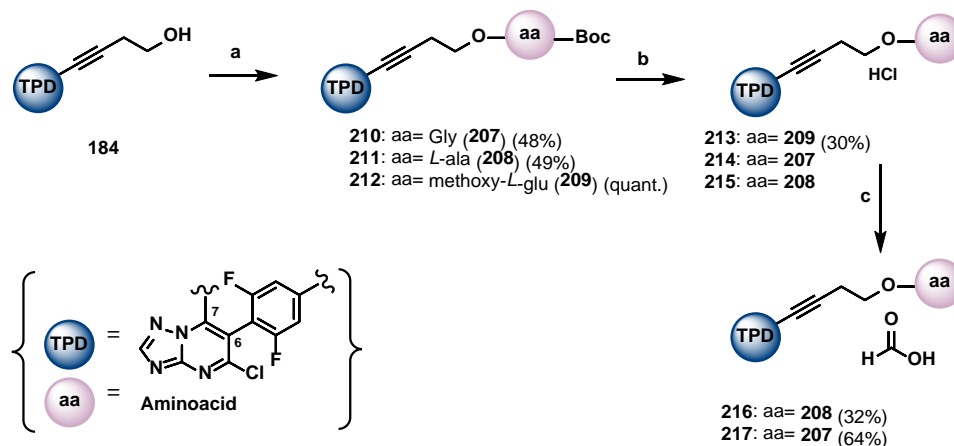# 3.7 BL-0884, privileged scaffold to access amino acids pro-drugs

Compound **184** is a versatile molecule thanks to its exposed hydroxyl moiety part of the aliphatic side-chain linked to the acetylene suitable for a chemical expansion, in order to generate novel analogs possessing a wide range of application including pro drugs and active targeting for cancer chemotherapy. For this reason, a focused series of TPDs was synthesized by exploring new chemical spaces via decoration of **184** hydroxyl group with different amino acid functions.

Eight novel diverse amino acid derivatives of **184** of which six esters and two amides were prepared by adapting well-known synthetic strategies.[46, 253]

3.7.1 Synthesis of amino acid esters of 184

Esterification reaction between **184** and the appropriate commercially available protected amino acid (**207**, Boc-Gly, **208**, Boc *L*-Ala or **209**, (*S*)-2-((*tert*-butoxycarbonyl)amino)-5-methoxy-5-oxopentanoic acid), in presence of EDCl as a coupling agent and DMAP as a base in THF at rt afforded intermediates **210**-**212**. Further cleavage of the Boc protecting group from these latter under acidic condition yielded **213**-**215** and a final purification of the isolated HCl salts (**214** and **215**) via preparative-HPLC reverse phase chromatography gave the corresponding formic acid salts in high purity however in low yields (**216**-**217**, Scheme 3.5).

Scheme 3.5 General chemical procedure employed for the synthesis of amino acid derivatives **210, 211, 213, 216, 217**.

184

210: aa= Gly (**207**) (48%)
211: aa= *L*-ala (**208**) (49%)
212: aa= methoxy-*L*-glu (**209**) (quant.)

213: aa= **209** (30%)
214: aa= **207**
215: aa= **208**

216: aa= **208** (32%)
217: aa= **207** (64%)

Reagents and conditions. a) **207** or **208** or **209**, EDCl, DMAP, THF, rt, on; b) HCl 4M, 1,4-dioxane, rt, 1-2 h; c) HPLC-prep.

The synthesis of analog **218** featuring the *L*-Ser moiety was instead performed following prior protection of the the amino acid chain and subsequently the previously mentioned multi-step procedure depicted in Scheme 3.6.

First, Boc-protection of the amine group of *L*-Ser (**219**) afforded **220** in quantitative yield, which was treated with *tert*-butyldimethylsilyl chloride yielding **221**. Afterwards **221** was employed in a sequential coupling reaction in the same experimental conditions previously described in Scheme 3.1 to give **222**, followed by a deprotection reaction for HCl treatment and a final preparative-HPLC reverse phase chromatography yielding the title compound **218**.

Scheme 3.6 Synthesis of the non-commercially available Boc and TBDMS protected *L*-Ser and of the formic acid salt of its deprotected ester **218**.
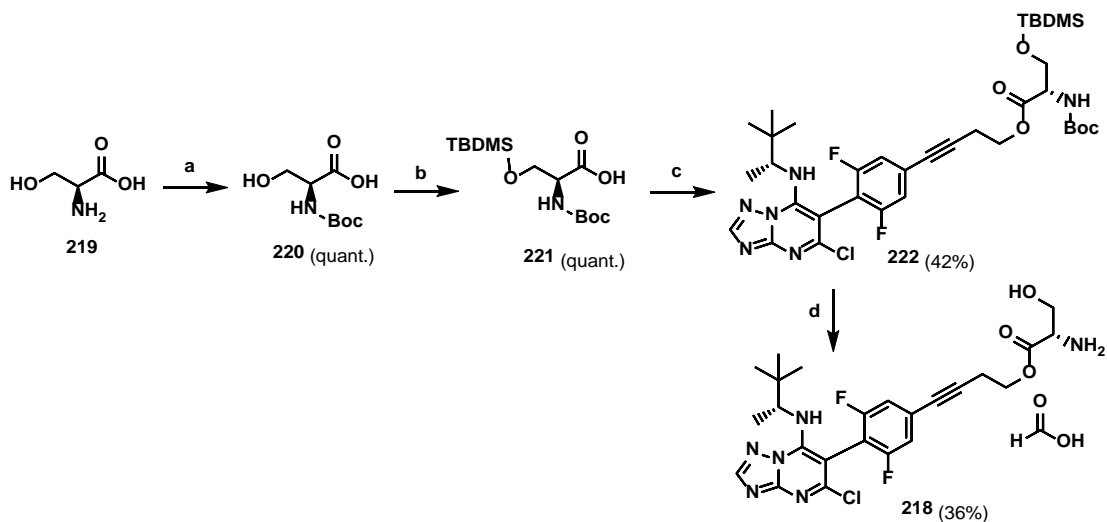

Reagents and conditions. a) (Boc)₂O, NaOH aq. (1M), 1,4-dioxane, 3 h, rt; b) imidazole, TBDMSCl, DMF, rt on; c) **184**, EDCl, DMAP, THF, rt, on, d) HCl (4M), 1,4-dioxane, 1 h, rt.

3.7.1.1 Towards the synthesis of phosphate ester of 184

Throughout the chemical exploration of the hydroxyl function of compound **184**, chemical synthesis of the corresponding phosphate ester was attempted to evaluate the versatility of the chemical scaffold.

Therefore, 1,3,5-trifluoro-2-iodobenzene (**223**, Scheme 3.7) an analogous compound resembling the central tetrasubstituted phenyl moiety of **184,** was coupled in the established Sonogashira cross-coupling conditions obtaining derivative **224**.

Scheme 3.7 Chemical strategy for the synthesis of phosphate ester **226**.
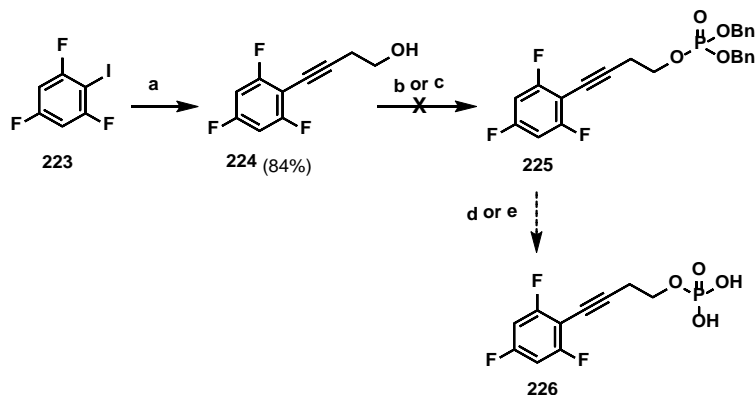
Reagents and conditions. a) but-3-yn-1-ol, CuI, TEA, Pd(PPh$_3$)$_4$, anhydrous DMF, 8 h, rt; b) i. dibenzyl *N,N*-diisopropylphosphoramidite, tetrazole, MeCN, 1 h, 0 °C ii. H$_2$O$_2$ 30% w/w 30 min, rt; c) (BnO)$_2$P(O)H, CCl$_4$, DIEA, DMAP, CH$_3$CN, on, rt.

Synthesis of the desired phosphate ester **226** was attempted through the use of dibenzyl *N,N*-diisopropylphosphoramidite as source of phophate,[275] in addition to the Atherton-Todd reaction.[276] However, neither of these approaches resulted in a positve outcome.

## 3.7.2 Ac-Tub and α-Tub levels quantification of amino acids derivatives

All novel synthetized TPD acetylene derivatives were tested to evaluate their MT-stabilization capability and cytotoxicity in order to compare activity with the Class I compounds such as the parent analog **184** and the nitrile containing derivative **182** together with the prior phase II anti-cancer candidate **180**.[263] In line with previous TPDs SARs studies conducted by Prof. C. Ballatore and collaborators, the synthetized esters confirmed their potential as anti-tauopathies tools by showing in some cases, higher MT-stabilizing activity compared to the parent compound **184** (Table 3.2). However, this activity might be the result of the amino acid moiety cleavage once entered the cells. Thus, in order to better understand and justify the intrinsic activity of the

synthetized esters, the corresponding *L*-Ala and Gly amide derivatives of **184** were also prepared.

3.7.3 Synthesis and evaluation of the amino acid amides 232 and 233.

Amide coupling of the commercially available but-3-yn-1-amine HCl salt (**227**) and **207** or **208** , in the presence of HATU as a coupling agent and DIPEA as base gave the corresponding Boc-protected amides intermediates **228** and **229** (Scheme 3.8). A further Sonogashira cross-coupling of these latter with aryl iodide intermediate **192** and the final cleavage of the Boc protecting group gave the desired products **232** and **233** as formic acid salts.
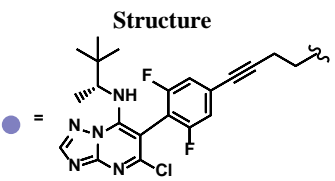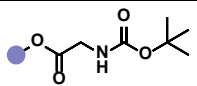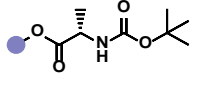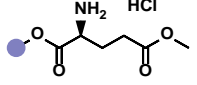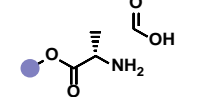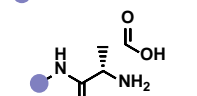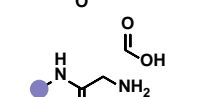
Scheme 3.8. Multi-step preparation of amide derivatives **232** and **233**.
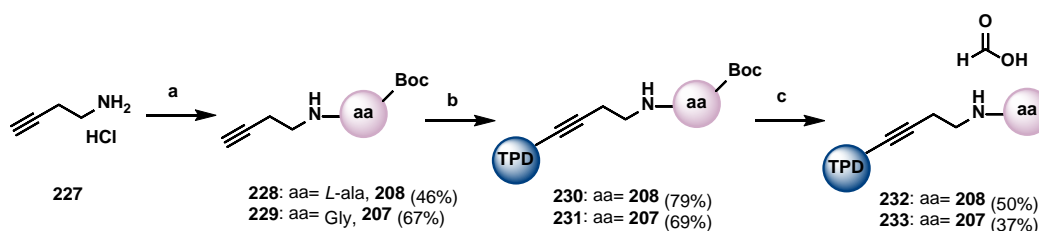
Reagents and conditions. a) **207** or **208**, HATU, DIPEA, DCM, 0 °C to rt, on; b) **192**, TEA, CuI, Pd(PPh₃)₄, DMF, rt on c) HCl 4M, 1,4-dioxane, rt, on.

In-cell evaluation of these last two synthetized amides showed significant MT-stabilizing activity with a marked effect compare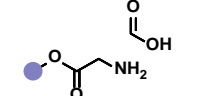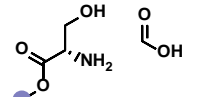d to the starting compound **184** and the previously synthetized ester analogues and a cytotoxic effect in HEK cells comparable to that of **180** (Table 3.2).

Table 3.2 MT-stabilizing activity of **BL-0884** (**184**) amino acid esters and amides. Fold-changes in AcTub and total α-Tub levels in QBI293 cells after 4 h of incubation with test compounds at either 1 or 10 μM concentration.

Structure	#	AcTub		α-Tub			HEK CC$_{50}$ Ave (nM)
		1 μM	10 μM	1 μM	10 μM	Class	
	210	5.07**± 0.25 (0.80)	5.54** ±0.04 (0.87)	0.93 ± 0.03	0.91 ± 0.03	I	40.5 ± 2.8
	211	6.63** ± 0.34 (0.84)	9.03** ±0.94 (1.14)	0.86 ± 0.11	0.90 ± 0.10	I	34.2 ± 6.3
	213	7.14** ±1.65 (0.90)	8.01** ± 1.93 (1.01)	0.88 ± 0.03	0.92 ± 0.02	I	62.3 ± 8.3
	216	5.29** ± 0.73 (0.83)	6.22** ± 0.55 (0.98)	0.86 ± 0.01	0.94 ± 0.03	I	31.5 ± 2.8
	217	4.60** ± 0.16 (0.72)	7.06** ± 0.13 (1.11)	0.95 ± 0.07	0.93 ± 0.01	I	32.3 ± 5.6
	218	4.71** ± 0.23 (0.74)	6.72** ± 0.12 (1.06)	0.84** ±0.01	0.86 ± 0.02	I	40.1 ± 9.3
	232	9.98** ± 0.31 (1.26)	11.9** ± 0.33 (1.50)	0.99 ± 0.17	1.06 ± 0.01	I	47.2 ± 7.6
	233	5.85** ± 0.05 (0.74)	12.3** ± 0.37 (1.55)	0.90 ± 0.01	0.98 ±0.01	I	70.5 ± 3.9

Reported values for AcTub and α-Tub represent the fold-change over control (DMSO)-treated cells (*p < 0.05 and **p < 0.01 by one-way ANOVA); numbers in parentheses represent the fold-change of AcTub over positive control-treated cells. Class I compounds are those producing a concentration-dependent increase in AcTub levels and that do not cause >15% reduction in α-Tub at either concentration; Class II compounds are those that cause >15% decrease in α-Tub at either 1 or 10 μM compound concentration.

Among them, amide **232**, featuring the *L*-Ala moiety attached to the parent compound, showed the most important MT-stabilizing phenotypic behavior (Figure 3.12).
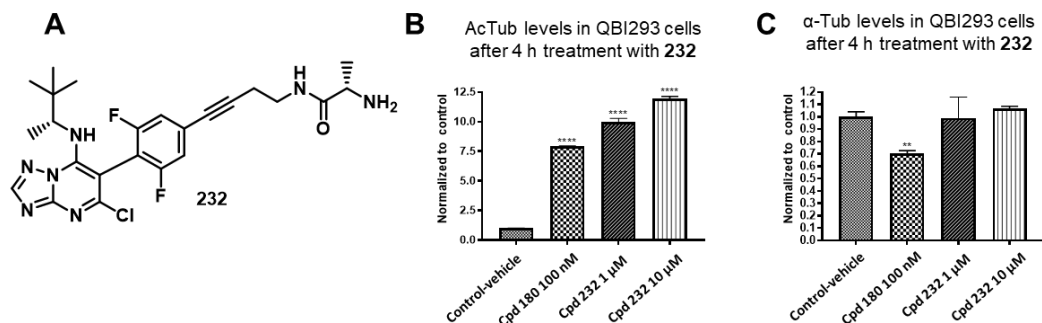
Figure 3.12 A) Chemical structure of **232**; B) ELISA measuring AcTub levels and C) total α-Tub levels in response to 4 h treatment with TPD **180** (100 nM, used as positive control) or **226** at different concentrations.

3.8 Conclusions and future perspectives

Certainly, these compounds warrant further investigation. The chemical space of the amino acid derivatives needs to be expanded to better elucidate the mechanism underlining their activity in addition to direct chemical and biological investigation towards the most promising hits.

Further derivatives are currently under development within Prof. C. Ballatore Lab to better explore the reactivity also of other structurally similar TPDs and to answer to these open questions.

In the meantime, taking together the obtained preliminary results, it is noteworthy that these novel amino acid-based acetylene derivatives hold considerable promise as potential therapeutic candidates for neurodegenerative tauopathies. Furthermore, compounds **210**, **211**, **213**, **216**-**218**, **232**, and **233** bore cytotoxicity values similar to the anti-cancer agent **180**, suggesting their potential application as possible MT-stabilizing anti-mitotic tools to be employed in a targeted delivery approach for cancer therapy.

Chapter 4

4. Concluding remarks

The multifactorial etiology of tau-related disorders still represents a major hurdle that needs to be overcome for drug discovery. MTDLs purposely designed as straightforward CNS tools to put into practice the insights of network medicine are gaining ever-increasing attention.

As discussed in the introductory chapter, in the last decade scientists have taken a meaningful step forward in the understanding of these diseases, allowing for a therapeutic jump towards a cause-directed treatment. This has been confirmed by the approval of the monoclonal antibodies Aducanumab and Lecanemab targeting Aβ in AD, conversely to what observed with previously employed symptomatic cures such as acetylcolinesterase inhibitors (AChEIs), which have demonstrated very low efficacy in improving cognition in AD patients. Furthermore, current therapeutic interventions have not proven adequate to support patients in the late stage of the disease. For this reason, the development of not invasive and efficient biomarkers together with an appropriate prevention, in a similar fashion to cancer screening, is crucial to avoid diagnosis in the late stage of these lethal and burdening neurodegenerative syndromes, timeframe where it is hard to intervene.

Attracted by the great potential of multi-target drugs, during my Ph.D. the rational design and synthesis of multi-target PKs inhibitors together with the development of brain-penetrant MT-stabilizing agents were carried to combat AD and related tauopathies.

In chapter 2, the MTDLs paradigm was applied to pursuit the multifactorial nature of NDDs through the simultaneous modulation of GSK-3β, FYN, and DYRK1A, three independent yet interconnected PKs possessing a pivotal role in the aberrant tau protein hyperphosphorylation. With the aim to develop first-in-class well-balanced triple inhibitors of these PKs, a computer-assisted SAR exploration starting from **ARN25068 (72)** was undertaken. **72** was selected among a large set of small molecules tested against 172 different PKs, as a promising hit thanks to its well-balanced *in vitro* low nanomolar inhibitory potency against GSK-3β and FYN and micromolar potency against DYRK1A. Notably, this compound showed efficacy in reducing the extent of tau protein phosphorylation in an *in vitro* model of AD and emerged as a promising prototype for further SAR explorations. Three different series of analogs were rationally designed and synthetized by inserting one single properly addressed modification on the 2,4-di-substituted pyrimidine thiophene core of **72**.

New series of hybrid compounds (series IV) in which the best modifications of derivatives of series I-III were merged were also developed allowing to gain insights on the pharmacophoric traits useful to either retain well-balanced activity against GSK-3β and FYN or improved potency of DYRK1A. This intense medicinal chemistry effort culminated in the discovery of two novel compounds (**147**, **148**) characterized by improved affinity against DYRK1A (IC$_{50}$ = 461.0 nM and 242.0 nM, respectively), and low nanomolar potency against the other two PKs, and a quite well-balanced triple nanomolar inhibitor **159** (GSK-3β: IC$_{50}$ = 126.0 nM; FYN: IC$_{50}$ = 83.0 nM; DYRK1A: IC$_{50}$ = 199.0 nM). Both derivatives **148** and **159** showed good *in vitro* ADME properties and have been selected for further *in vivo* pharmacokinetic and BBB

permeability studies with the final goal of identifying the best candidates to progress into lead optimization campaigns.

The promising findings obtained represent a proof-of-concept of the feasibility to exploit triple inhibitors of GSK-3β, FYN, and DYRK1A as innovative chemical tools for AD and related tauopathies treatment.

In chapter 3, the direct stabilization of MTs has been pursued by developing compounds based on the TPD scaffold, which have been shown to provide therapeutic benefits in mouse models of tauopathy by normalizing axonal MTs and, consequently, by restoring axonal transport. As part of a follow-up SAR exploration, I reported my chemical effort for the scaling-up of the seven-steps procedure used to access the brain penetrant **BL-0884** (**184**), selected for *in vivo* investigations. In addition, the synthesis of possible *in vivo* metabolites of **184** has been carried out to aid *in vivo* studies.

Remarkably, compound **184** exhibits excellent PK/PD profiles offering several opportunities for CNS-directed MT-stabilizing therapies.

The suitability of its exposed hydroxyl moiety for late-stage functionalization inspired the development of a small library of amino acids ester of **184** as prodrugs with improved solubility, formulation and oral delivery compared to the parent compound or active-targeting agents for a safer and directed-cancer therapy. The eight novel amino acid derivatives showed MT-stabilizing activity when tested in cell (QBI293)-based assays deserving attention for further studies with the final goal to develop novel promising therapeutic candidates for tauopathies and other possible indications such as targeted delivery approaches.

To conclude, the development of PKs inhibitors may be a very successful strategy to apply at the initial stages of AD and tau-related disease pathologies. Moreover, MTs stabilizers can be considered supplementary therapeutic targets for the treatment of AD.[246, 247] The combination of these strategies would pave the way to

effectively block the pathogenic cascades typical of complex and heterogeneous NDDs, to obtain a disease-modifying effect.

Chapter 5

5. Experimental section

5.1 General information

Solvents and reagents were purchased from commercial suppliers (Acros, Aldrich, Merck, Fluorochem, TCI or Alfa Aesar) and used without further purification. Anhydrous solvents were purchased from Sigma-Aldrich. Thin-layer chromatography (TLC) analyses were performed using pre-coated E. Merck or Supelco silica gel on TLC Al foils 0.2 mm and visualized by UV (254 nm). Automated column chromatography purification were carried out using a Teledyne ISCO apparatus (CombiFlash® Rf) and Biotage® Selekt with pre-packed silica gel or basic alumina columns of different sizes (from 4 g to 48 g) and mixtures of increasing polarity of cyclohexane and ethyl acetate (EtOAc), chloroform ($CHCl_3$) or dichloromethane (CH_2Cl_2) and methanol (MeOH) or ethanol (EtOH) enriched with NH_3 1 M solution, were specified. Silica gel column chromatography was manually performed for part II entries with silica gel 60 (particle size 0.040−0.062 mm) supplied by Silicycle and Sorbent Technologies.

NMR experiments were run on a Bruker Avance III 400 system, equipped with a BBI probe and Z-gradients and on a Bruker UltrashieldTM Plus FT-NMR 600 MHz Avance III, equipped with a CryoProbeTM QCI 1H/19F/13C/15N and with a SampleJet autosampler and temperature control. Spectra were acquired at 300 K, using deuterated dimethyl sulfoxide (DMSO-d_6), deuterated chloroform (CDCl$_3$) or acetone (acetone-d_6) as solvents. Chemical shifts for ^{1}H and ^{13}C spectra were recorded in parts per million using the residual non-deuterated solvent as the internal standard (for DMSO-d_6: 2.50 ppm, ^{1}H; 39.52 ppm, ^{13}C). Data are reported as follows: chemical shift (ppm), multiplicity (indicated as: br., broad signal; s, singlet; d, doublet; t triplet; q = quartet, quint = quintet, td = triplet of doublets, dd, doublet of doublets, dq, doublet of quartets; m, multiplet and combinations thereof), coupling constants (*J*) in Hertz (Hz) and integrated intensity.

Not all ^{13}C signals were detectable for compounds **83**-**88**, **101**-**111**, **131**, **132**, **141**-**148**, **159**, **178**, **232** despite multiple attempts with exhaustive signal averaging. The missing signals are expected to be difficult to detect for compounds **83**-**88**, **101**-**111**, **131**, **132**, **141**-**148**, **159**, **178** due to the long relaxation times of tertiary and quaternary carbons in the system where two tautomeric species are present in different abundance. Similarly, the aromatic ring conjugated with an alkyne in **232**, resulted in longer relaxation times. Moreover, the presence of a ^{19}F in the same compound (**232**) resulted in a reduced intensity of the coupled signals (indicated as multiplet, m).^{13}C NMR spectra of compounds **184**, **210**, **211**, **213**, **216**-**218**, **233** were not featured for the same reasons of low signal/noise ratio.

UPLC-MS analysis of part I entries were run on a Waters ACQUITY UPLC/MS system consisting of a SQD (Single Quadropole Detector) Mass Spectrometer equipped with an Electrospray Ionization interface and a Photodiode Array Detector (Part I). The PDA range was 210-400 nm. The analyses were performed on an ACQUITY UPLC BEH C$_{18}$ (50x2.1 mmID, particle size 1.7μm) with a

VanGuard BEH C_{18} pre-column (5x2.1 mmID, particle size 1.7 µm). The mobile phase was 10 mM NH_4OAc in H_2O at pH 5 adjusted with AcOH (A) and 10 mM NH_4OAc in ACN-H_2O (95:5) at pH 5 (B). Three types of gradients were employed at the UPLC-MS depending on the polarity of the compounds: an apolar method where the mobile phase B was increased from 0% to 50% in min, a generic method where the mobile phase B was increased from 5% to 95% in 2.5 min and a polar method where the mobile phase B was increased from 50% to 100% in 2.5 min. MW reactions were performed using Explorer-48 positions apparatus (CEM). Electrospray ionization in positive and negative mode was applied in the mass scan range 100-750 Da. LC-MS analysis of part II entries were performed on a InfinityLab Poroshell 120 PhenylHexyl 2.7 micron from Agilent with a standard method of 5-95% ACN/H_2O in 7 min with a flow rate of 0.6 ml/min. High-resolution mass spectra for part II entries were measured using an Agilent 6230 time-of-flight mass spectrometer with a Jet stream electrospray ionization source. HPLC was performed with a Gilson HPLC equipped with UV and a mass detector. All samples were analyzed employing a linear gradient from 10 to 90% of ACN in H_2O over 8 min and flow rate of 1 ml/min. Preparative reverse-phase HPLC purifications were performed on a Gilson instrument employing Waters SunFire preparative C18 OBD columns (5 µm 19 mm Å~ 50 mm or 19 mm Å~ 100 mm). LC-MS analysis were performed following the general method from 5-95% ACN in 7 min with a flow rate of 0.6ml/min. in a InfinityLab Poroshell 120 PhenylHexyl 2.7 micron column from Agilent.

The quality control (QC) analysis of the final compound was performed on a Waters ACQUITY UPLC/MS system consisting of a SQD (single quadrupole detector) mass spectrometer equipped with an electrospray ionization interface and a photodiode array detector. Electrospray ionization in positive and negative mode was applied in the mass scan range 110-750 Da and the PDA range was 210-400 nm. The analysis was run on an ACQUITY UPLC BEH C_{18} (100x2.1 mmID, particle size 1.7µm) with

a VanGuard BEH C_{18} pre-column (5x2.1 mm ID, particle size 1.7 µm), using 10 mM NH_4OAc in H_2O at pH 5 adjusted with AcOH (A) and 10 mM NH_4OAc in ACN-H_2O (95:5) at pH 5 (B) as mobile phase. A linear gradient was applied starting from 10% of the mobile phase B, holding for 0.20 min. Then increasing B from 10% to 90% in 6 min 90-100%B in 0.10 min and 100% B hold for 0.70 min with a total run time of 7 min.

Compounds were named according to iupac nomenclature using the naming algorithm developed by CambridgeSoft Corporation and used in ChemDraw professional 20.0. All final compounds were found to be >95% pure by LC-MS.

5.2 Chemical procedures of compounds reported in chapter 2

General procedure A: SN_{Ar} of the C4 of the pyrimidine core (**75**, **95**, **96**, **97**, **99**)

Triethylamine (2.2 equiv.) was added to a mixture of 2,4-dichlorosubstituted [3,2-*d*]pyrimidine (1 equiv.) and the appropriate 5-substituted amino pyrazole (2.5 equiv.). The resulting mixture was allowed to react at room temperature for 2 days under inert atmosphere (Ar). After complete conversion of the starting material, the reaction mixture was precipitated with water (5 ml) and filtered under *vacuum* to afford the desired products.

General procedure B: SN_{Ar} of the C4 of the pyrimidine core (**98**, **100**, **151**-**153**)

2,4-dichloro-substituted[3,2-*d*]pyrimidine (1 equiv.), the appropriate 5-substituted amino pyrazole (2.5 equiv.) and triethylamine (2.2 equiv.) were suspended in anhydrous 2-propanol (4 ml). The reaction mixture was stirred for 2-3 days at room temperature or where otherwise specified at 80 °C, under Ar. After complete

conversion of the starting material, the reaction mixture was precipitated with water (5 ml), filtered under *vacuum* and the obtained powder was either used in the following step without any further purification or purified via flash column chromatography when specified.

General procedure C: SN$_{Ar}$ of the C2 of the pyrimidine core (**72**, **83**-**85**, **101**-**103**)

To intermediates **75**, **87**, **95**-**97**, **99**, **112**-**114** (1 equiv.), the appropriate benzylamine (5 equiv.) was added. *N*-butanol (0.7 ml) was added and the reaction mixture was heated up to 110 °C for 2 days under Ar. After observing starting material complete conversion, the reaction mixture was cooled down to room temperature and concentrated to dryness. The resulting crude was purified by normal phase flash chromatography to obtain the desired products.

General procedure D: SN$_{Ar}$ of the C2 of the pyrimidine core (**86**, **88**, **104**, **106** **107**,**109**, **110**, **111**, **116**, **131**, **132**, **143**, **144**, **146**-**148**)

To intermediates **75**, **98**, **100**, **151**-**153** (1 equiv.), the appropriate benzylamine (1.5 equiv.), DIPEA (2.5 equiv.) and *n*-butanol (1.37 ml) were added. The resulting suspension was sonicated and heated for 6-8 h under MW irradiation at 180 °C, under Ar. After observing complete conversion of the starting material, the reaction mixture was cooled down to room temperature and concentrated to dryness. The resulting crude was purified by normal phase flash chromatography.

General Procedure E: Synthesis of benzyloxy derivatives (**108**, **141**, **142**, **145**)

To the appropriate 4-substituted bicyclic-pyrimidine (**75**, **97**, **98**, **151**) (1 equiv.), sodium benzyloxide solution (1 M, 1.1 equiv.) was added. The resulting mixture was suspended in anhydrous THF (2.7 ml) and heated under MW irradiation for 7 h at 150 °C, under Ar. After completion, the reaction was concentrated in vacuo

and the resulting solid was washed with water (10 ml x 3) and extracted with EtOAc (10 ml x 3). The organic layers were combined and dried under Na_2SO_4, filtrated and concentrated under vacuum. The resulting crude products were purified by flash chromatography to yield the title compounds.

*N*2-benzyl-*N*4-(5-cyclopropyl-1*H*-pyrazol-3-yl)thieno[3,2-*d*]pyrimidine-2,4-diamine (ARN25068, 72).
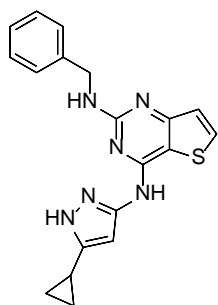
Compound **72** was synthesized following the general procedure C starting from 0.556 g (1.905 mmol) of **75** and **76** (1.042 ml, 9.527 mmol) dissolved in of *n*-butanol (6.35 ml). The crude product was purified by normal phase chromatography - Silica 12g Gold-Solvent A: CH_2Cl_2 - Solvent B: CH_2Cl_2/EtOH 9:1 Detection: 260/286 nm -Gradient: 10-40% of solvent B, followed by a final trituration with CH_2Cl_2 (7 ml) to yield the desired product as a white powder (466 mg, 68%). UPLC-MS (generic method): Rt = 1.89 min, MS (ESI) *m/z*: 363.1 [M+H]$^+$, $C_{19}H_{19}N_6S^+$ [M+H]$^+$ calculated: 363.1. QC analysis: Rt = 3.74 min, UPLC-MS purity (UV at 215 nm): 99%. Both ^{1}H- and ^{13}C-NMR spectra in DMSO-d_6 were consistent with the isolation of two different tautomeric forms a and b in a dynamic equilibrium as described in the *appendix A* (Figure A1 and A2); The presence of only tautomeric form a was observed in acetone-d_6 (Figure A3, *appendix A*). ^{1}H NMR (400 MHz, DMSO-d_6) δ 12.57 (br. s, 1Hb), 12.07 (br. s, 1Ha), 10.26 (br.s, 1Hb), 9.60 (br.s, 1Ha), 7.90 (br. s, 1Ha), 7.68 (br. s, 1Hb), 7.46 – 6.90 (m, 7Ha, 7Hb), 6.34 (s, 1Ha), 5.66 (s, 1Hb), 4.55 (d, *J* = 6.2 Hz, 2Ha, 2Hb), 1.83 (dq, *J* = 1.2 , 4.9 Hz, 1Ha, 1Hb), 0.87 (br. s, 2Ha, 2Hb), 0.63 (br. s, 2Ha, 2Hb). (Figure A1). ^{1}H NMR (400 MHz, acetone-d_6) δ 11.73 (br. s 1H), δ 8.92 (br. s 1H), 7.84 (d, *J* = 5.4 Hz, 1H), 7.43 7. (d, *J* = 7.29, 1H), 7.30 (t, *J* = 7.5 Hz, 2H), 7.22 (t, *J* = 7.3 Hz, 1H), 7.08 (d, *J* = 5.4 Hz, 1H), 6.72 (s, 1H), 6.72 (br. s, 1H), 6.12 (br. s, 1H) 4.71 (d, *J* = 6.0 Hz, 2H), 1.87 (tq, *J* = 5.1, 1.65 Hz,

1H), 0.86 (dd, J = 4.21, 2.0 Hz, 2H), 0.66 (dd, J = 4.15, 2.2 Hz, 2H). (Figure A2). ^{13}C NMR (151 MHz, DMSO-d_6) δ 162.30, 160.60, 154.72, 153.05, 152.28, 147.43, 145.12, 141.08, 140.18, 133.14, 128.04, 126.80, 126.23, 123.34, 122.83, 105.36, 94.90, 88.41, 44.13, 9.22, 7.61, 6.75. (Figure A2).

2-chloro-*N*-(5-cyclopropyl-1*H*-pyrazol-3-yl)thieno[3,2-*d*]pyrimidin-4-amine (75).
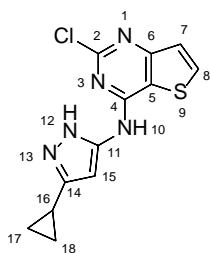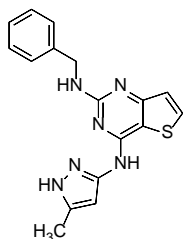

Compound **75** was synthesized following the general procedure A using 2,4-dichlorothieno[3,2-*d*]pyrimidine (**73**) 0.500 g (2.438 mmol) and 0.751 g (6.094 mmol) of 3-cyclopropyl-1*H*-pyrazol-5-amine (**74**) in presence of triethylamine (0.748 ml, 5.363 mmol). Precipitation in water (10 ml) and final trituration of the solid with ACN (7 ml) afforded intermediate **75** as a white powder (556 mg, 78%). UPLC-MS (generic method): Rt = 1.69 min, MS (ESI) *m/z*: 292.4/294.1 [M+H]$^+$, $C_{12}H_{11}ClN_5S^+$ [M+H]$^+$ calculated: 292.0/294.0. ^{1}H NMR (400 MHz, DMSO-d_6) δ 12.41 (br. s, 1H, H10), 10.46 (br. s, 1H, H12), 8.19 (d, J = 5.4 Hz, 1H, H8), 7.34 (d, J = 5.4 Hz, 1H, H7), 6.24 (br. s, 1H, H15), 1.93 (dq, J = 5.1, 1.5 Hz, 1H, H16), 0.95 (dd, J = 4.1, 1.8, 2H, H17 or H18) 0.72 (dd, J = 4.1, 1.8 Hz, 2H, H17 or H18). (Figure A4 and A6 of Appendix A). ^{13}C NMR (151 MHz, DMSO-d_6) δ 161.81 (C*6*), 155.94 (C*2*, C*4*), 146.12 (C*11*), 145.81 (C*14*), 136.63 (C*7*), 123.04 (C*8*), 113.38 (C*5*), 96.51 (C*15*), 7.81 (C*17*, C*18*), 6.83 (C*16*). (Figure A5 and A6 of Appendix A). (*See appendix A for regiochemistry determination*).

*N*2-benzyl-*N*4-(1*H*-pyrazol-3-yl)thieno[3,2-*d*]pyrimidine-2,4-diamine (83)
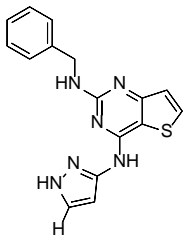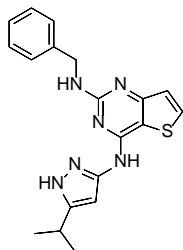
Compound **83** was synthesized following the general procedure C starting from 80.0 mg (0.318 mmol) of **95** and 1.589 mmol of **76** (0.174 ml) dissolved in *n*-butanol (0.060 ml). The crude product was purified by normal phase chromatography - Silica 12g Gold-Solvent A: CH_2Cl_2 - Solvent B: CH_2Cl_2/MeOH 9:1 Detection: 260/286 nm -Gradient: of 5-20% solvent B, followed by a sequential trituration with CH_2Cl_2 (7 ml) yielded the desired product as a white powder (81.1 mg, 79%). UPLC-MS (generic method): Rt = 1.66 min, MS (ESI) *m/z*: 323.1 [M+H]$^+$, $C_{16}H_{15}N_6S^+$ [M+H]$^+$ calculated: 323.1. QC analysis: Rt = 3.09 min, UPLC-MS purity (UV at 215 nm): 99.5%. Both ^{1}H- and ^{13}C-NMR spectra in DMSO-*d$_6$* were consistent with the isolation of two different tautomeric forms a and b in a dynamic equilibrium with a corresponding to the major and b to the minor in abundance ^{1}H NMR (600 MHz, DMSO-*d$_6$*) δ 13.05 (br. s., 1Hb), 12.35 (br. s., 1Ha), 10.42 (br. s., 1Hb), 9.72 (br. s., 1Ha), 7.91 (br. s., 1Hb; 1Ha), 7.61 (br. s., 1Hb; 1Ha), 7.59 – 6.49 (m, 7Hb; 7Ha), 6.70 (br.s. 1Ha), 5.95 (br. s., 1Hb), 4.54 (d, *J* = 6.1 Hz, 2Ha; 2Hb). ^{13}C NMR (151 MHz, DMSO-*d$_6$*) δ 162.45, 160.73, 160.60, 154.97, 147.50, 141.13, 140.32, 138.00, 133.31, 128.16, 127.16, 127.11, 127.06, 126.43, 123.04, 105.55, 98.81, 91.81, 44.32.

_N_2-benzyl-_N_4-(5-methyl-1_H_-pyrazol-3-yl)thieno[3,2-_d_]pyrimidine-2,4-diamine (84)
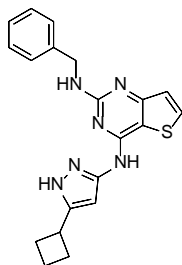
Compound **84** was synthesized following the general procedure C starting from 66 mg (0.248 mmol) of **96** and 1.242 mmol of benzylamine (0.14 ml) dissolved in 0.81 ml of _n_-butanol. Purification by normal phase flash chromatography employing a 12 g gold silica cartridge (-Solvent A: CH_2Cl_2 -Solvent B: CH_2Cl_2/MeOH 9:1 -Detection: 240/260 nm -Gradient: 0.05-40% solvent B) and a final trituration by using cold diethyl ether (7 ml) yielded the desired product as a white powder (34.1 mg, 41%). UPLC-MS (generic method): Rt = 1.79 min, MS (ESI) _m/z_: 337.1 [M+H]$^+$, $C_{17}H_{17}N_6S^+$ [M+H]$^+$ calculated: 337.11. QC analysis: Rt = 3.21 min, UPLC-MS purity (UV at 215 nm): 99.5%. ^{1}H spectrum in DMSO-d_6 was consistent with the isolation of two different tautomeric forms a and b in a dynamic equilibrium, with a corresponding to the major and b to the minor in abundance. ^{1}H NMR (600 MHz, DMSO-d_6) δ 12.62 (br. s, 1Hb), 12.00 (br. s., 1Ha), 10.29 (br. s., 1Hb), 9.59 (br. s., 1H), 7.88 (br. s., 1H), 7.68 – 6.94 (m, 7Ha and 7Hb), 6.41 (br. s., 1H), 5.75 (s, 1H), 4.53 (d, _J_ = 6.2 Hz, 2Ha and 2Hb), 2.18 (br. s., 3Ha and 3 Hb). ^{13}C NMR (151 MHz, DMSO-d_6) δ 162.40, 160.71, 154.91, 147.66, 141.21, 137.87, 137.82, 133.20, 128.11, 126.97, 126.90, 126.30, 123.49, 123.01, 122.94, 105.57, 98.15, 44.30, 10.80.

N2-benzyl-N4-(5-isopropyl-1H-pyrazol-3-yl)thieno[3,2-d]pyrimidine-2,4-diamine (85)

Compound **85** was synthesized following the general procedure C starting from 74.3 mg (0.253 mmol) of **97** and 1.265 mmol of **76** (0.14 ml) dissolved in 0.843 ml of *n*-butanol. Purification by normal phase flash chromatography employing a 12 g gold silica cartridge (-Solvent A: CH_2Cl_2 -Solvent B: CH_2Cl_2/1N NH_3 in MeOH 9:1 -Detection: 240/260 nm -Gradient: 0.25-35% solvent B) and a final trituration by using cold diethyl ether (7 ml) yielded the desired product as a white powder (49.1 mg, 53%). UPLC-MS (generic method): Rt = 1.96 min, MS (ESI) *m/z*: 365.2 $[M+H]^+$, $C_{19}H_{21}N_6S^+$ $[M+H]^+$ calculated: 365.15. QC analysis: Rt = 3.93 min, UPLC-MS purity (UV at 215 nm): 99.5%. ^{1}H NMR (600 MHz, DMSO-d_6) δ 12.04 (br. s., 1H), 9.59 (br. s., 1H), 7.88 (br. s, 1H), 7.48 – 6.91 (m, 6H), 6.45 (br. s., 1H), 4.56 (d, *J* = 6.3 Hz, 2H), 2.87 (m, 1H), 1.19 (d, *J* = 6.9 Hz, 6H). ^{13}C NMR (151 MHz, DMSO-d_6) δ 162.44, 160.78, 154.94, 149.06, 147.29, 141.24, 140.30, 133.25, 128.12, 126.92, 126.33, 122.91, 105.48, 95.50, 44.25, 25.46, 22.36.

N2-benzyl-N4-(5-cyclobutyl-1H-pyrazol-3-yl)thieno[3,2-d]pyrimidine-2,4-diamine (86)

Compound **86** was synthesized following the general procedure D starting from 100 mg (0.327 mmol) of intermediate **98**, **76** (0.053 ml, 0.490 mmol), DIPEA (0.142 ml, 0.817 mmol) dissolved in 1.63 ml of *n*-butanol and stirred at 180 °C for 8 h. After completion, the reaction mixture was concentrated in vacuo and the resulting crude product was purified by normal phase flash chromatography employing a 12 g gold silica cartridge (-Solvent A: $CHCl_3$ -Solvent B: $CHCl_3$/EtOH 8:2 -Detection: 240/260 nm -Gradient: 5-10% of solvent B). The isolated fraction was

concentrated under high *vacuum* and lyophilized to yield a white solid (57.51 mg, 47%). UPLC-MS (method generic), MS (ESI) *m/z*: 377.0 $[M+H]^+$, $C_{20}H_{21}N_6S^+$ $[M+H]^+$ calculated: 377.14. QC analysis: Rt = 4.03 min, UPLC-MS purity (UV at 215 nm): 99.5%. Both ^{1}H- and ^{13}C-NMR spectra in DMSO-d_6 were consistent with the isolation of two different tautomeric forms a and b in a dynamic equilibrium.^{1}H NMR (400 MHz, DMSO-d_6) δ 12.66 (br. s., 1Hb), 12.06 (br. s, 1Ha), 10.30 (br. s., 1Hb), 9.64 (br. s., 1Ha), 7.90 (br. s, 1Ha, 1Hb), 7.42 – 6.87 (m, 7Ha, 7Hb), 6.51 (br. s., 1Ha), 5.79 (br. s., 1Hb), 4.57 (d, *J* = 6.2 Hz, 2Ha, 2Hb), 3.43 (p, *J* = 8.6 Hz, 1Ha, 1Hb), 2.31 – 1.75 (m, 6Ha, 6Hb). ^{13}C NMR (151 MHz, DMSO-d_6) δ 162.44, 160.80, 154.87, 147.52, 146.92, 141.25, 140.36, 133.24, 128.12, 126.86, 126.31, 122.93, 105.51, 96.07, 44.24, 28.99, 18.13.

*N*2-benzyl-*N*4-(5-phenyl-1*H*-pyrazol-3-yl)thieno[3,2-*d*]pyrimidine-2,4-diamine (87)
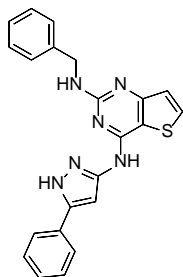
Compound **87** was synthesized following the general procedure C starting from 68.8 mg (0.209 mmol) of **99** and **76** (0.114 ml, 1.046 mmol) dissolved in 0.7 ml of *n*-butanol. Purification by normal phase flash chromatography employing a 12 g gold silica cartridge (-Solvent A: CH$_2$Cl$_2$ -Solvent B: CH$_2$Cl$_2$/EtOH 9:1 - Detection: 240/260 nm -Gradient: 10-30% of solvent B) and a final trituration by diethyl ether (7 ml), and solvent removal via lyophilization and high vacuum, yielded the desired product as a white powder (37 mg, 45%). UPLC-MS (generic method): Rt = 2.09 min, MS (ESI) *m/z*: 399.1 $[M+H]^+$, $C_{22}H_{19}N_6S^+$ $[M+H]^+$ calculated: 399.13. QC analysis: Rt = 4.31 min, UPLC-MS purity (UV at 215 nm): 99.5%. [1]H spectrum in DMSO-d_6 was consistent with the isolation of two different tautomeric forms a and b in a dynamic equilibrium, with a corresponding to the major and b to the minor in abundance. ^{1}H NMR (400 MHz, DMSO-d_6) δ 12.97 (br.s., 1Ha,

1Hb), 10.50 (br.s., 1Hb), 9.91 (br. s., 1Ha), 7.96 (br.s., 1Ha, 1Hb), 7.75 (br.s., 2Ha,2Hb), 7.44 – 7.37 (m, 5Ha,5Hb), 7.34 – 7.29 (m,3Ha, 3Hb), 7.25 (m, 1Ha, 1Hb), 7.11 (br.s., 1Ha, 1Hb), 6.39 (br. s., 1Ha, 1Hb), 4.59 (d, J = 6.1 Hz, 2Ha, 2Hb). ^{13}C NMR (151 MHz, DMSO-d_6) δ 162.94, 162.57, 160.68, 160.43, 148.79, 141.34, 133.99, 133.49, 128.74, 128.24, 127.38, 126.54, 124.92, 123.52, 123.17, 105.61.

*N*2-benzyl-*N*4-(5-(pyridin-3-yl)-1*H*-pyrazol-3-yl)thieno[3,2-*d*]pyrimidine-2,4-diamine (88)
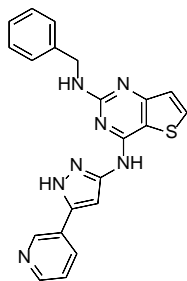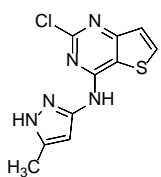
Compound **88** was synthesized following the general procedure D starting from 62 mg (0.189 mmol) of **100**, **76** (0.031 ml, 0.282 mmol), DIPEA (0.082 ml, 0.471 mmol) dissolved in 0.941 ml of *n*-butanol and stirred for 6 h.Purification by normal phase flash chromatography employing a 24 g alumina (Al$_2$O$_3$ pH=7) cartridge (-Solvent A: CH$_2$Cl$_2$ -Solvent B: CH$_2$Cl$_2$/EtOH 9:1 -Detection: 240/260 nm -Gradient: 0-60% of solvent B) and a final trituration by cold diethyl ether (7 ml x 2) yielded, after freeze drying, the desired product as a pale yellow powder (29.3 mg, 47%). UPLC-MS generic method: Rt = 1.93 min, MS (ESI) *m/z*: 398.0 [M-H]$^-$, C$_{21}$H$_{16}$N$_7$S$^-$ [M-H]$^-$ calculated: 398.13. QC analysis: Rt = 3.54 min, UPLC-MS purity (UV at 215 nm): 99.5%.^{1}H NMR (400 MHz, DMSO-d_6) δ 13.24 (br. s., 1H), 10.59 (br. s, 1H), 9.01 (br. s., 1H), 8.51 (dd, J = 4.7, 1.5 Hz, 1H), 8.12 (br. s., 1H), 7.98 (br. s., 1H), 7.70 – 7.12 (m, 8H), 6.58 (br. s. 1H), 4.59 (d, J = 6.0 Hz, 2H). ^{13}C NMR (151 MHz, DMSO-d$_6$) δ 162.58, 160.42, 153.41, 148.50, 146.27, 140.37, 133.59, 132.05, 129.60, 128.26, 127.32, 126.59, 123.81, 123.43, 105.61, 89.37, 44.36.

2-chloro-N-(1*H*-pyrazol-3-yl)thieno[3,2-d]pyrimidin-4-amine (95)
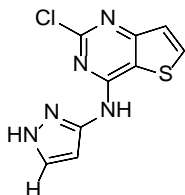
Compound **95** was synthesized following the general procedure A by reaction of 2,4-dichlorothieno[3,2-*d*]pyrimidine (**73**) (100 mg, 0.487 mmol) and 1*H*-pyrazol-5-amine (**89**) (101.29 mg, 1.219 mmol) in presence of triethylamine 0.149 ml (1.073 mmol). The crude product was purified by normal phase chromatography (Silica 12 g gold cartridge -Solvent A: CH_2Cl_2 -Solvent B: CH_2Cl_2/MeOH 9:1 -Detection: 260/286 nm -Gradient: 0-40% of solvent B) to afford 80.6 mg (66%) of the desired product as a yellow powder. UPLC-MS (generic method): Rt = 1.31 min; MS (ESI) *m/z*: 250 [M-H]$^-$ and 252 [M+H]$^+$), $C_9H_7ClN_5S^+$ [M+H]$^+$ calculated: 251.0/253.0. ^{1}H NMR (400 MHz, DMSO-*d$_6$*) δ 12.66 (s, 1H), 10.61 (s, 1H), 8.21 (d, *J* = 5.4 Hz, 1H), 7.76 (s, 1H), 7.36 (d, *J* = 5.4 Hz, 1H), 6.59 (s, 1H).

2-chloro-*N*-(5-methyl-1*H*-pyrazol-3-yl)thieno[3,2-*d*]pyrimidin-4-amine (96)

Compound **96** was synthesized following the general procedure A by reaction of 2,4-dichlorothieno[3,2-*d*]pyrimidine (**73**) (100 mg, 0.487 mmol) and 3-methyl-1*H*-pyrazol-5-amine (**90**) (118.39 mg, 1.219 mmol) in presence of triethylamine 0.149 ml (1.073 mmol). The crude product was purified by normal phase chromatography (Silica 12g gold cartridge -Solvent A: $CHCl_3$ -Solvent B: $CHCl_3$/MeOH 9:1 -Detection: 260/286 nm - Gradient: 0-40% of solvent B) to afford 66.1 mg (51%) of the desired product as a white powder. UPLC-MS (generic method): Rt = Rt.1.54 min; MS (ESI) *m/z*: 266 [M+H] $^+$, $C_{10}H_9Cl_5S^+$ [M+H]$^+$ calculated: 266.02. ^{1}H NMR (400 MHz, DMSO-*d$_6$*) δ 12.34 (br. s., 1H), 10.51 (br. s., 1H), 8.20 (d, *J* = 5.4 Hz, 1H), 7.34 (d, *J* = 5.4 Hz, 1H), 6.34 (br. s., 1H), 2.27 (s, 3H).

**2-chloro-*N*-(5-isopropyl-1*H*-pyrazol-3-yl)thieno[3,2-*d*]pyrimidin-4-amine (97)**
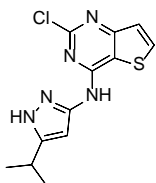
Compound **97** was synthesized following the general procedure A by reaction of **73** (100 mg, 0.487 mmol) and 3-isopropyl-1*H*-pyrazol-5-amine (**91**) (152.4 mg, 1.2175 mmol) in presence of triethylamine 0.149 ml (1.073 mmol). The crude product was purified by normal phase chromatography (Silica 12 g gold cartridge -Solvent A: CHCl$_3$ -Solvent B: CHCl$_3$/MeOH 9:1 -Detection: 260/286 nm -Gradient: 0-35% of solvent B) to afford 92.2 mg (64%) of the desired product as a pink powder. UPLC-MS (generic method): Rt = 1.82 min; MS (ESI) *m/z*: 294 [M+H]$^+$, C$_{12}$H$_{13}$ClN$_5$S$^+$ [M+H]$^+$ calculated: 294.0/296.0. ^{1}H NMR (400 MHz, DMSO-*d$_6$*) δ 12.41 (s, 1H), 10.48 (s, 1H), 8.20 (d, *J* = 5.4 Hz, 1H), 7.34 (d, *J* = 5.4 Hz, 1H), 6.33 (s, 1H), 3.15 – 2.75 (m, 1H), 1.25 (d, *J* = 6.9 Hz, 6H).

2-chloro-*N*-(5-cyclobutyl-1*H*-pyrazol-3-yl)thieno[3,2-*d*]pyrimidin-4-amine (98)
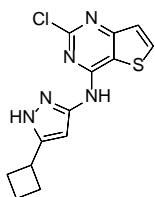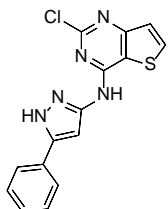
Compound **98** was synthesized following the general procedure B using **73** 175.36 mg (0.855 mmol) and 293.2 mg (2.137 mmol) of 3-amino-5-cyclobutyl-1*H*-pyrazole (**92**) in presence of triethylamine 0.262 ml (1.880 mmol) and 2.85 ml of anhydrous 2-propanol for 3 days. Precipitation in water (10 ml), filtration under *vacuum* afforded intermediate **98** as a white powder (212 mg, 81%). UPLC-MS (generic method): Rt = 1.90 min, MS (ESI) *m/z*: 306/308 [M+H]$^+$, C$_{13}$H$_{13}$ClN$_5$S$^+$ [M-H]$^+$ calculated: 306.05/308.04. ^{1}H NMR (400 MHz, DMSO-*d$_6$*) δ 12.45 (s, 1H), 10.46 (br. s., 1H), 8.20 (d, *J* = 5.5 Hz, 1H), 7.35 (d, *J* = 5.5 Hz, 1H), 6.40 (s, 1H), 3.53 (q, *J* = 8.6 Hz, 1H), 2.44 – 2.09 (m, 4H), 2.07 – 1.90 (m, 2H).

2-chloro-*N*-(5-phenyl-1*H*-pyrazol-3-yl)thieno[3,2-*d*]pyrimidin-4-amine (99)
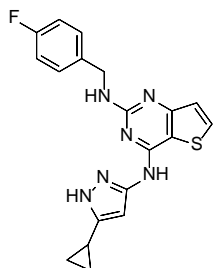
Compound **99** was synthesized following the general procedure A by reaction of **73** (200 mg, 0.975 mmol) and 3-phenyl-1*H*-pyrazol-5-amine (**93**) (388.1 mg, 2.438 mmol) in presence of triethylamine 0.299 ml (2.145 mmol) and stirred for 3 days. The reaction mixture was precipitated in water (7 ml) and the resulting crude was purified by normal phase chromatography (Silica 12g gold cartridge -Solvent A: CH_2Cl_2 -Solvent B: CH_2Cl_2/MeOH 9:1 -Detection: 260/286 nm -Gradient: 10-30% of solvent B) to afford, after precipitation of the product in CH_2Cl_2/cyclohexane 9:1 (10 ml), 77 mg (25%) of the desired product as a white powder. UPLC-MS (generic method): Rt = Rt.1.95 min; MS (ESI) *m/z*: 328/330 [M+H]$^+$, $C_{15}H_{11}ClN_5S^+$ [M+H]$^+$ calculated: 328.03/330.03 . ^{1}H NMR (600 MHz, DMSO-*d*$_6$) δ 13.22 (s, 1H), 10.68 (s, 1H), 8.23 (d, *J* = 5.0 Hz, 1H), 7.77 (d, *J* = 7.1 Hz, 2H), 7.49 (t, *J* = 7.1 Hz, 2H), 7.38 (m, 2H), 6.99 (s, 1H).

2-chloro-*N*-(5-(pyridin-3-yl)-1*H*-pyrazol-3-yl)thieno[3,2-*d*]pyrimidin-4-amine (100)
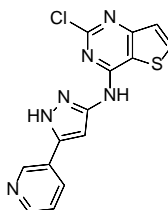
Compound **100** was synthesized following the general procedure B using **73** (0.976 mmol) and 0.392 g (2.438 mmol) of 3-(pyridin-3-yl)-1*H*-pyrazol-5-amine (**94**) in presence of triethylamine (0.296 ml, 2.14 mmol) and 4.0 ml of anhydrous 2-propanol for 4 days. Precipitation in water (10 ml), filtration under *vacuum* and sequential trituration in EtOH (7 ml) afforded intermediate **100** as a white powder (64 mg, 20%). UPLC-MS (generic method): Rt = 1.56 min, MS (ESI) *m/z*: 327.0 [M-H]$^-$, $C_{14}H_8ClN_6S^-$ [M-H]$^-$ calculated: 327.03. ^{1}H NMR (400 MHz, DMSO-*d*$_6$) δ 13.39 (br. s., 1H), 10.73 (br. s., 1H), 9.01 (br. s, 1H), 8.57 (d, *J* = 3.5 Hz, 1H), 8.24 (d, *J* = 5.4 Hz, 1H), 8.15 (d, *J* = 8.0 Hz, 1H), 7.52 (br. s., 1H), 7.39 (d, *J* = 5.4 Hz, 1H), 7.11 (br. s., 1H).

N4-(5-cyclopropyl-1H-pyrazol-3-yl)-N2-(4-fluorobenzyl)thieno[3,2-d]pyrimidine-2,4-diamine (101)
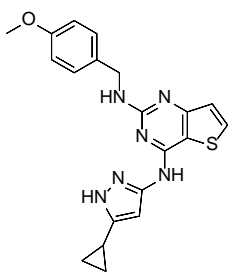
Compound **101** was synthesized following the general procedure C starting from 80 mg (0.275 mmol) of **75** and 1.242 mmol of 4-fluorobenzylamine (**112)** (0.157 ml, 1.37 mmol) dissolved in 0.92 ml of *n*-butanol. Purification by normal phase flash chromatography employing a 12 g gold silica cartridge (-Solvent A: CH$_2$Cl$_2$ -Solvent B: CH$_2$Cl$_2$/EtOH 9:1 -Detection: 240/260 nm -Gradient: 10-40% solvent B) and a final trituration with CH$_2$Cl$_2$ (7 ml) yielded, after removing solvents under *vacuum* at 80 °C, the desired product as a white powder (85 mg, 74%). UPLC-MS (generic method): Rt = 2.07 min, MS (ESI) *m/z*: 381 [M+H]$^+$), C$_{19}$H$_{18}$FN$_6$S$^+$ [M+H]$^+$ calculated: 381.12. QC analysis: Rt = 3.83 min, UPLC-MS purity (UV at 215 nm): 99.5%. ^{1}H NMR (400 MHz, DMSO-*d$_6$*) δ 12.14 (br. s., 1H), 9.70 (br. s., 1H), 7.90 (d, *J* = 5.4 Hz, 1H), 7.37 (dd, *J* = 8.3, 5.6 Hz, 2H), 7.11 (t, *J* = 8.9 Hz, 2H), 7.05 (d, *J* = 5.4 Hz, 1H), 6.12 (br. s., 1H), 4.51 (d, *J* = 6.2 Hz, 2H), 1.83 (dq, 1H), 0.87 (dd, *J* = 8.4, 2.4 Hz, 2H), 0.62 (br. s., 2H). ^{13}C NMR (151 MHz, DMSO-*d$_6$*) δ 162.38, 161.21 (C-F *J* = 239.5 Hz), 160.19, 154.88, 152.38, 147.51, 145.21, 137.33, 136.53, 133.27, 129.22 (C-F *J* = 62.1 Hz), 123.46, 122.92, 114.88 (C-F *J* = 20.8 Hz), 105.58, 95.07, 43.55, 7.71.

N2-(4-chlorobenzyl)-N4-(5-cyclopropyl-1H-pyrazol-3-yl)thieno[3,2-d]pyrimidine-2,4-diamine (102)
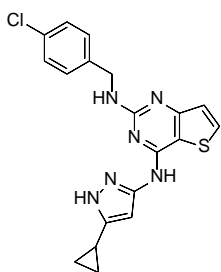
Compound **102** was synthesized following the general procedure C starting from 80 mg (0.275 mmol) of **75** and 4-chlorobenzylamine (**113**) (0.167 ml, 1.37 mmol) dissolved in 0.92 ml of *n*-butanol. Purification by normal phase flash chromatography employing a 12 g gold silica cartridge   (-Solvent A: CH_2Cl_2 - Solvent B: CH_2Cl_2/EtOH 9:1 -Detection: 240/260 nm -Gradient: 0-40% of solvent B) and a final trituration with CH_2Cl_2 (7 ml) and water (7 ml) to remove a basic impurity yielded, after freeze drying, the desired product as a white powder (62.7 mg, 62%). UPLC-MS (generic method): Rt = 2.19 min, MS (ESI) *m/z*: 397/399 [M+H]$^+$ and 395/397 [M-H]$^-$) $C_{19}H_{18}ClN_6S^+$ [M+H]$^+$ calculated: 397.09. QC analysis: Rt = 4.15 min, UPLC-MS purity (UV at 215 nm): 98%. ^{1}H NMR (400 MHz, DMSO-d_6) δ 12.07 (br. s., 1H), 9.69 (br. s., 1H), 7.91 (d, *J* = 4.4 Hz, 1H), 7.36 (br. s., 5H), 7.04 (d, *J* = 4.4 Hz, 1H), 6.13 (br. s., 1H), 4.52 (d, *J* = 6.2 Hz, 2H), 1.84 (m, 1H), 0.87 (d, J= 7.17 Hz, 2H), 0.62 (br. s., 2H). ^{13}C NMR (151 MHz, DMSO-d_6) δ 162.36, 160.63, 160.22, 154.90, 152.42, 147.50, 145.20, 140.33, 133.24, 129.11, 128.71, 128.65, 128.62, 128.05, 122.89, 105.63, 95.08, 43.59, 7.71, 6.84.

N4-(5-cyclopropyl-1H-pyrazol-3-yl)-N2-(4-methoxybenzyl)thieno[3,2-d]pyrimidine-2,4-diamine (103)

Compound **103** was synthesized following the general procedure C starting from 80 mg (0.275 mmol) of **75** and 4-methoxybenzylamine (**114**) (0.179 ml, 1.37 mmol) dissolved in 0.92 ml of *n*-butanol. Purification by normal phase flash chromatography employing a 12 g gold silica cartridge (-Solvent A: CH_2Cl_2 -Solvent B: CH_2Cl_2/EtOH 9:1 -Detection:

240/260 nm -Gradient: 10-30% solvent B) and a final trituration by CH_2Cl_2 (7 ml) yielded the desired product as a white powder (48 mg, 45%). UPLC-MS (generic method): Rt = 1.99 min, MS (ESI) m/z: 393.1 [M+H]$^+$, $C_{20}H_{21}N_6OS^+$ [M+H]$^+$ calculated: 393.14. QC analysis: Rt = 3.57 min, UPLC-MS purity (UV at 215 nm): 99%. ^{1}H NMR (400 MHz, DMSO-d_6) δ 12.07 (br. s., 1H), 9.60 (br. s., 1H), 7.91 (br. s., 1H), 7.27 (d, J = 8.22 Hz, 2H), 7.05 (br. s., 1H), 6.87 (d, J= 8.22 Hz, 2H), 6.32 (br. s., 1H), 4.46 (d, J = 6.1 Hz, 2H), 3.71 (s, 3H), 1.84 (tt, J = 8.7, 5.1 Hz, 1H), 0.87 (d, J = 5.5 Hz, 2H), 0.64 (br. s., 2H). ^{13}C NMR (151 MHz, DMSO-d_6) δ 162.41, 160.69, 158.00, 157.93, 154.81, 147.58, 145.20, 133.13, 128.65, 128.18, 128.09, 123.47, 122.93, 113.57, 105.41, 95.05, 55.02, 43.72, 7.72

4-(((4-((5-cyclopropyl-1*H*-pyrazol-3-yl)amino)thieno[3,2-*d*]pyrimidin-2-yl)amino)methyl)benzonitrile (104)
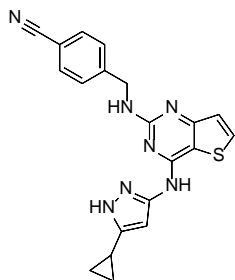
Compound **104** was synthesized following the general procedure D starting from 110 mg (0.377 mmol) of **75**, 4-cyanobenzylamine (**115**) (74.75 mg, 0.566 mmol), DIPEA (0.164 ml, 0.942 mmol) dissolved in 1.5 ml of *n*-butanol and stirred for 6 h. After completion, the reaction mixture was concentrated in vacuo, dissolved in H_2O and the pH was adjusted to 7. The aqueous phase was extracted with EtOAc (10 ml x 3), the organic layers were collected and dried under Na_2SO_4 and concentrated under vacuum. The resulting crude product was purified by normal phase flash chromatography employing a 12 g gold silica cartridge (-Solvent A: CH_2Cl_2 Solvent B: CH_2Cl_2/1N NH_3 in MeOH 9:1 -Detection: 240/260 nm -Gradient: 10-20% of solvent B). The isolated fraction was concentrated under high *vacuum* and lyophilized to yield a white solid (42.5 mg, 29%). UPLC-MS (generic method): Rt = 1.90 min, MS (ESI) m/z: 388.1 [M+H]$^+$, $C_{20}H_{18}N_7S^+$ [M+H]$^+$ calculated: 388.13. QC analysis: Rt = 3.42 min, UPLC-MS purity (UV at 215 nm): 98%. Both ^{1}H-

and ^{13}C-NMR spectra in DMSO-d_6 were consistent with the isolation of two different tautomeric forms a and b in a dynamic equilibrium. ^{1}H NMR (400 MHz, DMSO-d_6) δ 12.55 (br. s., 1Hb), 12.08 (br. s., 1Ha), 10.28 (br. s., 1Hb), 9.64 (br. s., 1Ha), 7.90 (br. s., 1Ha, 1Hb), 7.77 7(d, J = 8.0 , 2Ha, 2Hb), 7.52 (d, J = 8.0 Hz, 2Ha, 2Hb), 7.26 (br. s., 1Ha, 1Hb), 7.03 (br. s., 1Ha, 1Hb), 6.27 (br. s, 1Hb), 5.68 (br. s., 1Ha), 4.62 (d, J = 6.3 Hz, 2Ha, 2Hb), 1.83 (br. m , J = 1Ha, 1Hb), 0.88 (br. s, 2Ha, 2Hb), 0.62 (br. s., 2Ha, 2Hb). ^{13}C NMR (151 MHz, DMSO-d_6) δ 162.31, 160.57, 154.96, 153.26, 152.47, 147.47, 146.69, 145.20, 133.35, 133.21, 132.14, 127.99, 127.97, 127.93, 127.72, 122.89, 119.04, 109.03, 105.82, 95.14, 44.08, 44.05, 9.37, 7.70, 6.83.

4-(((4-((5-cyclopropyl-1H-pyrazol-3-yl)amino)thieno[3,2-d]pyrimidin-2-yl)amino)methyl)phenol (105)
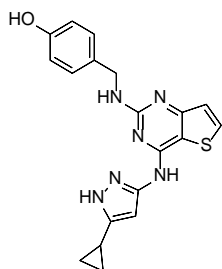
In a 25 ml round flask with a stir bar, intermediate **116** (220 mg, 0.357 mmol) and KHF$_2$ (69.70 mg, 0.892 mmol) were stirred in anhydrous MeOH (3.57 ml) at room temperature overnight. TLC analysis in CH$_2$Cl$_2$/MeOH 9.5/0.5 and UPLC-MS analysis revealed the presence of the desired deprotected product **105**. Evaporation of the reaction solvent in vacuo gave the corresponding crude product, which was directly purified by normal-flash column chromatography by employing a 12 g gold silica cartridge (-Solvent A: CHCl$_3$ -Solvent B: CH$_2$Cl$_2$/MeOH 9:1 -Detection: 240/260 nm -Gradient: 20-100% of solvent B), a sequential change of the elution phase during the course of the separation into 8:2 EtOH/MeOH, gave, after trituration in CH$_2$Cl$_2$ (10 ml) and 3 h under direct high *vacuum* at 80 °C, 80 mg (60%) of the pure product as a white solid. UPLC-MS generic method: Rt = 1.58 min, MS (ESI) *m/z*: 379.0 [M+H]$^+$, C$_{19}$H$_{19}$N$_6$OS$^+$ [M+H]$^+$ calculated: 379.13. QC analysis: Rt = 2.81 min, UPLC-MS purity (UV at 215 nm): 96%. Both ^{1}H- and ^{13}C-NMR spectra in DMSO-d_6 were consistent with the isolation of two different tautomeric forms a and b in a dynamic

equilibrium. ^{1}H NMR (600 MHz, DMSO-d_6) δ 12.56 (br. s., 1Hb), 12.08 (br. s., 1Ha), 10.23 (br. s, 1Hb), 9.60 (br. s., 1Ha), 9.24 (s, 1Ha, 1Hb), 7.90 (s, 2Ha, 2Hb), 7.53 (br. s., 1Hb), 7.15 (d, J = 7.3 Hz, 1Ha, 1Hb), 7.04 (br. s., 2Ha, 2Hb), 6.69 (d, J = 7.3, 1Ha, 1Hb), 6.34 (br. s., 1Hb), 5.59 (br. s., 1Ha), 4.41 (d, J = 6.1 Hz, 2Ha, 2Hb), 1.84 (m, 1Ha, 1Hb), 0.87 (br. s., 2Ha, 2Hb), 0.64 (br. s., 2Ha, 2Hb). ^{13}C NMR (151 MHz, DMSO-d_6) δ 162.49, 160.61, 156.06, 134.54, 133.28, 128.65, 128.47, 123.18, 114.99, 105.40, 43.92, 7.82.

4-(((4-((5-cyclopropyl-1H-pyrazol-3-yl)amino)thieno[3,2-d]pyrimidin-2-yl)amino)methyl)benzamide (106)
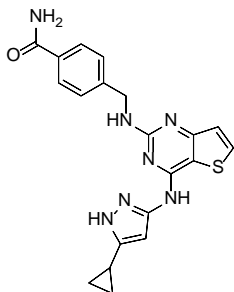
Compound **106** was synthesized adapting the general procedure D starting from 108.24 mg (0.371 mmol) of **75**, 4-(aminomethyl)benzamide, trifluoroacetic salt (**123**) (147 mg, 0.556 mmol), DIPEA (0.151 ml, 0.866 mmol 3.5 eq) dissolved in 1.85 ml of n-butanol and stirred for 8 h. After completion, the reaction mixture was cooled down to room temperature and filtrated under vacuum. A final trituration with EtOH (5 ml x 2) of the obtained solid yielded the pure product as a pale yellow solid (98.3 mg, 65%). UPLC-MS (generic method): Rt = 1.43 min, MS (ESI) m/z: 406.0 [M+H]$^+$, C$_{20}$H$_{20}$N$_7$OS$^+$ [M+H]$^+$ calculated: 406.14. QC analysis: Rt = 2.45 min, UPLC-MS purity (UV at 215 nm): 96%. Both ^{1}H- and ^{13}C-NMR spectra in DMSO-d_6 were consistent with the isolation of two different tautomeric forms a and b in a dynamic equilibrium. ^{1}H NMR (400 MHz, DMSO-d_6) δ 12.57 (br. s., 1Hb), 12.06 (br. s, 1Ha), 10.26 (br. s., 1Hb), 9.61 (br. s., 1Ha), 7.88 (br. s., 2Ha, 2Hb), 7.81 (d, J = 7.3 Hz, 2Ha, 2Hb), 7.4 - 7.03 (m, 5Ha, 5Hb), 6.31 (br. s., 1Ha), 5.66 (br. s., 1Hb), 4.59 (d, J = 6.0 Hz, 2Ha, 2Hb), 1.86 – 1.80 (m, 1Ha, 1Hb), 0.92 – 0.82 (m, 2Ha, 2Hb), 0.63 (br. s, 2Ha, 2Hb). ^{13}C NMR (151 MHz, DMSO-d$_6$) δ 167.77, 162.39, 160.65, 154.86, 147.52, 145.22, 144.68, 143.08, 133.32,

132.45, 132.41, 127.43, 126.81, 126.56, 122.95, 105.59, 95.06, 60.36, 44.04, 13.86, 13.60, 7.81, 7.72, 6.86.

*N*2-(benzo[d][1,3]dioxol-5-ylmethyl)-*N*4-(5-cyclopropyl-1*H*-pyrazol-3-yl)thieno[3,2-d]pyrimidine-2,4-diamine (107)
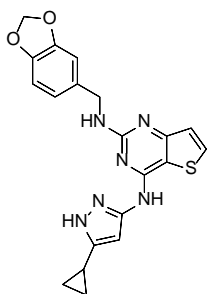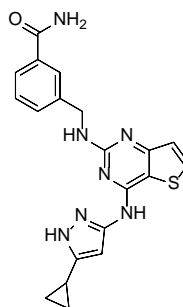

Compound **107** was synthesized following the general procedure D starting from 150 mg (0.369 mmol) of **75**, 1,3-benzodioxole-5-methylamine (**218**) (0.096 ml, 0.771 mmol), DIPEA (0.223 ml, 1.284 mmol) dissolved in 2.6 ml of *n*-butanol and stirred for 6 h. After completion, the reaction mixture was concentrated in vacuo and the resulting crude product was purified by normal phase flash chromatography employing a 12 g gold silica cartridge (-Solvent A: CH_2Cl_2 - Solvent B: CH_2Cl_2/1N NH_3 in MeOH 9:1 -Detection: 240/260 nm -Gradient: 10-30% of solvent B). The isolated fraction was precipitated in CH_2Cl_2 (10 ml) and filtrated under *vacuum* to yield a white solid (83.6 mg, 56%). UPLC-MS (generic method): Rt = 2.00 min, MS (ESI) *m/z*: 407.0 [M+H]$^+$, $C_{20}H_{19}N_6O_2S^+$ [M+H]$^+$ calculated: 407.12. QC analysis: Rt = 3.52 min, UPLC-MS purity (UV at 215 nm): 97%. ^{1}H spectrum in DMSO-d_6 was consistent with the isolation of two different tautomeric forms a and b in a dynamic equilibrium, with a corresponding to the major and b to the minor in abundance. ^{1}H NMR (400 MHz, DMSO-d_6) δ 12.54 (br. s., 1Hb), 12.08 (br. s., 1Ha), 10.24 (br. s., 1Hb), 9.59 (br. s., 1Ha), 7.90 (br. s., 1Ha), 7.59 (br. s., 1Hb), 7.04 – 6.65 (m, 5Ha, 5Hb), 6.35 (br. s., 1Ha), 5.95 (s, 2Ha, 2Hb), 5.67 (br. s., 1Hb), 4.44 (d, *J* = 6.2 Hz, 2Ha, 2Hb), 1.84 (m, 1Ha, 1Hb), 0.88 (br. s., 2Ha, 2Hb), 0.64 (br. s., 2Ha, 2Hb). ^{13}C NMR (151 MHz, DMSO-d_6) δ 162.46, 160.71, 160.26, 154.88, 153.21, 152.43, 147.60, 147.15, 145.73, 145.27, 140.30, 135.21, 134.21, 133.25, 122.94, 120.51, 119.96, 108.00, 107.95, 107.67, 107.61, 100.69, 95.09, 9.39, 7.76, 7.72, 6.88, 6.83.

2-(benzyloxy)-*N*-(5-cyclopropyl-1*H*-pyrazol-3-yl)thieno[3,2-*d*]pyrimidin-4-amine (108)
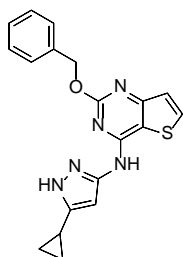
Compound **108** was synthesized starting from intermediate (**75**) (125 mg, 0.428 mmol), according to the general procedure E. The resulting crude product was purified by normal phase flash chromatography employing a 12 g gold silica cartridge (-Solvent A: CH_2Cl_2 Solvent B: CH_2Cl_2/1N NH_3 in MeOH 9:1 -Detection: 240/260 nm -Gradient: 10-20% solvent B to give 79.1 mg of the desired product as a white solid (51%). UPLC-MS (generic method): Rt = 2.14 min, MS (ESI) *m/z*: 364.0 [M+H]$^+$ $C_{19}H_{18}N_5OS^+$ [M+H]$^+$ calculated: 364.11. QC analysis: Rt = 4.12 min, UPLC-MS purity (UV at 215 nm): 99%. ^{1}H NMR (400 MHz, DMSO-*d$_6$*) δ 12.24 (br. s, 1H), 10.04 (br. s., 1H), 8.07 (d, *J* = 5.4 Hz, 1H), 7.46 – 7.29 (m, 5H), 7.23 (d, *J* = 5.4 Hz, 1H), 6.26 (br. s., 1H), 5.39 (s, 2H), 1.99 – 1.87 (m, 1H), 0.92 (d, *J* = 7.2 Hz, 2H), 0.79 – 0.51 (m, 2H). ^{13}C NMR (151 MHz, DMSO-*d$_6$*) δ 162.95, 162.08, 156.52, 146.63, 145.70, 137.43, 135.06, 128.35, 127.71, 127.66, 123.13, 109.48, 96.06, 67.65, 7.76, 6.84.

3-(((4-((5-cyclopropyl-1*H*-pyrazol-3-yl)amino)thieno[3,2-*d*]pyrimidin-2-yl)amino)methyl)benzamide (109)

Compound **109** was synthesized following the general procedure D starting from 80 mg (0.274 mmol) of intermediate **75**, 3-(aminomethyl)benzamide (**219**) (61.72 mg, 0.411 mmol), DIPEA (0.119 ml, 0.685 mmol) dissolved in 1.37 ml of *n*-butanol and stirred for 8 h. After completion, the reaction mixture was concentrated in vacuo and the resulting crude product was purified by normal phase flash chromatography employing a 12 g gold silica cartridge (-Solvent A: CH_2Cl_2 - Solvent B: CH_2Cl_2/MeOH 9:1 -Detection: 240/260 nm -Gradient: 10-60% of solvent

B) followed by a trituration in CH$_2$Cl$_2$ (3 ml x 2) to give 38 mg of the desired product with impurities. A sequential purification employing 4 g gold silica cartridge (-Solvent A: CH$_2$Cl$_2$ Solvent B: CH$_2$Cl$_2$/1N NH$_3$ in MeOH 9:1 -Detection: 240/260 nm - Gradient: 0-50% of solvent B) yielded 27 mg (24%) of the pure product as a white solid. UPLC-MS (generic method): Rt = 1.46 min, MS (ESI) *m/z*: 406.2 [M+H]$^+$, C$_{20}$H$_{20}$N$_7$OS$^+$ [M+H]$^+$ calculated: 406.14. QC analysis: Rt = 2.56 min, UPLC-MS purity (UV at 215 nm): 99%. Both ^{1}H- and ^{13}C-NMR spectra in DMSO-*d*$_6$ were consistent with the isolation of two different tautomeric forms a and b in a dynamic equilibrium. ^{1}H NMR (400 MHz, DMSO-*d*$_6$) δ 12.58 (br. s., 1Hb), 12.06 (br. s., 1Ha), 10.30 (br. s., 1Hb), 9.62 (br. s., 1Ha), 7.93 (s, 1Ha,1Hb), 7.88 (s, 1Ha,1Hb), 7.72 (d, *J* = 7.7 Hz, 1Ha,1Hb), 7.49 (d, *J* = 7.0 Hz, 1Ha,1Hb), 7.37 (t, *J* = 7.4 Hz, 1Ha, 1Hb), 7.31 (br. s., 1Ha, 1Hb), 7.17 (br. s., 1Hb), 7.04 (br. s., 1Ha), 6.32 (br. s., 1Hb), 5.67 (br. s., 1Ha), 4.59 (d, *J* = 6.2 Hz, 2Ha, 2Hb), 1.86 - 1.80 (m, 1Ha, 1Hb), 0.87 (br. s., 2Ha, 2Hb), 0.63 (br. s., 2Ha, 2Hb). ^{13}C NMR (151 MHz, DMSO-*d*$_6$) δ 168.20, 162.45, 160.63, 141.17, 134.28, 133.44, 130.01, 128.17, 126.46, 125.60, 123.21, 105.72, 44.26, 7.85.

_N_4-(5-cyclopropyl-1_H_-pyrazol-3-yl)-_N_2-(pyridin-3-ylmethyl)thieno[3,2-_d_]pyrimidine-2,4-diamine (110)
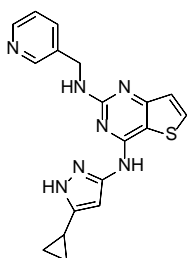
Compound **110** was synthesized following the general procedure D starting from 125 mg (0.539 mmol) of intermediate **75**, 3-picolylamine (**120**) (0.082 ml, 0.809 mmol), DIPEA (0.235 ml, 1.348 mmol) dissolved in 2.7 ml of *n*-butanol and stirred for 8 h. After completion, the reaction mixture was concentrated in vacuo and the resulting crude product was purified by normal phase flash chromatography employing 48 g alumina (Al$_2$O$_3$ pH=7) cartridge (-Solvent A: CHCl$_3$ Solvent B: CHCl$_3$/EtOH 9:1 -Detection: 240/260 nm -Gradient: 5-50% of solvent B). A second purification via normal phase chromatography employing a 4 g gold silica cartridge (-Solvent A:

CH$_2$Cl$_2$ Solvent B: CH$_2$Cl$_2$/MeOH 9:1 in NH$_3$ 1 N - detection: 240/260 nm gradient: 10-40% of solvent B) yielded the pure product which fraction was concentrated under high *vacuum* and lyophilized to yield a white solid (17 mg, 9%). UPLC-MS (generic method): Rt, 1.49 min, MS (ESI) *m/z*: 364.0 [M+H]$^+$, C$_{18}$H$_{18}$N$_7$S $^+$ [M+H]$^+$ calculated: 364.13. QC analysis: Rt = 2.63 min, UPLC-MS purity (UV at 215 nm): 98%. Both ^{1}H- and ^{13}C-NMR spectra in DMSO-d_6 were consistent with the isolation of two different tautomeric forms a and b in a dynamic equilibrium. ^{1}H NMR (400 MHz, DMSO-d_6) δ 12.48 (br. s., 1Hb), 12.11 (br. s., 1Ha), 10.20 (br. s., 1Hb), 9.69 (br. s., 1Ha), 8.57 (br. s. 1Ha, 1Hb), 8.42 (d, *J* = 4.4 Hz, 1Ha, 1Hb), 7.92 (br. s. , 1Ha, 1Hb), 7.74 (d, *J* = 7.6 Hz, 1Ha, 1Hb), 7.32 (dd, *J* = 7.6, 5.2 Hz, 1Ha, 1Hb), 7.25 (br. s., 1Ha, 1Hb), 7.06 (br. s, 1Ha, 1Hb), 6.27 (br. s., 1Ha, 1Hb), 4.55 (d, *J* = 6.2 Hz, 2Ha, 2Hb), 1.84 (m, 1Ha, 1Hb), 1.03 – 0.77 (d, J = 7.12 Hz, 2Ha, 2Hb), 0.64 (br. s. 2Ha, 2Hb). ^{13}C NMR (151 MHz, DMSO-d$_6$) δ 162.34, 160.53, 155.00, 148.79, 147.75, 145.33, 136.49, 134.94, 133.42, 123.40, 122.97, 105.75, 95.20, 42.03, 7.75, 6.88.
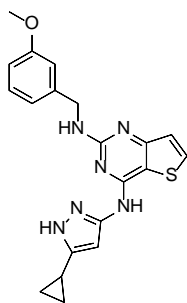
*N*4-(5-cyclopropyl-1H-pyrazol-3-yl)-*N*2-(3-methoxybenzyl)thieno[3,2-*d*]pyrimidine-2,4-diamine (111)

Compound **111** was synthesized following the general procedure D starting from 80 mg (0.274 mmol) of intermediate **75**, 3-methoxybenzylamine (**221**) (0.052 ml, 0.411 mmol), DIPEA (0.119 ml, 0.685 mmol) dissolved in 1.37 ml of *n*-butanol and stirred for 8 h. After completion, the reaction mixture was concentrated in vacuo and the resulting crude product was purified by normal phase flash chromatography employing a 12 g gold silica cartridge (-Solvent A: CHCl$_3$ -Solvent B: CHCl$_3$/MeOH 9:1 -Detection: 240/260 nm -Gradient: 5-20% of solvent B) followed by a final trituration in cold CH$_2$Cl$_2$ (3 ml x 2) to yield the pure product 50 mg (47%) of a white solid. UPLC-MS generic method: Rt = 1.90 min, MS (ESI) *m/z*: 393.1

[M+H]$^+$, C$_{20}$H$_{21}$N$_6$OS$^+$ [M+H]$^+$ calculated: 393.14. QC analysis: Rt = 3.66 min, UPLC-MS purity (UV at 215 nm): 99%. ^{1}H NMR (400 MHz, DMSO-d_6) δ 12.21 (br. s., 1H), 9.74 (br. s., 1H), 7.90 (d, J = 5.3 Hz, 1H), 7.21 (t, J = 8.0 Hz, 1H), 7.05 (d, J = 5.4 Hz, 1H), 6.92 (s, 1H), 6.91 (s, 1H), 6.77 (d, Hz, 1H), 6.12 (br. s., 1H), 4.52 (d, J = 6.2 Hz, 2H), 3.70 (s, 3H), 1.88 - 1.79 (m, 1H), 0.92 - 0.84 (m, 2H), 0.63 (br. s., 2H). ^{13}C NMR (151 MHz, DMSO-d_6) δ 162.42, 160.68, 159.32, 154.42, 142.64, 133.34, 129.30, 123.16, 119.34, 112.87, 111.79, 105.64, 54.97, 44.32, 7.82.
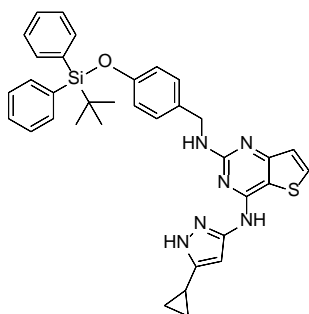
*N*2-(4-((tert-butyldiphenylsilyl)oxy)benzyl)-*N*4-(5-cyclopropyl-1*H*-pyrazol-3-yl)thieno[3,2-*d*]pyrimidine-2,4-diamine (116)

Compound **116** was synthesized following the general procedure D starting from 140.92 mg (0.483 mmol) of intermediate **75**, TBDPS-protected intermediate **127** (262 mg, 0.725 mmol), DIPEA (0.210 ml, 1.2077 mmol) dissolved in 2.41 ml of *n*-butanol and stirred for 6 h. After completion, the reaction mixture was concentrated in vacuo. Purification of the resulting crude by normal phase flash chromatography employing a 12 g gold silica cartridge (-Solvent A: CHCl$_3$ -Solvent B: CHCl$_3$/MeOH 9:1 -Detection: 240/260 nm -Gradient: 0-30% of solvent B), furnished 220 mg (73%) of the pure product as a white solid. UPLC-MS apolar method: Rt, 2.43 min, MS (ESI) *m/z*: 615.4 [M-H]$^-$, C$_{35}$H$_{35}$N$_6$OSSi$^-$ [M-H]$^-$ calculated: 615.2. Both ^{1}H- and ^{13}C-NMR spectra in DMSO-d_6 were consistent with the isolation of two different tautomeric forms a and b in a dynamic equilibrium. ^{1}H NMR (600 MHz, DMSO-d_6) δ 12.55 (br. s., 1H b), 12.05 (br. s., 1Ha), 10.26 (br. s., 1Hb), 9.67 (br. s., 1Ha), 7.87 (br. s., 1Ha, 1Hb), 7.59- 6.63 (m, 4Ha, 4Hb), 7.49 – 7.40 (m, 6Ha, 6Hb), 7.10 (br. s., 1Ha, 1Hb), 7.07 (m, 2Ha, 2Hb) 6.67 (br. s.,1Ha, 1Hb), 6.66 (m, 2Hb, 2Ha) 6.32 (br. s, 1Hb), 5.65 (br. s, 1Ha), 4.40 (d,

J = 6.1 Hz, 2Ha, 2Hb), 1.80 (br. s., 1Ha, 1Hb), 1.03 (m, 9Ha, 9Hb), 0.85 (br. s., 2Ha, 2Hb), 0.62 (br. s., 2Ha, 2Hb).

4-(aminomethyl)benzamide, trifluoroacetic salt (123)
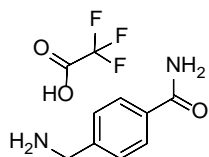
In a round flask, Intermediate **125** (200 mg, 0.799 mmol) was dissolved in 7.7 ml of anhydrous CH_2Cl_2 at 0 °C. Trifluoroacetic acid (0.9 ml, 11.7 mmol) was added dropwise while stirring and the reaction was stirred at room temperature for 1 h. Once completed, 7.7 ml of cold diethyl ether were added to the solution and the resulting white precipitate was filtered under *vacuum* yielding 175.9 mg (83%) of the pure product as a white powder, which was employed in the following step without any further purification. ^{1}H NMR (400 MHz, DMSO-d_6) δ 8.30 (br. s., 3H), 8.01 (br. s., 1H), 7.91 (d, J = 8.3 Hz, 2H), 7.52 (d, J = 8.3 Hz, 2H), 7.41 (br. s, 1H), 4.09 (s, 2H).

tert-butyl (4-carbamoylbenzyl)carbamate (125)
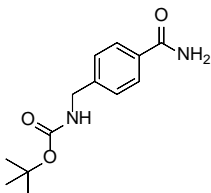
In a 50 ml round flask under Ar, 4-(aminomethyl) benzoic acid) (**124**) (0.2 g, 1.323 mmol) in anhydrous 1,4-dioxane (13.23 ml) were stirred at room temperature. Di-*tert*-butyl dicarbonate (4.33 g, 19.84 mmol) and pyridine (0.534 ml, 6.615 mmol) were added to the suspension followed by addition of ammonium bicarbonate (1.57 g, 19.84 mmol). The resulting mixture heated under MW irradiation at 105 °C for 3 h and once completed concentrated under *vacuum* and purified by normal phase chromatography employing a 24 g gold silica cartridge (-Solvent A: CH_2Cl_2 Solvent B: CH_2Cl_2/ EtOH 9:1 - Detection: 240/280 nm -Gradient: 10-40% of solvent B) yielded the pure product as a white solid (156 mg, 47%). UPLC-MS (generic method): Rt = 1.51 min, MS (ESI) *m/z*: 251.1 [M+H]$^+$, $C_{13}H_{19}N_2O_3^+$ [M+H]$^+$ calculated: 251.13. ^{1}H NMR (400 MHz, DMSO-d_6) δ 7.90 (br. s., 1H), 7.81 (d, J = 8.2 Hz, 2H), 7.42 (t, J = 6.1 Hz, 1H), 7.28 (d, J = 8.2 Hz, 3H), 4.16 (d, J = 6.1 Hz, 2H), 1.39 (s, 9H).

(4-((*tert*-butyldiphenylsilyl)oxy)phenyl)methanamine (127)
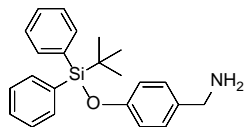
Tert-butyldiphenylsilyl chloride (0.158 ml, 0.609 mmol) was added dropwise to a stirred suspension of 4-hydroxybenzylamine (**126**) (50 mg, 0.406 mmol) in THF (1.624 ml) at room temperature under Ar. Imidazole (55.28 mg, 0.812 mmol) was subsequently added and the reaction mixture was stirred for 10 h. Subsequently, water (5 ml) was added and the resulting mixture was extracted with EtOAc (5 ml x 3). Combined organic layers were dried over anhydrous Na_2SO_4 and concentrated under high vacuum. The crude product was purified by normal phase flash chromatography employing a 12 g gold silica cartridge (-Solvent A: $CHCl_3$ -Solvent B: $CHCl_3$/MeOH 8:2 -Detection: 240/260 nm -Gradient: 10-20% of solvent B) to yield the pure product as a white dense solid (78.2 mg, 58%). UPLC-MS apolar method: Rt, 1.44 min, MS (ESI) *m/z*: 346.1 $[M+H]^+$, $C_{23}H_{28}NOSi^+$ $[M+H]^+$ calculated: 362.18 (no ionization observed).^{1}H NMR (600 MHz, DMSO-d_6) δ 7.69 – 7.65 (m, 4H), 7.63 (br. s., 2H), 7.51 – 7.45 (m, 2H), 7.45 – 7.41 (m, 4H), 7.08 – 7.05 (m, 2H), 6.66 – 6.64 (m, 2H), 4.12 (br. s, 2H), 1.03 (s, 9H).

*N*2-benzyl-*N*4-(5-cyclopropyl-1*H*-pyrazol-3-yl)furo[3,2-*d*]pyrimidine-2,4-diamine (131)
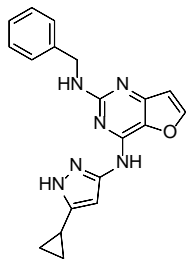
Compound **131** was synthesized following the general procedure D starting from 70 mg (0.254 mmol) of intermediate **151**, **76** (0.042 ml, 0.380 mmol), DIPEA (0.111 ml, 0.635 mmol) dissolved in *n*-butanol (1.3 ml) and stirred for 8 h. After completion, the reaction mixture was concentrated in vacuo and the resulting crude product was purified by normal phase flash chromatography employing 24 g alumina (Al_2O_3 pH=7) cartridge (-Solvent A: CH_2Cl_2 -Solvent B: CH_2Cl_2/MeOH 9:1 -

Detection: 240/260 nm -Gradient: 0-30% of solvent B) followed by a final trituration in cold CH_2Cl_2 (5 ml), furnished the pure product, which fraction was concentrated under high *vacuum* and lyophilized to yield 31.1 mg (35%) of a white solid. UPLC-MS (generic method): Rt = 1.75 min, MS (ESI) *m/z*: 347.0 [M+H]$^+$, $C_{19}H_{19}N_6O^+$ [M+H]$^+$ calculated: 347.15. QC analysis: Rt = 3.47 min, UPLC-MS purity (UV at 215 nm): 99%. Both ^{1}H- and ^{13}C-NMR spectra in DMSO-d_6 were consistent with the isolation of two different tautomeric forms a and b in a dynamic equilibrium. ^{1}H NMR (400 MHz, DMSO-d_6) δ 12.45 (br. s., 1Hb), 11.98 (br. s. , 1Ha), 10.48 (br. s., 1Hb), 9.65 (br. s, 1Ha), 8.01 (br. s., 1Ha, 1Hb), 7.35 – 7.19 (m, 5Ha, 5Hb), 7.07 (br. s., 1Ha, 1Hb), 6.68 (br. s., 1Ha, 1Hb), 6.35 (br. s, 1Ha), 5.68 (br. s, 1Hb), 4.51 (d, *J* = 6.0 Hz, 2Ha, 2Hb), 1.85-1.79 (m, 1Ha, 1Hb), 0.86 (d, *J* = 6.3 Hz, 2Ha, 2Hb), 0.62 (br. s., 2Ha, 2Hb). ^{13}C NMR (101 MHz, DMSO-d_6) δ 159.41, 151.74, 149.39, 144.78, 140.99, 128.76, 128.19, 127.07, 126.44, 106.87, 44.62, 7.73.
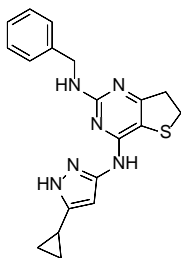
*N*2-benzyl-*N*4-(5-cyclopropyl-1*H*-pyrazol-3-yl)-6,7-dihydrothieno[3,2-*d*]pyrimidine-2,4-diamine (132)

Compound **132** was synthesized following the general procedure D starting from 125 mg (0.425 mmol) of **152**, **76** (0.069 ml, 0.637mmol), DIPEA (0.184 ml, 1.062 mmol) dissolved in 2.12 ml of *n*-butanol and stirred for 6 h. Purification by normal phase flash chromatography employing a 12 g gold silica cartridge (-Solvent A: CH_2Cl_2 -Solvent B: CH_2Cl_2/EtOH 9:1 -Detection: 240/260 nm - Gradient: 0-40% of solvent B) and a final trituration by diethyl ether (7 ml) yielded the desired product as a white powder (77.1 mg, 50%). UPLC-MS (generic method): Rt = 1.87 min, MS (ESI) *m/z*: 365.0 [M+H]$^+$). $C_{19}H_{21}N_6S^+$ [M+H]$^+$ calculated: 365.15. QC analysis: Rt = 3.85 min, UPLC-MS purity (UV at 215 nm): 99%. ^{1}H spectrum in

DMSO-d_6 was consistent with the isolation of two different tautomeric forms a and b in a dynamic equilibrium, with a corresponding to the major and b to the minor in abundance. ^{1}H NMR (400 MHz, DMSO-d_6) δ 12.32 (br. s., 1Hb), 11.94 (br. s., 1Ha), 9.27 (br. s., 1Hb), 8.31 (br. s., 1Ha), 7.30 (d, J = 4.20 Hz, 4Ha, 4Hb), 7.20 (m, 1Hb, 1Ha), 5.88 (br. s, 1Hb, 1Ha), 4.47 (d, J = 6.4 Hz, 2Ha, 2Hb), 3.22 (t, J = 7.3 Hz, 2Ha, 2Hb), 3.00 (t, J = 7.3 Hz, 2Ha, 2Hb), 1.78 (m, 1Ha, 1Hb), 0.83 (d, J = 5.7 Hz, 2Ha, 2Hb), 0.56 (br. s., 2Ha, 2Hb). ^{13}C NMR (151 MHz, DMSO-d$_6$) δ 168.90, 160.67, 153.81, 147.66, 145.16, 140.73, 128.14, 126.93, 126.41, 126.11, 101.50, 94.12, 44.29, 36.85, 29.13, 7.57.

2-bromo-4-chlorobenzenethiol (135)
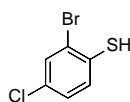
To a suspension of 2-bromo-4-chloroaniline (**134**) (1 g, 4.84 mmol) in water (3.38 ml) at 0 °C a 6M solution of HCl (2.00 ml) was added. A solution of sodium nitrite (400.89 mg, 5.81 mmol) in water (1.45 ml) was then added dropwise and the reaction mixture was stirred at 0 °C for 45 min. The diazonium salt prepared was thus transferred via pipette over 5-10 min to a solution of potassium ethyl xanthogenate (1.4 g, 8.23 mmol) in water (2.38 ml) at 75 °C. The stirring was maintained at the same temperature for 1 h. After cooling to room temperature, the aqueous phase was extracted with Et$_2$O (20 ml x 3). The organic layer was washed with saturated NaHCO$_3$ (20 ml), with water (20 ml) and concentrated in vacuo. The red oil thus obtained was added to a hot solution of KOH (1.4 mg, 24.22 mmol) in water (0.65 ml) and EtOH (5.88 ml) and refluxed for 21 h. Then, the reaction was cooled down to room temperature, water (5 ml) was added and the mixture was acidified to pH=2 with HCl conc. The aqueous phase was extracted three times with EtOAc (20 ml), and the combined organic layers were dried over Na$_2$SO$_4$, filtrated and concentrated in vacuo to obtain the 650 mg (60%) of the desired product **135**, which was used in the following step without any further purification. UPLC-MS (generic

method): Rt = 2.45 min, MS (ESI) m/z: 220.8/222.8./224.7 [M-H]⁻,C_6H_3BrClS [M-H]⁻ calculated: 222.89. ¹H NMR (400 MHz, CDCl₃) δ 7.55 (d, *J* = 2.2 Hz, 1H), 7.28 (d, *J* = 8.4 Hz, 1H), 7.16 (dd, *J* = 8.5, 2.2 Hz, 1H), 3.98 (s, 1H).

(2-bromo-4-chlorophenyl)(2,2-dimethoxyethyl)sulfane (137)
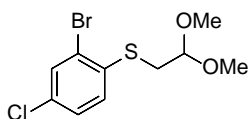
In a 25 ml round bottom flask, 2-bromo-4-chlorobenzenethiol (**135**) (650 mg, 2.91 mmol), 1-dimethoxyethane (**136**) (0.344 ml, 2.91 mmol) were dissolved in anhydrous DMF (4.2 ml) at room temperature and treated with K₂CO₃ (602.59 mg, 4.36 mmol) at the same temperature. The reaction mixture was gradually heated up to 70 °C and stirred at the same temperature for 3 h. The mixture was diluted with iced water and the aqueous layer was extracted with diethyl ether (15 ml x 3) and the combined organic phase was washed with water (15 ml), brine (15 ml), dried over Na₂SO₄ filtrated and concentrated in vacuo. The residue obtained was purified by flash chromatography (-Solvent A: Cyclohexane -Solvent B: EtOAc -Gradient 5-10% of solvent B - Detection 254/210 nm) giving the desired product 666.2 mg (74%) which was employed in the next step without any further purification. UPLC-MS (generic method): Rt = 1.67 min, no ionization was observed in the UPLC-MS chromatogram. ¹H NMR (400 MHz, CDCl₃) δ 7.57 (d, *J* = 2.2 Hz, 1H), 7.29 (d, *J* = 8.5 Hz, 1H), 7.25 (dd, *J* = 3.0 Hz, 2.2 Hz, 1H), 4.57 (t, *J* = 5.5 Hz, 1H), 3.38 (s, 6H), 3.11 (d, *J* = 5.5 Hz, 2H).

7-bromo-5-chlorobenzo[*b*]thiophene (138)
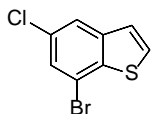
In a two neck flame dried 25 ml round flask, polyphosphoric acid (7.221 g, 0.021 mol) was previously weighted, the viscous oil **137** (0.666 g, 0.002 mol) was dissolved in 6.47 ml of chlorobenzene and added at room temperature. The reaction mixture obtained was refluxed overnight under Ar

atmosphere. After complete conversion, it was cooled down to room temperature, diluted with water (10 ml) and extracted with toluene (10 ml x 3). The combined organic phase was washed with water (20 ml), saturated Na_2CO_3 (20 ml), brine (20 ml), dried over anhydrous Na_2SO_4 and filtered. The solution was concentrated in vacuo giving 519 mg (98%) the desired intermediate **138**, which was employed 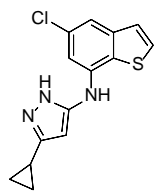in the next step without any further purification. UPLC-MS (apolar method): Rt. 1.98 min, no ionization was observed in the UPLC-MS chromatogram. ^{1}H NMR (400 MHz, CDCl$_3$) δ 7.76 (d, J = 2.2 Hz, 1H), 7.57 (d, J = 5.7 Hz, 1H), 7.50 (d, J = 2.2 Hz, 1H), 7.37 (d, J = 5.7 Hz, 1H).

_N_-(5-chlorobenzo[_b_]thiophen-7-yl)-3-cyclopropyl-1_H_-pyrazol-5-amine (139)

To a dried MW vial 3-cyclopropyl-1_H_-pyrazol-5-amine (**74**) (29.80 mg, 0.242 mmol), 7-bromo-5-chlorobenzo[_b_]thiophene **138** (50 mg, 0.202 mmol), Pd$_2$(dba)$_3$ (18.50 mg, 0.0202 mmol), BINAP (25.15 mg, 0.0404 mmol), and Cs$_2$CO$_3$ (98.72 mg, 0.303 mmol) were add. The flask was degassed and backfilled with Ar followed by addition of previously degassed anhydrous toluene (0.34 ml) and the mixture was heated to 150 °C for 10 h under MW irradiation. After complete conversion, the reaction was diluited with EtOAc (20 ml), washed with water (10 ml), brine (10 ml) and concentrated under _vacuum_. The crude product was purified by flash chromatography (-Solvent A: Cyclohexane -Solvent B: EtOAc -Gradient: 0-10% of solvent B -Detection: 254/210 nm) giving the desired product **139** (13.6 mg, 23%) as a red oil. UPLC-MS (apolar method): Rt. 1.12 min, MS (ESI) m/z: 289.8/291.8 [M+H]$^+$, C$_{14}$H$_{13}$ClN$_3$S$^+$ [M+H]$^+$ calculated: 290.01/292.01. ^{1}H NMR (400 MHz, DMSO-_d$_6$_) δ 11.92 (s, 1H), 8.36 (s, 1H), 7.88 (s, 1H), 7.77 (d, J = 5.4 Hz, 1H), 7.36 (d, J = 5.4 Hz, 1H), 7.34 (d, J = 1.8 Hz, 1H), 5.71 (s, 1H), 1.88 (m, 1H), 0.92 (dq, J = 8.8, 2.2 Hz, 2H), 0.68 (dq, J = 5.0, 2.2 Hz, 2H).

2-(benzyloxy)-*N*-(5-cyclobutyl-1*H*-pyrazol-3-yl)thieno[3,2-*d*]pyrimidin-4-amine (141)
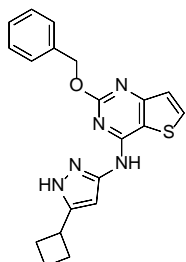
Compound **141** was synthesized starting from intermediate **98** (80 mg, 0.262 mmol) and sodium benzyloxide (**122**) (1 M sol., 0.288 ml) according to the general procedure E. The resulting crude product was purified by normal phase flash chromatography employing a 12 g gold silica cartridge (-Solvent A: CH_2Cl_2 Solvent B: CH_2Cl_2/1N NH_3 in MeOH 9:1 -Detection: 240/260 nm -Gradient: 10-50% of solvent B) to give 44.3 mg of the desired product (45%). UPLC-MS (generic method): Rt = 2.09 min, MS (ESI) *m/z*: 378.0 $[M+H]^+$ $C_{20}H_{20}N_5OS^+$ $[M+H]^+$ calculated: 378.13. QC analysis: Rt = 4.53 min, UPLC-MS purity (UV at 215 nm): 98%. ^1H NMR (400 MHz, DMSO-d_6) δ 12.29 (s, 1H), 10.08 (s, 1H), 8.07 (d, *J* = 5.4 Hz, 1H), 7.45 (d, *J* = 7.5 Hz, 2H), 7.37 (t, *J* = 7.1 Hz, 2H), 7.35 – 7.27 (m, 1H), 7.24 (d, *J* = 5.4 Hz, 1H), 6.40 (s, 1H), 5.41 (s, 2H), 3.54 - 3.43 (m, 1H), 2.28 (qt, *J* = 8.3, 2.9 Hz, 2H), 2.12 (pd, *J* = 9.1, 2.6 Hz, 2H), 2.00-1.78 (m, 2H). ^{13}C NMR (151 MHz, DMSO-d_6) δ 163.06, 162.14, 156.57, 137.51, 135.12, 128.44, 127.76, 123.25, 67.75, 29.06, 18.19.

2-(benzyloxy)-*N*-(5-isopropyl-1*H*-pyrazol-3-yl)thieno[3,2-*d*]pyrimidin-4-amine (142)
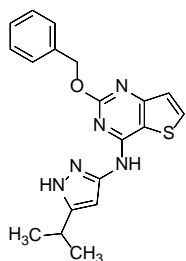
Compound **142** was synthesized starting from intermediate **97** (80 mg, 0.272 mmol), and sodium benzyloxide (**122**) 1 M solution (0.408 ml) according to the general procedure E. The resulting crude product was purified by normal phase flash chromatography employing a 12 g gold silica cartridge (-Solvent A: CH_2Cl_2 Solvent B: CH_2Cl_2/1N NH_3 in MeOH 9.9:0.1 -Detection: 240/260 nm -Gradient: 60-100% of solvent B. A sequential trituration in CH_2Cl_2 (5 ml x 2) furnished 43 mg of the desired

product (43%). UPLC-MS generic method: Rt = 2.18 min, MS (ESI) *m/z*: 366.1 [M+H]$^+$ $C_{19}H_{20}N_5OS^+$ [M+H]$^+$ calculated: 366.13. QC analysis: Rt = 4.34 min, UPLC-MS purity (UV at 215 nm): 99.5%. ^{1}H NMR (400 MHz, DMSO-*d*$_6$) δ 12.26 (br.s., 1H), 10.07 (br. S., 1H), 8.07 (d, *J* = 5.4 Hz, 1H), 7.45 (d, *J* = 6.9 Hz, 2H), 7.37 (t, *J* = 7.4 Hz, 2H), 7.32 (d, *J* = 7.2 Hz, 1H), 7.23 (d, *J* = 5.4 Hz, 1H), 6.36 (s. 1H), 5.41 (s, 2H), 2.95 (m, 1H), 1.22 (d, *J* = 7.0 Hz, 6H). ^{13}C NMR (151 MHz, DMSO-*d*$_6$) δ 163.01, 162.10, 156.56, 149.67, 146.41, 137.47, 135.06, 128.39, 127.73, 127.69, 123.19, 109.53, 96.15, 67.68, 25.52, 22.35.

*N*4-(5-cyclobutyl-1*H*-pyrazol-3-yl)-*N*2-(pyridin-3-ylmethyl)thieno[3,2-*d*]pyrimidine-2,4-diamine (143)
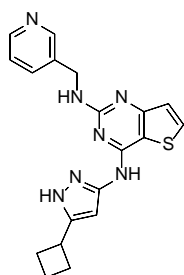
Compound **143** was synthesized following the general procedure D starting from 100 mg (0.327 mmol) of intermediate **98**, 3-picolylamine (**120**) (0.050 ml, 0.490 mmol), DIPEA (0.142 ml, 0.817 mmol) dissolved in 1.6 ml of *n*-butanol and stirred for 8 h. After completion, the reaction mixture was concentrated in vacuo and the resulting crude product was purified by normal phase flash chromatography employing a 4 g gold silica cartridge (-Solvent A: CH_2Cl_2 -Solvent B: CH_2Cl_2/MeOH 8:2 -Detection: 240/260 nm -Gradient: 10-20% of solvent B) followed by a final trituration in cold CH_2Cl_2 (3 ml x 2) adding few drops of cyclohexane, giving the pure product, which fraction was concentrated under high *vacuum* and lyophilized to yield 18 mg (15%) of a white solid. UPLC-MS (generic method): Rt = 1.60 min, MS (ESI) *m/z*: 378.1 [M+H]$^+$, $C_{19}H_{20}N_7S^+$ [M+H]$^+$ calculated: 378.15. QC analysis: Rt = 2.97 min, UPLC-MS purity (UV at 215 nm): 99.5% ^{1}H NMR (600 MHz, DMSO-*d*$_6$) δ 12.11 (br. s., 1H), 9.70 (br. s., 1H), 8.57 (s, 1H), 8.41 (d, *J* = 5 Hz, 1H), 7.91 (d, *J* = 3.5 Hz, 1H), 7.74 (d, *J* = 7.2 Hz, 1H), 7.32 (dd, *J* = 7.2, 5.0 Hz, 1H), 7.24 (br. s, 1H), 7.05 (br. s., 1H), 4.56 (d, *J* = 6.2 Hz, 2H), 2.27 - 2.22 (m, 2H), 2.09 (br. s., 2H), 1.99 – 1.87 (m,

2H), 1.81 (br. s., 2H). ^{13}C NMR (151 MHz, DMSO-d_6) δ 162.39, 160.59, 154.94, 148.78, 147.78, 136.45, 134.97, 133.46, 123.44, 123.10, 105.85, 96.08, 42.09, 31.32, 18.19.

3-(((4-((5-cyclobutyl-1*H*-pyrazol-3-yl)amino)thieno[3,2-*d*]pyrimidin-2-yl)amino)methyl)benzamide (144)
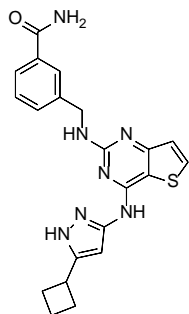
Compound **144** was synthesized following the general procedure D starting from 100 mg (0.327 mmol) of intermediate **98**, 3-(aminomethyl)benzamide (**219**) (73.6 mg, 0.490 mmol), DIPEA (0.142 ml, 0.817 mmol) dissolved in 1.63 ml of *n*-butanol and stirred for 8 h. After completion, the reaction mixture was concentrated in vacuo and the resulting crude product was purified by normal phase flash chromatography. A first purification employing a 12 g gold silica cartridge (-Solvent A: CH$_2$Cl$_2$ -Solvent B: CH$_2$Cl$_2$/MeOH 9:1 -Detection: 240/260 nm -Gradient: 10-60% of solvent B) followed by second purification using a 4 gold silica cartridge (-Solvent A: CH$_2$Cl$_2$ -Solvent B: CH$_2$Cl$_2$/1N NH$_3$ in MeOH 9:1 -Detection: 240/260 nm -Gradient: 10-40% of solvent B) gave the desired product with a minor impurity. Trituration in cold CH$_2$Cl$_2$ (3 ml) and subsequently in water (3 ml) gave 25 mg (18%) of the pure product as a white solid. UPLC-MS (generic method): Rt = 1.61 min, MS (ESI) *m/z*: 420.0 [M+H]$^+$, C$_{21}$H$_{22}$N$_7$OS$^+$ [M+H]$^+$ calculated: 420.15. QC analysis: Rt = 2.86 min, UPLC-MS purity (UV at 215 nm): 99.5%. ^{1}H NMR (400 MHz, DMSO-d_6) δ 12.09 (br. s, 1H), 9.69 (br. s., 1H), 7.91 (d, *J* = 6.55 Hz, 1H), 7.89 (s, 1H), 7.72 (d, *J* = 8.0 Hz, 1H), 7.50 (d, *J* = 7.28 Hz, 1H), 7.38 (t, *J* = 7.5 Hz, 1H), 7.31 (br. s., 1H), 7.05 (br. s., 1H), 6.34 (br. s., 1H), 4.60 (d, *J* = 5.7 Hz, 2H), 2.24 – 1.81 (m, 6H). ^{13}C NMR (151 MHz, DMSO-d_6) δ 167.97, 162.41, 160.71, 141.39, 134.20, 133.32, 129.70, 127.97, 126.26, 125.38, 122.95, 105.60, 44.18, 31.18, 28.99.

2-(benzyloxy)-N-(5-cyclopropyl-1*H*-pyrazol-3-yl)furo[3,2-*d*]pyrimidin-4-amine (145)
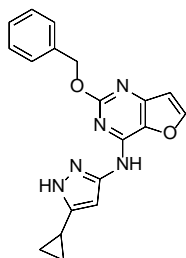
Compound **145** was synthesized starting from intermediate **151** (80 mg, 0.290 mmol) and sodium benzyloxide (**122**) 1 M solution (0.319 ml) according to the general procedure E. The resulting crude product was purified by normal phase flash chromatography employing a 12 g gold silica cartridge (-Solvent A: CH_2Cl_2 Solvent B: CH_2Cl_2/1N NH_3 in MeOH 9:1 -Detection: 240/260 nm -Gradient: 5-20% of solvent B) to give 27 mg of the desired product with impurities. A sequential purification employing 8 g alumina (Al_2O_3 pH=7) cartridge (-Solvent A: CH_2Cl_2 Solvent B: CH_2Cl_2/MeOH 99:1 - detection: 240/260 nm -Gradient: 10-100% of solvent B) yielded 15 mg of the pure product as a white solid (15%). UPLC-MS (generic method): Rt = 1.99 min, MS (ESI) *m/z*: 347.9 [M+H]$^+$ $C_{19}H_{18}N_5O_2^+$ [M+H]$^+$ calculated: 348.13. QC analysis: Rt = 3.85 min, UPLC-MS purity (UV at 215 nm): 96%. ^{1}H NMR (400 MHz, DMSO-*d*$_6$) δ 12.12 (br. s., 1H), 10.13 (br. s, 1H), 8.18 (d, *J* = 1.5 Hz, 1H), 7.44 – 7.29 (m, 5H), 6.87 (d, *J* = 2.0 Hz, 1H), 6.28 (br. s., 1H), 5.35 (s, 2H), 1.89 (dq, 1H), 0.91 (qd, *J* = 4.1, 2.0 Hz, 2H), 0.66 (qd, *J* = 4.1, 2.0 Hz, 2H). ^{13}C NMR (151 MHz, DMSO-*d*$_6$) δ 160.96, 151.73, 150.66, 146.32, 137.49, 130.68, 128.41, 127.73, 127.71, 107.22, 94.51, 67.99, 7.77.

N4-(5-cyclopropyl-1*H*-pyrazol-3-yl)-*N*2-(pyridin-3-ylmethyl)furo[3,2-*d*]pyrimidine-2,4-diamine (146)

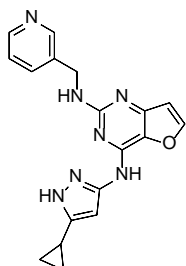Compound **142** was synthesized following the general procedure D starting from 100 mg (0.363 mmol) of intermediate **151**, 3-picolylamine (**120**) (0.055 ml, 0.544 mmol), DIPEA (0.158 ml, 0.907 mmol) dissolved in 1.81 ml of *n*-butanol and stirred for 8 h. After completion, the reaction mixture was concentrated in vacuo and the resulting crude product was purified by normal phase flash chromatography employing a 12 g gold silica cartridge (-Solvent A: CH_2Cl_2 -Solvent B: CH_2Cl_2/MeOH 9:1 - Detection: 240/260 nm -Gradient: 5-45% of solvent B) followed by a final trituration in cold CH_2Cl_2 (2 ml) and cold MeOH (2 ml) gave the pure product, which fraction was concentrated under high *vacuum* and lyophilized to yield 17 mg (14%) of a pale yellow solid. UPLC-MS (generic method): Rt = 1.41 min, MS (ESI) *m/z*: 348.1 [M+H]$^+$, $C_{18}H_{18}N_7O^+$ [M+H]$^+$ calculated: 348.15. QC analysis: Rt = 2.40 min, UPLC-MS purity (UV at 215 nm): 99% ^{1}H NMR (600 MHz, DMSO-*d*$_6$) δ 12.03 (br. s., 1H), 9.77 (br. s., 1H), 8.55 (s, 1H), 8.42 (d, *J* = 4.3 Hz, 1H), 8.02 (s, 1H), 7.73 (d, *J* = 7.8 Hz, 1H), 7.32 (dd, *J* = 7.7, 5.13 Hz, 1H), 7.19 (br. s., 1H), 6.69 (s, 1H), 6.19 (br. s., 1H), 4.51 (d, *J* = 6.1 Hz, 2H), 1.83 (m, 1H), 0.87 (d, *J* = 7.22 Hz, 2H), 0.62 (br. s, 2H). ^{13}C NMR (151 MHz, DMSO-*d*$_6$) δ 159.24, 151.70, 149.48, 148.77, 147.79, 144.78, 136.38, 134.97, 128.88, 123.44, 106.88, 93.58, 42.35, 7.75.

N4-(5-cyclobutyl-1H-pyrazol-3-yl)-N2-(pyridin-3-ylmethyl)furo[3,2-d]pyrimidine-2,4-diamine (147)
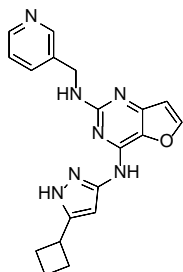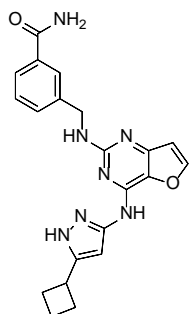
Compound **147** was synthesized following the general procedure D starting from 100 mg (0.345 mmol) of intermediate **153**, 3-picolylamine (**120**) (0.053 ml, 0.518 mmol), DIPEA (0.150 ml, 0.863 mmol) dissolved in 1.73 ml of *n*-butanol and stirred for 10 h. After completion, the reaction mixture was concentrated in vacuo and the resulting crude product was purified by normal phase flash chromatography employing a 12 g gold silica cartridge (-Solvent A: CH_2Cl_2 -Solvent B: CH_2Cl_2/1N NH_3 in MeOH 9:1 -Detection: 240/260 nm -Gradient: 10-30% of solvent B) followed by a final trituration in cold CH_2Cl_2 (3 ml x 2) to furnish the pure product 31 mg (25%) of a pale yellow solid. UPLC-MS (generic method): Rt = 1.57 min, MS (ESI) *m/z*: 362.0 $[M+H]^+$, $C_{19}H_{20}N_7O^+$ $[M+H]^+$ calculated: 362.16. QC analysis: Rt = 2.78 min, UPLC-MS purity (UV at 215 nm): 99.5%. Both ^{1}H- and ^{13}C-NMR spectra in DMSO-d_6 were consistent with the isolation of two different tautomeric forms a and b in a dynamic equilibrium. ^{1}H NMR (600 MHz, DMSO-d_6) δ 12.50 (br. s., 1Hb), 12.00 (br. s, 1Ha), 10.53 (br. s., 1Hb), 9.71 (br. s., 1Ha), 8.56 (s, 1Ha, 1Hb), 8.41 (d, *J* = 7.4 Hz, 1Ha, 1Hb), 8.02 (br. s., 1Ha, 1Hb), 7.73 (d, *J* = 7.8 Hz, 1Ha, 1Hb), 7.32 (t, *J* = 6.3 Hz, 1Ha, 1Hb), 7.13 (br. s, 1Ha, 1Hb), 6.68 (s, 1Ha,1Hb), 6.50 (br. s., 1Hb), 5.80 (br. s., 1Ha), 4.53 (d, *J* = 6.4 Hz, 2Ha, 2Hb), 3.43 (m,1Ha, 1Hb) 2.27 - 2.21 (m, 2Ha, 2Hb), 2.09 (br. s., 2Ha, 2Hb), 1.97 - 1.89 (m, 1Ha, 1Hb), 1.84 - 1.79 (m, 1Ha, 1Hb). ^{13}C NMR (151 MHz, DMSO-d_6) δ 159.29, 149.41, 148.77, 148.71, 147.76, 147.70, 147.67, 136.53, 134.82, 128.97, 123.34, 106.85, 106.79, 94.96, 42.34, 28.97, 18.13.

3-(((4-((5-cyclobutyl-1*H*-pyrazol-3-yl)amino)furo[3,2-*d*]pyrimidin-2-yl)amino)methyl)benzamide (148)

Compound **148** was synthesized following the general procedure D starting from 100 mg (0.345 mmol) of intermediate **153**, 3-(aminomethyl)benzamide (**219**) (77.79 mg, 0.518 mmol), DIPEA (0.150 ml, 0.863 mmol) dissolved in 1.73 ml of *n*-butanol and stirred for 8 h. After good conversion of the starting material into the desired product, the reaction mixture was concentrated in vacuo. The resulting crude was purified by normal phase flash chromatography employing a 12 g gold silica cartridge (-Solvent A: CH_2Cl_2 -Solvent B: CH_2Cl_2/MeOH 9:1 - Detection: 240/260 nm -Gradient: 10-40% of solvent B) followed by a first trituration in cold CH_2Cl_2 (2 ml), and a sequential trituration in distillated water (2 ml) to furnish, after freeze drying, 18.5 mg (13%) of the pure product as a pale yellow powder. UPLC-MS (generic method): Rt = 1.54 min, MS (ESI) *m/z*: 402.2 [M-H]$^-$, $C_{21}H_{20}N_7O_2^-$ [M-H]$^-$ calculated: 402.17.14. QC analysis: Rt = 2.71 min, UPLC-MS purity (UV at 215 nm): 99.5%. ^{1}H NMR (400 MHz, DMSO-d_6) δ 12.03 (br. s., 1H), 9.85 (br. s, 1H), 8.03 (br. s., 1H), 7.93 (br. s., 1H), 7.88 (s, 1H), 7.82 (br. s. 1H), 7.72 (d, *J* = 7.5 Hz, 1H), 7.48 (d, *J* = 7.5 Hz, 1H), 7.37 (t, *J* = 7.5 Hz, 1H), 7.31 (br. s., 1H), 6.69 (s, 1H), 6.43 (br. s., 1H), 4.57 (d, *J* = 6.0 Hz, 2H), 2.28-2.17 (m, 2H), 2.07 (br. s., 2H), 1.97 - 1.88 (m, 1H), 1.80 (br. s., 1H). ^{13}C NMR (151 MHz, DMSO-d_6) δ 168.10, 159.16, 151.30, 149.52, 145.05, 141.21, 134.25, 129.82, 128.07, 126.30, 125.50, 106.72, 44.56, 29.04, 18.21.

2-chloro-*N*-(5-cyclopropyl-1*H*-pyrazol-3-yl)furo[3,2-*d*]pyrimidin-4-amine (151)
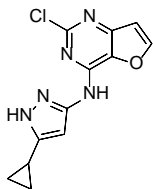
Intermediate **151** was obtained starting from 2,4-dichlorofuro[3,2-*d*]pyrimidine (**149**) 150 mg (0.794 mmol) and 243.86 mg (1.98 mmol) of 3-cyclopropyl-1*H*-pyrazol-5-amine in presence of triethylamine (0.243 ml, 1.75 mmol) and 2.65 ml of 2-propanol at room temperature under Ar for 3 days according to the general procedure B. Precipitation in water (10 ml) afforded intermediate x as a bright yellow powder (170 mg, 81%). UPLC-MS (generic method): Rt = 1.57 min, MS (ESI) *m/z*: 276/278 [M+H]$^+$, C$_{12}$H$_{11}$ClN$_5$O $^+$ [M+H]$^+$ calculated: 276.05/278.05. ^{1}H NMR (400 MHz, DMSO-*d$_6$*) δ 12.23 (s, 1H), 10.57 (s, 1H), 8.33 (d, *J* = 2.0 Hz, 1H), 7.00 (d, *J* = 2.0 Hz, 1H), 6.29 (s, 1H), 1.96 - 1.89 (m, 1H), 0.94 (dq, *J* = 4.5, 1.7 Hz, 2H), 0.70 (dq, *J* = 4.5, 1.7 Hz, 2H). ^{13}C NMR (101 MHz, DMSO-*d$_6$*) δ 153.18, 152.17, 151.60, 146.29, 132.55, 107.21, 94.83, 7.73, 7.53, 6.87.

2-chloro-*N*-(5-cyclopropyl-1*H*-pyrazol-3-yl)-6,7-dihydrothieno[3,2-*d*]pyrimidin-4-amine (152)
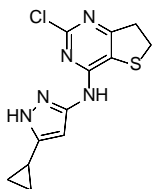
Compound **152** was synthesized following the general procedure B using 2,4-dichloro-6,7-dihydrothieno[3,2-*d*]pyrimidine (**150**) 0.200 g (0.966 mmol) and 0.297 g (2.415 mmol) of 3-cyclopropyl-1*H*-pyrazol-5-amine in presence of triethylamine (0.296 ml, 2.125 mmol) and 3.22 ml of anhydrous 2-propanol at 80 °C under Ar, for 3 days. Precipitation in water (10 ml) afforded intermediate **152** as a white powder (145.8 mg, 52%). UPLC-MS (generic method): Rt = 1.65 min, MS (ESI) *m/z*: 294.0 [M+H]$^+$, C$_{12}$H$_{13}$ClN$_5$S$^+$ [M+H]$^+$ calculated: 294.05. ^{1}H NMR (400 MHz, DMSO-*d$_6$*) δ 12.21 (s, 1H), 9.45 (s, 1H), 6.10 (s, 1H), 3.17 (t, *J* = 8.7, 7.1 Hz, 2H), 1.88 (m, 1H), 0.92 (d, *J* = 7.24 Hz, 2H), 0.68 (m, 2H).

2-chloro-*N*-(5-cyclobutyl-1*H*-pyrazol-3-yl)furo[3,2-*d*]pyrimidin-4-amine (153)
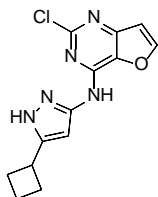
Intermediate **153** was obtained starting from 2,4-dichlorofuro[3,2-*d*]pyrimidine (**149**) 200 mg (1.058 mmol) and 362.9 mg (2.645 mmol) of 3-amino-5-cyclobutyl-1*H*-pyrazole (**92**) in presence of triethylamine (0.324 ml, 2.328 mmol) and 3.53 ml of 2-propanol at room temperature under inert atmosphere, for 3 days according to the general procedure B. Precipitation in water (10 ml) afforded intermediate x as a yellow powder (235.6 mg, 77%). The product was employed in the next steps without any further purification UPLC-MS: Rt = 1.87 min, MS (ESI) *m/z*: 290.0/291.9 [M+H]$^+$, C$_{13}$H$_{13}$ClN$_5$O$^+$ [M+H]$^+$ calculated: 290.07/292.07. ^{1}H NMR (400 MHz, DMSO-*d$_6$*) δ 12.29 (s, 1H), 10.61 (s, 1H), 8.32 (d, *J* = 2.2 Hz, 1H), 7.00 (d, *J* = 2.2 Hz, 1H), 6.44 (s, 1H), 3.62 – 3.43 (m, 1H), 2.34 – 2.26 (m, 2H), 2.19 – 2.20 (m, 2H), 2.02– 2.91 (m, 1H), 1.89 – 1.80 (m, 1H).

4-((3-cyclobutyl-1*H*-pyrazol-5-yl)amino)furo[3,2-*d*]pyrimidin-2-ol (157)
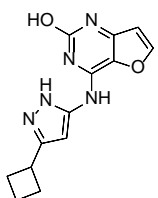
To a pressure tube charged with intermediate **153** (100 mg, 0.345 mmol) 3.00 ml of AcOH were added. The reaction mixture was heated at 120 °C and stirred for two days. The reaction was then quenched with the addition of saturated NaHCO$_3$ solution and the aqueous phase was extracted with CH$_2$Cl$_2$/MeOH 8:2 mixture. The organic layer was separated, washed with brine, dried over Na$_2$SO$_4$ and the volatiles were removed in vacuo. The obtained crude residue was subjected to column chromatography separation (-Solvent A: CH$_2$Cl$_2$ -Solvent B: CH$_2$Cl$_2$/MeOH 9:1 -Detection: 254/210 nm -Gradient: 0-100% of solvent B) to give the pure product 61.21 mg (65%) as an off-yellow solid. UPLC-MS (generic method): Rt = 1.33 min, MS (ESI) *m/z*: 272.0 [M+H]$^+$, C$_{13}$H$_{14}$N$_5$O$_2$$^+$ [M+H]$^+$ calculated: 272.11. ^{1}H NMR (400 MHz, DMSO-*d$_6$*) δ 7.72 (s, 1H), 6.34 (s, 1H), 5.80

(br. s., 1H), 2.32 – 2.19 (m, 2H), 2.21 – 2.03 (m, 2H), 2.03 – 1.89 (m, 1H), 1.91 – 1.77 (m, 1H), 1.56 (s, 1H).

4-(5-((2-((cyclopropylmethyl)amino)thieno[3,2-*d*]pyrimidin-4-yl)amino)-1*H*-pyrazol-3-yl)benzamide (159)
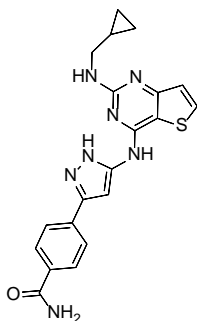
The salt **178** (0.016 g, 39 µmol) suspension in MeOH/ACN 1:0.5 (2 ml) was gently heated at 40 °C to aid solubility, and purified by a cation exchange column SCX previously packed with MeOH. Once adsorbed to the resin, the product was eluted with 1N NH₃ in MeOH obtaining the free base of the desired product 7 mg (5%) UPLC-MS (generic method): Rt = 1.65 min, MS (ESI) *m/z*: 404.1 [M-H]⁻, $C_{20}H_{18}N_7OS^-$ [M-H]⁻ calculated: 404.13. QC analysis: Rt = 2.85 min, UPLC-MS purity (UV at 215 nm): 95%. ¹H NMR (400 MHz, DMSO-*d₆*) δ 13.16 (br. d, 1H), 10.34 (br. d, 1H), 8.01 – 7.96 (m, 2H), 7.96 – 7.86 (m, 4H), 7.82 (d, *J* = 8.3 Hz, 1H), 7.38 (br. s., 1H), 7.12 (br. s., 1H), 6.43 (br. s., 1H), 3.22 (t, *J* = 6.0 Hz, 2H), 1.12 (br. s., 1H), 0.47 (br. d., 2H), 0.26 (q, *J* = 4.8 Hz, 2H). ¹³C NMR (151 MHz, DMSO-*d₆*) δ 167.48, 141.78, 133.58, 124.60, 54.93, 45.49, 10.95, 3.39.

2-chlorothieno[3,2-*d*]pyrimidin-4(3*H*)-one (172)
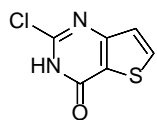
2,4-dichlorothieno[3,2-*d*]pyrimidine (**73**) (1 g, 5 mmol) was dissolved in a mixture of anhydrous tetrahydrofuran (8 ml) and water (2 ml), sodium hydroxide 6M solution (2 ml, 10 mmol) was added dropwise to the reaction mixture, which was heated up to 50 °C and stirred for overnight. The reaction was monitored by TLC in CH₂Cl₂/MeOH 9.5:0.5, noticing complete conversion of the starting material. Thus, the temperature was cooled down to 35 °C and AcOH (0.6 ml, 10 mmol) was added dropwise and stirred for 2 h. After 2 h, it was quenched with water (10 ml) and extracted three times with EtOAc (30 ml), washed

with brine and dried over Na$_2$SO$_4$. The resulting organic layer was concentrated under *vacuum* to obtain 2-chlorothieno[3,2-*d*]pyrimidin-4(3*H*)-one **172** (0.9 g, 99%), which was used in the next step without any further purification. UPLC-MS (generic method): Rt = 1.04 min, MS (ESI) *m/z*: 186.8/188.7 [M+H]$^+$, C$_6$H$_4$ClN$_2$OS$^+$ [M+H]$^+$ calculated: 186.96/188.96. ^{1}H NMR (600 MHz, DMSO-*d$_6$*) δ 8.22 (d, *J* = 4.6 Hz, 1H), 7.37 (d, *J* = 4.6 Hz, 1H).

2-((cyclopropylmethyl)amino)thieno[3,2-*d*]pyrimidin-4(3*H*)-one (174)
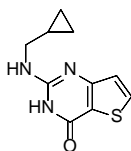
In a MW vial 2-chlorothieno[3,2-*d*]pyrimidin-4(3*H*)-one **172** (150 mg, 0.80 mmol) was dissolved in anhydrous *n*-butanol (4.03 ml). DIPEA (0.35 ml, 2.01 mmol) and cyclopropylmethanamine (**173**)(0.07 ml, 0.80 mmol) were sequentially added and the reaction was let go for 6 h at 160 °C under MW irradiation. The reaction was set up three times in parallel in the same experimental conditions. When LC-MS and TLC (CH$_2$Cl$_2$/MeOH 9.5:0.5) confirmed complete conversion of the starting material, the reaction mixtures were mixed together and concentrated under *vacuum*. Purification via flash chromatography 100% CH$_2$Cl$_2$ gave the desired 2-((cyclopropylmethyl)amino)thieno[3,2-*d*]pyrimidin-4(3*H*)-one **174** (0.53 g, 99%) UPLC-MS (generic method): Rt = 1.47 min, MS (ESI) *m/z*: 221.8/223.1 [M+H]$^+$, C$_{10}$H$_{12}$N$_3$OS$^+$ [M+H]$^+$ calculated: 222.06/223.06. ^{1}H NMR (600 MHz, DMSO-*d$_6$*) δ 10.79 (s, 1H), 7.95 (d, *J* = 5.2 Hz, 1H), 7.05 (d, *J* = 5.2 Hz, 1H), 6.32 (t, *J* = 5.4 Hz, 1H), 3.15 (t, *J* = 6.2 Hz, 2H), 1.08-1.04 (m, 1H), 0.47 – 0.44 (m, 2H), 0.25-0.22 (m, 2H).

4-chloro-*N*-(cyclopropylmethyl)thieno[3,2-*d*]pyrimidin-2-amine (175)
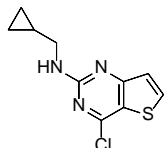
In an oven dried pressure tube under nitrogen atmosphere, a catalytic amount of dimethyl sulfoxide (1 µl, 14.08 µl) was added to a suspension of **174** (200 mg, 0.904 mmol) in phosphoryl trichloride (1.77 ml, 19.0 mmol). The resulting mixture was stirred for 3 h at 110 °C. When complete conversion of the starting material was observed by TLC (CH_2Cl_2/MeOH 9.5:0.5), the reaction was cooled down to 0 °C and quenched by addition of ice. The aqueous layer was extracted with EtOAc (20 ml x 3). The combined organic layers were washed with brine and dried with Na_2SO_4. The crude was purified by silica gel with 100% CH_2Cl_2 obtaining the desired product, **175** (94 mg, 43%) as a white solid. UPLC-MS (generic method): Rt = 2.40 min, MS (ESI) *m/z*: 239.9/241.9 $[M+H]^+$, $C_{10}H_{11}ClN_3S^+$ $[M+H]^+$ calculated: 240.03/242.03. ^{1}H NMR (600 MHz, $CDCl_3$) δ 7.81 (d, *J* = 5.2 Hz, 1H), 7.19 (d, *J* = 5.2 Hz, 1H), 5.38 (br. s, 1H), 3.32 (t, *J* = 5.2 Hz, 2H), 1.12 – 1.05 (m, 1H), 0.54 (d, *J* = 7.4 Hz, 2H), 0.27 (d, *J* = 5.0 Hz, 2H).

4-(5-amino-1*H*-pyrazol-3-yl)benzamide (177)
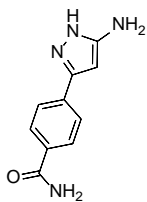
In a oven dried MW vial 3-bromo-1*H*-pyrazol-5-amine (**168**) (150 mg, 0.926 mmol), (4-carbamoylphenyl)boronic acid (**176**) (305 mg, 1.85 mmol), tetrakis(triphenylphosphine)palladium(0) (161 mg, 0.139 mmol) were added. The solid mixture was suspended in anhydrous 1,4-dioxane (1.85 ml) and a 2M solution of potassium carbonate (2.31 ml, 4.63 mmol) was added. The reaction mixture was degassed and backfilled with nitrogen and stirred for 2 h at 130 °C under MW irradiation. After checking by LC-MS and TLC (CH_2Cl_2/MeOH 8:2), evidence of product was observed, therefore the reaction mixture was quenched with water (5 ml) and washed with EtOAc (10 ml x 3, to remove apolar impurities). The aqueous phase was concentrated under *vacuum* and purified by silica gel

chromatography (-Solvent A: CH$_2$Cl$_2$ -Solvent B: MeOH -Gradient 10-20% of MeOH and then (-Solvent A: EtOH -Solvent B: MeOH -Gradient: 0-20% of solvent B) to obtain 4-(5-amino-1*H*-pyrazol-3-yl)benzamide (**177**) (95 mg, 51%) as a pale yellow powder. UPLC-MS generic method: Rt = 0.84 min, MS (ESI) *m/z*: 202.9 [M+H]$^+$, C$_{10}$H$_{11}$N$_4$O$^+$ [M+H]$^+$ calculated: 201.08. ^{1}H NMR (600 MHz, DMSO-d_6) δ 7.86 (d, *J* = 8.3 Hz, 2H), 7.71 (d, *J* = 8.3 Hz, 2H), 7.32 (br. s, 1H), 5.82 (s, 1H), 4.87 (br. s, 2H).

4-(5-((2-((cyclopropylmethyl)amino)thieno[3,2-*d*]pyrimidin-4-yl)amino)-1*H*-pyrazol-3-yl)benzamide, formic acid salt (178)
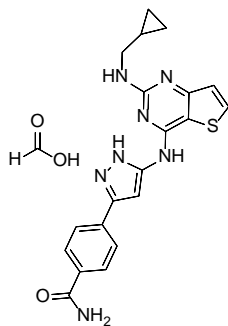
In a MW vial 4-chloro-*N*-(cyclopropylmethyl)thieno[3,2-*d*]pyrimidin-2-amine **175** (94 mg, 0.39 mmol) and 4-(5-amino-1*H*-pyrazol-3-yl)benzamide (**177**) (0.12 g, 0.59 mmol) were dissolved in anhydrous *n*-butanol (2.0 ml) under inert atmosphere (N$_2$). DIPEA (51 mg, 68 μl, 0.39 mmol) was added to the solution and the reaction was let go for 8 h at 180 °C under MW irradiation according to the general chemical procedure D. When TLC (CH$_2$Cl$_2$/MeOH 9.5:0.5) confirmed complete conversion of the starting material, the reaction mixture was concentrated under vacuum. Purification via flash chromatography (-Solvent A: CH$_2$Cl$_2$ -Solvent B: MeOH -Gradient: 0-10% of solvent B) gave the desired product which was purified by HPLC-prep (H$_2$O/ACN 0.1% FA from 5 to 95% of ACN in 18 min, flow rate: 30 min/ml) to furnish the formic acid salt of 4-(5-((2-((cyclopropylmethyl)amino)thieno[3,2-*d*]pyrimidin-4-yl)amino)-1*H*-pyrazol-3-yl)benzamide **178** (0.016 g, 10%). UPLC-MS (generic method): Rt = 1.60 min, MS (ESI) *m/z*: 406.0 [M+H]$^+$, C$_{20}$H$_{20}$N$_7$OS$^+$ [M+H]$^+$ calculated: 406.13. ^{1}H NMR (400 MHz, DMSO-d_6) δ 8.13 (s, 1H), 8.06 (br. s., 1H), 8.05 (br. s., 1H), 7.99 – 7.90 (m, 2H), 7.87 (m, 2H), 7.81 (d, *J* = 8.4 Hz, 1H), 7.41 (br. s., 1H), 7.20 (d, *J* = 5.4 Hz, 1H), 1.16 (br. s., 1H), 0.52-0.48 (m, 2H), 0.30-026 (m, 2H).

5.2 Chemical procedures for compounds reported in chapter 3

(*R*)-4-(4-(5-chloro-7-((3,3-dimethylbutan-2-yl)amino)-[1,2,4]triazolo[1,5-*a*]pyrimidin-6-yl)-3,5-difluorophenyl)but-3-yn-1-ol (184)
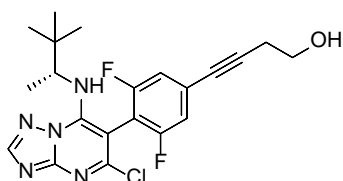
To a solution of (*R*)-5-chloro-6-(2,6-difluoro-4-iodophenyl)-*N*-(3,3-dimethylbutan-2-yl)-[1,2,4]triazolo[1,5-*a*]pyrimidin-7-amine **192** (80 mg, 0.16 mmol) in degassed DMF (0.81 ml), copper(I) iodide (4.6 mg, 24 µmol), triethylamine (68 µL, 0.49 mmol) and but-3-yn-1-ol (**193**) (37 µL, 0.49 mmol) were added. The mixture was degassed and backfilled with N_2 before tetrakis(triphenylphosphine)palladium(0) (19 mg, 16 µmol) was added. The mixture was degassed and backfilled with N_2 three times and stirred at room temperature overnight. The reaction mixture was quenched with water (5 ml) and extracted with EtOAc (20 ml x 3). The combined organic layers were washed with brine, dried with Na_2SO_4 and concentrated in vacuo. The crude residue was purified over silica (-Solvent A: hexane -Solvent B: EtOAc -Gradient: 10-50% of solvent B) to give x (55 mg, 78%) as a white powder. ^{1}H NMR (600 MHz, $CDCl_3$) δ 8.34 (s, 1H), 7.15 – 7.09 (d, 2H), 6.43 (s, 1H), 3.88 (t, *J* = 6.3 Hz, 2H), 3.14 (s, 1H), 2.75 (t, *J* = 6.3 Hz, 2H), 1.01 (d, *J* = 6.7 Hz, 3H), 0.84 (s, 9H). ^{1}H NMR was in agreement with data reported in literature.[253]

diethyl 2-(2,6-difluoro-4-nitrophenyl)malonate (186)
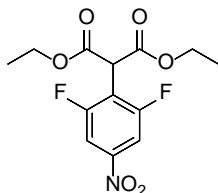
To a solution of sodium hydride (1.4 g, 59.30 mmol) in THF (60 ml) at 0 °C, diethyl malonate (8.61 ml, 56.47 mmol) was added dropwise. The resulting reaction mixture was let stir for 1 h. 1,2,3-trifluoro-5-nitrobenzene (185) (3.29 ml, 28.24 mmol) was added dropwise to the reaction mixture, which was stirred for 4 h at room temperature. Once the reaction was over, it was quenched with NH_4Cl saturated solution (10 ml) and extracted with EtOAc (200 ml x 3). The organic layers were collected, washed with water (100 ml) and brine (100 ml), dried over Na_2SO_4, and concentrated under *vacuum*. The crude product was purified by flash chromatography (-Solvent A: hexane -Solvent B: EtOAc -Gradient: 0-10% of solvent B) obtaining the desired product 186 (8.9 g 99%) as a yellow oil with traces of diethyl malonate ^1H NMR (600 MHz, CDCl$_3$) δ 7.82 (d, *J* = 7.2 Hz, 2H), 4.99 (s, 1H), 4.25 (qd, *J* = 7.1, 1.1 Hz, 4H), 1.31 – 1.19 (m, 6H). ^1H NMR was in agreement with data reported in literature.[253]

diethyl 2-(4-amino-2,6-difluorophenyl)malonate (187)
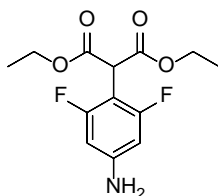
To a solution of diethyl 2-(2,6-difluoro-4-nitrophenyl)malonate (186) (5 g, 0.02 mol) in methanol (100 ml) under inert atmosphere (N_2), palladium on carbon (2 g, 10% Wt, 2 mmol) was added. The resulting mixture was flushed with N_2 three times, subsequently flushed with H_2 and stirred for 2 h. After 2 h the stirring was stopped, the reaction mixture was filtered through a celite pad and concentrated under *vacuum*. The crude product was purified by flash chromatography (-Solvent A: hexane -Solvent B: EtOAc -Gradient: 5-30% of solvent B) to give the desired product 187 1.864 g (40%) over two steps. ^1H NMR (600 MHz, CDCl$_3$) δ 6.20 (d, *J* = 9.7 Hz, 2H),

4.80 (s, 1H), 4.23 (q, J = 7.1 Hz, 4H), 1.26 (t, J = 7.22 Hz, 6H). ^{1}H NMR was in agreement with data reported in literature.[253]

diethyl 2-(2,6-difluoro-4-iodophenyl)malonate (188)
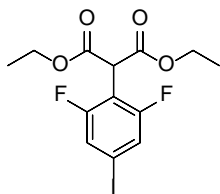
3.4 ml of a 2.6M solution of sodium nitrite (0.62 g, 9.1 mmol) in water was added dropwise to a solution of diethyl 2-(4-amino-2,6-difluorophenyl)malonate **187** (2.6 g, 9.1 mmol) in 6M HCl (15 ml, 91 mmol) at 0 °C. The resulting suspension was added dropwise to 6.3 ml of a 6M solution of potassium iodide (6.2 g, 38 mmol) in water keeping the temperature at 0 °C. The reaction mixture was allowed to warm to room temperature and stirred for 3 h. Then, it was stopped and extracted with EtOAc (100 ml x 3). The combined layers were washed in with 10% $Na_2S_2O_3$ (100 ml) and brine (100 ml), dried over Na_2SO_4 and concentrated under *vacuum*. The crude residue was purified over silica (-Solvent A: hexane -Solvent B: EtOAc -Gradient: 0-25% of solvent B) to give the title compound **188** (2.423 g, 67%) as a yellow oil.^{1}H NMR (600 MHz, CDCl$_3$) δ 7.31 (d, J = 7.0 Hz, 2H), 4.89 (s, 1H), 4.24 (q, J = 7.1 Hz, 4H), 1.27 (t, J = 7.22 Hz, 6H). ^{1}H NMR was in agreement with data reported in literature.[253]

5,7-dichloro-6-(2,6-difluoro-4-iodophenyl)-[1,2,4]triazolo[1,5-a]pyrimidine (190)
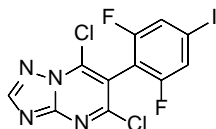
<u>Step I</u>: In a pressure flask flushed with N_2, were charged diethyl 2-(2,6-difluoro-4-iodophenyl)malonate **188** (1.276 g, 3.205 mmol), 1*H*-1,2,4-triazol-3-amine (**189**) (282.9 mg, 3.365 mmol) and tributylamine (0.81 ml, 3.365 mmol). The mixture was heated to 170 °C for 3 h. Then, 5 ml of toluene were added at 110 °C followed by a 50% solution of sodium hydroxide (0.51 ml, 9.615 mmol) at 50 °C. Once at room temperature, the mixture was filtered over sintered glass and rinsed twice with toluene (5 ml) to furnish the 6-(2,6-difluoro-

4-iodophenyl)-[1,2,4]triazolo[1,5-*a*]pyrimidine-5,7-diol (0.55 g, 99%) that was engaged in the next step without further purification.

Step 2: In a round bottom flask charged with the intermediate 6-(2,6-difluoro-4-iodophenyl)-[1,2,4]triazolo[1,5-*a*]pyrimidine-5,7-diol (2.0 g, 4.608 mmol) was added phosphoryl trichloride (5.33 ml, 57.05 mmol) and the mixture was heated to 130 °C for 6 h. The reaction was poured on ice, the aqueous phase was extracted with CH$_2$Cl$_2$ (50 ml x 2) and the combined organic fractions were washed with brine (50 ml), dried over Na$_2$SO$_4$ and concentrated in vacuo. The crude residue was purified over silica (-Solvent A: hexane -Solvent B: EtOAc -Gradient: 0-30% of solvent B) to give the title compound **190** (971 mg, 71.0% over two steps) as an off-white solid. ^{1}H NMR (600 MHz, CDCl$_3$) δ 8.62 (s, 1H), 7.52 (d, *J* = 6.3 Hz, 2H). ^{1}H NMR was in agreement with data reported in literature.[253]

(*R*)-5-chloro-6-(2,6-difluoro-4-iodophenyl)-*N*-(3,3-dimethylbutan-2-yl)-[1,2,4]triazolo[1,5-*a*]pyrimidin-7-amine (192)
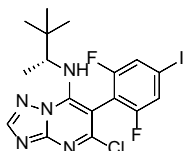
To a solution of 5,7-dichloro-6-(2,6-difluoro-4-iodophenyl)-[1,2,4]triazolo[1,5-*a*]pyrimidine **190** (0.325 g, 0.761 mmol) in DMF (2.1 ml) (*R*)-3,3-dimethylbutan-2-amine, HCl (**191**) (157 mg, 1.14 mmol) and triethylamine (0.318 ml, 2.28 mmol) were added, and the resulting mixture was stirred for 1 h at room temperature. The reaction was quenched by addition of water (30 ml) and the aqueous layer was extracted with EtOAc (50 ml x 3). The combined organic fractions were washed with brine (50 ml), dried over Na$_2$SO$_4$ and concentrated in vacuo. The crude residue was purified over silica (-Solvent A: hexane -Solvent B: EtOAc -Gradient: 0-30% of solvent B) to yield **192** (357 mg, 95.4%) as an off-white solid. ^{1}H NMR (600 MHz, CDCl$_3$) δ 8.34 (s, 1H), 7.48 (d, *J* = 6.0 Hz, 2H), 6.43 (s, 1H), 3.12 (s, 1H), 1.03 (d, *J* = 6.7 Hz, 3H), 0.84 (s, 9H). ^{13}C NMR (151 MHz, CDCl$_3$) δ 160.67 (dd, *J* = 254.9, 6.2 Hz), 160.40 (dd, *J* = 254.8, 6.0 Hz),

157.59, 154.89, 153.58, 146.03, 121.82 (dd, J = 21.7, 3.9 Hz), 121.67 (dd, J = 21.7, 3.9 Hz), 111.23 (t, J = 18.2 Hz), 94.41 (t, J = 10.1 Hz), 88.71, 58.10, 34.74, 25.77, 16.56, 16.55. HRMS (ES$^+$) calculated for $C_{17}H_{18}N_5F_2ICl$ [M+H]$^+$, 492.0258; found 492.0256. Analytical data were in agreement with data reported in literature.[253]

4-(4-(7-amino-5-chloro-[1,2,4]triazolo[1,5-*a*]pyrimidin-6-yl)-3,5-difluorophenyl)but-3-yn-1-ol (194)

To a solution of 5-chloro-6-(2,6-difluoro-4-iodophenyl)-[1,2,4]triazolo[1,5-*a*]pyrimidin-7-amine **196** (80 mg, 0.20 mmol) in degassed DMF (0.98 ml), copper(I) iodide (5.6 mg, 29 µmol), triethylamine (82 µl, 0.59 mmol) and but-3-yn-1-ol (45 µl, 0.59 mmol) were added. The mixture was degassed and backfilled with N$_2$ before tetrakis(triphenylphosphine)palladium(0) (23 mg, 20 µmol) was added. The mixture was degassed and backfilled with N$_2$ three times and stirred at room temperature overnight. The reaction mixture was quenched with water (5 ml) and extracted with EtOAc (30 ml x 3). The combined organic layers were washed with brine (30 ml), dried over Na$_2$SO$_4$ and concentrated in vacuo. The crude residue was purified by reverse phase HPLC (water/ACN with 0.1% FA, 10-90% ACN in 18 min, flow rate: 20 ml/min), to obtain 4-(4-(7-amino-5-chloro-[1,2,4]triazolo[1,5-*a*]pyrimidin-6-yl)-3,5-difluorophenyl)but-3-yn-1-ol **194** (36 mg, 52%). LC-MS (standard method): Rt. 3.89 min, MS (ESI) m/z: 350.1 [M+H]$^+$, $C_{15}H_{11}ClF_2N_5O^+$ [M+H]$^+$ calculated: 350.05. ^{1}H NMR (600 MHz, DMSO-d_6) δ 8.58 (s, 1H), 8.54 (bs, 2H), 7.33 (d, J = 7.6 Hz, 2H), 4.95 (s, 1H), 3.61 (t, J = 7.0 Hz, 2H), 2.61 (t, J = 7.0 Hz, 2H). ^{13}C NMR (151 MHz, DMSO-d_6) δ 160.70 (C-F, d, J = 248.15 Hz), 160.56 (C-F, d, J = 248.15 Hz) 155.46, 154.65, 153.88, 148.20, 126.98 (C-F, t, J = 13.0 Hz), 115.38-115.12 (m), 109.02 (C-F, t, J = 22.0 Hz), 92.46, 89.10, 79.23, 79.19, 79.15, 59.53,

54.97, 48.64, 23.35. HRMS (ES$^+$) calculated for C$_{15}$H$_{11}$ClF$_2$N$_5$O$^+$ [M+H]$^+$: 350.0615, found 350.0617.
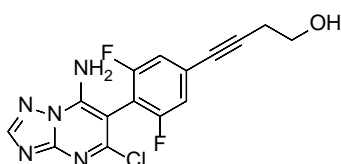
5-chloro-6-(2,6-difluoro-4-iodophenyl)-[1,2,4]triazolo[1,5-*a*]pyrimidin-7-amine (196)
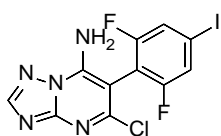
To a solution of 5,7-dichloro-6-(2,6-difluoro-4-iodophenyl)-[1,2,4]triazolo[1,5-*a*]pyrimidine **190** (150 mg, 351 µmol) in a mixture of MeOH (0.878 ml) and DMF (0.100 ml) a 7M solution of NH$_3$ in MeOH (50.2 µl, 351 µmol) was slowly added at 0 °C and the resulting mixture was stirred at room temperature for 30 min. After complete conversion of the starting material, the stirring was stopped and concentrated in vacuo. The crude product was employed in the following step without any further purification. ^{1}H NMR (600 MHz, MeOD$_4$) δ 8.40 (s, 1H), 7.97 (br. s., 2H), 7.61 (d, *J* = 7.1 Hz, 2H).

but-3-ynoic acid (197)
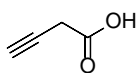
6.49 ml of water were added to a 10 ml single neck round bottom flask fitted with a magnetic stir bar. nitric acid (24.9 µl, 65% wt, 357 µmol), sodium dichromate (18.7 mg, 71.3 µmol), sodium periodate (3.36 g, 15.7 mmol) were subsequently added and the mixture was stirred vigorously on an ice bath for 15 min. but-3-yn-1-ol (**193**) (540 µL, 7.13 mmol) dissolved in chilled water (6.49 ml) was added dropwise to this mixture and the reaction was stirred overnight (ice bath was not removed to let the ice melt and temperature of reaction mixture rise slowly to room temperature). The reaction was checked by TLC 100% EtOAc by using KMnO$_4$ stain. After this time, product was extracted with EtOAc (50 ml x 3), the separated organic layer was washed with brine (50 ml) and dried over Na$_2$SO$_4$. The solvent was

evaporated on rotary evaporator to give an orange/yellowish viscous liquid. Subsequent addition of diethyl ether (5 ml) and removal of solvent under high *vacuum* gave but-3-ynoic acid **197** as an off white solid (428 mg, 71.4%) ^{1}H NMR (600 MHz, CDCl$_3$) δ 3.38 (d, *J* = 2.68 Hz, 2H), 2.24 (t, *J* = 2.68 Hz, 1H).

benzyl but-3-ynoate (201)
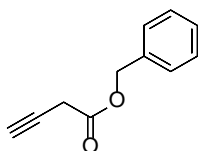
A solution of but-3-ynoic acid **197** (200 mg, 2.38 mmol), phenylmethanol (742 µl, 7.14 mmol) and conc. HCl (24.5 µl, 238 µmol) in water was stirred at room temperature for 15 h. After reacting overnight, CH$_2$Cl$_2$ (5 ml) was added and the mixture was washed with saturated aqueous NaHCO$_3$ solution (5 ml). The separated organic layer was dried over Na$_2$SO$_4$, filtered and concentrated in vacuo. Purification of the crude product by column chromatography (100% hexane) gave the title benzyl but-3-ynoate **201** (151 mg, 36.4%) as a colorless oil. ^{1}H NMR (600 MHz, CDCl$_3$) δ 7.37 (s, 5H), 5.19 (s, 2H), 3.34 (s, 2H), 2.21 (s, 1H).

(*R*)-4-(4-(5-chloro-7-((3,3-dimethylbutan-2-yl)amino)-[1,2,4]triazolo[1,5-*a*]pyrimidin-6-yl)-3,5-difluorophenyl)but-3-yn-1-yl (*tert*-butoxycarbonyl)glycinate (210)
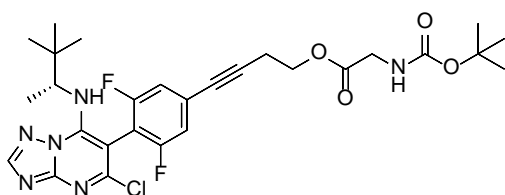
184 (40 mg, 92 µmol) was dissolved in anhydrous THF (0.46 ml) and the solution was cooled to 0 °C. To this was added (*tert*-butoxycarbonyl)glycine (21 mg, 0.12 mmol) followed by EDC·HCl (29 mg, 0.13 mmol) and DMAP (23 mg, 0.18 mmol). The reaction was allowed to warm to room temperature and stirred overnight. The stirring was stopped and the mixture was concentrated under *vacuum*. The resulting crude product was purified by reverse phase HPLC (Water/ACN with 0.1% FA , 5-95% of

ACN in 18 min, flow rate: 20 ml/min) to yield **210** (26 mg, 48%) as a white solid. LC-MS (standard method): Rt. 5.35 min, MS (ESI) m/z: 591.3 $[M+H]^+$, $C_{28}H_{34}ClF_2N_6O_4^+$ $[M+H]^+$ calculated: 591.22.^{1}H NMR (600 MHz, $CDCl_3$) δ 8.30 (s, 1H), 7.09 (d, $J = 8.6$ Hz, 2H), 6.41 (s, 1H), 5.15 (s, 1H), 4.33 (t, $J = 6.5$ Hz, 2H), 3.95 (br. s., $J = 6.2$ Hz, 2H), 3.45 (s, 1 H), 3.10 (br. s. 1H), 1.42 (s, 9H), 0.98 (d, $J = 6.9$ Hz, 3H), 0.80 (s, 9H). HRMS (ES^+) calculated for $C_{28}H_{34}ClF_2N_6O_4^+$ $[M+H]^+$: 591.2293, found 591.2290.

4-(4-(5-chloro-7-(((*R*)-3,3-dimethylbutan-2-yl)amino)-[1,2,4]triazolo[1,5-*a*]pyrimidin-6-yl)-3,5-difluorophenyl)but-3-yn-1-yl (*tert*-butoxycarbonyl)-*L*-alaninate (211)
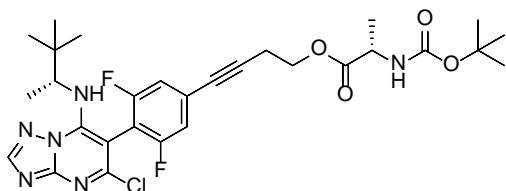
184 (20 mg, 46 µmol) was dissolved in anhydrous THF (0.23 ml). The solution was cooled to 0 °C and **208** (8.7 mg, 46 µmol) followed by EDC·HCl (15 mg, 65 µmol) and DMAP (11 mg, 92 µmol) were added. The reaction was allowed to warm to room temperature and stirred overnight. The stirring was stopped and the mixture was concentrated under *vacuum*. The resulting crude product was purified by reverse phase HPLC (Water/ACN with 0.1% FA, 5-95% ACN in 18 min, flow rate: 20 ml/min) to yield **211** (14 mg, 49%). LC-MS (standard method): Rt = 5.45 min, MS (ESI) m/z: 605.3 $[M+H]^+$, $C_{29}H_{36}ClF_2N_6O_4^+$ $[M+H]^+$ calculated: 605.23.^{1}H NMR (600 MHz, $CDCl_3$) δ 8.36 (s, 1H), 7.11 (d, $J = 8.4$ Hz, 2H), 6.43 (s, 1H), 5.02 (s, 1H), 4.41 – 4.31 (m, 2H), 4.12 (q, $J = 7.1$ Hz, 1H), 3.13 (s, 1H), 2.83 (t, $J = 6.7$ Hz, 2H), 1.45 (s, 9H), 1.42 (d, $J = 7.2$ Hz, 3H), 1.02 (d, $J = 6.6$ Hz, 3H), 0.84 (s, 9H). HRMS (ES^+) calculated for $C_{29}H_{36}ClF_2N_6O_4^+$ $[M+H]^+$: 605.2449, found 605.2452.

1-(4-(4-(5-chloro-7-(((*R*)-3,3-dimethylbutan-2-yl)amino)-[1,2,4]triazolo[1,5-*a*]pyrimidin-6-yl)-3,5-difluorophenyl)but-3-yn-1-yl)   5-methyl (*tert*-butoxycarbonyl)-*L*-glutamate (212)
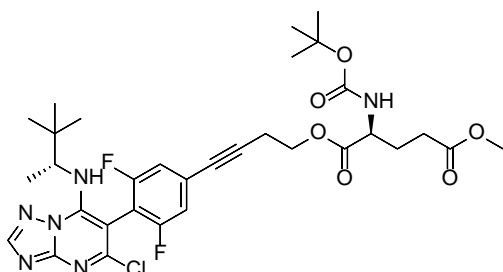
184 (20 mg, 46 µmol) was dissolved in anhydrous THF (0.23 ml) and the solution was cooled to 0 °C. To this was added **209** (16 mg, 60 µmol) followed by EDC·HCl (15 mg, 65 µmol) and DMAP (11 mg, 92 µmol). The reaction was allowed to warm to room temperature and stirred overnight. The reaction was checked by TLC (100% EtOAc) noticing good conversion of the starting material. Therefore, the stirring was stopped and the mixture was concentrated under vacuum. The resulting yellow pale oil crude product was employed in the following step without any further purification. **212** (31 mg, quantitative) ^{1}H NMR (600 MHz, CDCl$_3$) δ 8.33 (s, 1H), 7.12 (d, *J* = 8.1 Hz, 2H), 6.55 (s, 1H), 5.13 (d, *J* = 8.4 Hz, 1H), 4.35 (td, *J* = 6.7, 4.1 Hz, 2H), 3.67 (s, 3H), 2.83 (t, 2H), 2.51 – 2.37 (m, 3H), 2.00 – 1.73 (m, 2H), 1.44 (s, 9H), 1.01 (d, *J* = 6.7 Hz, 3H), 0.83 (s, 9H). HRMS (ES$^+$) calculated for C$_{32}$H$_{40}$ClF$_2$N$_6$O$_6^+$ [M+H]$^+$: 677.2660, found 677.2656.

1-(4-(4-(5-chloro-7-(((R)-3,3-dimethylbutan-2-yl)amino)-

[1,2,4]triazolo[1,5-a]pyrimidin-6-yl)-3,5-difluorophenyl)but-3-yn-1-yl)   5-methyl

***L*-glutamate (213)**
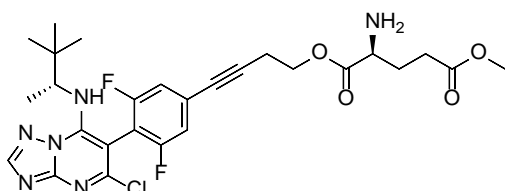
212 (31 mg, 46 µmol) in 4M HCl solution in 1,4-dioxane (69 µl, 0.27 mmol) was stirred overnight under inert atmosphere. The reaction was checked by TLC (100% EtOAc) noticing complete conversion of the starting material, therefore the mixture was concentrated in vacuo. The crude was purified by preparative HPLC (water/ACN with 0.1% FA, 5-80% ACN in 18 min, flow rate: 30 ml/min) to obtain **213** (9 mg, 30%) as a white powder. LC-MS (standard method): Rt. 4.54 min, MS (ESI) m/z: 577.3 [M+H]$^+$, $C_{15}H_{10}ClF_2N_5O^+$ [M+H]$^+$ calculated: 577.213. ^{1}H NMR (600 MHz, MeOD$_4$) δ 8.47 (s, 1H), 7.30 (d, 2H), 4.59 – 4.34 (m, 2H), 4.17 (t, 1H), 3.68 (s, 3H), 2.94 (t, J = 6.3 Hz, 2H), 2.64 (m, 2H), 2.31 – 2.15 (m, 2H), 1.37 (t, J = 6.6 Hz, 1H), 1.30 (s, 1H), 1.07 (d, J = 6.8 Hz, 3H), 0.83 (s, 9H). HRMS (ES$^+$) calculated for $C_{27}H_{32}ClF_2N_6O_4^+$ [M + H]$^+$: 577.213, found 577.214

4-(4-(5-chloro-7-(((*R*)-3,3-dimethylbutan-2-yl)amino)-[1,2,4]triazolo[1,5-

a]pyrimidin-6-yl)-3,5-difluorophenyl)but-3-yn-1-yl *L*-alaninate, formic acid (216)
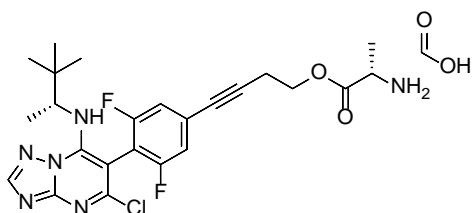
211 (34 mg, 0.056 mmol) was dissolved in 4 M HCl in 1,4-dioxane (0.084 ml, 0.34 mmol) at room temperature and stirred overnight. The solvent was evaporated to give a sticky colorless oil that was purified by reverse HPLC preparative (Water/ACN with 0.1% of FA, 5-95% of ACN in 18 min, flow rate: 20 ml/min) to yield **216** (10 mg, 32%) as a white solid. ^{1}H NMR (600 MHz, CD$_3$CN) δ 8.34 (s, J = 2.8 Hz, 1H), 7.23 (d, J =

9.1 Hz, 2H), 6.49 (s, 1H), 4.34 – 4.22 (m, 2H), 3.73 – 3.67 (m, 1H), 3.29 (b. s., 1H), 2.82 (d, J = 2.8 Hz, 2H), 1.34 – 1.29 (m, 3H), 1.04 – 1.00 (m, 3H), 0.80 (s, 9H). HRMS (ES$^+$) calculated for $C_{24}H_{28}ClF_2N_6O_2^+$ [M+H]$^+$: 505.1925, found 505.1927.

(R)-4-(4-(5-chloro-7-((3,3-dimethylbutan-2-yl)amino)-[1,2,4]triazolo[1,5-a]pyrimidin-6-yl)-3,5-difluorophenyl)but-3-yn-1-yl glycinate, formic acid (217)
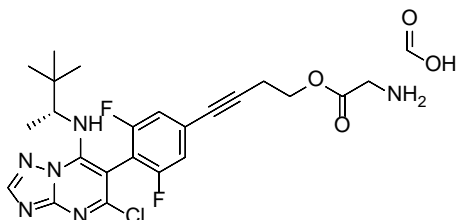
210 (24 mg, 41 µmol) was dissolved in 4M HCl (61 µl, 0.24 mmol) in 1,4-dioxane at room temperature and stirred overnight. The solvent was evaporated and the crude product was purified by reverse HPLC preparative (Water/ACN with 0.1% of FA, 5-95% of ACN in 18 min, flow rate: 20 ml/min) to yield **217** (14 mg, 64%) as a white solid. ^{1}H NMR (600 MHz, CD$_3$CN) δ 8.35 (s, 1H), 8.21 (br. s., 1H), 7.25 (d, 2H), 6.49 (br. s., 1H), 4.32 (t, J = 6.27 Hz, 2H), 3.56 (s, 2H), 2.83 (t, J = 6.6, 2.7 Hz, 2H), 1.26 (br. s., 1H), 1.02 (d, J = 6.6, 2.8 Hz, 3H), 0.80 (s, J = 3.1 Hz, 9H). ^{13}C NMR (101 MHz, DMSO-d_6) δ 161.76, 156.00, 155.12, 146.90, 115.43-115.06 (m), 93.41, 78.89, 62.11, 59.41, 57.98, 57.92, 35.25, 25.63, 19.35, 15.22. HRMS (ES$^+$) calculated for $C_{23}H_{26}ClF_2N_6O_2^+$ [M+H]$^+$: 491.1768, found 491.1766.

4-(4-(5-chloro-7-(((R)-3,3-dimethylbutan-2-yl)amino)-[1,2,4]triazolo[1,5-a]pyrimidin-6-yl)-3,5-difluorophenyl)but-3-yn-1-yl L-serinate, formic acid (218)
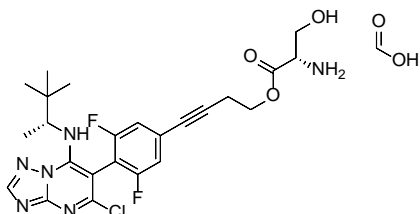
A solution of **222** (36 mg, 49 µmol) in 4M HCl in 1,4-dioxane (0.17 ml, 0.69 mmol) was stirred overnight under inert atmosphere (N$_2$). The reaction was stopped and concentrated in vacuo. The crude was purified by preparative HPLC preparative (Water/ACN with 0.1% FA, 5-80% ACN in 18 min, flow rate: 20 ml/min) to obtain **218** (10 mg, 36%) as a white

powder. ^{1}H NMR (600 MHz, DMSO) δ 8.64 (s, 1H), 8.42 (s, 1H), 7.68 (s, 1H), 7.47 (d, J = 9.5 Hz, 2H), 5.62 (br. s., 1H), 4.37 (t, J = 6.5, 2.3 Hz, 2H), 4.24 (s, 1H), 3.94 – 3.73 (m, 2H), 2.91 (t, J = 6.3 Hz, 2H), 1.03 (s, 3H), 0.85 (t, J = 7.0 Hz, 1H), 0.74 (s, 9H). HRMS (ES$^+$) calculated for $C_{24}H_{28}Cl\ F_2N_6O_3^+$ [M+H]$^+$: 521.1874, found 521.1870.

(*tert*-butoxycarbonyl)-*L*-serine (220)
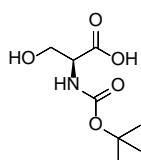
A solution of di-*tert*-butyl dicarbonate (249 mg, 1.14 mmol) in 1,4-dioxane (0.952 mL) was added at 0 °C to a solution of *L*-serine (**219**) (100 mg, 0.952 mmol) in 1M sodium hydroxide (1.05 ml, 1.05 mmol). After stirring at room temperature for 3 h, an aqueous 1M solution of sodium hydrogen sulfate (1.05 ml, 1.05 mmol) was added at 0 °C. The stirring was stopped and the aqueous phase was extracted with EtOAc (5 ml x 3). The combined organic phases were dried over Na$_2$SO$_4$ and evaporation of the solvent gave (*tert*-butoxycarbonyl)-*L*-serine **220** (0.19 g, 99%) as colorless oil. ^{1}H NMR (600 MHz, CDCl$_3$) δ 6.87 (s, 1H), 5.66 (s, 1H), 4.37 (s, 1H), 4.21 (s, 1H), 4.10 – 3.83 (m, 2H), 1.46 (s, 9H).

N-(*tert*-butoxycarbonyl)-*O*-(*tert*-butyldimethylsilyl)-*L*-serine (221)
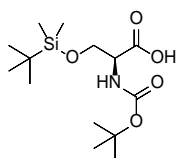
A suspension of **220** (190 mg, 926 µmol) in anhydrous DMF (3.09 ml) was treated with 1*H*-imidazole (126 mg, 1.85 mmol) and *tert*-butylchlorodimethylsilane (154 mg, 1.02 mmol). The resulting solution was stirred at room temperature overnight. The volatiles were removed under *vacuum* and the obtained residue was suspended in water (10 ml) and hexane (10 ml). The separated organic layer was washed with brine (10 ml), dried over Na$_2$SO$_4$ and concentrated under *vacuum* affording a colorless oil consistent with the desired product **221** (71 mg, 99%). ^{1}H NMR (600 MHz, CDCl$_3$) δ 5.36 (d, J = 8.3 Hz, 1H), 4.34 (s, 1H), 4.17 – 3.72 (m, 2H), 1.45 (s, 9H), 0.88 (s, 9H), 0.10 (s, 6H).

4-(4-(5-chloro-7-(((*R*)-3,3-dimethylbutan-2-yl)amino)-[1,2,4]triazolo[1,5-*a*]pyrimidin-6-yl)-3,5-difluorophenyl)but-3-yn-1-yl *N*-(*tert*-butoxycarbonyl)-*O*-(*tert*-butyldimethylsilyl)-*L*-serinate (222)
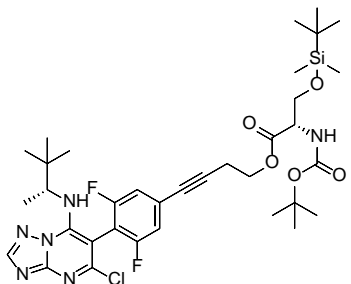
184 (50 mg, 0.12 mmol) was dissolved in anhydrous THF (0.58 ml) and the solution was cooled to 0 °C. To this was added **221** (48 mg, 0.15 mmol) followed by EDC·HCl (37 mg, 0.16 mmol) and DMAP (28 mg, 0.23 mmol). The reaction was allowed to warm to room temperature and stirred overnight. Once completed, the stirring was stopped and the mixture was concentrated under *vacuum*. The resulting crude product was purified by reverse phase HPLC (Water/ACN with 0.1% of FA, 5-95% of ACN in 18 min, flow rate: 30 ml/min) to yield (**222**) (36 mg, 42%) as a white solid. ^{1}H NMR (600 MHz, CDCl$_3$) δ 8.33 (s, 1H), 7.11 (d, *J* = 8.4 Hz, 2H), 6.42 (s, 1H), 5.35 (d, *J* = 8.8 Hz, 1H), 4.46 – 4.29 (m, 2H), 4.15 – 4.06 (m, 1H), 3.86 (dd, *J* = 10.1, 3.2 Hz, 1H), 3.13 (s, 1H), 2.81 (t, *J* = 6.8 Hz, 2H), 2.04 (s, 1H), 1.46 (s, 9H), 1.68 (s, 3H) 1.02 (d, *J* = 6.6 Hz, 3H), 0.81 (s, 9H), 0.07 (s, 6H). HRMS (ES$^+$) calculated for C$_{35}$H$_{50}$ClF$_2$N$_6$O$_5$Si$^+$ [M+H]$^+$: 735.3263, found 735.3264.

4-(2,4,6-trifluorophenyl)but-3-yn-1-ol (224)
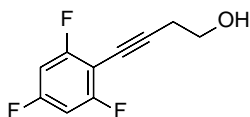
To a solution of 1,3,5-trifluoro-2-iodobenzene (**223**) (80 mg, 0.31 mmol) in degassed DMF (1.6 ml), were added copper(I) iodide (9.0 mg, 0.15 Eq, 0.047 mmol), triethylamine (94 mg, 0.13 mL, 3 Eq, 0.93 mmol) and but-3-yn-1-ol (65 mg, 70 µL, 3 Eq, 0.93 mmol). The mixture was degassed and backfilled with Nitrogen before tetrakis(triphenylphosphine)palladium(0) (36 mg, 0.10 Eq, 0.031 mmol)was added. The mixture was degassed and backfilled with Nitrogen three times and stirred at room

temperature overnight before it was quenched with water and extracted with EtOAc (30 ml x 3). The combined organic fractions were washed with brine (30 ml) dried and concentrated under reduced pressure. The crude residue was purified over silica (Hexanes/Ethyl Acetate 0-20% of Ethyl Acetate) to give 52 mg of the desired product **224** as a yellow solid. ^{1}H NMR (600 MHz, CDCl3) δ 6.68 (d, J = 8.0 Hz, 2H), 3.85 (t, J = 6.3 Hz, 2H), 2.76 (t, J = 6.2 Hz, 2H) ppm.

tert-butyl (*S*)-(1-(but-3-yn-1-ylamino)-1-oxopropan-2-yl)carbamate (228)
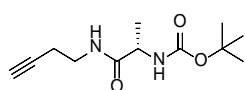
but-3-yn-1-amine, HCl (**227**) (59 µl, 0.47 mmol) was dissolved in anhydrous CH_2Cl_2 (4.7 ml) and cooled to 0 °C. To this solution HATU (0.29 g, 0.76 mmol), **208** (0.18 g, 0.95 mmol), and DIPEA (0.33 ml, 1.9 mmol) were added. The reaction mixture was allowed to warm up to room temperature and stirred overnight. The reaction was quenched with water (5 ml), extracted with CH_2Cl_2 (10 ml x 3) and washed with brine (10 ml) to obtain the crude product, which was purified through silica gel chromatography (-Solvent A: CH_2Cl_2 - Solvent B: MeOH -Gradient: 0-5% of solvent B) to obtain **228** (52 mg, 46%) as a white powder. ^{1}H NMR (600 MHz, CDCl3) δ 6.47 (s, 1H), 4.99 (s, 1H), 4.15 (s, 1H), 3.46 – 3.35 (m, 2H), 2.40 (td, *J* = 6.5, 2.7 Hz, 2H), 1.99 (t, *J* = 2.7 Hz, 1H), 1.44 (s, 9H), 1.36 (d, *J* = 7.1 Hz, 3H).

tert-butyl (2-(but-3-yn-1-ylamino)-2-oxoethyl)carbamate (229)
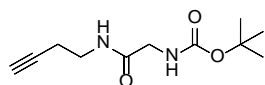
227 (50 mg, 0.47 mmol) was dissolved in anhydrous CH_2Cl_2 (4.7 ml) and cooled to 0 °C. To this solution **207** (0.17 g, 0.95 mmol), HATU (0.29 g, 0.76 mmol), and DIPEA (0.33 ml, 1.9 mmol) were added. The reaction mixture was allowed to warm up to room temperature and stirred overnight. The reaction was quenched with water (5 ml) and extracted with CH_2Cl_2 (10 ml x 3) and washed with brine (10 ml) to obtain the crude product, which was purified

through silica gel chromatography (-Solvent A: CH_2Cl_2 -Solvent B: MeOH -Gradient: 0-5% of solvent B) to obtain **229** (72 mg, 67%) as a colorless oil. ^{1}H NMR (600 MHz, CDCl₃) δ 6.80 (br. s., 1H), 5.46 (t, J = 5.9 Hz, 1H), 3.75 (d, J = 5.7 Hz, 2H), 3.38 (q, J = 6.4 Hz, 2H), 2.36 (td, J = 6.6, 2.7 Hz, 2H), 1.97 (t, J = Hz, 1H), 1.40 (s, 9H).

tert-butyl ((_S_)-1-((4-(4-(5-chloro-7-(((_R_)-3,3-dimethylbutan-2-yl)amino)-[1,2,4]triazolo[1,5-_a_]pyrimidin-6-yl)-3,5-difluorophenyl)but-3-yn-1-yl)amino)-1-oxopropan-2-yl)carbamate (230)
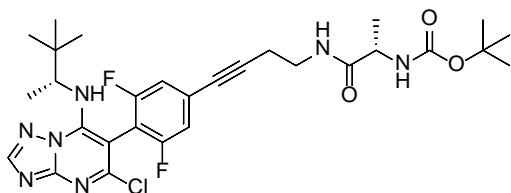
To a solution of **192** (28 mg, 69 µmol) in degassed DMF (1.0 ml), copper(I) iodide (2.0 mg, 10 µmol), triethylamine (29 µl, 0.21 mmol) and _tert_-butyl (_S_)-(1-(but-3-yn-1-ylamino)-1-oxopropan-2-yl)carbamate (**228**) (50 mg, 0.21 mmol) were added. The mixture was degassed and backfilled with N₂ before tetrakis(triphenylphosphine)palladium(0) (8.0 mg, 6.9 µmol) was added. The mixture was degassed and backfilled with N₂ three times and stirred at room temperature overnight. TLC in 100% EtOAc showed complete conversion of the starting material; therefore, the stirring was stopped and the reaction mixture was quenched with water (1 ml) and extracted with EtOAc (5 ml x 3). The combined organic layers were washed with brine (5 ml), dried over Na₂SO₄ and concentrated in vacuo. The crude residue was purified over silica (-Solvent A: hexane -Solvent B: EtOAc -Gradient: 20-50% of solvent B) to give **230** (33 mg, 79%) as a colorless oil. ^{1}H NMR (600 MHz, CDCl₃) δ 8.34 (s, 1H), 7.14 (d, J = 7.4 Hz, 2H), 6.43 (s, 1H), 4.93 (s, 1H), 4.17 (s, 2H), 3.59 – 3.47 (m, 2H), 2.68 (t, J = 5.9 Hz, 2H), 2.48 (s, 1H), 1.44 (s, 9H), 1.39 (s, 3H), 1.02 (d, J = 6.7 Hz, 3H), 0.84 (s, 9H). HRMS (ES+) calculated for $C_{29}H_{37}ClF_2N_7O_3^+$ [M+H]+: 604.2609, found 604.2605.

***Tert*-butyl (*R*)-(2-((4-(4-(5-chloro-7-((3,3-dimethylbutan-2-yl)amino)-[1,2,4]triazolo[1,5-*a*]pyrimidin-6-yl)-3,5-difluorophenyl)but-3-yn-1-yl)amino)-2-oxoethyl)carbamate (231)**
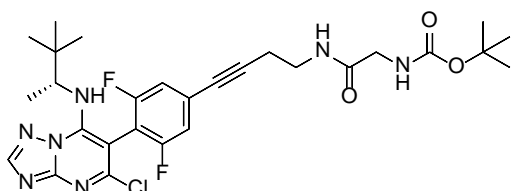
To a solution of **192** (45 mg, 0.11 mmol) in degassed DMF (0.55 ml), copper(I) iodide (3.2 mg, 17 µmol), triethylamine (46 µl, 0.33 mmol) and **229** (75 mg, 0.33 mmol) were added. The mixture was degassed and backfilled with N_2 before tetrakis(triphenylphosphine)palladium(0) (13 mg, 11 µmol) was added. The mixture was degassed and backfilled with N_2 three times and stirred at room temperature overnight. TLC in 100% EtOAc showed complete conversion of the starting material, therefore the stirring was stopped and the reaction mixture was quenched with water (1 ml) and extracted three times with EtOAc (5 ml x 3). The combined organic layers were washed with brine (5 ml), dried over Na_2SO_4 and concentrated in vacuo. The crude residue was purified over silica (-Solvent A: hexane -Solvent B: EtOAc -Gradient: 20-50% of EtOAc) to furnish **231** (45 mg, 69%) as a colorless oil. ^{1}H NMR (600 MHz, CDCl$_3$) δ 8.47 (br. s., 1H), 7.13 (d, *J* = 8.2 Hz, 2H), 6.56 (s, 1H), 6.43 (br. s., 1H), 5.14 (s, 1H), 3.83 (d, *J* = 5.5 Hz, 2H), 3.55 (d, *J* = 6.2 Hz, 1H), 2.70 (t, *J* = 6.5 Hz, 2H), 1.44 (s, 9H), 1.02 (d, *J* = 6.6 Hz, 3H), 0.83 (s, 9H) ppm. HRMS (ES$^+$) calculated for C$_{28}$H$_{35}$ClF$_2$N$_7$O$_3$$^+$ [M+H]$^+$: 590.2452, found 590.2444.

(*S*)-2-amino-*N*-(4-(4-(5-chloro-7-(((*R*)-3,3-dimethylbutan-2-yl)amino)-[1,2,4]triazolo[1,5-*a*]pyrimidin-6-yl)-3,5-difluorophenyl)but-3-yn-1-yl)propanamide, formic acid (232)
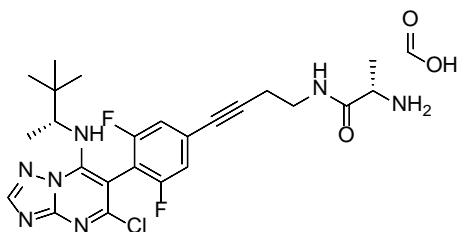
A solution of **230** (33 mg, 55 µmol) in 4M HCl solution in 1,4-dioxane (82 µl, 0.33 mmol) was stirred overnight under N$_2$ atmosphere. The reaction was checked by TLC (100% EtOAc) noticing complete conversion of the starting material; therefore, the stirring was stopped and the mixture was concentrated in vacuo. The crude was purified by preparative HPLC (Water/ACN with 0.1% FA, 5-80% ACN in 18 min, flow rate: 30 ml/min) to obtain **232** (15 mg, 50%) as a white powder. ^{1}H NMR (600 MHz, CD$_3$CN) δ 8.35 (s, 1H), 7.25 (d, *J* = 9.3 Hz, 2H), 6.50 (s, 1H), 5.35 (s, 1H), 4.01 (q, *J* = 7.2 Hz, 1H), 3.73 – 3.15 (m, 2H), 2.67 (d, *J* = 6.7 Hz, 2H), 1.48 (d, *J* = 7.1 Hz, 3H), 1.02 (d, *J* = 6.7 Hz, 3H), 0.81 (s, 9H). ^{13}C NMR (151 MHz, DMSO-*d$_6$*) δ 169.75, 158.00, 157.69, 155.87-114.85 (m), 146.84, 127.28, 115.39, 92.61, 79.17, 57.91, 48.24, 37.54, 35.23, 25.61, 19.64, 17.32, 15.20. HRMS (ES+) calculated for C$_{24}$ H$_{29}$ Cl F$_2$ N$_7$ O$^+$ [M+H]$^+$: 504.2085, found 504.2084.

(*R*)-2-amino-*N*-(4-(4-(5-chloro-7-((3,3-dimethylbutan-2-yl)amino)-[1,2,4]triazolo[1,5-*a*]pyrimidin-6-yl)-3,5-difluorophenyl)but-3-yn-1-yl)acetamide, formic acid (233)
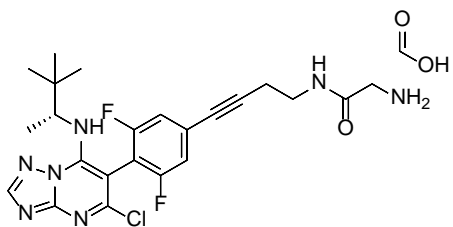
A solution of **231** (45 mg, 76 µmol) in HCl in 1,4-Dioxane solution (17 mg, 0.11 ml, 4 molar, 0.46 mmol) was stirred 6 h under inert atmosphere. The reaction was checked by TLC (EtOAc 100%) noticing complete conversion of

the starting material, therefore the mixture was concentrated in vacuo. The crude was purified twice by preparative HPLC (Water/ACN with 0.1% FA, 5-80% ACN in 18 min, flow rate: 30 ml/min) to obtain **233** (15 mg, 28 µmol, 37%) as a white powder. ^{1}H NMR (600 MHz, CD$_3$CN) δ 8.35 (s, 1H), 7.46 (br. s., 1H), 7.26 (d, J = 9.2 Hz, 2H), 7.17 (s, 1H), 3.69 (s, 2H), 3.47 (q, J = 6.6 Hz, 2H), 2.66 (t, J = 6.7 Hz, 2H), 1.03 (d, J = 6.7 Hz, 3H), 0.81 (s, 9H). HRMS (ES$^+$) calculated for C$_{23}$H$_{27}$ClF$_2$N$_7$O$^+$ [M+H]$^+$: 490.1928, found 490.1927.

Biological assays:

Human CMGC Kinase Enzymatic Radiometric Assay [Km ATP], KinaseProfiler (performed at Eurofins Cerep, Poitiers, France):

h-Fyn is incubated with 50 mM Tris pH 7.5, 0.1 mM EGTA, 0.1 mM Na$_3$VO$_4$, 250 µM KVEKIGEGTYGVVYK (Cdc2 peptide), 10 mM Magnesium Acetate and [gamma-33P]-ATP (specific activity and concentration as required). The reaction is initiated by the addition of the Mg/ATP mix. After incubation for 40 minutes at room temperature, the reaction is stopped by the addition of phosphoric acid to a concentration of 0.5%. An aliquot of the reaction is then spotted onto a filter and washed four times for 4 minutes in 0.425% phosphoric acid and once in methanol prior to drying and scintillation counting.

h-GSK-3β is incubated with 8 mM MOPS pH 7.0, 0.2 mM EDTA, 20 µM YRRAAVPPSPSLSRHSSPHQS(p) EDEEE (phospho GS2 peptide), 10 mM Magnesium Acetate and [gamma-33P]-ATP (specific activity and concentration as required). The reaction is initiated by the addition of the Mg/ATP mix. After incubation for 40 minutes at room temperature, the reaction is stopped by the addition of phosphoric acid to a concentration of 0.5%. An aliquot of the reaction is then spotted

onto a filter and washed four times for 4 minutes in 0.425% phosphoric acid and once in methanol prior to drying and scintillation counting.

h-DYRK1A is incubated with 8 mM MOPS pH 7.0, 0.2 mM EDTA, 50 µM RRRFRPASPLRGPPK, 10 mM Magnesium Acetate and [gamma-33P]-ATP (specific activity and concentration as required). The reaction is initiated by the addition of the Mg/ATP mix. After incubation for 40 minutes at room temperature, the reaction is stopped by the addition of phosphoric acid to 21 a concentration of 0.5%. An aliquot of the reaction is then spotted onto a filter and washed four times for 4 minutes in 0.425% phosphoric acid and once in methanol prior to drying and scintillation counting.

h-CDK5/p25 is incubated with 8 mM MOPS pH 7.0, 0.2 mM EDTA, 0.1 mg/ml histone H1, 10 mM Magnesium Acetate and [g- 33P]-ATP (specific activity and concentration as required). The reaction is initiated by the addition of the Mg/ATP mix. After incubation for 40 minutes at room temperature, the reaction is stopped by the addition of phosphoric acid to a concentration of 0.5%. An aliquot of the reaction is then spotted onto a filter and washed four times for 4 minutes in 0.425% phosphoric acid and once in methanol prior to drying and scintillation counting.

For all tested PKs the Pan-kinase inhibitor Staurosporine was used as a reference compound.

LANCE® Ultra system time-resolved fluorescence resonance energy transfer (TR-FRET) assay (performed by D.R. and I.P.)

GSK-3β,Fyn-A and DYRK-1A Kinase Assays

Inhibition of GSK-3β, FYNα and DYRK-1A activity has been evaluated using the LANCE Ultra technology from PerkinElmer according to the manufacturer's instructions. LANCE® Ultra system is based on the TR-FRET between a donor

fluorophore (LANCE Europium Chelate) and an acceptor dye called ULight^{TM}, a small molecular weight dye with a red-shifted fluorescent emission.

The synthetic peptide surrounding Ser 641 of human Muscle Glycogen Synthase (ULight-GS (Ser 641/pSer 657)) has been selected as substrate for GSK-3β and DYRK-1A, while the synthetic 28-amino acid peptide containing eight Tyr residues placed in different amino acid contexts (ULightTM-TK (PT66)) was used for FYNα assay.

The kinases reaction has been detected using EnVision 2014 Multilabel Reader (PerkinElmer, Massachusetts, USA) after irradiation at 320 nm and the fluorescence measured at 615 and 665 nm. The latter signal is specific for the energy transfer occurring between donor and acceptor when are in close proximity (~10 nm). The calculated signal ratio at 665/615 nm is proportional to the extent of ULight-substrate phosphorylation.

Protocol

GSK-3β, DYRK-1A and FYNα kinase assays were run in 384 well microplates (OptiPlate^{TM}-384, White, Perkin Elmer) in a total reaction volume of 20 µL. The inhibitory potency against human recombinant GSK-3β, DYRK-1A and FYNα (Carna Biosciences) was evaluated using the LANCE® Ultra (Perkin Elmer) time-resolved fluorescence resonance energy transfer (TR-FRET) by measuring the phosphorylation of the ULight-labeled substrate, according to the manufacturer's instructions.

The synthetic peptide surrounding Ser641 of human Muscle Glycogen Synthase (ULight-GS (Ser641/pSer657)) has been selected as specific substrate for GSK-3β and DYRK-1A, while the synthetic 28-amino acid peptide containing eight Tyr residues placed in different amino acid contexts (ULightTM-TK (PT66)) was used for FYNα assay.

Briefly, test compounds, staurosporine or harmine (reference compounds for GSK-3 β/Fynα and DYRK-1A, respectively) or DMSO (control) were mixed with the enzyme (2 nM, 4 nM and 1 nM, respectively) in a buffer containing 50 mM Hepes (pH 7.5), 1 mM EGTA, 10 mM $MgCl_2$, 2 mM DTT and 0.01% Tween-20.

The reaction is initiated by adding 50 nM of the substrate and 1.2, 1.7 or 8 µM ATP (GSK-3β, DYRK-1A and FYNα, respectively), and the mixture is incubated for 60 (GSK-3β and DYRK-1A) or 90 (FYNα) minutes, respectively, at 23 °C. Following incubation, the reaction is stopped by adding 8 mM EDTA. After 5 min, the anti-phospho antibody labeled with europium chelate is added. After 1 more hour, the kinase reaction is monitored by irradiation at 320 nm, and the fluorescence measured at 615 and 665 nm, using EnVision 2014 Multilabel Reader (PerkinElmer). The calculated signal ratio at 665/615 nm is proportional to the extent of ULight-GS phosphorylation. The compounds were first tested at three concentrations and in 11-points dose-response (range 100 pM – 10 µM for GSK-3β and FYNα and 1 nM - 100 µM for DYRK-1A), in triplicates. The results were expressed as a percent inhibition of the control enzyme activity.

Analysis of the Biological Data

Dose-response curves were run at least in three independent experiments, performed in three technical replicates. IC_{50} values for GSK-3β, DYRK-1Aand FYNα assays were determined by non-linear regression analysis of the Log [concentration]/response curves generated with mean replicate values using a four parameter Hill equation curve fitting with GraphPad Prism 8 (GraphPad Software Inc., CA – USA).

Cellular kinase NanoBRET™ Assay, **performed at Reaction Biology (PA, USA)**

HEK293 cells were purchased from ATCC. FuGENEHD Transfection Reagent, Kinase-NanoLucfusion plasmids, Transfection Carrier DNA, NanoBRETTracers and dilution buffer, NanoBRETNano-Glo Substrate, Extracellular NanoLucInhibitor were obtained from Promega. Compounds were purchased from Selleckchem or made in house.

Assays were conducted following Promega assay protocol with some modifications. HEK293 Cells were transiently transfected with Kinase-NanoLucFusion Vector DNA by FuGENEHD Transfection Reagent. Testing compounds were delivered into 384 well assay plate by Echo 550 (LabcyteInc, Sunnyvale, CA). Transfected cells were harvested and mixed with NanoBRETTracer Reagent and dispensed into 384 well plates and incubated the plates at 37 °C in 5% CO_2 cell culture incubator for 1 h. The NanoBRETNano-Glo Substrate plus Extracellular NanoLucInhibitor Solution were added into the wells of the assay plate and incubated for 2–3 min at room temperature. The donor emission wavelength (460 nm) and acceptor emission wavelength (600 nm) were measured in the EnVisionplate reader. The BRET Ratio were calculated. BRET Ratio = [(Acceptor sample÷Donor sample)–(Acceptor no-tracer control÷Donor no-tracer control)]. The IC_{50} values of compounds were calculated with Prism GraphPad program.

Tau Phosphorylation Assay in human recombinant Tau0N4R-TM-tGFP U2OS cells, performed at Innoprot (Spain)

Dose-response assays were performed using a cellular fluorescence bundle formation assay after compound addition in human recombinant Tau0N4R-TM-tGFP U2OS stable cell line. The formation of tau and MT bundles after treatment was

measured in triplicate. Medium (OptiMem) and Vehicle (DMSO) were used as negative controls and LiCl 30 mM as positive control. Bundles were quantified using the Cell Insight CX7 from Thermofisher. The error bars represent the standard deviation among the 3 replicate wells.

In vitro ADME-PK evaluation (performed by G.O. at the IIT analytical facility)

In vitro mouse plasma stability

Compounds were diluted in preheated (37 °C) mouse plasma (Rockland Immunochemicals Inc.) with 5% DMSO to favor solubilization. The final compound concentration was 2.0 μM. At time points (0, 5, 15, 30, 60, 120 min), a 30 μL aliquot of the incubation solution was diluted in 200 μL of cold acetonitrile spiked with 200 nM Warfarin, as internal standard. After vortexing for 30 s, the solution was centrifuged at 3500g for 15 min at 4 °C, and the supernatant transferred for LC-MS/MS analysis on a Waters Acquity UPLC/MS TQD system. Compound stability was evaluated on the basis of the corresponding peak areas plotted *vs* time. The compounds' half-lives were calculated using a one-phase fitting decay of the peak area *vs* time profiles.

In vitro mouse liver microsomes stability

10mM DMSO stock solution of test compound was pre-incubated at 37 ˚C for 15 min with liver microsomes (Sekisui Xenotech, LCC), 0.1M Tris-HCl buffer (pH 7.4), and 10% DMSO. The final concentration was 4.6 μM. After pre-incubation, the cofactors (NADPH, G6P, G6PDH, MgCl2 pre-dissolved in 0.1M Tris-HCl) were added to the incubation mixture and the incubation was continued at 37 ˚C for 1h. At each time point (0, 5, 15, 30, 60 min), 30μl of incubation mixture was diluted with 200 μl cold acetonitile spiked with 200 nM of warfarin as internal standard, followed by

centrifugation at 3500 g for 30 min. The supernatant was further diluted with H2O (1:1) for analysis. An aliquot of 200 μl of the supernatant was removed, and the concentration of the test compound was quantified by LC-MS/MS. The percentage of the test compound remaining at each time point relative to t=0 was calculated. The half-lives (t½) were determined by a one-phase decay equation using a non-linear regression of compound concentration *vs* time.

In vitro **human liver microsomes stability.**

Human (BD Gentest) hepatocytes were thawed in Hepatocyte Plating Supplement pack (Life Technologies) and placed in 37 ± 1 °C shaking water. Hepatocytes were re-suspended in Williams E medium containing Cell Maintenance Supplement Pack (Life Technologies), and counted using Trypan blue solution to a final concentration of 0.25 x 106 cells/ml. Samples of the test compound at 10 μM were incubated for 0, 10, 30, 60, 120, and 240 min at 37 °C. Blank samples were prepared by incubating 250 μl of cell solution without any compound for 240 min. The incubations were quenched 1:1 with ice-cold acetonitrile spiked with 600 nM labetalol as internal standard. Samples were then centrifuged at 12000 rpm for 5 min at 4 °C. Aliquots of 200 μl of the supernatant were removed and the concentration of the test compound was quantified by LC-MS/MS. The percentage of the test compound remaining at each time point relative to t=0 was calculated. The half-lives (t½) were determined by a one-phase decay equation using a non-linear regression of compound concentration *vs* time.

X-ray studies, protein purification (performed by S.K.T.):

GSK-3β:

Human full length GSK3β sequence (1-400) was overexpressed in High 5 insect cells as previously described.[227] For purification a cell pellet of $900x10^6$ cells was thawed and re-suspended in lysis buffer (20 mM TRIS pH 8.0, 0.5 M NaCl, 10 mM Imidazole, 1 mM DTT, 5 mM MgCl2, 0.5x protease inhibitor EDTA free *(Roche)*, 5% glycerol, 0.01% Tween20) and lysed by sonication (12' pulse at 60-70% intensity). After sonication, lysate solution was incubated for 20 minutes at 4 °C with DNAseI (5 ug/ml final working concentration), and centrifuged for 1 h at 30000 g in 4 °C. The supernatant solution, containing the protein of interest, was used for further purification. First, the clarified supernatant was incubated for 2 h with Ni-NTA agarose resin (Qiagen). The protein bound resin was washed with binding buffer (20 mM TRIS pH 8.0, 0.5 M NaCl, 10 mM Imidazole, 5% glycerol, 1 mM DTT). Protein elution was obtained by addition of 300 mM Imidazole to the binding buffer. Eluted protein solution was further purified using a cationic exchange column *HiTrap HP SP,* equilibrated with buffer A (20 mM Hepes pH 7.5, 40 mM NaCl, 5% glycerol, 1 mM DTT). Different isoforms, corresponding to different GSK3β phosphorelation states, were separated by applying a linear gradient to Buffer B (20 mM Hepes pH 7.5, 1 M NaCl, 5% glycerol, 1 mM DTT). The GSK3β isoforms were separately collected and stored at -80 °C.

DYRK1A:

For DYRK1A, a pET28a vector, inserted with codon optimized C-DNA sequence (coding for DYRK1A kinase domain residue 127-485) between NcoI/XhoI site was used. The expressed DYRK1A Kinase domain, contained a N-terminal Hexa-His tag separated from the protein by a 3C protease cleavage tag. *E.coli* cells

(BL21DE3) transfected with this vector, were used to overexpress the protein. Briefly, an overnight culture was used to inoculate 1 L Luria-Bertani (LB) medium supplemented with 50 µM kanamycin. Protein overexpression was induced by addition of 0.5 mM IPTG when OD_{600} reached 0.6. After overnight bacteria growth at 25 °C, cells were pelleted, and lysis was performed in 50 mM potassium phosphate pH 7.4, 500 mM NaCl, 1 mM DTT, 5% glycerol, 0.5x protease inhibitor (EDTA free) using sonication. The first purification step was a His-trap affinity chromatography using the equilibration buffer: 50 mM potassium phosphate pH 7.4, 500 mM NaCl, 1 mM DTT, 5% glycerol and 5 mM imidazole. After an initial wash with the 25 mM imidazole buffer, the elution was performed using 200 mM imidazole. His-tag was removed by overnight incubation of the purified protein with 3C protease at 4 °C. His-trap affinity chromatography was then run, to remove the un-cleaved protein and the His-Tag. The final purification step was performed with a Superdex 200 increase (GE Healthcare) column with the following running buffer:50 mM Mes 6.5, 100 mM KCl, 1 mM DTT and 5% glycerol. The purified protein was finally stored at -80 °C.

Protein Crystallization:

GSK3β protein was concentrated to 4 mg/ml in the buffer 20 mM Hepes p 7.5, 150 mM NaCl and 1 mM DTT. Compound solution was prepared (0.5 – 2 mM final concentration) in the buffer 20 mM Hepes p 7.5, 150 mM NaCl. This buffer was mixed with protein solution to get final protein concentration of 2 mg/ml and compound concentration of 0.25 to 1 mM. Complex crystallization was performed using hanging drop vapor diffusion method. Drops were prepared by mixing 1µl of protein solution with 1 µl of reservoir solution (20 mM Hepes 7.5, 15-20% Polyethylene glycol 3350, 100 mM NaCl). The same protocol was used for all the compounds and resulted in crystals next day. Crystals were allowed to grow for one week. Crystals were soaked

in the reservoir buffer supplemented with 20% glycerol for cryoprotection before being frozen by plunging directly into liquid nitrogen.

DYRK1A crystallization was also performed by the hanging drop method. Final protein concentration was 4-5 mg/ml in 50 mM Mes 6.5, 100 mM KCl, 1 mM DTT, 5% glycerol. Reservoir buffer was 50 mM Mes 6.5, 150 mM KCl, 15-20% polyethylene glycol 1000. Protein solution was mixed with the reservoir buffer in a 1:1 ratio, and equilibrated against the reservoir buffer. Crystals appeared in one day and grew for a weak. Crystals were soaked for 5-6 h in 50 mM Mes 6.5, 150 mM KCl, 20% PEG 1000 buffer and 1-2 mM compound concentrations. Here also same soaking protocol was used for all the compounds. Crystals were frozen in liquid nitrogen after scooping directly from the soaking solution.

Diffraction data collection on protein crystals:

X-ray diffraction data were collected at the XRD2 beamline in Elettra Synchrotron, Trieste, Italy. For all the crystals, total 720 diffraction images were collected each corresponding to 0.5 degree rotation, finally covering entire 360 degree of reciprocal space. Data integration was performed using iMOSFLM in CCP4 (1). Data scaling is performed using AIMLESS.[277] Structures were solved by molecular replacement using PHASER in CCP4.[278] For molecular replacement the following available structures were used: PDB ID 6H0U (for GSK3β) and 3ANQ (for DYRK1A). Structures were refined using REFMAC.[279] Model modification, visualization and evaluation was performed using Coot.[280] Images were prepared using Pymol. [281]

Computational modeling and chemical docking (performed by C.S.).

Multiple relevant published structures of each of the human proteins GSK-3β, CDK5, DYR1A, and FYN were obtained from PDB and combined into conformational

stacks using ICM pro software, version 3.9-2b. From these stacks, flexible receptor 4D grids were generated, and compound **72** was docked *in silico*. Binding scores representing Gibbs free energy were calculated, also using ICM pro.[282]

QBI293 Cell and Neuronal Culture Acetyl-Tubulin and α-Tubulin Determinations

Compound-induced changes in acetylated-tubulin and α-tubulin in QBI293 cells or primary mouse or rat neurons were as previously described.[46, 283] For compound testing, QBI293 cells were plated at a density of 2×105 cells/well in 12-well plates. The plated cells were incubated overnight, after which the medium was aspirated and fresh medium containing vehicle (0.25−0.3% DMSO) or test compound was added. Test compounds were prepared as 4−20 mM stock solutions in 100% DMSO, and these were diluted in culture medium prior to addition to the QBI293 cells. After 4 h incubation, whole-cell extracts were prepared from the QBI293 cells as described[283] and the supernatant fraction from each sample was assessed for protein content by bicinchoninic acid (BCA) assay. The amount of acetyl-tubulin (AcTub) and α-tubulin (αTub) within the cell extract samples was quantified using specific enzyme-linked immunosorbent assays (ELISA), as previously described.[283] Acetyltubulin levels were determined in a similar manner in rat or mouse cortical neuron cultures in which embryonic dissociated cortical neurons were plated at 3×105 cells/well in poly-D-lysine-coated 12well plates, essentially as previously described.[283] The neurons were allowed to grow for 10 days before they were treated for 8 h with 15 nM okadaic acid in the presence or absence of test compound prepared as described above, or vehicle (0.25% DMSO). Culture homogenates were prepared for the determination of AcTub levels by ELISA as previously described.[283]

Determination of Plasma Pharmacokinetics of Compound 184 (performed at the Center for Neurodegenerative Disease Research-UPenn - Prof. Kurt R. Brunden's Lab)

Studies to determine the pharmacokinetic properties of compound **184** were conducted at Touchstone Biosciences (Plymouth Meeting, PA). For the determination of plasma pharmacokinetics, three male CD-1 mice (2−3 months of age) were injected i.v. (tail vein) with test compound at a dose of 5 mg/kg in a solution of 10% DMSO, 40% polyethylene glycol, and 50% water. Blood samples were collected from the saphenous or submandibular veins at multiple time points after dosing and collected in Greiner MiniCollect K2EDTA tubes. Compound levels in plasma were determined by LC-MS/MS, using protocols similar to those previously described.[284, 285]

Assessment of Glu-Tubulin in Brain Tissue after treatment with 184 (performed at the Center for Neurodegenerative Disease Research-UPenn - Prof. Kurt R. Brunden's Lab)

All animal protocols were approved by the University of Pennsylvania Institutional Animal Care and Use Committee (IACUC). Groups of four CD-1 mice received two i.p. injections of compounds **184** at 1 mg/kg or vehicle only spaced approximately 24 h apart. Compounds were diluted from 20 or 40 mM DMSO stock solutions into 30% Kolliphor EL (Sigma-Aldrich) phosphate-buffered saline, pH 7.4. After 4 h following the second injection, mice were euthanized and cortices and hippocampi were isolated from each brain and placed in 0.2 mL of ice-cold radioimmunoprecipitation assay (RIPA) buffer (50 mM Tris, 150 mM NaCl, 5 mM EDTA, 0.5% sodium deoxycholate, 1% NP-40, 0.1% sodium dodecyl sulfate (SDS), pH 8.0) containing protease inhibitor (PI) cocktail (Sigma-Aldrich), 1 mM phenylmethylsulfonyl fluoride (PMSF) (Sigma-Aldrich), and 3 μM trichostatin A

(TSA) (SigmaAldrich). The brain samples were homogenized with a handheld battery-operated mixer and subsequently sonicated. After centrifugation at 100,000g for 30 min at 4 °C, supernatant samples were transferred to a new tube and the pellets were resuspended in 0.15 mL of RIPA buffer and again homogenized, sonicated, and centrifuged. The supernatant from the second centrifugation was pooled with that from the first. The combined supernatant samples were assessed for protein concentration using a BCA assay (Thermo Fisher Scientific), and equal protein amounts from each brain sample underwent separation by 10% sodium dodecyl sulfate polyacrylamide gel electrophoresis (SDS-PAGE) followed by transfer onto nitrocellulose membranes essentially as previously described.[283] Membranes were incubated overnight in primary antibodies in blocking buffer at 4 °C, utilizing antibodies to de-tyrosinated (Glu)-tubulin, α-tubulin, and glyceraldehyde-3-phosphate dehydrogenase as previously described.[283]

Figures 1.1, 1.9, 1.10, 1.21, 2.25, 3.3, 3.8 have been created with BioRender.com.

Appendix

^{1}H and ^{13}C spectra of compound **72** (**ARN25068**).
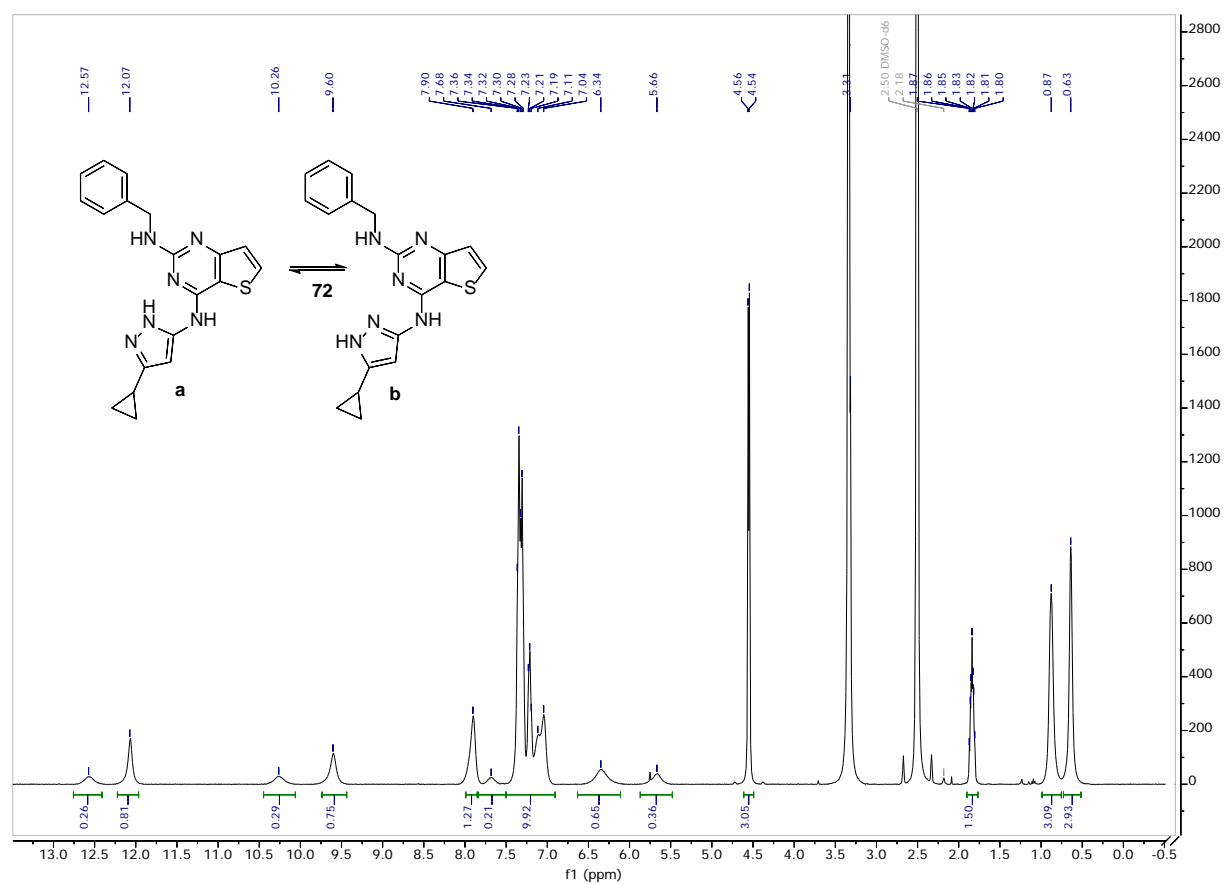
Figure A1 ^{1}H NMR (600 MHz, DMSO-d_6) of compound **72** (**ARN25068**).
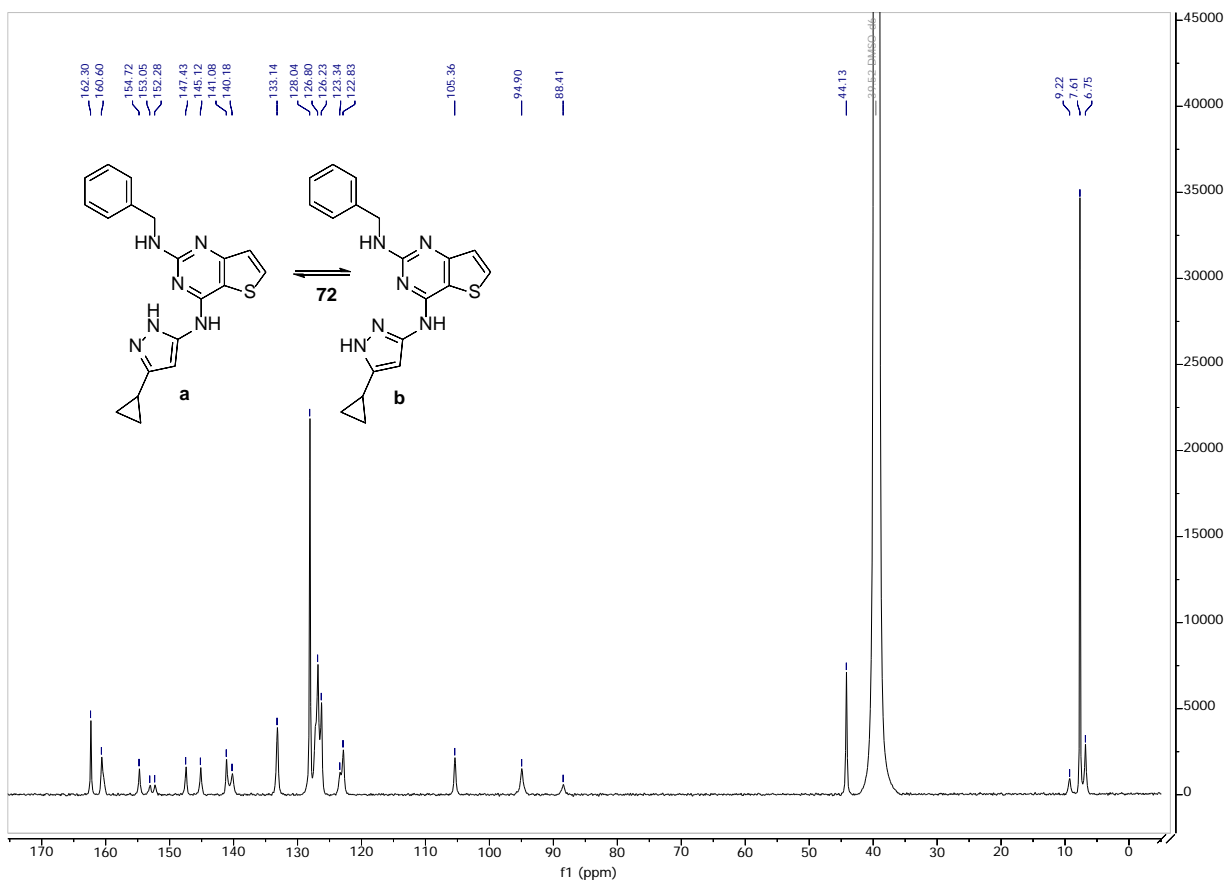
Figure A2 ^{13}C NMR (151 MHz, DMSO-d_6) of compound **72** (**ARN25068**).
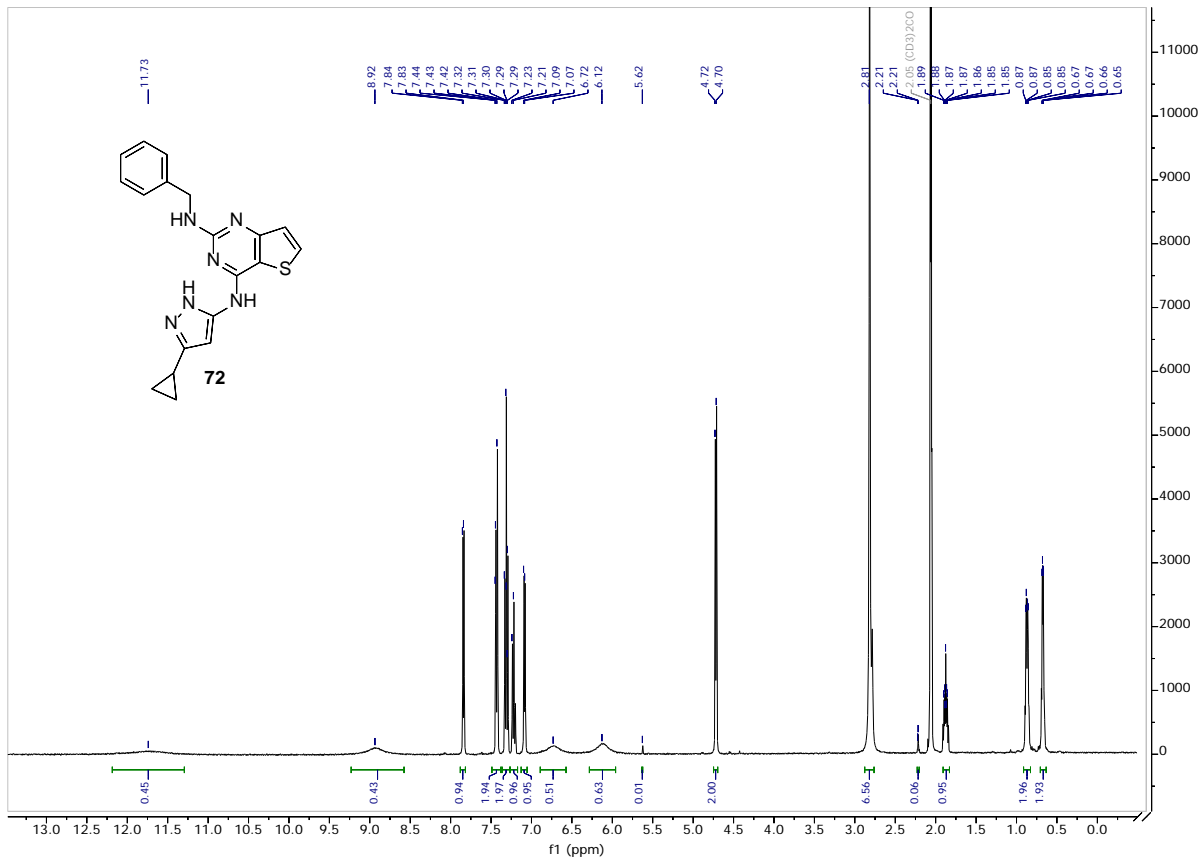
Figure A3 ^{1}H NMR (400 MHz, acetone-d_6) of compound **72**
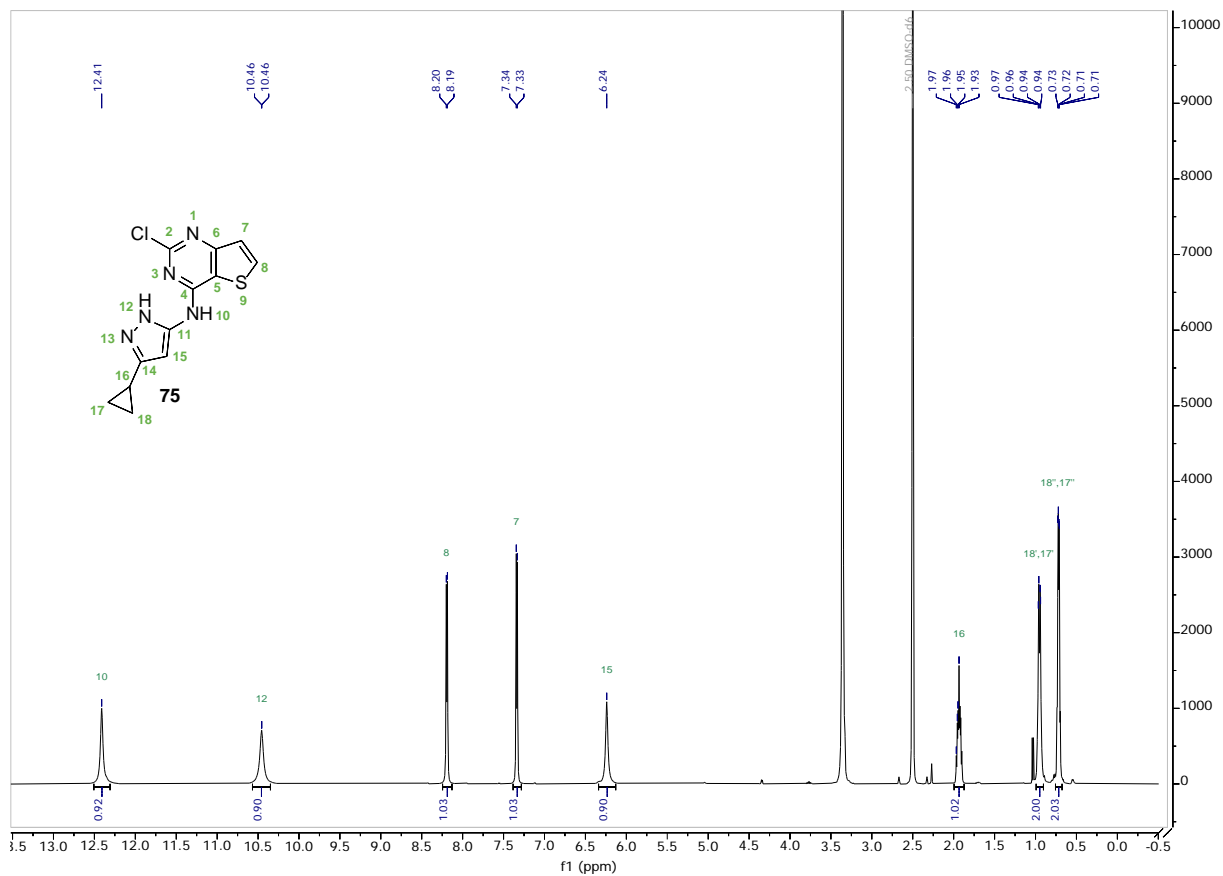
Figure A4 ^{1}H NMR (400 MHz, DMSO-d_6) of intermediate **75**.
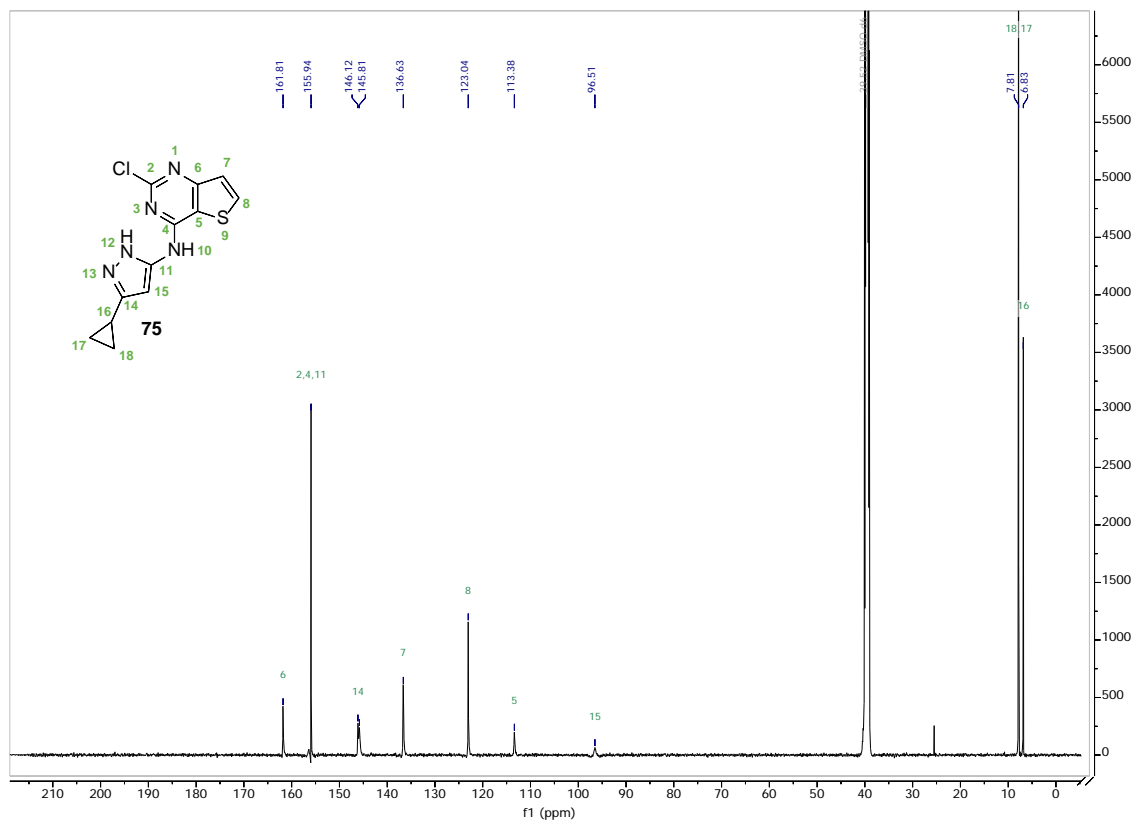
Figure A5 ^{13}C NMR (151 MHz, DMSO-d_6) of intermediate **75**.
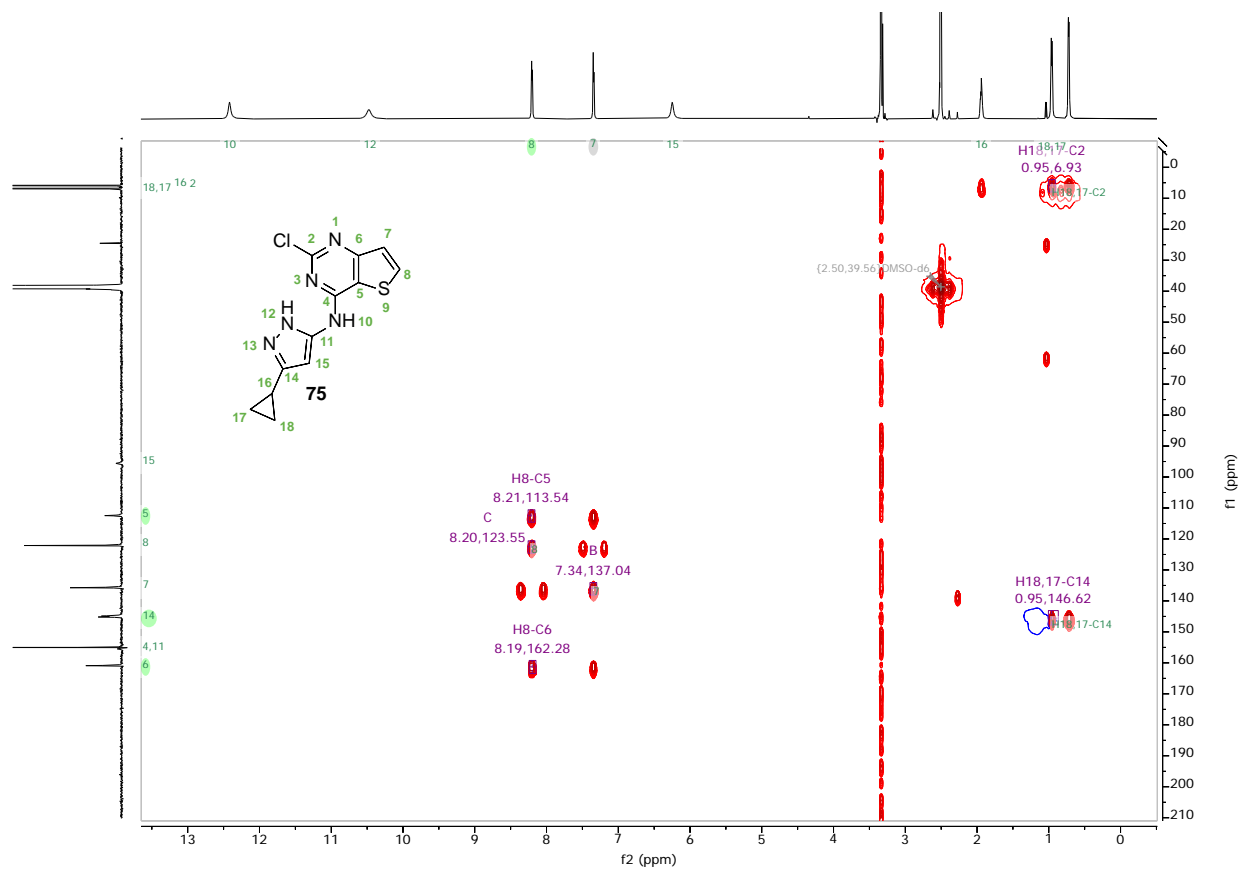
Figure A6 ^{1}H -^{13}C HMBC (600 MHz, DMSO-d_6) of intermediate **75**

References

1.   Kapitein, L. C.; Hoogenraad, C. C., Building the neuronal microtubule cytoskeleton. *Neuron* **2015,** *87* (3), 492-506.

2.   McIntosh, J. R., Mitosis. *Cold Spring Harb Perspect Biol* **2016,** *8* (9).

3.   Ganguly, A.; Yang, H.; Sharma, R.; Patel, K. D.; Cabral, F., The role of microtubules and their dynamics in cell migration. *J Biol Chem* **2012,** *287* (52), 43359-69.

4.   Goodson, H. V.; Jonasson, E. M., Microtubules and Microtubule-Associated Proteins. *Cold Spring Harb Perspect Biol* **2018,** *10* (6).

5.   Manka, Szymon W.; Moores, Carolyn A., Microtubule structure by cryo-EM: snapshots of dynamic instability. *Essays in Biochemistry* **2018,** *62* (6), 737-751.

6.   Zhang, R.; Alushin, G. M.; Brown, A.; Nogales, E., Mechanistic Origin of Microtubule Dynamic Instability and Its Modulation by EB Proteins. *Cell* **2015,** *162* (4), 849-59.

7.   Xiao, Q.; Xue, T.; Shuai, W.; Wu, C.; Zhang, Z.; Zhang, T.; Zeng, S.; Sun, B.; Wang, Y., High-resolution X-ray structure of three microtubule-stabilizing agents in complex with tubulin provide a rationale for drug design. *Biochem Biophys Res Commun* **2021,** *534*, 330-336.

8.   Conde, C.; Caceres, A., Microtubule assembly, organization and dynamics in axons and dendrites. *Nat Rev Neurosci* **2009,** *10* (5), 319-32.

9.   Mitchison, T.; Kirschner, M., Dynamic instability of microtubule growth. *Nature* **1984,** *312* (5991), 237-42.

10.   Akhmanova, A.; Steinmetz, M. O., Control of microtubule organization and dynamics: two ends in the limelight. *Nat Rev Mol Cell Biol* **2015,** *16* (12), 711-26.

11. Nogales, E., Structural insights into microtubule function. *Annual Review of Biophysics and Biomolecular Structure* **2001,** *30*, 397-420.

12. Nogales, E.; Wolf, S. G.; Downing, K. H., Structure of the alpha beta tubulin dimer by electron crystallography. *Nature* **1998,** *391* (6663), 199-203.

13. Roll-Mecak, A., The tubulin code in microtubule dynamics and information encoding. *Dev Cell* **2020,** *54* (1), 7-20.

14. Moritz, M.; Braunfeld, M. B.; Sedat, J. W.; Alberts, B.; Agard, D. A., Microtubule nucleation by gamma-tubulin-containing rings in the centrosome. *Nature* **1995,** *378* (6557), 638-40.

15. Janke, C.; Magiera, M. M., The tubulin code and its role in controlling microtubule properties and functions. *Nat Rev Mol Cell Biol* **2020,** *21* (6), 307-326.

16. MacTaggart, B.; Kashina, A., Posttranslational modifications of the cytoskeleton. *Cytoskeleton (Hoboken)* **2021,** *78* (4), 142-173.

17. Song, Y.; Kirkpatrick, Laura L.; Schilling, Alexander B.; Helseth, Donald L.; Chabot, N.; Keillor, Jeffrey W.; Johnson, Gail V. W.; Brady, Scott T., Transglutaminase and polyamination of tubulin: posttranslational modification for stabilizing axonal microtubules. *Neuron* **2013,** *78* (1), 109-123.

18. Al-Bassam, J.; Corbett, K. D., alpha-Tubulin acetylation from the inside out. *Proc Natl Acad Sci U S A* **2012,** *109* (48), 19515-6.

19. Fourest-Lieuvin, A.; Peris, L.; Gache, V.; Garcia-Saez, I.; Juillan-Binard, C.; Lantez, V.; Job, D., Microtubule regulation in mitosis: tubulin phosphorylation by the cyclin-dependent kinase Cdk1. *Mol Biol Cell* **2006,** *17* (3), 1041-50.

20. Ori-McKenney, K. M.; McKenney, R. J.; Huang, H. H.; Li, T.; Meltzer, S.; Jan, L. Y.; Vale, R. D.; Wiita, A. P.; Jan, Y. N., Phosphorylation of beta-Tubulin by the Down Syndrome kinase, Minibrain/DYRK1a, regulates microtubule dynamics and dendrite morphogenesis. *Neuron* **2016,** *90* (3), 551-63.

21.   Sweeney, H. L.; Holzbaur, E. L. F., Motor Proteins. *Cold Spring Harb Perspect Biol* **2018,** *10* (5).

22.   Guillaud, L.; El-Agamy, S. E.; Otsuki, M.; Terenzio, M., Anterograde Axonal Transport in Neuronal Homeostasis and Disease. *Front Mol Neurosci* **2020,** *13*, 556175.

23.   Liem, R. K., Cytoskeletal Integrators: The Spectrin Superfamily. *Cold Spring Harb Perspect Biol* **2016,** *8* (10).

24.   Cassimeris, L., Microtubule Associated Proteins in Neurons. In *Encyclopedia of Neuroscience*, Squire, L. R., Ed. Academic Press: Oxford, 2009; pp 865-870.

25.   Weingarten, M. D.; Lockwood, A. H.; Hwo, S. Y.; Kirschner, M. W., A protein factor essential for microtubule assembly. *Proc Natl Acad Sci U S A* **1975,** *72* (5), 1858-62.

26.   Ballatore, C.; Lee, V. M.; Trojanowski, J. Q., Tau-mediated neurodegeneration in Alzheimer's disease and related disorders. *Nat Rev Neurosci* **2007,** *8* (9), 663-72.

27.   Wegmann, S.; Biernat, J.; Mandelkow, E., A current view on Tau protein phosphorylation in Alzheimer's disease. *Curr Opin Neurobiol* **2021,** *69*, 131-138.

28.   Goedert, M.; Spillantini, M. G.; Jakes, R.; Rutherford, D.; Crowther, R. A., Multiple isoforms of human microtubule-associated protein tau: sequences and localization in neurofibrillary tangles of Alzheimer's disease. *Neuron* **1989,** *3* (4), 519-26.

29.   Wang, Y.; Mandelkow, E., Tau in physiology and pathology. *Nat Rev Neurosci* **2016,** *17* (1), 5-21.

30.   Chen, J.; Kanai, Y.; Cowan, N. J.; Hirokawa, N., Projection domains of MAP2 and tau determine spacings between microtubules in dendrites and axons. *Nature* **1992,** *360* (6405), 674-677.

31.   Rosenberg, K. J.; Ross, J. L.; Feinstein, H. E.; Feinstein, S. C.; Israelachvili, J., Complementary dimerization of microtubule-associated tau protein: Implications

for microtubule bundling and tau-mediated pathogenesis. *Proc Natl Acad Sci U S A* **2008,** *105* (21), 7445-50.

32.   Goode, B. L.; Denis, P. E.; Panda, D.; Radeke, M. J.; Miller, H. P.; Wilson, L.; Feinstein, S. C., Functional interactions between the proline-rich and repeat regions of tau enhance microtubule binding and assembly. *Mol Biol Cell* **1997,** *8* (2), 353-65.

33.   Kadavath, H.; Hofele, R. V.; Biernat, J.; Kumar, S.; Tepper, K.; Urlaub, H.; Mandelkow, E.; Zweckstetter, M., Tau stabilizes microtubules by binding at the interface between tubulin heterodimers. *Proceedings of the National Academy of Sciences* **2015,** *112* (24), 7501-7506.

34.   Barbier, P.; Zejneli, O.; Martinho, M.; Lasorsa, A.; Belle, V.; Smet-Nocca, C.; Tsvetkov, P. O.; Devred, F.; Landrieu, I., Role of Tau as a Microtubule-Associated Protein: Structural and Functional Aspects. *Front Aging Neurosci* **2019,** *11*, 204.

35.   Bachmann, S.; Bell, M.; Klimek, J.; Zempel, H., Differential Effects of the Six Human TAU Isoforms: Somatic Retention of 2N-TAU and Increased Microtubule Number Induced by 4R-TAU. *Front Neurosci* **2021,** *15*, 643115.

36.   Kellogg, E. H.; Hejab, N. M. A.; Poepsel, S.; Downing, K. H.; DiMaio, F.; Nogales, E., Near-atomic model of microtubule-tau interactions. *Science* **2018,** *360* (6394), 1242-1246.

37.   Cehlar, O.; Bagarova, O.; Hornakova, L.; Skrabana, R., The structure of the unstructured: mosaic of tau protein linear motifs obtained by high-resolution techniques and molecular simulation. *Gen Physiol Biophys* **2021,** *40* (6), 479-493.

38.   Breuzard, G.; Hubert, P.; Nouar, R.; De Bessa, T.; Devred, F.; Barbier, P.; Sturgis, J. N.; Peyrot, V., Molecular mechanisms of Tau binding to microtubules and its role in microtubule dynamics in live cells. *J Cell Sci* **2013,** *126* (Pt 13), 2810-9.

39.   Santarella, R. A.; Skiniotis, G.; Goldie, K. N.; Tittmann, P.; Gross, H.; Mandelkow, E. M.; Mandelkow, E.; Hoenger, A., Surface-decoration of microtubules by human tau. *J Mol Biol* **2004,** *339* (3), 539-53.

40.   Martinho, M.; Allegro, D.; Huvent, I.; Chabaud, C.; Etienne, E.; Kovacic, H.; Guigliarelli, B.; Peyrot, V.; Landrieu, I.; Belle, V.; Barbier, P., Two Tau binding sites on tubulin revealed by thiol-disulfide exchanges. *Sci Rep* **2018,** *8* (1), 13846.

41.   Kadavath, H.; Jaremko, M.; Jaremko, L.; Biernat, J.; Mandelkow, E.; Zweckstetter, M., Folding of the Tau Protein on Microtubules. *Angew Chem Int Ed Engl* **2015,** *54* (35), 10347-51.

42.   Kimura, T.; Sharma, G.; Ishiguro, K.; Hisanaga, S. I., Phospho-Tau Bar Code: Analysis of Phosphoisotypes of Tau and Its Application to Tauopathy. *Front Neurosci* **2018,** *12*, 44.

43.   Xia, D.; Li, C.; Gotz, J., Pseudophosphorylation of Tau at distinct epitopes or the presence of the P301L mutation targets the microtubule-associated protein Tau to dendritic spines. *Biochim Biophys Acta* **2015,** *1852* (5), 913-24.

44.   Xia, Y.; Prokop, S.; Giasson, B. I., "Don't Phos Over Tau": recent developments in clinical biomarkers and therapies targeting tau phosphorylation in Alzheimer's disease and other tauopathies. *Mol Neurodegener* **2021,** *16* (1), 37.

45.   Martin, L.; Latypova, X.; Wilson, C. M.; Magnaudeix, A.; Perrin, M. L.; Terro, F., Tau protein phosphatases in Alzheimer's disease: the leading role of PP2A. *Ageing Res Rev* **2013,** *12* (1), 39-49.

46.   Oukoloff, K.; Nzou, G.; Varricchio, C.; Lucero, B.; Alle, T.; Kovalevich, J.; Monti, L.; Cornec, A. S.; Yao, Y.; James, M. J.; Trojanowski, J. Q.; Lee, V. M.; Smith, A. B., 3rd; Brancale, A.; Brunden, K. R.; Ballatore, C., Evaluation of the Structure-Activity Relationship of Microtubule-Targeting 1,2,4-Triazolo[1,5-a]pyrimidines Identifies New Candidates for Neurodegenerative Tauopathies. *J Med Chem* **2021,** *64* (2), 1073-1102.

47.   Yadikar, H.; Torres, I.; Aiello, G.; Kurup, M.; Yang, Z.; Lin, F.; Kobeissy, F.; Yost, R.; Wang, K. K., Screening of tau protein kinase inhibitors in a tauopathy-

relevant cell-based model of tau hyperphosphorylation and oligomerization. *PLoS One* **2020,** *15* (7), 1-30.

48.   Silva, M. C.; Haggarty, S. J., Tauopathies: Deciphering Disease Mechanisms to Develop Effective Therapies. *Int J Mol Sci* **2020,** *21* (23).

49.   Association, A. s., Alzheimer's Disease Facts and Figures *Alzheimers Dement* **2022,** *18*, 1-118.

50.   Mazanetz, M. P.; Fischer, P. M., Untangling tau hyperphosphorylation in drug design for neurodegenerative diseases. *Nat Rev Drug Discov* **2007,** *6* (6), 464-79.

51.   Boyarko, B.; Hook, V., Human Tau Isoforms and Proteolysis for Production of Toxic Tau Fragments in Neurodegeneration. *Front Neurosci* **2021,** *15*, 1-19.

52.   Shi, Y.; Zhang, W.; Yang, Y.; Murzin, A. G.; Falcon, B.; Kotecha, A.; van Beers, M.; Tarutani, A.; Kametani, F.; Garringer, H. J.; Vidal, R.; Hallinan, G. I.; Lashley, T.; Saito, Y.; Murayama, S.; Yoshida, M.; Tanaka, H.; Kakita, A.; Ikeuchi, T.; Robinson, A. C.; Mann, D. M. A.; Kovacs, G. G.; Revesz, T.; Ghetti, B.; Hasegawa, M.; Goedert, M.; Scheres, S. H. W., Structure-based classification of tauopathies. *Nature* **2021,** *598* (7880), 359-363.

53.   Zhang, Y.; Wu, K. M.; Yang, L.; Dong, Q.; Yu, J. T., Tauopathies: new perspectives and challenges. *Mol Neurodegener* **2022,** *17* (1), 1-29.

54.   Lippa, C. F., An individualized approach to treatment for alzheimer's disease, pick's disease, and other dementias. *Am J Alzheimers Dis Other Demen* **2006,** *21* (5), 354-9.

55.   Frederick, J., Pick disease: a brief overview. *Arch Pathol Lab Med* **2006,** *130* (7), 1063-6.

56.   Williams, D. R.; Lees, A. J., Progressive supranuclear palsy: clinicopathological concepts and diagnostic challenges. *The Lancet Neurology* **2009,** *8* (3), 270-279.

57.   Rowe, J. B.; Holland, N.; Rittman, T., Progressive supranuclear palsy: diagnosis and management. *Pract Neurol* **2021,** *21* (5), 376-383.

58.   Armstrong, M. J., Diagnosis and treatment of corticobasal degeneration. *Curr Treat Options Neurol* **2014,** *16* (3), 1-12.

59.   Rodriguez, R. D.; Grinberg, L. T., Argyrophilic grain disease: An underestimated tauopathy. *Dement Neuropsychol* **2015,** *9* (1), 2-8.

60.   Chung, D. C.; Carlomagno, Y.; Cook, C. N.; Jansen-West, K.; Daughrity, L.; Lewis-Tuffin, L. J.; Castanedes-Casey, M.; DeTure, M.; Dickson, D. W.; Petrucelli, L., Tau exhibits unique seeding properties in globular glial tauopathy. *Acta Neuropathol Commun* **2019,** *7* (1), 1-12.

61.   Yi, D. S.; Bertoux, M.; Mioshi, E.; Hodges, J. R.; Hornberger, M., Fronto-striatal atrophy correlates of neuropsychiatric dysfunction in frontotemporal dementia (FTD) and Alzheimer's disease (AD). *Dement Neuropsychol* **2013,** *7* (1), 75-82.

62.   Pottier, C.; Ravenscroft, T. A.; Sanchez-Contreras, M.; Rademakers, R., Genetics of FTLD: overview and what else we can expect from genetic studies. *J Neurochem* **2016,** *138 (Suppl. 1)*, 32-53.

63.   Bodea, L. G.; Eckert, A.; Ittner, L. M.; Piguet, O.; Gotz, J., Tau physiology and pathomechanisms in frontotemporal lobar degeneration. *J Neurochem* **2016,** *138 Suppl 1*, 71-94.

64.   Karageorgiou, E.; Miller, B. L., Frontotemporal lobar degeneration: a clinical approach. *Semin Neurol* **2014,** *34* (2), 189-201.

65.   Cummings, J., New approaches to symptomatic treatments for Alzheimer's disease. *Mol Neurodegener* **2021,** *16* (1), 1-13.

66.   Soderberg, L.; Johannesson, M.; Nygren, P.; Laudon, H.; Eriksson, F.; Osswald, G.; Moller, C.; Lannfelt, L., Lecanemab, Aducanumab, and Gantenerumab - Binding Profiles to Different Forms of Amyloid-Beta Might Explain Efficacy and Side Effects in Clinical Trials for Alzheimer's Disease. *Neurotherapeutics* **2022**, 1-12.

67.   Fesharaki-Zadeh, A., Chronic Traumatic Encephalopathy: A Brief Overview. *Front Neurol* **2019,** *10*, 1-6.

68.   Breen, P. W.; Krishnan, V., Recent Preclinical Insights Into the Treatment of Chronic Traumatic Encephalopathy. *Front Neurosci* **2020,** *14*, 616.

69.   Gelpi, E.; Hoftberger, R.; Graus, F.; Ling, H.; Holton, J. L.; Dawson, T.; Popovic, M.; Pretnar-Oblak, J.; Hogl, B.; Schmutzhard, E.; Poewe, W.; Ricken, G.; Santamaria, J.; Dalmau, J.; Budka, H.; Revesz, T.; Kovacs, G. G., Neuropathological criteria of anti-IgLON5-related tauopathy. *Acta Neuropathol* **2016,** *132* (4), 531-43.

70.   Madetko, N.; Marzec, W.; Kowalska, A.; Przewodowska, D.; Alster, P.; Koziorowski, D., Anti-IgLON5 Disease - The Current State of Knowledge and Further Perspectives. *Front Immunol* **2022,** *13*, 852215.

71.   Arnold, P., Über die Bejiehungen der senilen Hirnatrophie zur Aphasie. . *Prager Med Wochenschr* **1892,** *17*, 165-167.

72.   Snowden, J. S.; Neary, D.; Mann, D. M., Frontotemporal dementia. *Br J Psychiatry* **2002,** *180*, 140-3.

73.   Kertesz, A.; Munoz, D., Pick's Disease, Frontotemporal Dementia, and Pick Complex: Emerging Concepts. *Archives of Neurology* **1998,** *55* (3), 302-304.

74.   Götz, J.; Halliday, G.; Nisbet, R. M., Molecular Pathogenesis of the Tauopathies. *Annual Review of Pathology: Mechanisms of Disease* **2019,** *14* (1), 239-261.

75.   McKhann, G. M.; Albert, M. S.; Grossman, M.; Miller, B.; Dickson, D.; Trojanowski, J. Q., Clinical and pathological diagnosis of frontotemporal dementia: report of the Work Group on Frontotemporal Dementia and Pick's Disease. *Arch Neurol* **2001,** *58* (11), 1803-9.

76.   Steele, J. C.; Richardson, J. C.; Olszewski, J., Progressive supranuclear palsy. A heterogeneous degeneration involving the brain stem, basal ganglia and cerebellum

with vertical gaze and pseudobulbar palsy, nuchal dystonia and dementia. *Arch Neurol* **1964,** *10*, 333-59.

77.   Albert, M. L.; Feldman, R. G.; Willis, A. L., The `subcortical dementia' of progressive supranuclear palsy. *Journal of Neurology, Neurosurgery & Psychiatry* **1974,** *37* (2), 121-130.

78.   Alzheimer, A., Uber eine eigenartige Erkrankung der Hirnrinde. *Allg Zeitschrift Psychiatr* **1907,** *64*, 146–148.

79.   Alzheimer, A.; Stelzmann, R. A.; Schnitzlein, H. N.; Murtagh, F. R., An English translation of Alzheimer's 1907 paper, "Uber eine eigenartige Erkankung der Hirnrinde". *Clin Anat* **1995,** *8* (6), 429-31.

80.   Scheltens, P.; De Strooper, B.; Kivipelto, M.; Holstege, H.; Chételat, G.; Teunissen, C. E.; Cummings, J.; van der Flier, W. M., Alzheimer's disease. *The Lancet* **2021,** *397* (10284), 1577-1590.

81.   Holper, S.; Watson, R.; Yassi, N., Tau as a Biomarker of Neurodegeneration. *Int J Mol Sci* **2022,** *23* (13).

82.   Ittner, L. M.; Gotz, J., Amyloid-beta and tau--a toxic pas de deux in Alzheimer's disease. *Nat Rev Neurosci* **2011,** *12* (2), 65-72.

83.   Rezazadeh, M.; Khorrami, A.; Yeghaneh, T.; Talebi, M.; Kiani, S. J.; Heshmati, Y.; Gharesouran, J., Genetic Factors Affecting Late-Onset Alzheimer's Disease Susceptibility. *Neuromolecular Med* **2016,** *18* (1), 37-49.

84.   R, A. A., Risk factors for Alzheimer's disease. *Folia Neuropathol* **2019,** *57* (2), 87-105.

85.   Lane, C. A.; Hardy, J.; Schott, J. M., Alzheimer's disease. *Eur J Neurol* **2018,** *25* (1), 59-70.

86.   Bassil, F.; Brown, H. J.; Pattabhiraman, S.; Iwasyk, J. E.; Maghames, C. M.; Meymand, E. S.; Cox, T. O.; Riddle, D. M.; Zhang, B.; Trojanowski, J. Q.; Lee, V. M., Amyloid-Beta (Aβ) Plaques Promote Seeding and Spreading of Alpha-Synuclein

and Tau in a Mouse Model of Lewy Body Disorders with Aβ Pathology. *Neuron* **2020,** *105* (2), 260-275.

87.   Hampel, H.; Hardy, J.; Blennow, K.; Chen, C.; Perry, G.; Kim, S. H.; Villemagne, V. L.; Aisen, P.; Vendruscolo, M.; Iwatsubo, T.; Masters, C. L.; Cho, M.; Lannfelt, L.; Cummings, J. L.; Vergallo, A., The Amyloid-beta Pathway in Alzheimer's Disease. *Mol Psychiatry* **2021,** *26* (10), 5481-5503.

88.   Selkoe, D. J.; Hardy, J., The amyloid hypothesis of Alzheimer's disease at 25 years. *EMBO Mol Med* **2016,** *8* (6), 595-608.

89.   Frisoni, G. B.; Altomare, D.; Thal, D. R.; Ribaldi, F.; van der Kant, R.; Ossenkoppele, R.; Blennow, K.; Cummings, J.; van Duijn, C.; Nilsson, P. M.; Dietrich, P. Y.; Scheltens, P.; Dubois, B., The probabilistic model of Alzheimer disease: the amyloid hypothesis revised. *Nat Rev Neurosci* **2022,** *23* (1), 53-66.

90.   Cairns, N. J.; Bigio, E. H.; Mackenzie, I. R.; Neumann, M.; Lee, V. M.; Hatanpaa, K. J.; White, C. L., 3rd; Schneider, J. A.; Grinberg, L. T.; Halliday, G.; Duyckaerts, C.; Lowe, J. S.; Holm, I. E.; Tolnay, M.; Okamoto, K.; Yokoo, H.; Murayama, S.; Woulfe, J.; Munoz, D. G.; Dickson, D. W.; Ince, P. G.; Trojanowski, J. Q.; Mann, D. M., Neuropathologic diagnostic and nosologic criteria for frontotemporal lobar degeneration: consensus of the Consortium for Frontotemporal Lobar Degeneration. *Acta Neuropathol* **2007,** *114* (1), 5-22.

91.   Panza, F.; Lozupone, M.; Seripa, D.; Daniele, A.; Watling, M.; Giannelli, G.; Imbimbo, B. P., Development of disease-modifying drugs for frontotemporal dementia spectrum disorders. *Nat Rev Neurol* **2020,** *16* (4), 213-228.

92.   Neary, D.; Snowden, J.; Mann, D., Frontotemporal dementia. *The Lancet Neurology* **2005,** *4* (11), 771-780.

93.   Haass, C.; Neumann, M., Frontotemporal dementia: from molecular mechanisms to therapy. *J Neurochem* **2016,** *138 (Suppl. 1)*, 3-5.

94.   Koren, S. A.; Galvis-Escobar, S.; Abisambra, J. F., Tau-mediated dysregulation of RNA: Evidence for a common molecular mechanism of toxicity in frontotemporal dementia and other tauopathies. *Neurobiol Dis* **2020,** *141*, 104939.

95.   Jack, C. R., Jr.; Bennett, D. A.; Blennow, K.; Carrillo, M. C.; Dunn, B.; Haeberlein, S. B.; Holtzman, D. M.; Jagust, W.; Jessen, F.; Karlawish, J.; Liu, E.; Molinuevo, J. L.; Montine, T.; Phelps, C.; Rankin, K. P.; Rowe, C. C.; Scheltens, P.; Siemers, E.; Snyder, H. M.; Sperling, R.; Contributors, NIA-AA Research Framework: Toward a biological definition of Alzheimer's disease. *Alzheimers Dement* **2018,** *14* (4), 535-562.

96.   Jack, C. R., Jr.; Bennett, D. A.; Blennow, K.; Carrillo, M. C.; Feldman, H. H.; Frisoni, G. B.; Hampel, H.; Jagust, W. J.; Johnson, K. A.; Knopman, D. S.; Petersen, R. C.; Scheltens, P.; Sperling, R. A.; Dubois, B., A/T/N: An unbiased descriptive classification scheme for Alzheimer disease biomarkers. *Neurology* **2016,** *87* (5), 539-47.

97.   Hu, W. T.; Trojanowski, J. Q.; Shaw, L. M., Biomarkers in frontotemporal lobar degenerations--progress and challenges. *Prog Neurobiol* **2011,** *95* (4), 636-48.

98.   Younes, K.; Miller, B. L., Frontotemporal Dementia: Neuropathology, Genetics, Neuroimaging, and Treatments. *Psychiatr Clin North Am* **2020,** *43* (2), 331-344.

99.   Blennow, K.; Zetterberg, H., Biomarkers for Alzheimer's disease: current status and prospects for the future. *J Intern Med* **2018,** *284* (6), 643-663.

100.   Barthelemy, N. R.; Li, Y.; Joseph-Mathurin, N.; Gordon, B. A.; Hassenstab, J.; Benzinger, T. L. S.; Buckles, V.; Fagan, A. M.; Perrin, R. J.; Goate, A. M.; Morris, J. C.; Karch, C. M.; Xiong, C.; Allegri, R.; Mendez, P. C.; Berman, S. B.; Ikeuchi, T.; Mori, H.; Shimada, H.; Shoji, M.; Suzuki, K.; Noble, J.; Farlow, M.; Chhatwal, J.; Graff-Radford, N. R.; Salloway, S.; Schofield, P. R.; Masters, C. L.; Martins, R. N.; O'Connor, A.; Fox, N. C.; Levin, J.; Jucker, M.; Gabelle, A.;

Lehmann, S.; Sato, C.; Bateman, R. J.; McDade, E.; Dominantly Inherited Alzheimer, N., A soluble phosphorylated tau signature links tau, amyloid and the evolution of stages of dominantly inherited Alzheimer's disease. *Nat Med* **2020,** *26* (3), 398-407.

101.   Czako, C.; Kovacs, T.; Ungvari, Z.; Csiszar, A.; Yabluchanskiy, A.; Conley, S.; Csipo, T.; Lipecz, A.; Horvath, H.; Sandor, G. L.; Istvan, L.; Logan, T.; Nagy, Z. Z.; Kovacs, I., Retinal biomarkers for Alzheimer's disease and vascular cognitive impairment and dementia (VCID): implication for early diagnosis and prognosis. *Geroscience* **2020,** *42* (6), 1499-1525.

102.   Park, J. C.; Han, S. H.; Mook-Jung, I., Peripheral inflammatory biomarkers in Alzheimer's disease: a brief review. *BMB Rep* **2020,** *53* (1), 10-19.

103.   Shigemizu, D.; Mori, T.; Akiyama, S.; Higaki, S.; Watanabe, H.; Sakurai, T.; Niida, S.; Ozaki, K., Identification of potential blood biomarkers for early diagnosis of Alzheimer's disease through RNA sequencing analysis. *Alzheimers Res Ther* **2020,** *12* (1), 87.

104.   Tsai, R. M.; Boxer, A. L., Therapy and clinical trials in frontotemporal dementia: past, present, and future. *J Neurochem* **2016,** *138 Suppl 1* (Suppl 1), 211-21.

105.   Vaz, M.; Silva, V.; Monteiro, C.; Silvestre, S., Role of Aducanumab in the Treatment of Alzheimer's Disease: Challenges and Opportunities. *Clin Interv Aging* **2022,** *17*, 797-810.

106.   Hoy, S. M., Lecanemab: First Approval. *Drugs* **2023,** *83* (4), 359-365.

107.   van Dyck, C. H.; Swanson, C. J.; Aisen, P.; Bateman, R. J.; Chen, C.; Gee, M.; Kanekiyo, M.; Li, D.; Reyderman, L.; Cohen, S.; Froelich, L.; Katayama, S.; Sabbagh, M.; Vellas, B.; Watson, D.; Dhadda, S.; Irizarry, M.; Kramer, L. D.; Iwatsubo, T., Lecanemab in Early Alzheimer's Disease. *N Engl J Med* **2023,** *388* (1), 9-21.

108.   Frost, C. V.; Zacharias, M., From monomer to fibril: Abeta-amyloid binding to Aducanumab antibody studied by molecular dynamics simulation. *Proteins* **2020,** *88* (12), 1592-1606.

109.   Cummings, J.; Lee, G.; Zhong, K.; Fonseca, J.; Taghva, K., Alzheimer's disease drug development pipeline: 2021. *Alzheimer's Dement* **2021,** *7* (1), e12179.

110.   Miller, D. S.; Bauer, B.; Hartz, A. M., Modulation of P-glycoprotein at the blood-brain barrier: opportunities to improve central nervous system pharmacotherapy. *Pharmacol Rev* **2008,** *60* (2), 196-209.

111.   Danon, J. J.; Reekie, T. A.; Kassiou, M., Challenges and Opportunities in Central Nervous System Drug Discovery. *Trends in Chemistry* **2019,** *1* (6), 612-624.

112.   Ford, J. M.; Hait, W. N., Pharmacologic circumvention of multidrug resistance. *Cytotechnology* **1993,** *12* (1), 171-212.

113.   Kuhnke, D.; Jedlitschky, G.; Grube, M.; Krohn, M.; Jucker, M.; Mosyagin, I.; Cascorbi, I.; Walker, L. C.; Kroemer, H. K.; Warzok, R. W.; Vogelgesang, S., MDR1-P-Glycoprotein (ABCB1) Mediates Transport of Alzheimer's amyloid-beta peptides--implications for the mechanisms of Abeta clearance at the blood-brain barrier. *Brain Pathol* **2007,** *17* (4), 347-53.

114.   Ghose, A. K.; Herbertz, T.; Hudkins, R. L.; Dorsey, B. D.; Mallamo, J. P., Knowledge-Based, Central Nervous System (CNS) Lead Selection and Lead Optimization for CNS Drug Discovery. *ACS Chem Neurosci* **2012,** *3* (1), 50-68.

115.   Wager, T. T.; Hou, X.; Verhoest, P. R.; Villalobos, A., Central Nervous System Multiparameter Optimization Desirability: Application in Drug Discovery. *ACS Chem Neurosci* **2016,** *7* (6), 767-75.

116.   Rösler, T. W.; Costa, M.; Höglinger, G. U., Disease-modifying strategies in primary tauopathies. *Neuropharmacology* **2020,** *167*, 107842.

117.   Boiarska, Z.; Passarella, D., Microtubule-targeting agents and neurodegeneration. *Drug Discov Today* **2021,** *26* (2), 604-615.

118.   Dumontet, C.; Jordan, M. A., Microtubule-binding agents: a dynamic field of cancer therapeutics. *Nat Rev Drug Discov* **2010,** *9* (10), 790-803.

119.   Steinmetz, M. O.; Prota, A. E., Microtubule-Targeting Agents: Strategies To Hijack the Cytoskeleton. *Trends Cell Biol* **2018,** *28* (10), 776-792.

120.   Matthew, S.; Chen, Q. Y.; Ratnayake, R.; Fermaintt, C. S.; Lucena-Agell, D.; Bonato, F.; Prota, A. E.; Lim, S. T.; Wang, X.; Diaz, J. F.; Risinger, A. L.; Paul, V. J.; Oliva, M. A.; Luesch, H., Gatorbulin-1, a distinct cyclodepsipeptide chemotype, targets a seventh tubulin pharmacological site. *PNAS* **2021,** *118* (9), 1-11.

121.   Ballatore, C.; Brunden, K. R.; Huryn, D. M.; Trojanowski, J. Q.; Lee, V. M.; Smith, A. B., 3rd, Microtubule stabilizing agents as potential treatment for Alzheimer's disease and related neurodegenerative tauopathies. *J Med Chem* **2012,** *55* (21), 8979-96.

122.   Brunden, K. R.; Yao, Y.; Potuzak, J. S.; Ferrer, N. I.; Ballatore, C.; James, M. J.; Hogan, A. M.; Trojanowski, J. Q.; Smith, A. B., 3rd; Lee, V. M., The characterization of microtubule-stabilizing drugs as possible therapeutic agents for Alzheimer's disease and related tauopathies. *Pharmacol Res* **2011,** *63* (4), 341-51.

123.   Zhang, H.; Cao, X.; Tang, M.; Zhong, G.; Si, Y.; Li, H.; Zhu, F.; Liao, Q.; Li, L.; Zhao, J.; Feng, J.; Li, S.; Wang, C.; Kaulich, M.; Wang, F.; Chen, L.; Li, L.; Xia, Z.; Liang, T.; Lu, H.; Feng, X. H.; Zhao, B., A subcellular map of the human kinome. *Elife* **2021,** *10*.

124.   Gunosewoyo, H.; Yu, L.; Munoz, L.; Kassiou, M., Kinase targets in CNS drug discovery. *Future Medicinal Chemistry* **2017,** *9* (3), 303-314.

125.   Wilson, L. J.; Linley, A.; Hammond, D. E.; Hood, F. E.; Coulson, J. M.; MacEwan, D. J.; Ross, S. J.; Slupsky, J. R.; Smith, P. D.; Eyers, P. A.; Prior, I. A., New Perspectives, Opportunities, and Challenges in Exploring the Human Protein Kinome. *Cancer Res* **2018,** *78* (1), 15-29.

126.   Attwood, M. M.; Fabbro, D.; Sokolov, A. V.; Knapp, S.; Schiöth, H. B., Trends in kinase drug discovery: targets, indications and inhibitor design. *Nature Reviews Drug Discovery* **2021**.

127.   Wells, C. I.; Al-Ali, H.; Andrews, D. M.; Asquith, C. R. M.; Axtman, A. D.; Dikic, I.; Ebner, D.; Ettmayer, P.; Fischer, C.; Frederiksen, M.; Futrell, R. E.; Gray, N. S.; Hatch, S. B.; Knapp, S.; Lücking, U.; Michaelides, M.; Mills, C. E.; Müller, S.; Owen, D.; Picado, A.; Saikatendu, K. S.; Schröder, M.; Stolz, A.; Tellechea, M.; Turunen, B. J.; Vilar, S.; Wang, J.; Zuercher, W. J.; Willson, T. M.; Drewry, D. H., The Kinase Chemogenomic Set (KCGS): An Open Science Resource for Kinase Vulnerability Identification. *International Journal of Molecular Sciences* **2021,** *22* (2), 566.

128.   Krahn, A. I.; Wells, C.; Drewry, D. H.; Beitel, L. K.; Durcan, T. M.; Axtman, A. D., Defining the Neural Kinome: Strategies and Opportunities for Small Molecule Drug Discovery to Target Neurodegenerative Diseases. *ACS Chem Neurosci* **2020,** *11* (13), 1871-1886.

129.   Pardridge, W. M., Blood-brain barrier delivery. *Drug Discov Today* **2007,** *12* (1-2), 54-61.

130.   Hanks, S. K.; Hunter, T., Protein kinases 6. The eukaryotic protein kinase superfamily: kinase (catalytic) domain structure and classification. *Faseb j* **1995,** *9* (8), 576-96.

131.   Roskoski, R., Classification of small molecule protein kinase inhibitors based upon the structures of their drug-enzyme complexes. *Pharmacological Research* **2016,** *103*, 26-48.

132.   Ten Eyck, L. F.; Taylor, S. S.; Kornev, A. P., Conserved spatial patterns across the protein kinase family. *Biochim Biophys Acta* **2008,** *1784* (1), 238-43.

133.   McClendon, C. L.; Kornev, A. P.; Gilson, M. K.; Taylor, S. S., Dynamic architecture of a protein kinase. *PNAS* **2014,** *111* (43), E4623-E4631.

134.   Muller, S.; Chaikuad, A.; Gray, N. S.; Knapp, S., The ins and outs of selective kinase inhibitor development. *Nat Chem Biol* **2015,** *11* (11), 818-21.

135.   Arter, C.; Trask, L.; Ward, S.; Yeoh, S.; Bayliss, R., Structural features of the protein kinase domain and targeted binding by small-molecule inhibitors. *J Biol Chem* **2022,** *298* (8), 102247.

136.   Roskoski, R., Properties of FDA-approved small molecule protein kinase inhibitors: A 2021 update. *Pharmacological Research* **2021,** *165*, 105463.

137.   Ayala-Aguilera, C. C.; Valero, T.; Lorente-Macias, A.; Baillache, D. J.; Croke, S.; Unciti-Broceta, A., Small Molecule Kinase Inhibitor Drugs (1995-2021): Medical Indication, Pharmacology, and Synthesis. *J Med Chem* **2022,** *65* (2), 1047-1131.

138.   Fang, Y.; Wang, J.; Zhao, M.; Zheng, Q.; Ren, C.; Wang, Y.; Zhang, J., Progress and Challenges in Targeted Protein Degradation for Neurodegenerative Disease Therapy. *J Med Chem* **2022,** *65* (17), 11454-11477.

139.   Jiang, X.; Zhou, J.; Wang, Y.; Liu, X.; Xu, K.; Xu, J.; Feng, F.; Sun, H., PROTACs suppression of GSK-3beta, a crucial kinase in neurodegenerative diseases. *Eur J Med Chem* **2021,** *210*, 112949.

140.   Demuro, S.; Di Martino, R. M. C.; Ortega, J. A.; Cavalli, A., GSK-3β, FYN, and DYRK1A: Master Regulators in Neurodegenerative Pathways. *Int J Mol Sci* **2021,** *22* (16), 1-35.

141.   Durrenberger, P. F.; Fernando, F. S.; Kashefi, S. N.; Bonnert, T. P.; Seilhean, D.; Nait-Oumesmar, B.; Schmitt, A.; Gebicke-Haerter, P. J.; Falkai, P.; Grünblatt, E.; Palkovits, M.; Arzberger, T.; Kretzschmar, H.; Dexter, D. T.; Reynolds, R., Common mechanisms in neurodegeneration and neuroinflammation: a BrainNet Europe gene expression microarray study. *J Neural Transm (Vienna)* **2015,** *122* (7), 1055-68.

142.   Gan, L.; Cookson, M. R.; Petrucelli, L.; La Spada, A. R., Converging pathways in neurodegeneration, from genetics to mechanisms. *Nat Neurosci* **2018,** *21* (10), 1300-1309.

143.   Eldar-Finkelman, H.; Martinez, A., GSK-3 Inhibitors: Preclinical and Clinical Focus on CNS. *Front Mol Neurosci* **2011,** *4*, 32.

144.   Rippin, I.; Eldar-Finkelman, H., Mechanisms and Therapeutic Implications of GSK-3 in Treating Neurodegeneration. *Cells* **2021,** *10* (2).

145.   ter Haar, E.; Coll, J. T.; Austen, D. A.; Hsiao, H. M.; Swenson, L.; Jain, J., Structure of GSK3beta reveals a primed phosphorylation mechanism. *Nat Struct Biol* **2001,** *8* (7), 593-6.

146.   Bertrand, J. A.; Thieffine, S.; Vulpetti, A.; Cristiani, C.; Valsasina, B.; Knapp, S.; Kalisz, H. M.; Flocco, M., Structural Characterization of the GSK-3β Active Site Using Selective and Non-selective ATP-mimetic Inhibitors. *Journal of Molecular Biology* **2003,** *333* (2), 393-407.

147.   Andreev, S.; Pantsar, T.; Tesch, R.; Kahlke, N.; El-Gokha, A.; Ansideri, F.; Grätz, L.; Romasco, J.; Sita, G.; Geibel, C.; Lämmerhofer, M.; Tarozzi, A.; Knapp, S.; Laufer, S. A.; Koch, P., Addressing a Trapped High-Energy Water: Design and Synthesis of Highly Potent Pyrimidoindole-Based Glycogen Synthase Kinase-3β Inhibitors. *Journal of Medicinal Chemistry* **2021**.

148.   Sklirou, A. D.; Gaboriaud-Kolar, N.; Papassideri, I.; Skaltsounis, A. L.; Trougakos, I. P., 6-bromo-indirubin-3'-oxime (6BIO), a Glycogen synthase kinase-3beta inhibitor, activates cytoprotective cellular modules and suppresses cellular senescence-mediated biomolecular damage in human fibroblasts. *Sci Rep* **2017,** *7* (1), 11713.

149.   Meijer, L.; Thunnissen, A. M.; White, A. W.; Garnier, M.; Nikolic, M.; Tsai, L. H.; Walter, J.; Cleverley, K. E.; Salinas, P. C.; Wu, Y. Z.; Biernat, J.; Mandelkow, E. M.; Kim, S. H.; Pettit, G. R., Inhibition of cyclin-dependent kinases, GSK-3β and

CK1 by hymenialdisine, a marine sponge constituent. *Chemistry & Biology* **2000,** *7* (1), 51-63.

150.   Leost, M.; Schultz, C.; Link, A.; Wu, Y. Z.; Biernat, J.; Mandelkow, E. M.; Bibb, J. A.; Snyder, G. L.; Greengard, P.; Zaharevitz, D. W.; Gussio, R.; Senderowicz, A. M.; Sausville, E. A.; Kunick, C.; Meijer, L., Paullones are potent inhibitors of glycogen synthase kinase-3beta and cyclin-dependent kinase 5/p25. *Eur J Biochem* **2000,** *267* (19), 5983-94.

151.   Li, L.; Shao, X.; Cole, E. L.; Ohnmacht, S. A.; Ferrari, V.; Hong, Y. T.; Williamson, D. J.; Fryer, T. D.; Quesada, C. A.; Sherman, P.; Riss, P. J.; Scott, P. J.; Aigbirhio, F. I., Synthesis and Initial in Vivo Studies with [(11)C]SB-216763: The First Radiolabeled Brain Penetrative Inhibitor of GSK-3. *ACS Med Chem Lett* **2015,** *6* (5), 548-52.

152.   Palomo, V.; Martinez, A., Glycogen synthase kinase 3 (GSK-3) inhibitors: a patent update (2014-2015). *Expert Opin Ther Pat* **2017,** *27* (6), 657-666.

153.   Georgievska, B.; Sandin, J.; Doherty, J.; Mörtberg, A.; Neelissen, J.; Andersson, A.; Gruber, S.; Nilsson, Y.; Schött, P.; Arvidsson, P. I.; Hellberg, S.; Osswald, G.; Berg, S.; Fälting, J.; Bhat, R. V., AZD1080, a novel GSK3 inhibitor, rescues synaptic plasticity deficits in rodent brain and exhibits peripheral target engagement in humans. *J Neurochem* **2013,** *125* (3), 446-56.

154.   Tsui, H.; Zeng, Q.; Chen, K.; Zhang, X., 7.10 - Inhibiting Kinases in the CNS. In *Comprehensive Medicinal Chemistry III*, Chackalamannil, S.; Rotella, D.; Ward, S. E., Eds. Elsevier: Oxford, 2017; pp 408-446.

155.   Kypta, R. M.;   Hemming, A.; Courtneidge, S. A., Identification and characterization of p59fyn (a src-like protein tyrosine kinase) in normal and polyoma virus transformed cells. *EMBO J* **1988,** *7* (12), 3837-44.

156.   Tang, X.; Feng, Y.; Ye, K., Src-family tyrosine kinase fyn phosphorylates phosphatidylinositol 3-kinase enhancer-activating Akt, preventing its apoptotic

cleavage and promoting cell survival. *Cell Death & Differentiation* **2007,** *14* (2), 368-377.

157.   Sperber, B. R.; Boyle-Walsh, E. A.; Engleka, M. J.; Gadue, P.; Peterson, A. C.; Stein, P. L.; Scherer, S. S.; McMorris, F. A., A unique role for Fyn in CNS myelination. *J Neurosci* **2001,** *21* (6), 2039-47.

158.   Goldsmith, J. F.; Hall, C. G.; Atkinson, T. P., Identification of an alternatively spliced isoform of the fyn tyrosine kinase. *Biochem Biophys Res Commun* **2002,** *298* (4), 501-4.

159.   Schenone, S.; Brullo, C.; Musumeci, F.; Biava, M.; Falchi, F.; Botta, M., Fyn kinase in brain diseases and cancer: the search for inhibitors. *Curr Med Chem* **2011,** *18* (19), 2921-42.

160.   Wolfe, M. S., *Alzheimer's Disease II*. Springer International Publishing : Imprint: Springer: Cham, 2017.

161.   Angelopoulou, E.; Paudel, Y. N.; Julian, T.; Shaikh, M. F.; Piperi, C., Pivotal Role of Fyn Kinase in Parkinson's Disease and Levodopa-Induced Dyskinesia: a Novel Therapeutic Target? *Mol Neurobiol* **2020**.

162.   Thomas, S. M.; Brugge, J. S., Cellular functions regulated by Src family kinases. *Annu Rev Cell Dev Biol* **1997,** *13*, 513-609.

163.   Poli, G.; Lapillo, M.; Granchi, C.; Caciolla, J.; Mouawad, N.; Caligiuri, I.; Rizzolio, F.; Langer, T.; Minutolo, F.; Tuccinardi, T., Binding investigation and preliminary optimisation of the 3-amino-1,2,4-triazin-5(2H)-one core for the development of new Fyn inhibitors. *J Enzyme Inhib Med Chem* **2018,** *33* (1), 956-961.

164.   Davidson, D.; Viallet, J.; Veillette, A., Unique catalytic properties dictate the enhanced function of p59fynT, the hemopoietic cell-specific isoform of the Fyn tyrosine protein kinase, in T cells. *Molecular and Cellular Biology* **1994,** *14* (7), 4554-4564.

165.   Hennequin, L. F.; Allen, J.; Breed, J.; Curwen, J.; Fennell, M.; Green, T. P.; Lambert-van der Brempt, C.; Morgentin, R.; Norman, R. A.; Olivier, A.; Otterbein, L.; Ple, P. A.; Warin, N.; Costello, G., N-(5-chloro-1,3-benzodioxol-4-yl)-7-[2-(4-methylpiperazin-1-yl)ethoxy]-5- (tetrahydro-2H-pyran-4-yloxy)quinazolin-4-amine, a novel, highly selective, orally available, dual-specific c-Src/Abl kinase inhibitor. *J Med Chem* **2006,** *49* (22), 6465-88.

166.   Baselga, J.; Cervantes, A.; Martinelli, E.; Chirivella, I.; Hoekman, K.; Hurwitz, H. I.; Jodrell, D. I.; Hamberg, P.; Casado, E.; Elvin, P.; Swaisland, A.; Iacona, R.; Tabernero, J., Phase I safety, pharmacokinetics, and inhibition of SRC activity study of saracatinib in patients with solid tumors. *Clin Cancer Res* **2010,** *16* (19), 4876-83.

167.   Tang, S. J.; Fesharaki-Zadeh, A.; Takahashi, H.; Nies, S. H.; Smith, L. M.; Luo, A.; Chyung, A.; Chiasseu, M.; Strittmatter, S. M., Fyn kinase inhibition reduces protein aggregation, increases synapse density and improves memory in transgenic and traumatic Tauopathy. *Acta Neuropathologica Communications* **2020,** *8* (1), 96.

168.   Nygaard, H. B.; Wagner, A. F.; Bowen, G. S.; Good, S. P.; MacAvoy, M. G.; Strittmatter, K. A.; Kaufman, A. C.; Rosenberg, B. J.; Sekine-Konno, T.; Varma, P.; Chen, K.; Koleske, A. J.; Reiman, E. M.; Strittmatter, S. M.; van Dyck, C. H., A phase Ib multiple ascending dose study of the safety, tolerability, and central nervous system availability of AZD0530 (saracatinib) in Alzheimer's disease. *Alzheimer's Research & Therapy* **2015,** *7* (1), 35.

169.   van Dyck, C. H.; Nygaard, H. B.; Chen, K.; Donohue, M. C.; Raman, R.; Rissman, R. A.; Brewer, J. B.; Koeppe, R. A.; Chow, T. W.; Rafii, M. S.; Gessert, D.; Choi, J.; Turner, R. S.; Kaye, J. A.; Gale, S. A.; Reiman, E. M.; Aisen, P. S.; Strittmatter, S. M., Effect of AZD0530 on Cerebral Metabolic Decline in Alzheimer Disease: A Randomized Clinical Trial. *JAMA Neurol* **2019**.

170.	Marech, I.; Patruno, R.; Zizzo, N.; Gadaleta, C.; Introna, M.; Zito, A. F.; Gadaleta, C. D.; Ranieri, G., Masitinib (AB1010), from canine tumor model to human clinical development: where we are? *Crit Rev Oncol Hematol* **2014,** *91* (1), 98-111.

171.	Nygaard, H. B., Targeting Fyn Kinase in Alzheimer's Disease. *Biol Psychiatry* **2018,** *83* (4), 369-376.

172.	Piette, F.; Belmin, J.; Vincent, H.; Schmidt, N.; Pariel, S.; Verny, M.; Marquis, C.; Mely, J.; Hugonot-Diener, L.; Kinet, J. P.; Dubreuil, P.; Moussy, A.; Hermine, O., Masitinib as an adjunct therapy for mild-to-moderate Alzheimer's disease: a randomised, placebo-controlled phase 2 trial. *Alzheimers Res Ther* **2011,** *3* (2), 16.

173.	Tintori, C.; La Sala, G.; Vignaroli, G.; Botta, L.; Fallacara, A. L.; Falchi, F.; Radi, M.; Zamperini, C.; Dreassi, E.; Dello Iacono, L.; Orioli, D.; Biamonti, G.; Garbelli, M.; Lossani, A.; Gasparrini, F.; Tuccinardi, T.; Laurenzana, I.; Angelucci, A.; Maga, G.; Schenone, S.; Brullo, C.; Musumeci, F.; Desogus, A.; Crespan, E.; Botta, M., Studies on the ATP Binding Site of Fyn Kinase for the Identification of New Inhibitors and Their Evaluation as Potential Agents against Tauopathies and Tumors. *Journal of Medicinal Chemistry* **2015,** *58* (11), 4590-4609.

174.	Lau, W., C. Methods, compositions and uses of novel Fyn kinase inhibitors. WO2017044623, 2017.

175.	Paraselli, B. R.; Nangunoori, S. K.; Appala, V. R.; Kanthasamy, A. G.; Anatharam, V.; Guntupalli, P. Novel fyn kinase inhibitors. WO2017037604A1, 2017.

176.	Himpel, S.; Panzer, P.; Eirmbter, K.; Czajkowska, H.; Sayed, M.; Packman, L. C.; Blundell, T.; Kentrup, H.; Grötzinger, J.; Joost, H. G.; Becker, W., Identification of the autophosphorylation sites and characterization of their effects in the protein kinase DYRK1A. *Biochem J* **2001,** *359* (Pt 3), 497-505.

177.   Arbones, M. L.; Thomazeau, A.; Nakano-Kobayashi, A.; Hagiwara, M.; Delabar, J. M., DYRK1A and cognition: A lifelong relationship. *Pharmacology & Therapeutics* **2019,** *194*, 199-221.

178.   Soundararajan, M.; Roos, A. K.; Savitsky, P.; Filippakopoulos, P.; Kettenbach, A. N.; Olsen, J. V.; Gerber, S. A.; Eswaran, J.; Knapp, S.; Elkins, J. M., Structures of Down syndrome kinases, DYRKs, reveal mechanisms of kinase activation and substrate recognition. *Structure* **2013,** *21* (6), 986-96.

179.   Hammerle, B.; Ulin, E.; Guimera, J.; Becker, W.; Guillemot, F.; Tejedor, F. J., Transient expression of Mnb/Dyrk1a couples cell cycle exit and differentiation of neuronal precursors by inducing p27KIP1 expression and suppressing NOTCH signaling. *Development* **2011,** *138* (12), 2543-54.

180.   Park, J.; Oh, Y.; Yoo, L.; Jung, M. S.; Song, W. J.; Lee, S. H.; Seo, H.; Chung, K. C., Dyrk1A phosphorylates p53 and inhibits proliferation of embryonic neuronal cells. *J Biol Chem* **2010,** *285* (41), 31895-906.

181.   Ogawa, Y.; Nonaka, Y.; Goto, T.; Ohnishi, E.; Hiramatsu, T.; Kii, I.; Yoshida, M.; Ikura, T.; Onogi, H.; Shibuya, H.; Hosoya, T.; Ito, N.; Hagiwara, M., Development of a novel selective inhibitor of the Down syndrome-related kinase Dyrk1A. *Nat Commun* **2010,** *1*, 86.

182.   Kumar, K.; Man-Un Ung, P.; Wang, P.; Wang, H.; Li, H.; Andrews, M. K.; Stewart, A. F.; Schlessinger, A.; DeVita, R. J., Novel selective thiadiazine DYRK1A inhibitor lead scaffold with human pancreatic beta-cell proliferation activity. *Eur J Med Chem* **2018,** *157*, 1005-1016.

183.   Treiber, D. K.; Shah, N. P., Ins and outs of kinase DFG motifs. *Chem Biol* **2013,** *20* (6), 745-6.

184.   Guo, X.; Williams, J. G.; Schug, T. T.; Li, X., DYRK1A and DYRK3 promote cell survival through phosphorylation and activation of SIRT1. *J Biol Chem* **2010,** *285* (17), 13223-32.

185. Abbassi, R.; Johns, T. G.; Kassiou, M.; Munoz, L., DYRK1A in neurodegeneration and cancer: Molecular basis and clinical implications. *Pharmacology & Therapeutics* **2015,** *151*, 87-98.

186. Becker, W.; Weber, Y.; Wetzel, K.; Eirmbter, K.; Tejedor, F. J.; Joost, H. G., Sequence characteristics, subcellular localization, and substrate specificity of DYRK-related kinases, a novel family of dual specificity protein kinases. *J Biol Chem* **1998,** *273* (40), 25893-902.

187. Adarkwah, C. C.; Jegan, N.; Heinzel-Gutenbrunner, M.; Kuhne, F.; Siebert, U.; Popert, U.; Donner-Banzhoff, N.; Kurwitz, S., Time-to-event versus ten-year-absolute-risk in cardiovascular risk prevention - does it make a difference? Results from the Optimizing-Risk-Communication (OptRisk) randomized-controlled trial. *BMC Med Inform Decis Mak* **2016,** *16* (1), 152.

188. Nakano-Kobayashi, A.; Awaya, T.; Kii, I.; Sumida, Y.; Okuno, Y.; Yoshida, S.; Sumida, T.; Inoue, H.; Hosoya, T.; Hagiwara, M., Prenatal neurogenesis induction therapy normalizes brain structure and function in Down syndrome mice. *Proc Natl Acad Sci U S A* **2017,** *114* (38), 10268-10273.

189. Frost, D.; Meechoovet, B.; Wang, T.; Gately, S.; Giorgetti, M.; Shcherbakova, I.; Dunckley, T., beta-carboline compounds, including harmine, inhibit DYRK1A and tau phosphorylation at multiple Alzheimer's disease-related sites. *PLoS One* **2011,** *6* (5), e19264.

190. Gompel, M.; Leost, M.; De Kier Joffe, E. B.; Puricelli, L.; Franco, L. H.; Palermo, J.; Meijer, L., Meridianins, a new family of protein kinase inhibitors isolated from the ascidian Aplidium meridianum. *Bioorg Med Chem Lett* **2004,** *14* (7), 1703-7.

191. Debdab, M.; Carreaux, F.; Renault, S.; Soundararajan, M.; Fedorov, O.; Filippakopoulos, P.; Lozach, O.; Babault, L.; Tahtouh, T.; Baratte, B.; Ogawa, Y.; Hagiwara, M.; Eisenreich, A.; Rauch, U.; Knapp, S.; Meijer, L.; Bazureau, J. P., Leucettines, a class of potent inhibitors of cdc2-like kinases and dual specificity,

tyrosine phosphorylation regulated kinases derived from the marine sponge leucettamine B: modulation of alternative pre-RNA splicing. *J Med Chem* **2011,** *54* (12), 4172-86.

192.   Pathak, A.; Rohilla, A.; Gupta, T.; Akhtar, M. J.; Haider, M. R.; Sharma, K.; Haider, K.; Yar, M. S., DYRK1A kinase inhibition with emphasis on neurodegeneration: A comprehensive evolution story-cum-perspective. *Eur J Med Chem* **2018,** *158*, 559-592.

193.   Nguyen, T. L.; Fruit, C.; Herault, Y.; Meijer, L.; Besson, T., Dual-specificity tyrosine phosphorylation-regulated kinase 1A (DYRK1A) inhibitors: a survey of recent patent literature. *Expert Opin Ther Pat* **2017,** *27* (11), 1183-1199.

194.   Smith, B.; Medda, F.; Gokhale, V.; Dunckley, T.; Hulme, C., Recent Advances in the Design, Synthesis, and Biological Evaluation of Selective DYRK1A Inhibitors: A New Avenue for a Disease Modifying Treatment of Alzheimer's? *ACS Chemical Neuroscience* **2012,** *3* (11), 857-872.

195.   Becker, W.; Soppa, U.; Tejedor, F. J., DYRK1A: a potential drug target for multiple Down syndrome neuropathologies. *CNS Neurol Disord Drug Targets* **2014,** *13* (1), 26-33.

196.   Gockler, N.; Jofre, G.; Papadopoulos, C.; Soppa, U.; Tejedor, F. J.; Becker, W., Harmine specifically inhibits protein kinase DYRK1A and interferes with neurite formation. *FEBS J* **2009,** *276* (21), 6324-37.

197.   Hoon Kim, S. O. S., Rona R. Ramsay, Inhibition of Monoamine Oxidase A by β-Carboline Derivatives. *Archives of Biochemistry and Biophysics* **1997,** *337* (1), 137-142.

198.   Ruben, K.; Wurzlbauer, A.; Walte, A.; Sippl, W.; Bracher, F.; Becker, W., Selectivity Profiling and Biological Activity of Novel beta-Carbolines as Potent and Selective DYRK1 Kinase Inhibitors. *PLoS One* **2015,** *10* (7), e0132453.

199.   Franco, L. H.; Joffé, E. B. d. K.; Puricelli, L.; Tatian, M.; Seldes, A. M.; Palermo, J. A., Indole Alkaloids from the Tunicate Aplidium meridianum. *Journal of Natural Products* **1998,** *61* (9), 1130-1132.

200.   Yadav, R. R.; Sharma, S.; Joshi, P.; Wani, A.; Vishwakarma, R. A.; Kumar, A.; Bharate, S. B., Meridianin derivatives as potent Dyrk1A inhibitors and neuroprotective agents. *Bioorganic & Medicinal Chemistry Letters* **2015,** *25* (15), 2948-2952.

201.   Giraud, F.; Alves, G.; Debiton, E.; Nauton, L.; Thery, V.; Durieu, E.; Ferandin, Y.; Lozach, O.; Meijer, L.; Anizon, F.; Pereira, E.; Moreau, P., Synthesis, protein kinase inhibitory potencies, and in vitro antiproliferative activities of meridianin derivatives. *J Med Chem* **2011,** *54* (13), 4474-89.

202.   Kim, H.; Lee, K. S.; Kim, A. K.; Choi, M.; Choi, K.; Kang, M.; Chi, S. W.; Lee, M. S.; Lee, J. S.; Lee, S. Y.; Song, W. J.; Yu, K.; Cho, S., A chemical with proven clinical safety rescues Down-syndrome-related phenotypes in through DYRK1A inhibition. *Disease Models & Mechanisms* **2016,** *9* (8), 839-48.

203.   Chaikuad, A.; Diharce, J.; Schroder, M.; Foucourt, A.; Leblond, B.; Casagrande, A. S.; Desire, L.; Bonnet, P.; Knapp, S.; Besson, T., An Unusual Binding Model of the Methyl 9-Anilinothiazolo[5,4-f] quinazoline-2-carbimidates (EHT 1610 and EHT 5372) Confers High Selectivity for Dual-Specificity Tyrosine Phosphorylation-Regulated Kinases. *J Med Chem* **2016,** *59* (22), 10315-10321.

204.   Coutadeur, S.; Benyamine, H.; Delalonde, L.; de Oliveira, C.; Leblond, B.; Foucourt, A.; Besson, T.; Casagrande, A. S.; Taverne, T.; Girard, A.; Pando, M. P.; Désiré, L., A novel DYRK1A (dual specificity tyrosine phosphorylation-regulated kinase 1A) inhibitor for the treatment of Alzheimer's disease: effect on Tau and amyloid pathologies in vitro. *J Neurochem* **2015,** *133* (3), 440-51.

205.   Holzer, M.; Schade, N.; Opitz, A.; Hilbrich, I.; Stieler, J.; Vogel, T.; Neukel, V.; Oberstadt, M.; Totzke, F.; Schachtele, C.; Sippl, W.; Hilgeroth, A., Novel Protein

Kinase Inhibitors Related to Tau Pathology Modulate Tau Protein-Self Interaction Using a Luciferase Complementation Assay. *Molecules* **2018,** *23* (9), 2335.

206.   Kimura, T.; Ishiguro, K.; Hisanaga, S. I., Physiological and pathological phosphorylation of tau by Cdk5. *Frontiers in Molecular Neuroscience* **2014,** *7.*

207.   Das, T. K.; Jana, P.; Chakrabarti, S. K.; Abdul Hamid, M. R. W., Curcumin Downregulates GSK3 and Cdk5 in Scopolamine-Induced Alzheimer's Disease Rats Abrogating Aβ(40/42) and Tau Hyperphosphorylation. *J Alzheimers Dis Rep* **2019,** *3* (1), 257-267.

208.   Billingsley, M. L.; Kincaid, R. L., Regulated phosphorylation and dephosphorylation of tau protein: effects on microtubule interaction, intracellular trafficking and neurodegeneration. *Biochemical Journal* **1997,** *323* (3), 577-591.

209.   Liu, F.; Liang, Z.; Wegiel, J.; Hwang, Y. W.; Iqbal, K.; Grundke-Iqbal, I.; Ramakrishna, N.; Gong, C. X., Overexpression of Dyrk1A contributes to neurofibrillary degeneration in Down syndrome. *FASEB J* **2008,** *22* (9), 3224-33.

210.   Ittner, L. M.; Ke, Y. D.; Delerue, F.; Bi, M.; Gladbach, A.; van Eersel, J.; Wölfing, H.; Chieng, B. C.; Christie, M. J.; Napier, I. A.; Eckert, A.; Staufenbiel, M.; Hardeman, E.; Götz, J., Dendritic function of tau mediates amyloid-beta toxicity in Alzheimer's disease mouse models. *Cell* **2010,** *142* (3), 387-97.

211.   Woods, Y. L.; Cohen, P.; Becker, W.; Jakes, R.; Goedert, M.; Wang, X.; Proud, C. G., The kinase DYRK phosphorylates protein-synthesis initiation factor eIF2Bε at Ser539 and the microtubule-associated protein tau at Thr212 for DYRK as a glycogen synthase kinase 3-priming kinase. *Biochem J* **2001,** *355* (Pt 3), 609-15.

212.   Shi, J.; Zhang, T.; Zhou, C.; Chohan, M. O.; Gu, X.; Wegiel, J.; Zhou, J.; Hwang, Y.-W.; Iqbal, K.; Grundke-Iqbal, I.; Gong, C.-X.; Liu, F., Increased Dosage of Dyrk1A Alters Alternative Splicing Factor (ASF)-regulated Alternative Splicing of Tau in Down Syndrome. *Journal of Biological Chemistry* **2008,** *283* (42), 28660-28669.

213.   Lei, P.; Ayton, S.; Bush, A. I.; Adlard, P. A., GSK-3 in Neurodegenerative Diseases. *Int J Alzheimers Dis* **2011,** *2011*, 189246.

214.   Carreiras, C. M.; Mendes, E.; Perry, J. M.; Francisco, P. A.; Marco-Contelles, J., The Multifactorial Nature of Alzheimer's Disease for Developing Potential Therapeutics. *Current Topics in Medicinal Chemistry* **2013,** *13* (15), 1745-1770.

215.   Saha, P.; Sen, N., Tauopathy: A common mechanism for neurodegeneration and brain aging. *Mech Ageing Dev* **2019,** *178*, 72-79.

216.   Ramsay, R. R.; Popovic-Nikolic, M. R.; Nikolic, K.; Uliassi, E.; Bolognesi, M. L., A perspective on multi-target drug discovery and design for complex diseases. *Clinical and Translational Medicine* **2018,** *7* (1).

217.   Cavalli, A.; Bolognesi, M. L.; Minarini, A.; Rosini, M.; Tumiatti, V.; Recanatini, M.; Melchiorre, C., Multi-target-directed ligands to combat neurodegenerative diseases. *J Med Chem* **2008,** *51* (3), 347-72.

218.   Alcaro, S.; Bolognesi, M. L.; Garcia-Sosa, A. T.; Rapposelli, S., Editorial: Multi-Target-Directed Ligands (MTDL) as Challenging Research Tools in Drug Discovery: From Design to Pharmacological Evaluation. *Front Chem* **2019,** *7*, 71.

219.   Ramsay, R. R.; Popovic-Nikolic, M. R.; Nikolic, K.; Uliassi, E.; Bolognesi, M. L., A perspective on multi-target drug discovery and design for complex diseases. *Clin Transl Med* **2018,** *7*.

220.   De Simone, A.; Tumiatti, V.; Andrisano, V.; Milelli, A., Glycogen Synthase Kinase 3β: A New Gold Rush in Anti-Alzheimer's Disease Multitarget Drug Discovery? *Journal of Medicinal Chemistry* **2021,** *64* (1), 26-41.

221.   Morphy, R.; Kay, C.; Rankovic, Z., From magic bullets to designed multiple ligands. *Drug Discov Today* **2004,** *9* (15), 641-51.

222.   Morphy, R.; Rankovic, Z., Designed multiple ligands. An emerging drug discovery paradigm. *J Med Chem* **2005,** *48* (21), 6523-43.

223.   Zhou, J.; Jiang, X.; He, S.; Jiang, H.; Feng, F.; Liu, W.; Qu, W.; Sun, H., Rational Design of Multitarget-Directed Ligands: Strategies and Emerging Paradigms. *J Med Chem* **2019,** *62* (20), 8881-8914.

224.   Bain, J.; Plater, L.; Elliott, M.; Shpiro, N.; Hastie, C. J.; McLauchlan, H.; Klevernic, I.; Arthur, J. S.; Alessi, D. R.; Cohen, P., The selectivity of protein kinase inhibitors: a further update. *Biochem J* **2007,** *408* (3), 297-315.

225.   Laura, G.; Marinella, R.; Giovanni, B., Multi-Kinase Inhibitors. *Current Medicinal Chemistry* **2015,** *22* (6), 695-712.

226.   Schenone, S.; Brullo, C.; Musumeci, F.; Biava, M.; Falchi, F.; Botta, M., Fyn Kinase in Brain Diseases and Cancer: The Search for Inhibitors. *Current Medicinal Chemistry* **2011,** *18* (19), 2921-2942.

227.   Redenti, S.; Marcovich, I.; De Vita, T.; Perez, C.; De Zorzi, R.; Demitri, N.; Perez, D. I.; Bottegoni, G.; Bisignano, P.; Bissaro, M.; Moro, S.; Martinez, A.; Storici, P.; Spalluto, G.; Cavalli, A.; Federico, S., A Triazolotriazine-Based Dual GSK-3beta/CK-1delta Ligand as a Potential Neuroprotective Agent Presenting Two Different Mechanisms of Enzymatic Inhibition. *ChemMedChem* **2019,** *14* (3), 310-314.

228.   Lechner, C.; Flasshoff, M.; Falke, H.; Preu, L.; Loaec, N.; Meijer, L.; Knapp, S.; Chaikuad, A.; Kunick, C., [b]-Annulated Halogen-Substituted Indoles as Potential DYRK1A Inhibitors. *Molecules* **2019,** *24* (22), 1-19.

229.   Melchior, B.; Mittapalli, G. K.; Lai, C.; Duong-Polk, K.; Stewart, J.; Guner, B.; Hofilena, B.; Tjitro, A.; Anderson, S. D.; Herman, D. S.; Dellamary, L.; Swearingen, C. J.; Sunil, K. C.; Yazici, Y., Tau pathology reduction with SM07883, a novel, potent, and selective oral DYRK1A inhibitor: A potential therapeutic for Alzheimer's disease. *Aging Cell* **2019,** *18* (5), e13000.

230.   ACTRN12619000327189, A phase 1, open-label study evaluating the safety, tolerability, and pharmacokinetics of a single ascending dose of SM07883, a novel

DYRK1A inhibitor, following oral administration to healthy subjects. *Australian New Zealand Clinical Trials Registry* **2019**.

231.   Mariano, M.; Schmitt, C.; Miralinaghi, P.; Catto, M.; Hartmann, R. W.; Carotti, A.; Engel, M., First selective dual inhibitors of tau phosphorylation and Beta-amyloid aggregation, two major pathogenic mechanisms in Alzheimer's disease. *ACS Chem Neurosci* **2014,** *5* (12), 1198-202.

232.   Demuro, S.; Sauvey, C.; Tripathi, S. K.; Di Martino, R. M. C.; Shi, D.; Ortega, J. A.; Russo, D.; Balboni, B.; Giabbai, B.; Storici, P.; Girotto, S.; Abagyan, R.; Cavalli, A., ARN25068, a versatile starting point towards triple GSK-3β/FYN/DYRK1A inhibitors to tackle tau-related neurological disorders. *European Journal of Medicinal Chemistry* **2022,** *229*, 114054.

233.   Metz, J. T.; Johnson, E. F.; Soni, N. B.; Merta, P. J.; Kifle, L.; Hajduk, P. J., Navigating the kinome. *Nat Chem Biol* **2011,** *7* (4), 200-2.

234.   Zhao, Z.; Bourne, P. E. *Overview of Current Type I/II Kinase Inhibitors*; November 2018, 2018; pp 1-26.

235.   Ochoa, D.; Hercules, A.; Carmona, M.; Suveges, D.; Gonzalez-Uriarte, A.; Malangone, C.; Miranda, A.; Fumis, L.; Carvalho-Silva, D.; Spitzer, M.; Baker, J.; Ferrer, J.; Raies, A.; Razuvayevskaya, O.; Faulconbridge, A.; Petsalaki, E.; Mutowo, P.; Machlitt-Northen, S.; Peat, G.; McAuley, E.; Ong, C. K.; Mountjoy, E.; Ghoussaini, M.; Pierleoni, A.; Papa, E.; Pignatelli, M.; Koscielny, G.; Karim, M.; Schwartzentruber, J.; Hulcoop, D. G.; Dunham, I.; McDonagh, E. M., Open Targets Platform: supporting systematic drug-target identification and prioritisation. *Nucleic Acids Res* **2021,** *49* (D1), D1302-D1310.

236.   Martin, L.; Latypova, X.; Wilson, C. M.; Magnaudeix, A.; Perrin, M. L.; Yardin, C.; Terro, F., Tau protein kinases: involvement in Alzheimer's disease. *Ageing Res Rev* **2013,** *12* (1), 289-309.

237.   Eid, S.; Turk, S.; Volkamer, A.; Rippmann, F.; Fulle, S., KinMap: a web-based tool for interactive navigation through human kinome data. *BMC Bioinformatics* **2017,** *18* (1), 16.

238.   Shah, K.; Lahiri, D. K., Cdk5 activity in the brain - multiple paths of regulation. *J Cell Sci* **2014,** *127* (Pt 11), 2391-400.

239.   Allnutt, A. B.; Waters, A. K.; Kesari, S.; Yenugonda, V. M., Physiological and Pathological Roles of Cdk5: Potential Directions for Therapeutic Targeting in Neurodegenerative Disease. *ACS Chem Neurosci* **2020,** *11* (9), 1218-1230.

240.   Koyama, T.; Yamaotsu, N.; Nakagome, I.; Ozawa, S. I.; Yoshida, T.; Hayakawa, D.; Hirono, S., Multi-step virtual screening to develop selective DYRK1A inhibitors. *J Mol Graph Model* **2017,** *72*, 229-239.

241.   Guedj, F.; Pereira, P. L.; Najas, S.; Barallobre, M. J.; Chabert, C.; Souchet, B.; Sebrie, C.; Verney, C.; Herault, Y.; Arbones, M.; Delabar, J. M., DYRK1A: a master regulatory protein controlling brain growth. *Neurobiol Dis* **2012,** *46* (1), 190-203.

242.   Lee Walmsley, D.; Murray, J. B.; Dokurno, P.; Massey, A. J.; Benwell, K.; Fiumana, A.; Foloppe, N.; Ray, S.; Smith, J.; Surgenor, A. E.; Edmonds, T.; Demarles, D.; Burbridge, M.; Cruzalegui, F.; Kotschy, A.; Hubbard, R. E., Fragment-Derived Selective Inhibitors of Dual-Specificity Kinases DYRK1A and DYRK1B. *Journal of Medicinal Chemistry* **2021,** *64* (13), 8971-8991.

243.   Lakshman, M. K.; Tine, F. A.; Khandaker, T. A.; Basava, V.; Agyemang, N. B.; Benavidez, M. S. A.; Gaši, M.; Guerrera, L.; Zajc, B., KHF2: A Mild and Selective Desilylating Agent for Phenol tert-Butyldimethylsilyl (TBDMS) Ethers. *Synlett* **2017,** *28* (03), 381-385.

244.   Gu, J.; Chen, F.; Iqbal, K.; Gong, C. X.; Wang, X.; Liu, F., Transactive response DNA-binding protein 43 (TDP-43) regulates alternative splicing of tau exon

10: Implications for the pathogenesis of tauopathies. *J Biol Chem* **2017,** *292* (25), 10600-10612.

245.   Liu, Y. A.; Jin, Q.; Zou, Y.; Ding, Q.; Yan, S.; Wang, Z.; Hao, X.; Nguyen, B.; Zhang, X.; Pan, J.; Mo, T.; Jacobsen, K.; Lam, T.; Wu, T. Y.; Petrassi, H. M.; Bursulaya, B.; DiDonato, M.; Gordon, W. P.; Liu, B.; Baaten, J.; Hill, R.; Nguyen-Tran, V.; Qiu, M.; Zhang, Y. Q.; Kamireddy, A.; Espinola, S.; Deaton, L.; Ha, S.; Harb, G.; Jia, Y.; Li, J.; Shen, W.; Schumacher, A. M.; Colman, K.; Glynne, R.; Pan, S.; McNamara, P.; Laffitte, B.; Meeusen, S.; Molteni, V.; Loren, J., Selective DYRK1A Inhibitor for the Treatment of Type 1 Diabetes: Discovery of 6-Azaindole Derivative GNF2133. *J Med Chem* **2020,** *63* (6), 2958-2973.

246.   Lee, V. M.; Daughenbaugh, R.; Trojanowski, J. Q., Microtubule stabilizing drugs for the treatment of Alzheimer's disease. *Neurobiol Aging* **1994,** *15 Suppl 2*, S87-9.

247.   Das, G.; Ghosh, S., Why Microtubules Should Be Considered as One of the Supplementary Targets for Designing Neurotherapeutics. *ACS Chem Neurosci* **2019,** *10* (3), 1118-1120.

248.   Yao, Y.; Nzou, G.; Alle, T.; Tsering, W.; Maimaiti, S.; Trojanowski, J. Q.; Lee, V. M.; Ballatore, C.; Brunden, K., Correction of microtubule defects within Aβ plaque-associated dystrophic axons results in lowered Aβ release and plaque deposition. *Alzheimer's Dement.* **2020**, 1-13.

249.   Zhang, B.; Yao, Y.; Cornec, A.-S.; Oukoloff, K.; James, M. J.; Koivula, P.; Trojanowski, J. Q.; Smith, A. B.; Lee, V. M.-Y.; Ballatore, C.; Brunden, K. R., A brain-penetrant triazolopyrimidine enhances microtubule-stability, reduces axonal dysfunction and decreases tau pathology in a mouse tauopathy model. *Molecular Neurodegeneration* **2018,** *13* (1), 59.

250.   Makani, V.; Zhang, B.; Han, H.; Yao, Y.; Lassalas, P.; Lou, K.; Paterson, I.; Lee, V. M. Y.; Trojanowski, J. Q.; Ballatore, C.; Smith, A. B.; Brunden, K. R.,

Evaluation of the brain-penetrant microtubule-stabilizing agent, dictyostatin, in the PS19 tau transgenic mouse model of tauopathy. *Acta Neuropathologica Communications* **2016,** *4* (1), 1-12.

251.   Zhang, B.; Carroll, J.; Trojanowski, J. Q.; Yao, Y.; Iba, M.; Potuzak, J. S.; Hogan, A. M.; Xie, S. X.; Ballatore, C.; Smith, A. B., 3rd; Lee, V. M.; Brunden, K. R., The microtubule-stabilizing agent, epothilone D, reduces axonal dysfunction, neurotoxicity, cognitive deficits, and Alzheimer-like pathology in an interventional study with aged tau transgenic mice. *J. Neurosci.* **2012,** *32* (11), 3601-11.

252.   Brunden, K. R.; Zhang, B.; Carroll, J.; Yao, Y.; Potuzak, J. S.; Hogan, A. M.; Iba, M.; James, M. J.; Xie, S. X.; Ballatore, C.; Smith, A. B., 3rd; Lee, V. M.; Trojanowski, J. Q., Epothilone D improves microtubule density, axonal integrity, and cognition in a transgenic mouse model of tauopathy. *J Neurosci* **2010,** *30* (41), 13861-6.

253.   Alle, T.; Varricchio, C.; Yao, Y.; Lucero, B.; Nzou, G.; Demuro, S.; Muench, M.; Vuong, K. D.; Oukoloff, K.; Cornec, A.-S.; Francisco, K. R.; Caffrey, C. R.; Lee, V. M. Y.; Smith, A. B., III; Brancale, A.; Brunden, K. R.; Ballatore, C., Microtubule-Stabilizing 1,2,4-Triazolo[1,5-a]pyrimidines as Candidate Therapeutics for Neurodegenerative Disease: Matched Molecular Pair Analyses and Computational Studies Reveal New Structure–Activity Insights. *Journal of Medicinal Chemistry* **2023,** *66* (1), 435-459.

254.   Saez-Calvo, G.; Sharma, A.; Balaguer, F. A.; Barasoain, I.; Rodriguez-Salarichs, J.; Olieric, N.; Munoz-Hernandez, H.; Berbis, M. A.; Wendeborn, S.; Penalva, M. A.; Matesanz, R.; Canales, A.; Prota, A. E.; Jimenez-Barbero, J.; Andreu, J. M.; Lamberth, C.; Steinmetz, M. O.; Diaz, J. F., Triazolopyrimidines Are Microtubule-Stabilizing Agents that Bind the Vinca Inhibitor Site of Tubulin. *Cell Chem Biol* **2017,** *24* (6), 737-750 e6.

255.   Ojima, I., Tumor-targeting drug delivery of chemotherapeutic agents. *Pure and Applied Chemistry* **2011,** *83* (9), 1685-1698.

256.   Kovalevich, J.; Cornec, A. S.; Yao, Y.; James, M.; Crowe, A.; Lee, V. M.; Trojanowski, J. Q.; Smith, A. B.; Ballatore, C.; Brunden, K. R., Characterization of brain-penetrant pyrimidine-containing molecules with differential microtubule-stabilizing activities developed as potential therapeutic agents for Alzheimer's disease and related tauopathies. *J. Pharmacol. Exp. Ther.* **2016,** *357* (2), 432-50.

257.   Zhang, B.; Maiti, A.; Shively, S.; Lakhani, F.; McDonald-Jones, G.; Bruce, J.; Lee, E. B.; Xie, S. X.; Joyce, S.; Li, C.; Toleikis, P. M.; Lee, V. M. Y.; Trojanowski, J. Q., Microtubule-binding drugs offset tau sequestration by stabilizing microtubules and reversing fast axonal transport deficits in a tauopathy model. *Proc. Natl. Acad. Sci. U. S. A.* **2005,** *102* (1), 227-231.

258.   Cruciani, G.; Carosati, E.; De Boeck, B.; Ethirajulu, K.; Mackie, C.; Howe, T.; Vianello, R., MetaSite: Understanding Metabolism in Human Cytochromes from the Perspective of the Chemist. *Journal of Medicinal Chemistry* **2005,** *48* (22), 6970-6979.

259.   Bachmann, K., Chapter 8 - Drug Metabolism. In *Pharmacology*, Hacker, M.; Messer, W.; Bachmann, K., Eds. Academic Press: San Diego, 2009; pp 131-173.

260.   Stanley, L. A., Chapter 27 - Drug Metabolism. In *Pharmacognosy*, Badal, S.; Delgoda, R., Eds. Academic Press: Boston, 2017; pp 527-545.

261.   Conner, M. L.; Xu, Y.; Brown, M. K., Catalytic enantioselective allenoate-alkene [2 + 2] cycloadditions. *J Am Chem Soc* **2015,** *137* (10), 3482-5.

262.   Varidaki, A.; Hong, Y.; Coffey, E. T., Repositioning Microtubule Stabilizing Drugs for Brain Disorders. *Front Cell Neurosci* **2018,** *12*, 226.

263.   Wang-Gillam, A.; Arnold, S. M.; Bukowski, R. M.; Rothenberg, M. L.; Cooper, W.; Wang, K. K.; Gauthier, E.; Lockhart, A. C., A phase I dose escalation

study of TTI-237 in patients with advanced malignant solid tumors. *Invest New Drugs* **2012,** *30* (1), 266-72.

264.   Yang, J.; Yu, Y.; Li, Y.; Yan, W.; Ye, H.; Niu, L.; Tang, M.; Wang, Z.; Yang, Z.; Pei, H.; Wei, H.; Zhao, M.; Wen, J.; Yang, L.; Ouyang, L.; Wei, Y.; Chen, Q.; Li, W.; Chen, L., Cevipabulin-tubulin complex reveals a novel agent binding site on α-tubulin with tubulin degradation effect. *Science Advances* **2021,** *7* (21), eabg4168.

265.   Sanches, B. M. A.; Ferreira, E. I., Is prodrug design an approach to increase water solubility? *International Journal of Pharmaceutics* **2019,** *568*.

266.   Xia, X.; Zhou, Y.; Gao, H., Prodrug strategy for enhanced therapy of central nervous system disease. *Chem Commun (Camb)* **2021,** *57* (71), 8842-8855.

267.   Walther, R.; Rautio, J.; Zelikin, A. N., Prodrugs in medicinal chemistry and enzyme prodrug therapies. *Adv Drug Deliv Rev* **2017,** *118*, 65-77.

268.   Abet, V.; Filace, F.; Recio, J.; Alvarez-Builla, J.; Burgos, C., Prodrug approach: An overview of recent cases. *Eur J Med Chem* **2017,** *127*, 810-827.

269.   Rautio, J.; Meanwell, N. A.; Di, L.; Hageman, M. J., The expanding role of prodrugs in contemporary drug design and development. *Nat Rev Drug Discov* **2018,** *17* (8), 559-587.

270.   Meng, Z.; Lv, Q.; Lu, J.; Yao, H.; Lv, X.; Jiang, F.; Lu, A.; Zhang, G., Prodrug Strategies for Paclitaxel. *Int J Mol Sci* **2016,** *17* (5).

271.   Ballatore, C.; Aspland, S. E.; Castillo, R.; Desharnais, J.; Eustaquio, T.; Sun, C.; Castellino, A. J.; Smith, A. B., 3rd, A facile route to paclitaxel C-10 carbamates. *Bioorg Med Chem Lett* **2005,** *15* (10), 2477-80.

272.   Ayalew, L.; Acuna, J.; Urfano, S. F.; Morfin, C.; Sablan, A.; Oh, M.; Gamboa, A.; Slowinska, K., Conjugation of Paclitaxel to Hybrid Peptide Carrier and Biological Evaluation in Jurkat and A549 Cancer Cell Lines. *ACS Med Chem Lett* **2017,** *8* (8), 814-819.

273.   Ojima, I.; Geng, X.; Wu, X.; Qu, C.; Borella, C. P.; Xie, H.; Wilhelm, S. D.; Leece, B. A.; Bartle, L. M.; Goldmacher, V. S.; Chari, R. V., Tumor-specific novel taxoid-monoclonal antibody conjugates. *J Med Chem* **2002,** *45* (26), 5620-3.

274.   López Mendoza, C. M.; Alcántara Quintana, L. E., Smart Drug Delivery Strategies for Cancer Therapy. *Frontiers in Nanotechnology* **2022,** *3*.

275.   Cohen, F.; Aggen, J. B.; Andrews, L. D.; Assar, Z.; Boggs, J.; Choi, T.; Dozzo, P.; Easterday, A. N.; Haglund, C. M.; Hildebrandt, D. J.; Holt, M. C.; Joly, K.; Jubb, A.; Kamal, Z.; Kane, T. R.; Konradi, A. W.; Krause, K. M.; Linsell, M. S.; Machajewski, T. D.; Miroshnikova, O.; Moser, H. E.; Nieto, V.; Phan, T.; Plato, C.; Serio, A. W.; Seroogy, J.; Shakhmin, A.; Stein, A. J.; Sun, A. D.; Sviridov, S.; Wang, Z.; Wlasichuk, K.; Yang, W.; Zhou, X.; Zhu, H.; Cirz, R. T., Optimization of LpxC Inhibitors for Antibacterial Activity and Cardiovascular Safety. *ChemMedChem* **2019,** *14* (16), 1560-1572.

276.   Le Corre, S. S.; Berchel, M.; Couthon-Gourves, H.; Haelters, J. P.; Jaffres, P. A., Atherton-Todd reaction: mechanism, scope and applications. *Beilstein J Org Chem* **2014,** *10*, 1166-96.

277.   Evans, P. R.; Murshudov, G. N., How good are my data and what is the resolution? *Acta Crystallographica Section D* **2013,** *69* (7), 1204-1214.

278.   McCoy, A. J.; Grosse-Kunstleve, R. W.; Adams, P. D.; Winn, M. D.; Storoni, L. C.; Read, R. J., Phaser crystallographic software. *J Appl Crystallogr* **2007,** *40* (Pt 4), 658-674.

279.   Murshudov, G. N.; Vagin, A. A.; Dodson, E. J., Refinement of macromolecular structures by the maximum-likelihood method. *Acta Crystallogr D Biol Crystallogr* **1997,** *53* (Pt 3), 240-55.

280.   Emsley, P.; Lohkamp, B.; Scott, W. G.; Cowtan, K., Features and development of Coot. *Acta Crystallogr D Biol Crystallogr* **2010,** *66* (Pt 4), 486-501.

281.   DeLano, W. L., Pymol: An open-source molecular graphics tool. *CCP4 Newsl. Protein Crystallogr* **2002,** *40* (1), 82-92.

282.   Neves, M. A. C.; Totrov, M.; Abagyan, R., Docking and scoring with ICM: the benchmarking results and strategies for improvement. *Journal of Computer-Aided Molecular Design* **2012,** *26* (6), 675-686.

283.   Kovalevich, J.; Cornec, A. S.; Yao, Y.; James, M.; Crowe, A.; Lee, V. M.; Trojanowski, J. Q.; Smith, A. B., 3rd; Ballatore, C.; Brunden, K. R., Characterization of Brain-Penetrant Pyrimidine-Containing Molecules with Differential Microtubule-Stabilizing Activities Developed as Potential Therapeutic Agents for Alzheimer's Disease and Related Tauopathies. *J Pharmacol Exp Ther* **2016,** *357* (2), 432-50.

284.   Lou, K.; Yao, Y.; Hoye, A. T.; James, M. J.; Cornec, A. S.; Hyde, E.; Gay, B.; Lee, V. M.; Trojanowski, J. Q.; Smith, A. B., 3rd; Brunden, K. R.; Ballatore, C., Brain-penetrant, orally bioavailable microtubule-stabilizing small molecules are potential candidate therapeutics for Alzheimer's disease and related tauopathies. *J Med Chem* **2014,** *57* (14), 6116-27.

285.   Cornec, A. S.; James, M. J.; Kovalevich, J.; Trojanowski, J. Q.; Lee, V. M.; Smith, A. B., 3rd; Ballatore, C.; Brunden, K. R., Pharmacokinetic, pharmacodynamic and metabolic characterization of a brain retentive microtubule (MT)-stabilizing triazolopyrimidine. *Bioorg Med Chem Lett* **2015,** *25* (21), 4980-4982.

Acknowledgements

I would like to express my heartfelt gratitude to my supervisor, Professor Andrea Cavalli, for providing me with exceptional guidance throughout my Ph. D. journey. I am deeply grateful to him for giving me the opportunity to work on this project and for his invaluable support and encouragement.

I also extend my sincere thanks to Professor Ruben Abagyan, who, together with Professor Cavalli, conceptualized the idea behind the project. I had the privilege of meeting him during my time as a visiting student in San Diego, and his insights and advice proved invaluable to me.

My co-supervisor, Dr. Rita Di Martino, deserves special recognition for teaching me how to be a meticulous scientist and for fostering my critical thinking skills. Her outstanding supervision and her invaluable human support has been instrumental in my growth as a researcher.

I am also deeply grateful to Dr. Samuel Myers, who provided unwavering support and assistance during the final phase of my project. His contributions were invaluable to its successful completion.

I would like to thank Dr. Viola Previtali, for her constant support and encouragement throughout my studies. I must also acknowledge the invaluable support of the chemists in Professor Cavalli's Group, particularly Andrea Ciamarone who recently started his Ph.D. and Dr. Jose Ortega, who was always there to offer assistance and guidance.

My stay at IIT would not have been the same without the support of the colleagues in the D3 department, particularly Dr. Luce Mattio, whose presence brought positivity and light to my studies.

I am grateful to Professor Carlo Ballatore for hosting me in his lab at UCSD, where I had the privilege of meeting and working alongside brilliant and talented researchers, including Dr. Thibault Alle, Almost-Dr. Bobby Lucero, Dr. Karol Francisco, and Darius Yohannan.

I would also like to express my gratitude to all the friends I made in California, particularly Marta, and to my oldest friends Sara, Claudia e Martina, who have always been there to support me in all my adventures.

Finally, I would like to thank Andrea, whose unwavering support and love have been a constant source of strength throughout my studies. And last but not least, my heartfelt thanks go to my parents, who are the real heroes of this story. Without their love, guidance, and support, none of this would have been possible.

Ad maiora